Author:
Heinen, Benedict J

Title:
Internal resistive heating techniques in the diamond anvil cell

Internal Resistive Heating Techniques in the Diamond Anvil Cell

Benedict J. Heinen

Supervisors: Oliver T. Lord and Simon C. Kohn

School of Earth Sciences
University of Bristol

A dissertation submitted to the University of Bristol in accordance with the requirements for award of the degree of Doctor of Philosophy in the Faculty of Science

Word Count: 45870

Abstract

Recreating the extreme conditions of the deep Earth and other planetary interiors poses significant experimental difficulty. The primary tool for investigations of material properties at high pressure and temperature is the laser-heated diamond anvil cell. Laser heating can routinely generate temperatures of many thousand Kelvin at pressures well into the megabar range, but large thermal gradients and poor temperature stability introduces significant uncertainty, limits the accuracy of measured data, and prohibits analyses requiring long acquisition times. Resistive heating techniques provide greater temperature stability, more precise control, reduced thermal gradients, and temperature uncertainties an order of magnitude smaller. However, resistive heaters external to the diamond anvils are limited in accessible temperature range and cannot recreate the conditions of the Earth's lower mantle as the unpressurised diamonds begin to graphitise beyond ∼1500 K. Internal resistive heating (IRH), in which heat is generated only within the pressure chamber, can extend the accessible temperature range significantly. Experiments in which the metallic heater doubles as the sample can be performed up to several thousand Kelvin, but existing designs applicable to non-metallic samples are limited to 1900 K at pressures beyond 10 GPa.

Here I describe the development of a new IRH design capable of generating temperatures well in excess of 3000 K across a pressure range equivalent to 1000 km depth within the Earth. A novel 'split-gasket' approach is adopted which reduces the technical difficulty of performing IRH experiments, improves the isolation of the heating filament, and allows extremely stable, homogeneous heating of both metallic and non-metallic samples. The application of IRH to studies of both solids and melts is investigated and discussed. The IRH design is well suited for the rapid collection of high-resolution *P-V-T* datasets, the precise demarcation of phase boundaries (including melting), and for experiments requiring long acquisition times at high temperature. The IRH technique is also well suited to stabilising large volumes of melt at high-pressure, and tools for the analysis of liquid x-ray diffuse scattering data are developed and described. IRH provides a new and accessible tool for investigating material properties at extreme conditions.

Author's Declaration

I declare that the work in this dissertation was carried out in accordance with the requirements of the University's Regulations and Code of Practice for Research Degree Programmes and that it has not been submitted for any other academic award. Except where indicated by specific reference in the text, the work is the candidate's own work. Work done in collaboration with, or with the assistance of, others, is indicated as such. Any views expressed in the dissertation are those of the author.

SIGNED: ..... DATE: 16th March 2022

Acknowledgements

This thesis would not have been possible without a huge number of people who have helped in some way over the last four and a half years, and I would like to thank all the people who have collaborated on projects, given me advice or support, been excellent friends, and/or spent many long hours with me eating bad food and measuring things at the synchrotron.

Firstly, I would like to thank my supervisor, Oliver Lord, who provided a huge amount of advice and guidance over the years, spent many long hours with me in the lab, and always believed that IRH would work (even when no one else did). Thank you also to Simon Kohn, for stepping in as a co-supervisor and providing much needed guidance along the way. A big thank you to James Drewitt, for involving me on lots of projects and introducing me to the world of liquid total scattering. Special thanks also to Mike Walter, who guided me onto the path of becoming a high-pressure scientist.

Thank you to all the staff of the Earth Sciences workshop, particularly Charles Clapham and Gerald Mwale, for accommodating my requests to make all manner of components, borrow tools, and figure out odd screw sizes. Thank you to all the former members of the Bristol DAC-Lab who helped run experiments, collaborated, and/or sat through a lot of beamtime: David Edwards, Fei Qin, Chris Gregson, Marion Louvel, and Marzena Baron. Thank you to Andy Thomson at UCL for beamtime collaborations and providing data. Thank you to the beamline staff at I15 — Simone Anzellini, Annette Kleppe, and Dominik Daisenberger — who provided assistance during beamtime.

A big thank you to all my friends who have made the years so enjoyable: the G6 occupants, lab denizens, department friends, transitions crew, and 141 inhabitants. In lieu of taking two pages to thank everyone individually, here is a long list of things I am thankful to my friends for: climbs, pints, bicycles, gigs, music, long walks, tea, haircuts, adventures, board-games, wine, general fun, tents, advice, toast, wild swims, top-notch friendship, painting, tea, roasts, pints, dancing, camping, keeping me sane in lockdown, pints, science chat, non-science chat, very-non-science chat, good food, films, plants, and biscuits; and here is a long list of friends I am thankful to: Damaris, Jacob, Jen, Bob, Ailsa, Will, Ellie, Alex, Pradip, Apostolia, Fran, Max, Santi, George, Hannah, David, Pat, Kuba, Chris, Keith, Frances, Nick, Tim, Tom, Adam, Rich, Josh and Bonnie.

Finally, thank you to my family for putting up with me being 'busy' for the last four and a half years.

Contents

List of Figures

List of Tables

Chapter 1

Introduction

In 1989, after nearly two decades of drilling, the Kola Superdeep Borehole SG-3, located in the Arctic circle near the Russia-Norway border, reached a depth of 12,262 metres. The base of this borehole is the deepest point ever reached, yet although the drilling extended a third of the way through the continental crust of the Baltic Shield, this represents less than 0.2% of the distance to the planet's centre. Partial melting of the mantle at mid-ocean ridges, tectonic fragments of exhumed mantle rocks, and mantle xenoliths entrained in crustal rocks provide direct sampling of the uppermost mantle (Ringwood, 1975), and inclusions found in rare 'super-deep' diamonds that may originate at depths up to 1000 km offer windows into the deep Earth (e.g., Walter et al., 2011; Kaminsky, 2012; Pearson et al., 2014). However, as a consequence of the extreme conditions of pressure (P) and temperature (T) in the deep interior, the vast majority of the planet will forever remain inaccessible. Investigations of the planetary interior must therefore rely on geophysical remote sensing, numerical models, or simulating the conditions of the deep Earth in the laboratory.

1.1 The Lower Mantle

1.1.1 Internal Structure of the Earth and the Lower Mantle

The principal data that allow us a first order picture of Earth's interior are seismological. Compilations of global seismic travel times allow the construction of one-dimensional, radially averaged seismological profiles of the Earth which relate density to depth (Figure 1.1; e.g., Dziewonski & Anderson, 1981; Kennett et al., 1995). These models allow us to see the major internal structure of the Earth. In the simplest model the Earth consists of a metallic core and a rocky silicate mantle-crust. The Earth's core, primarily composed of an iron-nickel alloy, is separated into a liquid outer

core and a solid inner core with the boundary (inner core boundary, ICB) at ∼5150 km depth (e.g., see Terasaki & Fischer, 2016). Continual growth of the inner core by freezing of the liquid outer core at the ICB is the likely driver of convection currents in the outer core which in turn drive the geodynamo responsible for Earth's magnetic field (Jacobs, 1953; Lister & Buffett, 1995; Buffett, 2000; Gubbins et al., 2008). Beneath the crust (∼5 to 70 km) lies the Earth's silicate mantle, which is bounded at its base by the core-mantle boundary at ∼2890 km. The mantle is separated into upper and lower units by a transition zone, bounded by major seismic discontinuities at ∼410 and ∼660 km. The lower mantle is the largest of these structural Earth units, comprising nearly 50% of the planet by mass, and 56% by volume (Dziewonski & Anderson, 1981). Consequently, it is the largest reservoir for many elements, and small compositional variations have the potential to hugely bias elemental budgets for the bulk Earth. The lower mantle stores a record of both planetary formation processes and the exchange of material between the exosphere and deep interior over the course of Earth's history. Therefore, knowledge of the physical and chemical characteristics of the lower mantle provides important constraints on the evolution of our planet.

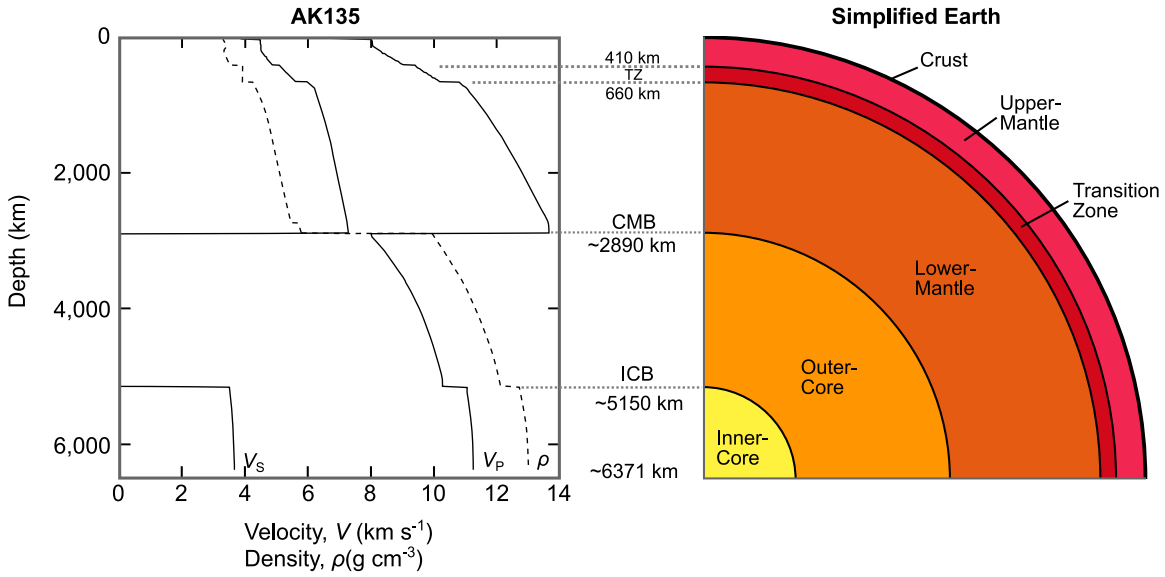

Figure 1.1: *Seismic structure of the Earth detailed by the AK135 velocity model (Kennett et al., 1995), along with a simplified cartoon of major Earth structure. Seismic discontinuities delineate the boundaries between major Earth units. V_S drops to zero in the outer core as it is liquid. The sudden drop in V_P at the ICB despite a density increase is due to the change in composition from the silicate mantle to the iron core.*

1.1.2 Heterogeneity in the Lower Mantle

One-dimensional radially averaged seismic profiles are not truly representative of actual three-dimensional Earth structure, and in particular can obscure the significant lateral heterogeneity that appears to exist (Helffrich, 2006; French & Romanowicz, 2014; Tkalčić et al., 2015; Ritsema & Lekić, 2020). In the lower mantle, seismic tomography reveals two vast low shear-wave velocity anomalies beneath Africa and the Pacific, termed large low shear-wave velocity provinces (LLSVPs; e.g., Mégnin & Romanowicz, 2000; Garnero & McNamara, 2008; Simmons et al., 2009; Ritsema et al., 2011; French & Romanowicz, 2014; Garnero et al., 2016). The observed anti-correlation between shear wave and bulk sound velocities along with the anti- or de-correlation of shear-wave velocity and density within LLSVPs suggests temperature alone is unlikely to provide an explanation for these features (e.g., Su & Dziewonski, 1997; Trampert et al., 2004; Hernlund & Houser, 2008; Mosca et al., 2012; Koelemeijer et al., 2016; Moulik & Ekström, 2016). LLSVPs have been implicated in plume generation due to their spatial correlation with hot spots and the reconstructed eruption sites of large igneous provinces, along with tomographic evidence for plume structures rooted at LLSVP margins (e.g., Torsvik et al., 2006, 2008; Austermann et al., 2014; Davies et al., 2015; French & Romanowicz, 2015; Doubrovine et al., 2016). As such, LLSVPs may provide an explanation for the anomalous geochemical signatures of ocean-island basalts that appear to indicate segregated reservoirs in the deep Earth (Zindler & Hart, 1986; White, 2010). Such material may have segregated early in Earth's history from the crystallisation of a basal magma ocean (e.g., Allègre et al., 1987; Trieloff et al., 2000; Boyet & Carlson, 2006; Labrosse et al., 2007; Jackson et al., 2010; Deschamps et al., 2011; Jackson & Carlson, 2011; Nakagawa & Tackley, 2014), or have accumulated over time as oceanic lithosphere is recycled back into the deep interior (e.g., Christensen & Hofmann, 1994; Coltice & Ricard, 1999; Brandenburg & Van Keken, 2007; Brandenburg et al., 2008; Rapp et al., 2008; Mulyukova et al., 2015). Combined evidence from seismic tomography and geodynamic modelling suggests that subducted oceanic crust can reach lower mantle depths, stagnating at the base of the transition zone, mid-lower mantle, or near the CMB (e.g., Li et al., 2008; Fukao & Obayashi, 2013; Obayashi et al., 2013; French & Romanowicz, 2014; Schmandt & Lin, 2014; Ballmer et al., 2015; Marquardt & Miyagi, 2015; Portner et al., 2020; Rodríguez et al., 2021). Evidence for slab subduction into the lower mantle and upwelling plumes throughout the mantle could be taken to imply efficient mixing, but geodynamic modelling suggests viscosity contrasts can preserve compositionally distinct regions over geologically significant timescales (Yamazaki & Karato, 2001; Ballmer et al., 2017; McNamara, 2019). Subducted oceanic crust would have a different composition to the bulk mantle, and so provides a mechanism to introduce significant heterogeneity into the lower mantle even if primordial domains do not exist (Helffrich & Wood, 2001).

Subduction may also return volatiles, including water, to the deep Earth. Computational studies suggest ∼30% of the subduction zone water input (bound in the downgoing slab and sediments) may reach beyond the depths of magma production at the arc front, constituting a significant return flux of exospheric water to the deep Earth (van Keken et al., 2011; Parai & Mukhopadhyay, 2012). In the lower mantle, water may be stored in hydrous minerals (particularly along a cool subduction geotherm; Ohtani et al., 2004; Komabayashi et al., 2005; Nishi et al., 2014; Walter et al., 2015; Ohtani, 2021), or incorporated as hydrogen point defects in the crystal structures of nominally anhydrous minerals (NAMs; e.g., Bell & Rossman, 1992; Bolfan-Casanova, 2005). Hydrogen point defects are known to reduce creep strength and viscosity, speeding up diffusive processes and convection that drives the tectonic engine (Chen et al., 1998; Mei & Kohlstedt, 2000; Regenauer-Lieb et al., 2001). At boundaries with a contrast in water storage capacity, water may also exist as a free fluid phase, leading to flux melting that has a huge influence on chemical differentiation and mass transfer, triggering volcanism at the surface and affecting the cycling of incompatible elements (Bercovici & Karato, 2003; Tatsumi, 2005; Hirschmann, 2006; Ohtani, 2020; Drewitt et al., 2022). The water content of the deep Earth is poorly constrained (e.g., see Bell & Rossman, 1992; Bolfan-Casanova, 2005; Hirschmann, 2006; Ohtani, 2021), but water-rich inclusions in 'super-deep' diamonds suggest it is at least locally hydrous (e.g., Pearson et al., 2014).

There are several other mechanisms that could lead to the presence of melt in the lower mantle. Melt layers or pockets may exist as remnants of a global magma ocean (e.g., Labrosse et al., 2007), form by extrusion of Fe-rich material from the core (e.g., Otsuka & Karato, 2012), or by partial melting of subducted MORB material in the lowermost mantle (e.g., Andrault et al., 2014a; Baron et al., 2017). Melt layers may provide an explanation for ultra-low velocity zones (ULVZs) observed near the CMB (e.g., Kendall & Silver, 1996; Williams & Garnero, 1996; Hall et al., 2004; Rost et al., 2005; Idehara, 2011; Cottaar & Romanowicz, 2012; Liu et al., 2016; Yuan & Romanowicz, 2017; Kim et al., 2019). ULVZs are likely to represent Fe-rich material, as this can account for the significant modelled density anomalies (∼10% increase) that best explain the observed seismic characteristics (Rost et al., 2005; McNamara, 2019). However, no consensus on their mode of formation has been reached (e.g., Otsuka & Karato, 2012; Andrault et al., 2014a; Brown et al., 2015; Pradhan et al., 2015; McNamara, 2019; Dannberg et al., 2021; Jenkins et al., 2021; Pachhai et al., 2022). Melt layers may also explain observed seismic anisotropy in the lower-most mantle, as even a tiny volume fraction of melt is likely to result in a seismically measurable signal (Kendall & Silver, 1998). Seismic anisotropy may also be a result of lattice preferred orientation produced by the dislocation creep deformation mechanisms of the lower mantle (e.g., Karato, 1998; McNamara et al., 2003; Cordier et al., 2004; Wenk et al., 2006; Hunt et al., 2009; Vanacore & Niu, 2011; Dobson et al., 2019; Ferreira et al., 2019; Fu et al., 2019b).

While seismic imaging provides direct information about the Earth's interior, it cannot easily distinguish between the effects of temperature, chemistry and phase relations. Theoretically, mantle mineralogy and temperature can be constrained by comparing seismic observations with accurate models of velocity structure for a given composition. Such inversions require accurate mineral physics data as a function of P and T for minerals expected to be present in the deep Earth, as well as knowledge of which phases are relevant along with their expected proportions by constraining the phase relations for a given bulk composition at lower mantle conditions. While high-P-T mineral physics and petrology have been active areas of research for many decades, significant uncertainties still exist for much this data. In the remainder of this chapter I will give a brief overview of constraints on the composition and mineralogy of the lower mantle from high-P-T experiments, and current mineral physics data for lower mantle phases. This is followed by an introduction to the experimental and analytical techniques used to derive these data, as well as a discussion of current high-P-T techniques used to generate extreme conditions and their limitations.

1.1.3 Mineralogy and Petrology of the Lower Mantle

The upper mantle is widely accepted to have a pyrolitic composition based on direct sampling (e.g., at mid-ocean ridges and xenoliths in crustal rocks; Ringwood, 1975; McDonough & Rudnick, 1998), but the chemistry of the lower mantle is not as well constrained. A homogeneous mantle (i.e., a pyrolitic lower mantle) was first proposed based on the fact that the 410 and 660 km discontinuities can be explained by isochemical phase transitions of olivine without invoking chemical layering (Ito & Takahashi, 1989). Most recent studies comparing measured or computed thermoelastic properties of lower mantle phases with radially averaged seismological reference models support this for the bulk lower mantle (Wang et al., 2015b; Sun et al., 2016; Kurnosov et al., 2017, 2018), although there is still some debate (Ricolleau et al., 2009; Murakami et al., 2012; Lin et al., 2018; Mashino et al., 2020). Furthermore, as described above, it appears clear that there are compositionally distinct domains (e.g., Dziewonski, 1984; Helffrich, 2006; Garnero & McNamara, 2008; French & Romanowicz, 2014; Tkalčić et al., 2015; McNamara, 2019).

The mineralogy of a pyrolitic composition is expected to be fairly simple throughout the range of lower mantle conditions. The perovskite structured mineral bridgmanite ($(Mg,Fe)(Si,Al)O_3$) is expected to comprise the majority of a pyrolitic lower mantle ($\sim$75 vol.%), with ferropericlase ($(Mg,Fe)O$) and calcium silicate perovskite ($CaSiO_3$) completing the assemblage ($\sim$18 and $\sim$7–8 vol.% respectively; e.g., Irifune et al., 2010; Fig. 1.2). At conditions corresponding to $\sim$2600 km depth ($\sim$120 GPa and 2500 K), bridgmanite undergoes a phase transition to a $CaIrO_3$-type structure — post-perovskite (Murakami et al., 2004; Oganov & Ono, 2004; Tateno et al., 2009). This transition, along with lattice preferred orientation of post-perovskite, may explain observed seismic

discontinuities and anisotropy in the D″ layer near the CMB (e.g., Iitaka et al., 2004; Wookey & Kendall, 2007; Miyagi et al., 2010). However, temperature variations in the deep mantle may mean that post-perovskite is not globally present due to the positive Clapeyron slope of the transition, or that double-crossings of the transition occur (Hernlund et al., 2005; Wookey et al., 2005). Computational evidence also suggests bridgmanite and calcium perovskite may form a single solid solution in hot, ferrous-iron rich (and Al-deficient) regions of the lowermost mantle (Muir et al., 2021), although the experimental evidence for this is inconclusive (Sinmyo & Hirose, 2013; Gu et al., 2016; Creasy et al., 2020a).

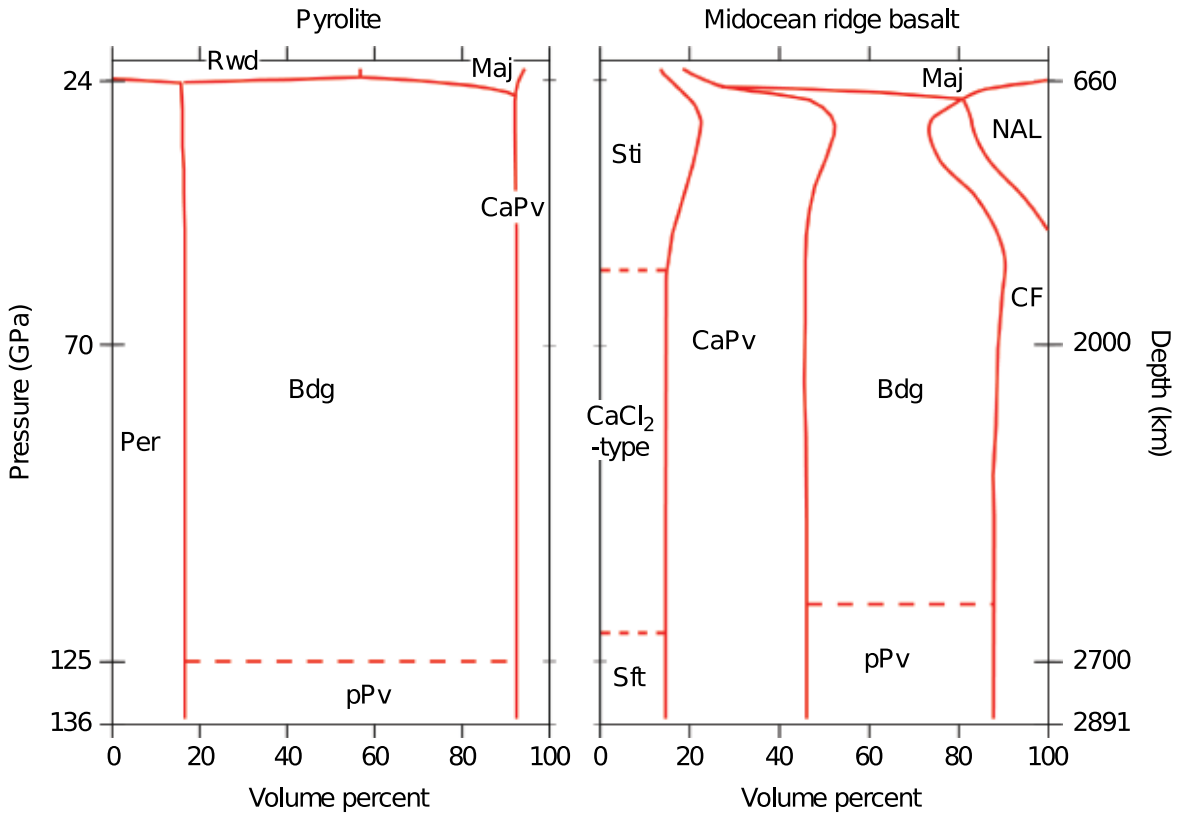

Figure 1.2: *Expected phase assemblages and proportions for pyrolite and MORB compositions in the lower mantle. Dashed lines indicate isochemical phase transitions. Abbreviations: Bdg, bridgmanite; Per, ferropericlase; CaPv, calcium-silicate perovskite; pPv, post-perovskite; Sti, stishovite; $CaCl_2$-type, $CaCl_2$-type SiO_2 (post-stishovite); Sft, seifertite; Rwd, ringwoodite; Maj, majorite; NAL, new aluminous phase; CF, calcium-ferrite type phase. Figure reprinted with permission from Wicks & Duffy, 2016 (based on data from Hirose et al., 2005, Irifune et al., 2010, and Ricolleau et al., 2010). © 2016 American Geophysical Union.*

Recycled oceanic crust in the deep interior is expected to have a significantly different phase assemblage. At lower mantle conditions subducted MORB material may be composed of up to 30% $CaSiO_3$ perovskite, 25% aluminous phases (the 'new aluminous phase', NAL, $<\sim$50 GPa and Ca-ferrite structured phase, CF-phase, at higher pressures) and up to 20% free-silica as stishovite or its higher pressure polymorphs post-stishovite (with the $CaCl_2$ structure) and seifertite (Figure 1.2; e.g., Ricolleau et al., 2010). Bridgmanite is likely to be much less abundant, comprising 20–50% of the phase assemblage depending on *P*-*T* conditions (Fig. 1.2). This assemblage may also be an important host for water in downgoing slabs (e.g., Bolfan-Casanova, 2005; Heinen, 2017; Ohtani, 2021). Alternatively, water in subducted slabs may be sequestered in a series of hydrous phases. Experiments suggest hydrous phases can be stabilised throughout the full range of mantle pressures (e.g., see the reviews by Ohtani, 2015, 2021). These phases may be important water carriers to the deep mantle but are unlikely to be stable outside of cold subducting slabs (Ohtani et al., 2004; Komabayashi et al., 2005; Nishi et al., 2014; Walter et al., 2015). Phase E and superhydrous phase B can carry water into the transition zone along a cool subduction geotherm (Ohtani et al., 2004; Komabayashi & Omori, 2006). Superhydrous phase B will decompose at the base of the transition zone if stagnating slabs reach temperatures above $\sim$1300 K, but can persist up to 900 km at cooler temperatures where it decomposes into ferropericlase, bridgmanite, and the hydrous phase D (Ohtani et al., 2001b, 2003; Komabayashi & Omori, 2006). Phase D is only stable up to $\sim$45 GPa, although incorporation of alumina expands its stability field (Xu et al., 2019). Phase H ($(Mg,Fe)SiO_2(OH)_2$) is stable to $\sim$60 GPa and 1600 K (Nishi et al., 2014; Ohtani et al., 2014). Phase egg ($AlSiO_3OH$) may also be stable throughout the transition zone and into the top of the lower mantle, where it would decompose into stishovite and δ-AlOOH (Eggleton et al., 1978; Schmidt, 1995; Sano et al., 2004; Abe et al., 2018). δ-AlOOH has a wide stability field up to 134 GPa and 2300 K (Suzuki et al., 2000; Ohtani et al., 2001a; Sano et al., 2008; Nishi et al., 2014; Duan et al., 2018). It is also isostructural with phase H, ε-FeOOH and post-stishovite, providing the possibility for extensive solid solutions between hydrous phases present in a variety of compositions (Sano-Furukawa et al., 2008; Gleason et al., 2013; Bindi et al., 2014; Kuribayashi et al., 2014; Yuan et al., 2019; Xu et al., 2019; Simonova et al., 2020; Thompson et al., 2020). Therefore, such δ-phase $AlOOH$–$FeOOH$–$MgSiO_2(OH)_2$–SiO_2 solid solutions may transport water in subducted material descending to the CMB. Synthetic phase H–δ-AlOOH solid solutions have been shown to coexist with alumina-depleted bridgmanite or post-perovskite up to 128 GPa and 2190 K (e.g., Nishi et al., 2014; Ohira et al., 2014). Dehydration of δ-phase solid solutions near the CMB has been suggested as a formation mechanism for ULVZs, and the effect on the post-perovskite transition of aluminium partitioning from bridgmanite has been implicated in observed seismic discontinuities in the D″ layer (e.g., Yuan et al., 2019). Additionally, pyrite-type $FeOOH_x$ may form as free water reacts with the outer core, storing hydrogen near the CMB (Nishi et al., 2017; Yuan et al., 2018).

1.1.4 Mineral Physics Data for Lower Mantle Phases

In addition to knowledge of the stable phases at lower mantle conditions and their expected proportions in relevant bulk compositions, accurate parameters describing their physical properties at lower mantle conditions are required. However, significant uncertainties exist for much of this data, or, for some phases, it is severely limited or non-existent. This limits geodynamic modelling and our ability to interpret seismic observations of the deep Earth.

1.1.4.1 Bridgmanite

Bridgmanite (Tschauner et al., 2021) is the most abundant mineral in the Earth and has been intensively studied, yet its physical properties in the lower mantle are not well constrained, particularly at high temperatures. It is particularly important to accurately constrain bridgmanite's physical properties at high P and T as even small variations have the potential to bias interpretations of geophysical data because bridgmanite will exert the strongest control on bulk lower-mantle properties. The room temperature compression behaviour of bridgmanite is fairly well known (e.g., Andrault et al., 2001, 2007; Lundin et al., 2008; Ballaran et al., 2012; Dorfman et al., 2013; Mao et al., 2015, 2017), but inconsistencies arise with the addition of temperature. P-V-T data above 2000 K are scarce, and studies are typically limited to ∼2500 K (e.g., Fiquet et al., 2000; Tange et al., 2012; Wolf et al., 2015; Sakai et al., 2016; Sun et al., 2018). Single crystal elasticity measurements of bridgmanite required to constrain anisotropy in the lower mantle have been made up to ∼79 GPa for the $MgSiO_3$ endmember (Criniti et al., 2021), but are limited to ∼40 GPa for the Al-Fe-bearing composition expected to present in the Earth, and the results are inconsistent between studies (Kurnosov et al., 2017; Fu et al., 2019b). Furthermore, no single crystal elasticity measurements of bridgmanite have been made at high temperature. The elastic properties of bridgmanite have been more widely investigated using polycrystalline samples (Jackson et al., 2004, 2005; Murakami et al., 2007b; McCammon et al., 2016; Fu et al., 2018; Mashino et al., 2020), but high-temperature data are also extremely limited (Murakami et al., 2012). The high-P-T physical properties of bridgmanite are also strongly dependent on composition and the combined effects of compositional variability are not well constrained, particularly at high temperatures. In particular, the effect of Al content (Andrault et al., 2007; Fukui et al., 2016; Huang et al., 2021; Nakatsuka et al., 2021), Fe content and redox state (e.g., Glazyrin et al., 2014; Kurnosov et al., 2017; Shim et al., 2017; Creasy et al., 2020a), incorporation of water and other volatiles (Fu et al., 2019a; Liu et al., 2019, 2021b), and the presence of a spin transition in iron (Catalli et al., 2011; Fujino et al., 2012; Mao et al., 2015, 2017; Fu et al., 2018) are not well understood.

1.1.4.2 Ferropericlase

Ferropericlase is probably the most widely studied lower mantle phase, in part due to its relatively simple crystal structure and chemistry. However, the effect of compositional variations as well as a change in the electronic configuration of iron (i.e., a spin crossover; Badro et al., 2003) in the lower mantle are not fully understood (particularly at high temperature) and may be significant (Lin et al., 2013; Badro, 2014). Experimental evidence suggests that the pressure induced transition of iron d-orbital electrons from a high-spin to low-spin state has the effect of a marked softening of the bulk modulus (e.g., Crowhurst et al., 2008; Marquardt et al., 2009a; Wicks et al., 2010; Mao et al., 2011; Yang et al., 2015; Wicks et al., 2017; Marquardt et al., 2018). This may result in a seismically detectable reduction in V_p/V_s ratio across the spin transition (Yang et al., 2015; Marquardt et al., 2018; Shephard et al., 2021), although the effect is not fully understood (Lin et al., 2006; Antonangeli et al., 2011; Chen et al., 2012; Wicks et al., 2010, 2017) and may be offset by temperature (Yang et al., 2016; Marquardt et al., 2018). Additionally, the spin transition appears to drastically increase shear anisotropy in ferropericlase, with the effect increasing at high pressure and with iron content (Marquardt et al., 2009b; Yang et al., 2016; Finkelstein et al., 2018). This may account for radial seismic shear anisotropy observed in the lower mantle, particularly at the margins of LLSVPs and in the D″ region (e.g., Creasy et al., 2017, 2020b; Immoor et al., 2018). Furthermore, an increase in iron-enriched (Mg,Fe)O (i.e., magnesiowüstite) has been suggested as a plausible explanation for ULVZs due to its measured strong shear anisotropy and significantly reduced sound velocities at deep lower mantle conditions (e.g., Wicks et al., 2010, 2017; Finkelstein et al., 2018). However, the broadening of the spin transition region at high temperature introduces significant complexity into the interpretation of lower mantle seismic signatures, and temperature is likely to alter some effects (Komabayashi et al., 2010; Mao et al., 2011; Lin et al., 2013; Badro, 2014). Currently, single-crystal elasticity data are limited to 900 K (Yang et al., 2016; Fan et al., 2019), and sound velocity measurements at lower mantle conditions consist of only a few data points (and only for endmember MgO periclase; Murakami et al., 2012).

1.1.4.3 Calcium-Silicate Perovskite

Calcium silicate perovskite (Ca-Pv, $CaSiO_3$), now with the name davemaoite (Tschauner et al., 2021), is believed to be the third most abundant phase in the lower mantle, comprising ∼7–8 vol.% of pyrolitic mantle and up to 25–30% of subducted MORB material (Figure 1.2; Irifune et al., 2010; Ricolleau et al., 2010; Sun et al., 2016). Ca-Pv is known to incorporate a wide variety of large cations in its structure, and so may be an important host for REE, heat-producing elements and volatiles (including water) in the lower mantle and play a key role in element recycling during mantle convection (Chakhmouradian & Mitchell, 2000; Corgne & Wood, 2002, 2005; Corgne et al., 2003, 2005; Stachel et al., 2004; Greaux et al., 2009; Wood & Corgne, 2015; Thomson et al., 2016a; Heinen,

2017; Tschauner et al., 2021). Ca-Pv enriched domains may form in the lower-mantle as subducted MORB material stagnates, or if the density of Ca-Pv rich residue from the partial melting of MORB is greater than the surrounding rock (Hirose et al., 2017). However, Ca-Pv can only be studied *in situ*, because it rapidly amorphises upon decompression to ambient conditions and the cubic structure expected to be present in the lower-mantle is only stable at elevated temperatures (Mao et al., 1989; Kubo et al., 1997). As a result of these technical challenges, experimental investigations of Ca-Pv's physical properties have been limited, and significant discrepancies exist between studies. *P-V-T* measurements of Ca-Pv by x-ray diffraction have been made up to 150 GPa and 2600 K, but disagreements between published experimental datasets lead to differences of up to ∼20% in estimates of bulk sound velocity, V_Φ (Shim et al., 2000; Noguchi et al., 2013; Sun et al., 2016), and compositional effects have not been fully investigated (e.g. Greaux et al., 2009). High-temperature thermodynamic and ab initio calculations of the thermoelastic properties of Ca-Pv at lower mantle conditions are also not in consensus (Li et al., 2006; Stixrude et al., 2007; Stixrude & Lithgow-Bertelloni, 2011; Tsuchiya, 2011; Kawai & Tsuchiya, 2015). Room temperature measurements of sound velocities in the tetragonal phase have been measured up to 133 GPa, and report anomalously low shear velocities (Sinelnikov et al., 1998; Kudo et al., 2012), but it is unclear if the tetragonal phase exists in the mantle (Kubo et al., 1997; Stixrude et al., 2007; Tsuchiya, 2011; Kudo et al., 2012; Thomson et al., 2019; Sagatova et al., 2021). Incorporation of titanium in Ca-Pv may stabilise the tetragonal phase in Ti-enriched cold subducting slabs, and the tetragonal-cubic phase transition may account for some seismic discontinuities in the mid-mantle (Thomson et al., 2019). Recent high *P-T* ultrasonic measurements of cubic Ca-Pv confirm an anomalously low shear modulus (Gréaux et al., 2019; Thomson et al., 2019), and suggest that its compressional and shear wave velocities are substantially lower than average seismic reference models at lower mantle conditions (Dziewonski & Anderson, 1981; Thomson et al., 2019). As a result, accumulation of recycled oceanic crust in the lower mantle is likely to be consistent with the seismic signatures of LLSVPs due to the higher proportion of Ca-Pv expected in meta-basaltic material (McNamara, 2019; Thomson et al., 2019). However, discrepancies between these studies arise with increasing temperature. This is likely in part due to the apparent high temperature dependence of seismic velocities in Ca-Pv (Thomson et al., 2019), and the affect of potentially large temperature gradients in one of the studies (Gréaux et al., 2019). Nevertheless, inferences about seismic velocities in the lower mantle rely on extrapolations from data collected at moderate *P* and *T* (∼12 GPa and <1500 K in Thomson et al., 2019; 23 GPa and <1700 K in Gréaux et al., 2019), and no direct sound velocity measurements of Ca-Pv have yet been made at lower mantle conditions.

1.1.4.4 Free Silica

Stishovite (Stishov & Belov, 1962) is likely to be a major component of subducted oceanic crust in the lower mantle (Figure 1.2; Ricolleau et al., 2010), and stishovite enriched domains may be preserved over long timescale due to its high viscosity (Xu et al., 2017). Stishovite is expected to undergo a ferroelastic, displacive phase transition from the tetragonal rutile structure to an orthorhombic $CaCl_2$-type structure (post-stishovite) in the mid-mantle (e.g., Andrault et al., 1998; Shieh et al., 2005; Lakshtanov et al., 2007). The phase transition is difficult to constrain on the basis of x-ray diffraction data as it is only characterised by subtle splitting of the (211) reflection, with the issue more significant at high temperature due to the strong thermal gradients induced by laser-heating (e.g., Andrault et al., 1998, 2003; Prakapenka et al., 2004; Shieh et al., 2005; Nomura et al., 2010; Fischer et al., 2018). However, the transition has been extensively studied, and constrained to ∼55 GPa at room temperature (e.g, Nomura et al., 2010; Singh et al., 2012; Yamazaki et al., 2014; Buchen et al., 2018; Fischer et al., 2018; Zhang et al., 2021). At high temperature in the lower mantle, the transition is expected to occur for the endmember composition between ∼70 and 80 GPa depending on temperature, corresponding to depths of ∼1600–1800 km (e.g., Fischer et al., 2018). However, alumina and water content exert a strong control on the transition pressure, and incorporation of mantle relevant amounts of both may lower the transition pressure by as much as 30 GPa (e.g., Lakshtanov et al., 2007). The post-stishovite transition has been proposed as an explanation for seismic scattering in the mid-mantle (e.g., Kaneshima & Helffrich, 2009, 2010; Vinnik et al., 2010; Jenkins et al., 2017; Helffrich et al., 2018) as, on the basis of *ab initio* computations, Landau theory analysis of x-ray diffraction data, and sound velocity measurements across the transition under deviatoric stress (and therefore lowered in pressure), a vanishing shear velocity along [110] is expected for the ferroelastic/Landau type transition, resulting in a significant average V_S reduction and extreme elastic anisotropy approaching the transition (Karki et al., 1997; Carpenter et al., 2000; Asahara et al., 2013; Yang & Wu, 2014; Buchen et al., 2018). Recent measurements of the full set of elastic moduli across the transition confirm the vanishing of $V_{S[110]}$ at ∼55 GPa and 300 K, although the calculated reduction in average V_S (∼5.4%) and increase in Poisson ratio (∼5.5%) are less significant than predicted (Zhang et al., 2021). However, the effect of temperature has not been investigated, and high temperature sound velocity measurements of lower mantle SiO_2 phases are limited in pressure (to ∼20 GPa), temperature (to 1700 K), and composition space (Gréaux et al., 2016).

SiO_2 undergoes a further phase transition from the $CaCl_2$-type structure to an α-PbO_2 structure (seifertite) at deep lower mantle conditions (Dubrovinsky et al., 2001b; Murakami et al., 2003). The phase transition occurs at ∼135 GPa at 2500 K for the endmember composition (i.e., at greater depths than the post-perovskite transition; Grocholski et al., 2013), but alumina incorporation lowers the transition pressure (∼115 GPa at 2500 K for ∼5 wt.% Al_2O_3; Andrault et al., 2014b; Sun et al., 2019). The two-phase stability field is narrow, but difficult to constrain as the phase transformation

requires long heating times (∼2 hours; e.g., Murakami et al., 2003; Sun et al., 2019). The density increase (and associated increase in V_Φ) across this transition may account for seismic discontinuities observed in the D″ region (Sun et al., 2019). Computational studies suggest shear wave velocities should decrease by several percent across the transition (e.g., Tsuchiya, 2011), making the seifertite transition a poor candidate for the D″ discontinuity itself (where V_S is expected to increase), but this has not been confirmed experimentally. Seifertite can be metastably recovered from >140 GPa to ambient conditions (Grocholski et al., 2013), but the significant technological challenges in making single crystal seifertite in a DAC has prohibited single-crystal studies. No compressional or shear wave velocity measurements of seifertite have been made.

1.1.4.5 Aluminous Phases

Mineral physics data on the aluminous NAL and CF phases are vital for the interpretation of the seismic signatures of deeply subducted slabs as they may compose up to 25% of recycled MORB material (Figure 1.2; Ricolleau et al., 2010). Both phases display complex chemistry (Imada et al., 2011; Guignot & Andrault, 2004), and computational evidence suggests they display significant seismic anisotropy that is strongly dependent on composition (Mookherjee, 2011; Mookherjee et al., 2012). However, relatively little data exists for these phases, and in particular the effect of composition and temperature on their physical properties is very poorly constrained. The equation of state for both phases has been investigated in a wide pressure range at room temperature (Ono et al., 2002; Vanpeteghem et al., 2003b; Guignot & Andrault, 2004; Imada et al., 2012), but high temperature data is very limited (Shinmei et al., 2005). Sound velocity measurements on polycrystalline samples of both phases have been made up to ∼70 GPa at room temperature (Dai et al., 2013), but single crystal data has only been collected for NAL (at 20 GPa and similarly limited to 300 K; Wu et al., 2016b). The results suggest NAL exhibits strong velocity anisotropy that is likely to contribute to observed seismic signals in the uppermost lower mantle. However, the effects of temperature and the widely variable composition are yet to be investigated. Furthermore, the presence of an iron spin transition in Fe-bearing NAL is likely to add significant complexity to the elastic behaviour at lower mantle conditions (Wu et al., 2016a).

1.1.4.6 Hydrous Phases

Very little mineral physics data exists for the possible hydrous lower mantle phases, but they may exert a strong control on lower mantle dynamics (Ohtani, 2021). An equation of state for phase H has been constrained with measurements up to 62 GPa and 1300 K, which covers the majority of its stability field (Nishi et al., 2018). Equations of state for phase Egg and superhydrous phase B have been measured up to ∼35 GPa, but are limited to ∼1300 K and ∼900 K respectively (Vanpeteghem

et al., 2003a; Inoue et al., 2006; Litasov et al., 2007; Li et al., 2021; Liu et al., 2021a). Single-crystal elasticity measurements of superhydrous phase B are limited to 12 GPa and 700 K (Li et al., 2016), and are limited to ambient conditions for phase D (Liu et al., 2004; Rosa et al., 2012). The thermal equation of state of δ-AlOOH has been studied up to 142 GPa and 2500 K by Duan et al. (2018), but the effect of a solid solution with phase H, ε-FeOOH, and/or SiO_2 is not well constrained (Ohira et al., 2014; Yuan et al., 2019; Xu et al., 2019). A spin transition in Fe-bearing variants of these phases may also result in further complexity, and has been suggested to explain seismic scattering in the mid lower mantle (e.g., Chang et al., 2013). The single crystal elasticity of endmember δ-AlOOH has been measured at ambient conditions (Wang et al., 2022), and Satta et al. (2021) recently made single crystal elasticity measurements on Fe-bearing (3%) δ-AlOOH at high pressure. Extrapolated to lower mantle conditions, the data suggest aggregate sound velocities of MORB would be substantially increased by the presence of a hydrous component despite a density reduction, but measurements were limited to <20 GPa and room temperature (Satta et al., 2021).

1.1.4.7 Melts and Fluid Phases

The physical properties of melts that may exist in the lower mantle are also poorly constrained. The high melting points of silicates and limited x-ray scattering power of low-Z materials presents significant technological challenges in making liquid structure and density measurements. Simple silicate glasses have been extensively used as proxies for silicate liquids at extreme conditions, and display complex behaviour including polyamorphic transitions (e.g., Xue et al., 1989; Meade et al., 1992; Lee et al., 2008; Sato & Funamori, 2008; Sanchez-Valle & Bass, 2010; Zeidler et al., 2014; Prescher et al., 2017; Salmon et al., 2019; Kono et al., 2014, 2018, 2020). However, fragile liquids such as natural silicate melts are difficult to quench to a glass and may undergo structural changes as they do, and so *in situ* experiments at high P and T are necessary for their characterisation (Giordano & Dingwell, 2003; Wilding et al., 2010; Drewitt et al., 2012). *In situ* experiments have generally been limited in pressure and/or temperature (e.g., Funamori et al., 2004; Yamada et al., 2007, 2011; Sanloup et al., 2013a,b; Drewitt et al., 2015). As such, there is a significant lack of experimental data on natural silicate melts at lower mantle conditions, despite the importance on the geodynamic stability and seismic properties of any melt that exists (Sanloup et al., 2013b; Petitgirard et al., 2015).

1.2 Experimental and Analytical Techniques in Mineral Physics

Obtaining data on the properties of lower mantle phases requires simulating the conditions of the deep Earth, either by using computational methods, or experimental techniques in the laboratory. Computational simulations of material properties at extreme conditions are now able to accurately predict a wide range of properties, including phase relations, elasticity, thermal conductivity, and rheology, and so provide a complementary approach to experimental techniques (e.g., see Karki et al., 2001; Gillan et al., 2006; Tse, 2019; Tsuchiya et al., 2020). However, computational uncertainties arising from approximations made in the calculations are still relatively large. Measurements made using high-*P*-*T* experimental techniques therefore also provide a way of benchmarking such calculations.

A wide variety of techniques can be used to generate static high pressure in the laboratory. High pressure research, initially using hydraulic presses to apply force to piston-cylinder type devices, has its roots in the late 19_{th} century (Parsons, 1907, 1920; Hemley, 2006). Significant technological advances in the latter half of the 20^{th} century, and the widespread adoption of high pressure techniques as a tool in the geoscience community, has led to the ability to generate the extreme conditions of deep planetary interiors (Bassett, 2009; Liebermann, 2011). Nevertheless, the extreme conditions required to study the lower mantle ($\sim$24 to 130 GPa and $\sim$1900 to 3000 K) still present significant experimental difficulty. The primary devices used for static pressure generation at these conditions are the Kawai-type multi anvil press (MAP) and the diamond anvil cell (DAC). Recent advances in MAP techniques have pushed its capabilities into the range of lower mantle conditions, and pressures in excess of 100 GPa have been reported (Liebermann, 2011; Ishii et al., 2019; Yamazaki et al., 2019). However, such experiments are far from routine, and MAP apparatus are typically limited to $\sim$20 to 30 GPa for routine experiments in most laboratories. In contrast, pressures encompassing mantle conditions can be generated routinely in the diamond anvil cell. Pressure is generated by compressing the sample between the polished tips of two opposed diamonds, relying on a small anvil surface area to generate extreme pressures with minimal force. The drawback is that this limits the sample volume to sub-millimetre scales. However, the transparency of the anvils across a broad frequency range allows *in situ* analyses with wide variety of techniques. Furthermore, experimental techniques have been developed which allow the simultaneous generation of extreme temperatures while at high pressure, from many thousand kelvin down to the millikelvin range (Palmer et al., 2015; Anzellini & Boccato, 2020). As a result, the DAC has been widely adopted as the experimental tool of choice for studying materials at lower mantle conditions, particularly when combined with brilliant synchrotron x-radiation that allows analysis of such tiny samples (Bassett, 2009; Shen & Mao, 2016). Diamond anvil cell design and techniques are introduced more comprehensively in section 1.3.

Measuring the physical properties of materials at extreme conditions generated by such devices relies on a wide range of techniques. In the following sections I will provide a brief overview of the main physical properties and techniques important to geophysical research, with a particular focus on their application to DAC samples.

1.2.1 Elasticity and Seismic Wave Speeds

Seismic imaging is important because it provides direct information about the Earth's interior, but it cannot easily distinguish between the effects of temperature, chemistry and phase relations. Theoretically, mantle mineralogy can be constrained by comparing seismic reference models with mineral physics estimates of the bulk seismic velocities for a given composition (although any fit in temperature-composition space may not be unique, Bina & Helffrich, 2014). Such comparisons require accurate measurements of the elastic and thermodynamic properties of relevant phases as a function of *P* and *T*, along with knowledge of what phases are expected to be present at conditions of the Earth's interior.

Only a few isotropic elastic properties are required to constrain the seismic wave velocity of a material to a first order approximation, namely the bulk modulus, K, shear modulus, μ, and density, ρ. The bulk modulus defines the incompressibility of a material, i.e., the response in volume, V, to an infinitesimal change in hydrostatic pressure (e.g., see the introduction given by Anderson, 1995):

$$K = -V\frac{dP}{dV}. \tag{1.1}$$

It can be defined in terms of constant temperature (the isothermal bulk modulus, K_T) or constant entropy (the isentropic or adiabatic bulk modulus, K_S). K_S can be calculated from K_T by:

$$K_S = K_T\left(1 + \gamma\alpha T\right), \tag{1.2}$$

where γ is the Grüneisen parameter and α is the thermal expansion coefficient:

$$\alpha = \frac{\gamma C_V V}{K_T}, \tag{1.3}$$

with C_V the isochoric heat capacity.

The shear modulus, μ, is a measure of a material's resistance to elastic shear, defined by the ratio of shear stress, τ, to shear strain, θ (i.e., $\mu = \tau/\theta$).

These elastic moduli, in combination with the density, allow the calculation (presuming isotropy) of both compressional (longitudinal) and shear (transverse) wave velocities, V_p and V_s (e.g., see Shearer, 2009):

$$V_p = \sqrt{\frac{K_S + \frac{4}{3}\mu}{\rho}}, \tag{1.4}$$

$$V_s = \sqrt{\frac{\mu}{\rho}}. \tag{1.5}$$

A bulk velocity, V_Φ, that combines V_s and V_p can also be defined, and is widely used for the interpretation of seismic data:

$$V_\Phi = \sqrt{V_p^2 - \frac{4}{3}V_s^2} = \sqrt{\frac{K_S}{\rho}}. \tag{1.6}$$

To compute sound velocities for a rock with multiple phases it is important to correctly average the elastic moduli (e.g., Cottaar et al., 2014). The volume and density of a multi-phase assemblage can be directly averaged, i.e.:

$$V = \sum_i n_i V_i, \tag{1.7}$$

and

$$\rho = \sum_i v_i \rho_i, \tag{1.8}$$

where V and ρ are the total molar volume and density of the assemblage, V_i and ρ_i are the molar volume and density of the ith individual phase, n_i is the molar fraction of the phase in the assemblage, and v_i is the volume fraction of the phase:

$$v_i = n_i \frac{V_i}{V}. \tag{1.9}$$

However, obtaining an average bulk or shear modulus for a multi-phase rock depends on assumptions about the distribution and orientation of the constituent minerals. Typically, several averaging schemes which make endmember assumptions are used so as to obtain bounds on the physical average. The most commonly used bounds are the Voigt and Reuss bounds. The Voigt bound assumes a constant strain field in response to a stress field across the material and gives the maximum possible moduli of the composite (Hill, 1963). The Voigt bound of a particular elastic modulus, M_{V}, can be calculated from the elastic moduli of the individual phases, M_i, by:

$$M_{\mathrm{V}} = \sum_i v_i M_i. \tag{1.10}$$

The Reuss bound, M_{R}, instead makes the assumption that the stress field remains constant, and is given by:

$$M_{\mathrm{R}} = \left(\sum_i \frac{v_i}{M_i} \right)^{-1}. \tag{1.11}$$

The actual elastic modulus of the material must fall between these bounds, but is not known. Typically, an arithmetic mean of the Voigt and Reuss bounds (the Voigt-Reuss-Hill average, M_{VRH}) is used to estimate the modulus of the bulk material:

$$M_{\mathrm{VRH}} = \frac{1}{2} \left(M_{\mathrm{V}} + M_{\mathrm{R}} \right). \tag{1.12}$$

Alternatively, Hashin-Shtrikman bounds (Watt et al., 1976), and their arithmetic mean, can be used instead of the Voigt-Reuss-Hill average. These are constructed based on the assumption that the

phase distribution within the rock is statistically isotropic, essentially minimising strain energy rather than averaging stress and strain fields, and as a result are generally much narrower than the Voigt-Reuss bounds. In some cases the Hashin-Shtrikman average may be more physically meaningful than the Voigt-Reuss-Hill average, but will be a poor estimate if anisotropy is high.

Seismic anisotropy is observed in many regions of the lower mantle, and so describing the elastic anisotropy of lower mantle phases is important (e.g., Kendall & Silver, 1996, 1998; Karato, 1998; Hall et al., 2004; Wookey & Kendall, 2007; Ferreira et al., 2019; Creasy et al., 2020b). All minerals will display elastic anisotropy to some extent, even those with cubic symmetry. The elasticity of a material in any direction can be defined by its elastic stiffness tensor, whose symmetry (or lack of symmetry) will describe the anisotropy. The elastic stiffness tensor (c_{ijkl}) describes the response of a crystal lattice to an external stress (σ) or strain (ϵ) through a generalisation of Hooke's law in three dimensions (e.g., see Shearer, 2009), i.e.:

$$\sigma_{ij} = \sum_{k=1}^{3} \sum_{l=1}^{3} c_{ijkl} \epsilon_{kl}. \tag{1.13}$$

The stress and strain tensors (σ_{ij} and ϵ_{kl}) describing a three dimensional body are rank 2 tensors and so can be written out as matrices, but the resulting stiffness tensor is 4$^{\text{th}}$ rank (with 81 individual components) and so cannot be written out on paper. However, as the stress and strain tensors are symmetric, $c_{ijkl} = c_{jikl}$ and $c_{ijkl} = c_{ijlk}$. The distinct elements can therefore be written out in matrix form using reduced (Voigt) notation, mapping c_{ijkl} to C_{ij} and leading to equation 1.13 expressed as:

$$\begin{bmatrix} \sigma_1 \\ \sigma_2 \\ \sigma_3 \\ \sigma_4 \\ \sigma_5 \\ \sigma_6 \end{bmatrix} = \begin{bmatrix} C_{11} & C_{12} & C_{13} & C_{14} & C_{15} & C_{16} \\ C_{21} & C_{22} & C_{23} & C_{24} & C_{25} & C_{16} \\ C_{31} & C_{32} & C_{33} & C_{34} & C_{35} & C_{16} \\ C_{41} & C_{42} & C_{43} & C_{44} & C_{45} & C_{16} \\ C_{51} & C_{52} & C_{53} & C_{54} & C_{55} & C_{56} \\ C_{61} & C_{62} & C_{63} & C_{64} & C_{65} & C_{66} \end{bmatrix} \begin{bmatrix} \epsilon_1 \\ \epsilon_2 \\ \epsilon_3 \\ \epsilon_4 \\ \epsilon_5 \\ \epsilon_6 \end{bmatrix}, \tag{1.14}$$

where σ_1–σ_3/ϵ_1–ϵ_3 are the normal stresses and strains, σ_4–σ_6/ϵ_4–ϵ_6 are the shear stresses and strains, and the 36 C_{ij} are the independent elastic constants (moduli) that fully describe an anisotropic material in the most general case. However, considerations of crystal symmetries reduces the number of independent elastic constants, with, for example, nine required for orthorhombic symmetry and

just three required for cubic minerals. An assumption of isotropy leads to just two elastic constants, which can be used to calculate the elastic moduli K_S and μ described above. The independent elastic constants (C_{ij}s) can also be similarly averaged for a polyphase medium (e.g., equations 1.10 to 1.12).

It should be noted that the relations given here assume linear elasticity, i.e., they only hold true for a perfectly elastic medium where there is no energy loss or attenuation as the material deforms in response to a stress. This is not strictly true for real Earth materials as is shown by seismic attenuation and dispersion, and anelastic effects at seismic frequencies on a smaller scale may also lead to seismic scattering (e.g., Anderson, 1967; Matas & Bukowinski, 2007; Umemoto et al., 2016). It has been argued that anelasticity does not exert a significant control on observed lower mantle seismic structure (e.g., Brodholt et al., 2007). However, consideration of anelastic effects may be required to accurately infer temperature variations, accurately model the seismic signatures of melts, and reconcile geophysical observations at different frequencies (e.g., Karato & Karki, 2001; Matas & Bukowinski, 2007; McCarthy & Takei, 2011; Lau & Faul, 2019; Schuberth & Bigalke, 2021).

1.2.2 X-Ray Diffraction

X-ray diffraction provides a powerful analytical tool for investigations of material properties. Light is elastically scattered by the electrons surrounding an atom. This is controlled by the electron density (and so atomic number, Z), with the scattering power of an atom described by its x-ray atomic form factor $f(Q)$ (where Q is the momentum transfer), which is the Fourier transform of the spatial electron charge density about the nucleus (e.g., see Warren, 1969).

Due to the periodic structure of crystals, and with the spacing of the lattice planes a similar order of magnitude to the wavelength of x-rays, crystalline materials act as three-dimensional diffraction gratings. Illuminating a crystal with an x-ray beam results in interference between the spherical waves emitted from each of the point scatterers (i.e., the atoms) in the crystal structure, leading to a diffraction pattern. Most this interference will be destructive, but when the wave fronts scattered from two parallel planes of atoms orientated normal to the diffraction vector have a path difference of an integer number of wavelengths constructive interference will result in a peak in the diffraction pattern. This is known as the Bragg condition (Fig. 1.3; see Warren, 1969, chap. 2):

$$\lambda = 2d_{hkl} \sin\theta, \tag{1.15}$$

where λ is the x-ray wavelength, θ is the diffraction angle and d_{hkl} is the spacing between adjacent lattice planes with Miller indices (hkl). As monochromatic x-rays are used for angle-dispersive diffraction measurements, the lattice spacing for each family of lattice planes (hkl) indexed in the diffraction pattern can be calculated from the diffraction angle of its peak.

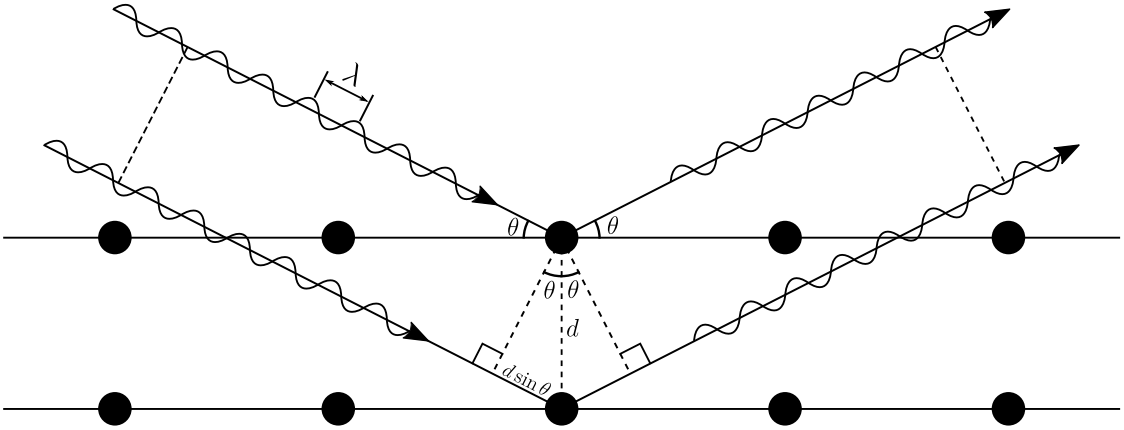

Figure 1.3: *Geometric illustration of Bragg's law. Two incident x-ray beams of wavelength λ arriving in-phase with angle of incidence θ will only remain in-phase after reflecting from two parallel planes of atoms if the path difference is equal to an integer number of wavelengths. The path difference of the two waves after reflection is $2d\sin\theta$, where d is the spacing between lattice planes.*

As diffraction peaks result from interference between the scattered waves from all atoms in the crystal, the diffraction intensity (I_{hkl}) is determined by the positions of atoms on the lattice planes and the scattering power of each of those atoms, and will be proportional to the structure factor which describes this:

$$I_{hkl} \propto |F_{hkl}|^2. \tag{1.16}$$

For a perfect crystal the structure factor, F_{hkl}, describes the basis and sums the scattering from all atoms in the unit cell in the direction of the (hkl) reflection to determine the amplitude and phase of the diffracted beam (see Warren, 1969, chap. 3):

$$F_{hkl} = \sum_{j=1}^{N} f_j e^{2\pi i(hx_j+ky_j+lz_j)}, \tag{1.17}$$

where the sum is over all N atoms in the unit cell, and for the j-th atom f_j is the atomic form factor (at its maximum in the (hkl) direction) and x_j,y_j,z_j are its fractional coordinates. The structure factor also governs the selection rules for a peak from a specific families of lattice planes appearing in the diffraction pattern (i.e., $I_{hkl} \neq 0$) for a particular crystal system. X-ray diffraction patterns therefore encode information about the crystal lattice and basis, and allow precise determination of the crystal structure, lattice parameters, unit cell volume, and density of a material.

For diffraction of a polycrystalline (powder) sample, the random orientation of the grains means that for each family of lattice planes a statistically significant percentage of crystallites will be orientated to satisfy the Bragg condition. This means that every possible reflection is present in the diffraction pattern. Furthermore, as rotating a crystal will rotate the reciprocal lattice, diffraction from a powder sample will result in a sphere of reciprocal lattice points that satisfy the Bragg condition for a given diffraction angle. The diffracted beams will therefore form cones at specific Bragg angles (2θ) for each reflection, resulting in rings at the detector image plate (Debye-Scherrer rings; Fig. 1.4). In an ideal powder sample, with thousands of uniformly distributed randomly orientated crystallites, these Debye-Scherre rings will be smooth, with uniform intensity around the full 360°. However, if there is not a statistically significant number of crystallites in the diffracted volume the resulting pattern will appear spotty. This can be an issue in high temperature experiments where grain growth reduces the number of individual crystallites, or in experiments with a very small sample volume. Preferred orientation of grains in the powder sample will also result in a textured diffraction pattern, where the intensity of Debye-Scherrer rings varies as a function of angle around its circumference.

In x-ray diffraction experiments the sample to detector distance must be known to determine diffraction angle (2θ) from the image. This is done by calibrating against a material with well known lattice parameters (e.g., NIST reference samples of CeO_2, LaB_6, etc.). Two-dimensional diffraction images are then typically reduced to one-dimensional profiles by integrating around the diffraction centre position of the area detector, with corrections applied for experiment geometry (e.g., azimuth offset of the image plate). Regions with shadows or scattering from outside the sample are also typically masked out at this stage. One-dimensional diffraction profiles then allow analysis of the material.

While the intensity of the diffraction peaks is primarily controlled by the phase properties, other factors must be accounted for. These include a contribution from background scattering, absorption (from inelastic scattering) described by the Beer-Lambert law, polarisation (described by the Lorentz polarisation factor), and temperature.

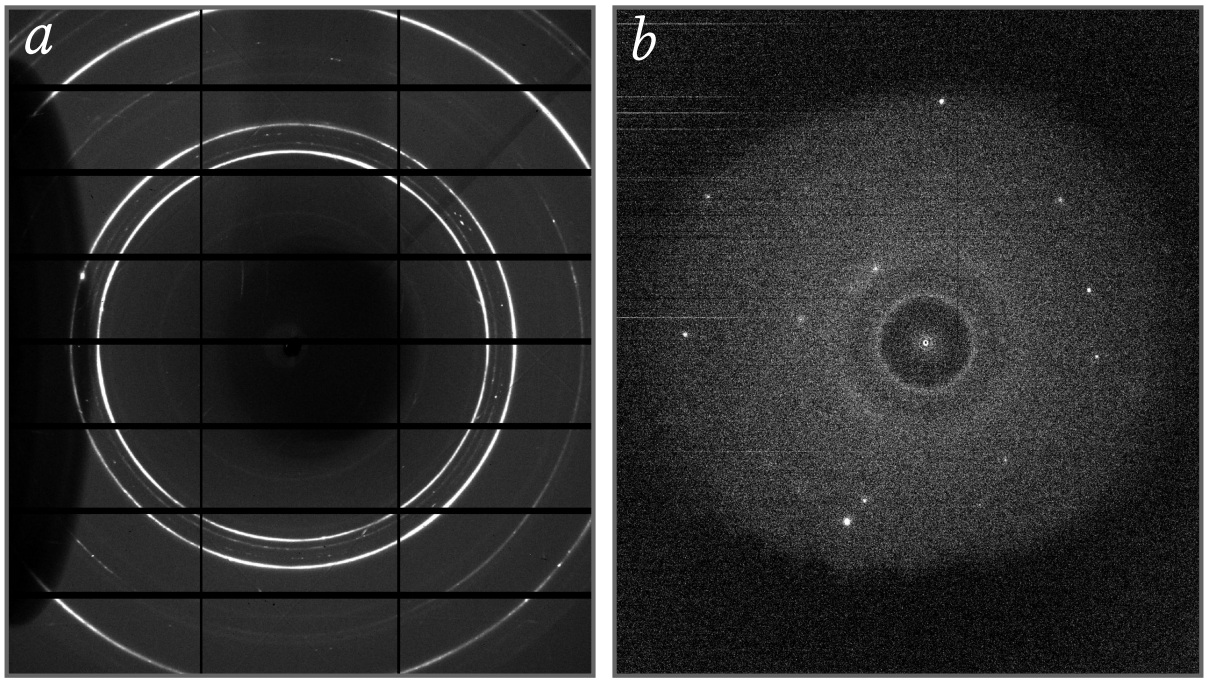

Figure 1.4: *Example raw 2D diffraction images from polycrystalline (a) and amorphous (b) materials. a) XRD image with Debye-Scherrer rings from Bragg reflections of polycrystalline KCl, molybdenum and rhenium at ∼1800 K and ∼50 GPa in a DAC. The shadows are from the beamstop (used to protect the detector from the direct beam) and optical components in the temperature measurement system. The gaps in the image are due to the use of a multi-panel area detector. b) Diffuse scattering from liquid gallium at ∼600 K and ∼11.5 GPa in a DAC. Single crystal spots from the diamond anvils and shadows from the beamstop and detector effects are also present.*

In powder XRD patterns the peak shape will also be broadened by the effects of grain size and microstrain within the sample as the peaks represent an average of all grains in the diffraction volume. Instrument broadening effects also occur but can be accounted for in calibration. This allows grain size and microstrain to be quantitatively analysed using the combined Scherrer and Stokes-Wilson equations (Patterson, 1939; Stokes & Wilson, 1942; Williamson & Hall, 1953; Warren, 1969):

$$\beta_{observed} - \beta_{instrument} = \beta_{size} + \beta_{strain} = \frac{K\lambda}{\tau \cos\theta} + 4\epsilon \tan\theta, \tag{1.18}$$

where β is the contribution to the full-width at half-maximum (FWHM) of the peak, K is the shape constant (usually $\sim$0.9), τ is the grain size, ϵ is the strain, λ is the wavelength, and θ the diffraction (half-)angle. This equation can be rearranged to a simple linear form:

$$\frac{\beta_{hkl} \cos\theta}{\lambda} = \frac{K}{\tau} + \epsilon \frac{4 \sin\theta}{\lambda}, \tag{1.19}$$

which then allows estimation of the strain and grain size from the slope and intercept of a plot respectively — the Williamson-Hall method (1953).

For structural analysis and phase identification of a material the individual indexed peaks in the diffraction pattern can be fit (typically with a pseudo-Voigt peak profile). The structure can then be solved and the lattice parameters describing the unit cell determined from the refined peak positions. Alternatively, full-profile fitting methods can be used. Full-profile refinement is particularly useful for multi-phase samples, as strongly overlapping peaks can be resolved. Rietveld (1969) refinement is the most common full-profile fitting method. It uses a least squares approach to fit a theoretical profile to the measured data, taking into account experimental geometry, crystal structure, atomic positions, structure factors, and peak broadening effects to calculate line widths, intensities and positions, and can be applied to multi-phase samples. The Le Bail (1988; 2005) method is a modification of the Rietveld approach in which intensities are allowed to freely vary. This is particularly useful for DAC experiments where axial compression can result in preferred orientation that effects the relative intensity of peaks.

In contrast to crystalline materials, amorphous materials like liquids and glasses do not show long-range order, and so sharp peaks are not observed in their diffraction patterns. However, liquids and glasses do exhibit ordering on short- to medium-range length scales as a result of chemical interactions that lead to local structural motifs (Kitaigorodskiy & Chomet, 1967). This leads to

broad, diffuse scattering bands in the diffraction pattern (Fig. 1.4). The total intensity of scattered radiation arises from coherent, incoherent (Compton), and self-scattering effects (see Warren, 1969; Waseda, 1980). In x-ray diffraction the quantity measured by the detector in the solid angle $d\Omega$ at a scattering angle 2θ is the differential cross-section, $d\sigma/d\Omega$. The total differential x-ray scattering cross section for a system of N scattering components can be considered a sum of the elastic and Compton differential cross sections:

$$\frac{1}{N}\left[\frac{d\sigma}{d\Omega}(Q)\right]^{\mathrm{x-ray}}_{\mathrm{Elastic}} = \left[\frac{d\sigma}{d\Omega}(Q)\right]^{\mathrm{x-ray}}_{\mathrm{Total}} - \left[\frac{d\sigma}{d\Omega}(Q)\right]^{\mathrm{x-ray}}_{\mathrm{Compton}}. \tag{1.20}$$

The differential cross-section of the elastically scattered radiation can be separated into a self-scattering term, which describes the isotropic diffraction of individual atomic sites, and the total x-ray interference function, $F(Q)$, which describes the interference of coherently scattered waves from different sites and so contains the useful structural information. This is given by (e.g., see Pings & Waser, 1968; Keen, 2001):

$$\frac{1}{N}\left[\frac{d\sigma}{d\Omega}(Q)\right]^{\mathrm{x-ray}}_{\mathrm{Elastic}} = F(Q) + \sum_{\alpha=1}^{n} c_\alpha f_\alpha(Q)^2, \tag{1.21}$$

where c_α and $f_\alpha(Q)$ are the atomic concentration and the Q-dependent atomic form factor of species α respectively, and Q is the magnitude of the scattering vector (Fig. 1.5). The total x-ray interference function, $F(Q)$, can be defined as (e.g., see Faber & Ziman, 1965; Waseda, 1980; Keen, 2001):

$$F(Q) = \sum_{\alpha=1}^{n}\sum_{\beta=1}^{n} c_\alpha c_\beta f_\alpha(Q) f_\beta(Q)\left[S_{\alpha\beta}(Q) - 1\right], \tag{1.22}$$

where the sum is performed over all possible pairs of α-β species in the sample, and $S_{\alpha\beta}$ is the partial structure factor for each correlated α-β pair. For a compositional unit with n atomic species there will be $n(n+1)/2$ atomic pair correlations. The total structure factor $S(Q)$ is the weighted sum of all partial structure factors which describe the system, but can also be obtained directly from the total interference function:

$$S(Q) = \sum_{\alpha=1}^{n}\sum_{\beta=1}^{n} W_{\alpha\beta} S_{\alpha\beta}(Q) = \frac{F(Q)}{\left(\sum_{\alpha=1}^{n} c_\alpha f_\alpha(Q)\right)^2} + 1 \tag{1.23}$$

where $W_{\alpha\beta}$ are the x-ray weighting factors for each α-β pair. The total structure factor can also be defined in terms of the Debye scattering equation:

$$S(Q) = 1 + \frac{1}{N}\sum_{\alpha=1}^{n}\sum_{\alpha\neq\beta}\frac{\sin Qr_{\alpha\beta}}{Qr_{\alpha\beta}} \tag{1.24}$$

where $r_{\alpha\beta}$ is the interatomic distance between correlated α-β atomic pairs, with each pair contributing a sinc function to the $S(Q)$. Fourier transformation of this quantity yields the pair distribution function, which describes the real-space variation in microscopic pair density with distance, proportional to the average (bulk) density. Variations arise when correlations between pairs of atoms are more likely to occur at a specific separation distance r, and so analysis of such real-space functions allow determination of local structure as well as liquid density.

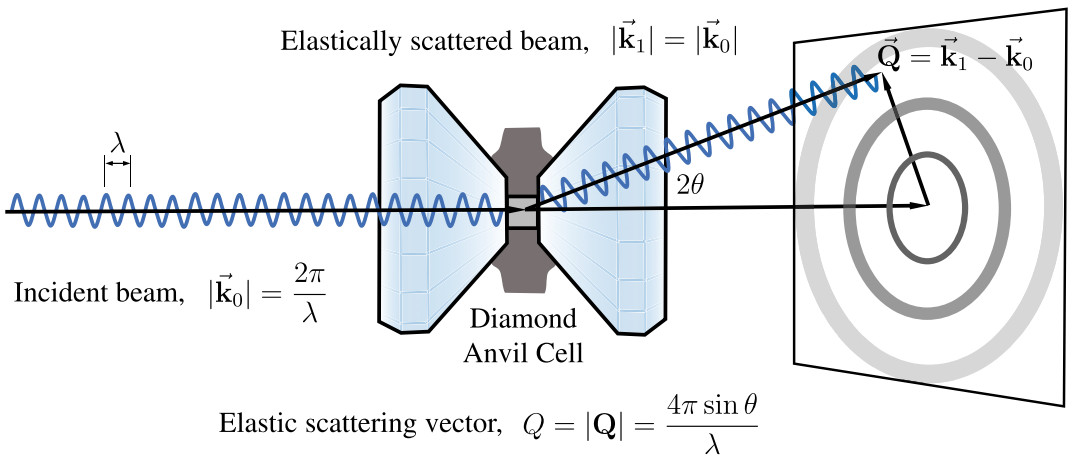

Figure 1.5: *Schematic illustration of angle-dispersive XRD in the DAC showing the relation between the wavelength of the incident x-ray beam, λ, scattering angle, 2θ, incident and scattered wavevectors, $\vec{\mathbf{k}}_0$ and $\vec{\mathbf{k}}_1$, and the scattering vector, $\mathbf{Q}$ (and its scalar value, Q). Figure reprinted with permission from Drewitt (2021). © 2021 J. W. E. Drewitt.*

X-ray diffraction of both crystalline and amorphous materials therefore allows determination of structure and density, alongside phase identification. When combined with high *P*-*T* techniques this can be used to map phase relations and phase transitions, and construct phase diagrams and melting curves. In addition, XRD can be used to measure density as a function of pressure and temperature, and so derive equation of state which describe the *P*-*V*-*T* relations of a material (section 1.2.4).

1.2.3 Synchrotron Light Sources

The small sample size in DAC experiments necessitates the use of synchrotron light sources for x-ray measurements instead of traditional lab sources (Andrault & Fiquet, 2001; Shen & Mao, 2016). Synchrotron light sources produce extremely intense beams of high-energy radiation. At user end-stations they can provide very coherent, brilliant x-rays that can be collimated or focused (with Kirkpatrick–Baez mirrors) to extremely narrow beams similar in size to the sample chamber ($\sim$5 to 100 µm), while providing sufficient intensity for (often rapid) analysis of the small sample volume (Willmott, 2019). Furthermore, synchrotron sources allow the use of higher energy x-rays than lab sources can provide. This is important for *in situ* x-ray diffraction measurements in the DAC, where the cell geometry limits the accessible scattering angle (see section 1.3). In particular, high energies are required for diffuse scattering measurements of amorphous materials, where data collection across a large Q-space is required for accurate structural interpretation (Benmore, 2012; Drewitt, 2021).

The large scale of synchrotrons mean they are mostly national facilities, such as Diamond Light Source (UK), ESRF (France), DESY (Germany), APS (USA), and Spring-8 (Japan). Synchrotron light sources utilise the extremely bright radiation emitted by charged particles when they are accelerated while travelling at relativistic speeds (synchrotron radiation). A good review of the fundamental concepts of synchrotron radiation and facilities, as well as synchrotron techniques and applications, can be found in Willmott (2019). Synchrotrons typically consist of a large storage ring (often 100s of metres in circumference) that high-energy electrons circulate, and a primary acceleration device (such as a linac or additional booster synchrotron) that creates and accelerates electrons before injection into the storage ring. In modern synchrotrons insertion devices (such as undulators or wigglers — essentially periodic structures of magnets) placed around the storage ring are used to create the highly brilliant, forward directed synchrotron radiation that is provided at each user beamline. Synchrotron facilities generally have many beamlines situated around the ring, with each optimised for a particular technique. While x-ray diffraction was the first synchrotron technique to be combined with the DAC (Manghnani et al., 1980), there is now a wide variety of methods that can be used to investigate DAC samples at synchrotrons. These include angle- and energy-dispersive x-ray diffraction, x-ray absorption spectroscopies (XAS, EXAFS, XANES, NEXAFS, etc.), x-ray emission and x-ray Raman spectroscopies (XES, XRS, etc.), x-ray fluorescence (XRF), nuclear resonance spectroscopies and synchrotron Mössbauer techniques (NFS, NIS, NSAS, SMS, etc.), inelastic x-ray scattering techniques (IXS, RIXS, etc.), and x-ray imaging and tomography (Bassett & Brown Jr, 1990; Andrault & Fiquet, 2001; Shen & Mao, 2016; Anzellini & Boccato, 2020).

1.2.4 Equations of State

X-ray diffraction provides a direct measure of the unit cell parameters of a crystalline material, and therefore its volume (section 1.2.2). If high quality XRD data are collected across a range of P-T conditions a thermal equation of state can be fit to the data, which fully describes the P-V-T relationship of the material, and the bulk modulus can be extracted along with other key thermodynamic properties. Equations of state that describe room temperature compression (i.e., isothermal EOS at 300 K) typically consider the isothermal bulk modulus at reference conditions (typically 10^5 Pa and 300 K), K_{T0}, and its derivative with respect to pressure, K'_{T0}, as fitting parameters to describe pressure (P) as a function of the change in volume (V) from the volume at reference conditions, V_0. Equations of state are typically constructed on the basis of a variety of thermodynamic relations, principally, the definition of pressure as a derivative of Helmholtz free energy with respect to volume. However, most EOS are semi-empirical, in that they make a variety of assumptions in order to match experimental data. A good introduction to the theoretical background of EOS can be found in Anderson (1995).

The Birch-Murnaghan EOS is probably the most widely used isothermal EOS. It is constructed on the basis of a Taylor expansion of Helmholtz free energy in terms of negative (i.e., compressive) finite Eulerian strain, f, where f is defined as:

$$f = \frac{1}{2}\left[\left(\frac{V}{V_0}\right)^{-2/3} - 1\right]. \tag{1.25}$$

Typically, a third order expansion is used. Defining the compression $x = V/V_0$, the Birch-Murnaghan EOS (Birch, 1947) in third order is:

$$P_{T_0}(x) = 1.5K_{T_0}\left(x^{-7/3} - x^{-5/3}\right)\left[1 + 0.75\left(K'_{T_0} - 4\right)\left(x^{-2/3} - 1\right)\right]. \tag{1.26}$$

When $K'_{T0} = 4$ the third-order Birch-Murnaghan EOS is equivalent to the second-order form. As K'_{T0} is ~4 for many geophysically relevant materials, the second-order is also commonly used as a good approximation. However, the Birch-Murnaghan EOS can struggle to describe the data for materials with large values of K'_{T0} ($\gtrsim$6–8; Hofmeister, 1993).

Probably the most common alternative isothermal EOS is the Vinet EOS (also called the Rose-Vinet, Vinet-Rydberg or Morse-Rydberg EOS; Vinet et al., 1987). The Vinet EOS is constructed on the basis of considering the binding energy of metals in terms of interatomic pair potentials. It is commonly applied in the case of metals, but can be applied to other materials, and is also particularly useful for describing liquids (which generally have large values of K'). The EOS is expressed as:

$$P_{T_0}(x) = 3K_{T_0}x^{-2/3}\left(1 - x^{1/3}\right) \cdot \exp\left[1.5\left(K'_{T_0} - 1\right)\left(1 - x^{1/3}\right)\right]. \tag{1.27}$$

A modification of this EOS proposed by Holzapfel (1991, 2002) is also sometimes used. It was designed to mitigate some of the deficiencies of the Vinet EOS at very strong compression caused by the use of the Rydberg potential in its construction. The form is:

$$P_{T_0}(x) = 3K_{T_0}x^{-5/3}\left(1 - x^{1/3}\right) \cdot \exp\left[1.5\left(K'_{T_0} - 3\right)\left(1 - x^{1/3}\right)\right]. \tag{1.28}$$

Equations 1.27 and 1.28 can be generalised as:

$$P_{T0}(x) = 3K_{T0}x^{-k/3}\left(1 - x^{1/3}\right) \cdot \exp\left[\left(1.5K'_{T0} - k + 0.5\right)\left(1 - x^{1/3}\right)\right]. \tag{1.29}$$

When $k = 2$ this is equivalent to the Vinet EOS (equation 1.27) and is equivalent to the Holzapfel EOS (equation 1.28) when $k = 5$. Kunc et al. (2003) have applied this form with k as an additional fitting parameter to find the most suitable form for the material and range of compression.

Aside from these, a wide range of other EOS formalisms have been used in the literature, including equations of state based on other definitions of finite strain (e.g., Lagrangian strain), other derivations from considerations of interatomic potentials, and derivations based on analytical relationships between EOS parameters. An example of an alternative EOS that can be used is the modified Tait EOS proposed by Huang & Chow (1974), which performs well at deep Earth conditions (Holland & Powell, 2011), and is easily invertible. This is a three parameters EOS, which includes the use of the second derivative of K_{T0}, K''_{T0}:

$$P = \frac{1}{b}\left[\left(\frac{x + a - 1}{a}\right)^{-1/c} - 1\right], \tag{1.30}$$

where

$$a = \frac{1 + K'_{T0}}{1 + K'_{T0} + K_{T0}K''_{T0}}, \tag{1.31}$$

$$b = \frac{K'_{T0}}{K_{T0}} - \frac{K''_{T0}}{1 + K'_{T0}}, \tag{1.32}$$

and

$$c = \frac{1 + K'_{T0} + K_{T0}K''_{T0}}{K'^2_{T0} + K'_{T0} - K_{T0}K''_{T0}}. \tag{1.33}$$

All EOS make some level of assumptions, and so the form that best fits the data is generally chosen. It is also important to note that the parameters K_{T0} and K'_{T0} are not necessarily equivalent between different EOS forms or different orders of expansion.

With the addition of high temperature data, a thermal EOS can be constructed that fully describes the *P-V-T* relationship, and relates isotherms at different temperatures. This is generally done by considering the total pressure as a sum of the pressure at 300 K and a thermal pressure term, ΔP_{th} (see Anderson, 1995):

$$P(V, T) = P_{T_0}(V) + \Delta P_{th}(V, T). \tag{1.34}$$

The Mie-Gruneisen-Debye model (e.g., see Jackson & Rigden, 1996) is the most common construction for calculating ΔP_{th}:

$$\Delta P_{th}(V, T) = \frac{\gamma}{V} \Delta E_{th}, \tag{1.35}$$

where γ is the Grüneisen parameter and ΔE_{th} is the additional internal thermal energy at elevated temperature compared to reference conditions:

$$\Delta E_{th} = E_{th}(V,T) - E_{th}(V,T_0). \tag{1.36}$$

$E_{th}(V,T)$ is calculated by the Debye model:

$$E_{th}(V,T) = 9nRT\left(\frac{\Theta}{T}\right)^{-3}\int_0^{\Theta/T}\frac{\xi^3}{e^{\xi}-1}d\xi, \tag{1.37}$$

where n is the number of atoms in the formula unit, R is the gas constant, and Θ is the Debye temperature. The integral term is computed over the range 0 to Θ/T by numerical approximation. Both the Debye temperature and the Grüneisen parameter are volume-dependent, as in the Mie-Grüneisen-Debye model γ is defined as:

$$\gamma = -\frac{\partial \ln \Theta}{\partial \ln V}. \tag{1.38}$$

The volume dependence of γ is described by defining an additional fitting parameter, q, as:

$$q = \frac{\partial \ln \gamma}{\partial \ln V}. \tag{1.39}$$

Integration then leads to the defintions of γ and θ as:

$$\gamma = \gamma_0\left(\frac{V}{V_0}\right)^q, \tag{1.40}$$

and

$$\Theta = \Theta_0 \exp\left(\frac{\gamma_0 - \gamma}{q}\right), \tag{1.41}$$

where γ_0, Θ_0, and q are the actual fitting parameters in the model.

A volume dependency on the parameter q has also been considered by some authors. However, describing the volume dependency of q in an analogous way to equations 1.38 and 1.39 leads to a difficult numerical integral to compute Θ. The volume dependency of γ and Θ can instead be described by defining two volume independent fitting parameters (a and b), with (Tange et al., 2009):

$$\gamma = \gamma_0 \left\{ 1 + a \left[\left(\frac{V}{V_0} \right)^b - 1 \right] \right\}, \tag{1.42}$$

and

$$\Theta = \Theta_0 \left(\frac{V}{V_0} \right)^{\gamma_0 (a-1)} \cdot \exp \left(\frac{\gamma_0 - \gamma}{b} \right). \tag{1.43}$$

Alternatively, the thermal pressure, ΔP_{th}, can be evaluated on the basis of thermodynamic relationships using the thermal expansion coefficient, α:

$$\Delta P_{th} = \int_{T0}^{T} \left[\alpha K_{T0} \right]_V dT. \tag{1.44}$$

A common assumption is that αK_T is independent of volume, in which case the thermal pressure can be calculated simply (Anderson, 1984):

$$\Delta P_{th} \approx \alpha K_{T0} \left(T - T_0 \right). \tag{1.45}$$

This assumption is reasonable when the temperature range of interest is significantly higher than the Debye temperature (Anderson, 1995), although approaches to describing the volume dependence of αK_T have also been described (e.g., Jackson & Rigden, 1996).

Constraining the bulk modulus and density as a function of P and T allows the interpretation of seismic data (section 1.2.1). However, uncertainties in elastic moduli have a significant effect on modelled seismic velocities (Cottaar et al., 2014). Equation of state parameters are typically constrained by a weighted non-linear least squares fit to the data, and a variance-covariance matrix de-

scribing the parameter uncertainties can be extracted from the refinement procedure (Angel, 2000). The covariances between fitted parameters can be significant, but unfortunately, many studies do not report the full covariance matrix in EOS fits. Extraction of uncertainties from a least squares fit assumes that the measured P, V, and T datasets are uncorrelated, and that there are enough data points for the uncertainties to be normally distributed statistically (Angel, 2000). However, the number of data points in EOS studies is often not large (particularly the number of high-T data points), and in some cases P, V and T will be correlated. For example, measuring pressure using the volume of an XRD calibrant (section 1.3.2.1) relies on the temperature measurement, and instrumental effects such as wavelength fluctuations will affect the volume of both the sample and calibrant (and therefore P and V). In typical high-P-T experiments the relative error on temperature will introduce the most uncertainty to the dataset. This is because the relative uncertainty on temperature is typically much greater than that on the volumetric measurement of the sample or pressure calibrant (section 1.3.4). The relative uncertainty on P is also typically high, due to not only the uncertainty on temperature, but inherited uncertainty from the pressure scale (section 1.3.2). More precise determination of EOS parameters can therefore be achieved by reducing the uncertainty on individual data points (particularly T), increasing the number of data points, or increasing the range of data while maintaining precision (Angel, 2000). Therefore, experimental techniques which can allow the collection of dense datasets across a wide P-T range, and with minimal uncertainties on T, even at high temperature, are key to accurate and precise determinations of equations of state.

1.2.5 Sound Velocity Measurements

The determination of shear modulus or the full set of elastic constants generally requires more involved techniques. As the diamond anvil cell is the only device which can routinely access the extreme pressures of the lower mantle, available techniques are limited by the small sample size (tens of microns). Ultrasonics can be used to directly measure acoustic wave velocities (for very high frequencies), but in the DAC require near optical wavelengths (e.g., GHz-ultrasonic-interferometry) due to the small sample size, and experiments are limited to specific configurations and pressure media (e.g., Jacobsen et al., 2005). A picosecond laser acoustic method for use in the DAC has also been developed, which involves generating stress waves with a pulsed laser that are detected again using laser-based interferometry (Decremps et al., 2014). However, the technique has only been applied to moderate temperatues, and is still currently at the forefront of experimental capabilities (Decremps et al., 2009, 2014, 2015; Ayrinhac et al., 2015; Wakamatsu et al., 2018; Edmund et al., 2020). The primary methods for determining elastic constants and/or sound velocities in DAC experiments are photon-phonon scattering techniques, particularly lab-based Brillouin spectroscopy (e.g, Murakami et al., 2009; Kurnosov et al., 2017) and synchrotron-based meV resolved inelastic x-ray scattering (IXS; e.g., Fukui et al., 2008).

Brillouin scattering is the inelastic scattering of light by ambient thermally induced elastic waves in a crystal lattice (i.e., scattering of photons by acoustic phonons). As the propagation velocity for a given wave manifests as a Doppler shift in the frequency of scattered radiation, the location of peaks in the Brillouin spectra is a function of acoustic velocity. Brillouin spectroscopy is analogous to Raman spectroscopy but probes lower frequency acoustic phonons rather than higher frequency vibrational modes (optical phonons; Polian, 2003).

Brillouin spectroscopy can be applied to samples as small as 30×30×8 μm and is therefore well suited to making measurements up to the megabar range (e.g., Murakami et al., 2012), but is limited to transparent samples as it is done in transmission (Polian, 2003). High pressure Brillouin spectroscopy is now a mature (with more than ten systems as of 2020; Marquardt & Thomson, 2020), high resolution technique that provides very accurate measurements of sound velocities and single-crystal elastic moduli (i.e., C_{ijkl}), but it does pose experimental difficulty (Murakami et al., 2009; Speziale et al., 2014; Ohira et al., 2016; Kurnosov et al., 2017). The signal to noise ratio can be low because of the thin samples and background scattering from the anvils (Kurnosov et al., 2017). Sample geometry is also extremely important as refraction of the light must be accounted for. Deviations from the ideal symmetric platelet scattering geometry including non-parallel diamond anvils and an inclined or imperfectly polished sample can introduce significant uncertainties in the measured sound velocities (Speziale et al., 2014), although systematic errors can be accounted for by making measurements through a 360° rotation of the DAC (Kurnosov et al., 2017). As Brillouin spectroscopy in the DAC records scattering by the anvils as well as the sample, the sample signal can also be obscured by the diamond signal. For example, at ∼40 GPa the V_P of bridgmanite approaches (and is masked by) the V_S of diamond (Kurnosov et al., 2017).

IXS can be applied to similarly sized DAC samples as x-ray beams can be focused to spot sizes of a few tens of microns. As the hard x-rays used in this technique are penetrating, it can also be applied to opaque samples, unlike Brillouin spectroscopy which is limited to optically transparent samples. This allows IXS to access a much wider pressure–composition (opacity) space than Brillouin scattering (Fukui et al., 2008; Baron, 2016a,b). IXS similarly probes the excitation and annihilation of phonons in the crystal lattice by photons, which is possible because the x-rays used have wavelengths comparable to interatomic distances. However, such x-rays have energies (∼10 keV) six orders of magnitude larger than typical phonon energies (∼10 meV) which makes resolving the relatively tiny shifts in photon energy extremely difficult (Burkel, 2000; Baron, 2016a,b). The development of large, complex spectrometers has helped achieve meV (and even sub meV) resolution but at the cost of x-ray flux, with IXS limited to a few synchrotron beamlines (ESRF, APS & Spring-8). In part due to the low flux in inelastic scattering experiments, x-ray beam dimensions are typically limited to ∼20 to $50\,\mu\mathrm{m}$ (FWHM), although a commissioning experiment on the Matter in Extreme Conditions endstation at the Linac Coherent Light Source (LCLS) achieved a spot size of 5 μm

(McBride et al., 2018). A typical IXS measurement involves moving the spectrometer geometry to collect for a momentum transfer of interest and scanning through energies of the incident beam by varying a high precision monochromator (Baron, 2016a). A phonon dispersion curve is obtained by fitting the energies of the intensity peak for several momentum transfers, and the sound velocities in the propagation direction of observed phonons can be extrapolated from the slope of the disperion curve at the $q = 0$ limit (Fiquet et al., 2004; Fukui et al., 2008).

IXS has been combined with external resistive heating DAC techniques to measure sound velocities at elevated *P-T* conditions up to ∼1000 K(e.g., Kantor et al., 2007; Ohtani et al., 2013, 2015). Laser-heating techniques (which can generate mantle-relevant conditions) have also been used with some success up to ∼3000 K (particularly for measurements of iron alloys), but laser-heating is difficult to interface with the IXS experimental geometry because of the small scattering angle, and laser-heating instability over the long timescales required (typical acquisition times are 6 to 12 hours for a single spectra) can lead to large temperature uncertainties (Fukui et al., 2013; Sakairi et al., 2018; Takahashi et al., 2019). The time constraints of IXS experiments is probably a major reason why its application to mantle materials has been limited (Fiquet et al., 2004; Fukui et al., 2008; Antonangeli et al., 2011; Finkelstein et al., 2018)

Brillouin spectroscopy has been more widely applied to mantle materials as it does not require synchrotron access (e.g., Sinogeikin et al., 2004; Jackson et al., 2005; Marquardt et al., 2009a,b; Kudo et al., 2012; Murakami et al., 2012; Kurnosov et al., 2017). At high temperature, external resistive heating experiments combined with Brillouin spectroscopy have generally been limited to ∼1000 K (Mao et al., 2012; Pamato et al., 2016; Yang et al., 2016; Schulze et al., 2018; Fan et al., 2019). The limitation of sample transparency means that IR-laser heating cannot be used (as radiation at this frequency is not absorbed by Fe-free/transparent non-metallic samples), but CO_2-laser heating has been combined with Brillouin spectroscopy to make measurements up to ∼2500 K at high pressure (e.g., Sinogeikin et al., 2004; Murakami et al., 2012; Zhang et al., 2015; Zhang & Bass, 2016). However, CO_2-laser heating presents more experimental difficulty than IR-laser heating and, similar to IXS, the long acquisition times of Brillouin spectroscopy (∼2-18 hours) results in uncertainties of several hundred K due to temperature fluctuations over the duration of experiments(e.g., Murakami et al., 2012). Both IXS and Brillouin spectroscopy can be applied to single crystal (e.g., IXS: Antonangeli et al., 2011; Finkelstein et al., 2018; Kamada et al., 2019; Brillouin: Yang et al., 2016; Kurnosov et al., 2017) or polycrystalline samples (e.g., IXS: Ohtani et al., 2015; Takahashi et al., 2019; Brillouin: Murakami et al., 2007a, 2012). Single crystal measurements are slow to perform (as they require measurements in different orientations), and so have been more widely made on crystals with cubic symmetry (e.g., majoritic garnet, Pamato et al., 2016; ringwoodite, Sinogeikin et al., 2001; Schulze et al., 2018; and ferropericlase, Marquardt et al., 2009a,b; Yang et al., 2015), although this can be sped up by placing multiple crystals with different orientations within the same

sample chamber (e.g. Kurnosov et al., 2017). Measurements of polycrystalline samples provide orientation averaged sounds velocities, which can still constrain bulk and shear moduli (e.g. Polian, 2003; Fiquet et al., 2004). Polycrystalline measurements are generally simpler to make, and take less time than those on single crystals. Furthermore, the use of powder samples allows measurements to be made of materials that cannot be recovered to ambient pressures (and so for which single crystals cannot be synthesised), including post-stishovite (Asahara et al., 2013), calcium perovskite (Kudo et al., 2012), and post-perovskite (Murakami et al., 2007a). However, measurements of polycrystalline samples may be sensitive to grain size, orientation, and stress distribution in the samples (Marquardt et al., 2011).

Measurements on single crystals in different crystallographic orientations can quantify the full elastic tensor required for a complete description of anisotropy. This is done by relating acoustic velocities along specific crystallographic axes to the independent elastic constants (C_{ij}) via the Christoffel equation (e.g., see Fedorov, 1968; Auld, 1973):

$$\sum_{ij} \left[\Gamma_{ij} - \rho v^2 \delta_{ij}\right] s_j = 0, \tag{1.46}$$

where v is the phase velocity of the plane wave (phonon), ρ is the crystal density, s_j is the polarisation vector, δ is the kronecker delta, and Γ_{ij} is the Christoffel matrix describing the elasticity in the orientation of interest, defined by:

$$\Gamma_{ij} = \sum_{kl} c_{ijkl} q_k q_l, \tag{1.47}$$

where c_{ijkl} is the stiffness tensor, and q_k and q_l are direction cosines defining direction of plane wave propagation through the crystal.

1.2.6 Raman Spectroscopy

When a sample is illuminated by a monochromatic light source the majority of photons will be scattered elastically (termed Rayleigh scattering), where the incident and scattered photons have the same frequency (ν_0). However, a small percentage ($\sim$1 in 10^{-7}; Ferraro et al., 2003; Osipov, 2019) of incident photons will be scattered by an excitation in the molecule, resulting in scattered photons with a different energy state. This inelastic scattering (the Raman effect) occurs due to the interaction of light with vibrational and rotational transitions in the sample, and results in scattered photons with frequencies of $\nu_0 \pm \nu_m$, where ν_m is a vibrational frequency. Raman spectroscopy utilises the Raman effect for photons in the UV–visible range to measure vibrational frequencies as a shift from the frequency of the incident beam. The intensity of Raman scattered light is related to the polarisability of a Raman active mode as a function of atomic motion. The Raman spectrum (Raman shift vs intensity) can therefore provide diagnostic information about molecular structure, geometry, symmetry and bond characteristics of a sample (Ferraro et al., 2003; Smith & Dent, 2019). The elastically scattered radiation (at the laser line wavelength) is typically filtered out, and the rest of the scattered light dispered onto a detector. The Stokes ($\nu_0 - \nu_m$) and anti-Stokes ($\nu_0 + \nu_m$) lines give the same information, but the Stokes process is stronger, so typically only this side of the spectrum is measured, and the frequency difference reported in terms of spectroscopic wavenumber, with units cm^{-1} (Smith & Dent, 2019). The selection rules for Raman scattering generally dictate that only fundamental vibrations are observed, with the rate of change of polarisability during a vibration also required to be non-zero for the vibration to be Raman active (typically this is true for symmetric modes). As these fundamental vibrational frequencies are specific to the chemical bonding and symmetries of a sample, Raman spectroscopy also allows fingerprint identification of phases (Neuville et al., 2014; Smith & Dent, 2019). Changes in the Raman spectrum as a function of pressure or temperature can indicate changes in bond strength and the strong selection rules often lead to obvious effects when passing through a phase transition (with peaks appearing or disappearing; Williams, 1995; Mao & Hemley, 1994; Neuville et al., 2014).

As the intensity of Raman scattered light is independent to the sample volume, it remains essentially constant with decreasing sample size. The minimum possible spot size will be controlled by the Abbé diffraction limit of the excitation laser wavelength used in the specific system, and the use of visible (or UV) wavelengths in Raman spectroscopy therefore allows a smaller spatial resolution compared to IR techniques (Williams, 1995; Ferraro et al., 2003). This makes micro-Raman spectroscopy a powerful tool that can be easily interfaced with the DAC despite the small sample size (Neuville et al., 2014). The spatial filtering of confocal micro-Raman system designs has been particularly useful for this approach (e.g. Chopelas, 1996; Shim et al., 2007; Tschauner et al., 2008; Drewitt et al., 2019). However, interfacing Raman spectroscopy with the DAC poses several issues. Diamond has a high refractive index (2.424 at 532 nm for type IIa diamond; Turri et al., 2017),

meaning measurements are made through an optically thick window. This causes geometric and chromatic abberations, affecting the signal collection efficiency and depth selectivity (Goncharov & Crowhurst, 2005b; Goncharov, 2012). At low frequencies the diamond anvils also specularly reflect laser light causing parasitic back reflections which decrease the signal to noise ratio (Goncharov, 2012). Furthermore, the fluorescence of diamond anvils in the laser beam can contribute significantly to the background level (Xu et al., 1986), although this effect can be minimised through the use of diamond anvils with no measurable nitrogen impurities (such as type IIas Raman diamonds with ultra-low fluorescence; Adams & Sharma, 1977). The spatial filtering of confocal systems can also help attenuate spurious radiation and at the same time decrease the depth of field, helping to remove background fluorescence (Goncharov, 2012).

Techniques for *in situ* Raman scattering measurements at extreme conditions in the DAC are currently limited to < 2000 K and < 150 GPa (Goncharov & Crowhurst, 2005b; Goncharov, 2012). In particular, detection of the weak Raman signal against strong thermal emission from the sample and/or heater assembly at high temperature is a challenge. Two main approaches are commonly used to combat this, often in combination. The first is to use spatial filtering of the thermal radiation by using a pinhole diaphragm in a confocal system which only allows light emitted from the small excited volume to pass (Goncharov & Crowhurst, 2005b; Osipov, 2019). Nevertheless, beyond ∼1400–1500 K the thermal radiation is generally too intense to obtain useable Raman spectra (Osipov, 2019). The second approach is to use time-resolved filtering of the Raman signal. This is done by using a pulsed excitation laser in combination with a gated detector synchronised to the laser pulse, so that scattered light is only collected during the short period of excitation (Goncharov & Crowhurst, 2005a; Osipov, 2019). In such systems the intensity of the thermal radiation will decrease with the pulse duration, while the intensity of the Raman signal remains essentially constant. Using a blue excitation laser (e.g., at 458 nm) can also help to spectrally discriminate the thermal radiation from the Raman scattered light (Lin et al., 2004b; Goncharov & Crowhurst, 2005a).

1.2.7 FTIR

Infrared spectroscopy provides another optical analysis technique. Fourier-transform infrared spectroscopy (FTIR) is the most widely used variant. In FTIR, high spectral resolution data can be collected over a wide spectral range simultaneously, making it very efficient. Materials absorb infrared radiation at the resonant frequencies of vibrational modes in their structure. IR absorption spectra are therefore characteristic of a particular material, and are very sensitive to small changes in structure or composition. This makes FTIR a useful technique for phase characterisation and identification of specific functional groups in the material. FTIR provides a complementary technique to Raman spectroscopy for phase identification as the selection rules for IR absorption are different

to those of Raman scattering. Griffiths & De Haseth (2007) provide a comprehensive introduction to the theoretical and practical background of FTIR.

IR absorption by OH^- groups is particularly efficient as they are strongly polar (Paterson, 1982; Rossman, 1988). This has made FTIR a powerful technique for measuring the water content of nominally anhydrous minerals, including lower mantle phases (e.g., Rossman, 1988; Bell et al., 1995; Bolfan-Casanova et al., 2000, 2002; Bolfan-Casanova, 2005; Kovács et al., 2012; Pearson et al., 2014; Panero et al., 2015). Quantitative information on water content can be obtained from FTIR spectra as absorbance (A) is governed by the Beer-Lambert law, $A = \epsilon lc$, where c is the molar concentration, l is the path length, and ϵ is the molar absorptivity determined by a calibration study (e.g., Paterson, 1982; Libowitzky & Rossman, 1997; Bell et al., 2003, 2004). Relative absorbance can also be dependent on the structural orientation of OH^- groups in the lattice, which can be investigated through the use of a linear polarised IR source (Rossman, 1988; Kovács et al., 2012). The exact frequency of the OH absorption peak (which is in the 3600 cm^{-1} region) is dependent on the hydrogen bond strength and O-H—O distance. These host dependencies on OH stretching energies and absorbance allows FTIR to provide information on incorporation mechanisms and defect structures, as well as water content (Berry et al., 2005; Demouchy & Mackwell, 2006; Sambridge et al., 2008; Kovács et al., 2010, 2012).

1.2.8 Mössbauer Spectroscopy

Mössbauer absorption spectroscopy is a sensitive technique that harnesses the recoil-free nuclear resonant fluorescence of gamma-rays in crystalline materials (the Mössbauer effect; Mössbauer, 1958). This effect occurs when nuclear gamma-rays with a specific energy emitted by one isotope are resonantly absorbed by nuclei of the same isotope within a sample (Nasu, 2013). The most widely used isotope is ^{57}Fe, which has made Mössbauer spectroscopy an important technique in Earth Science due to the abundance of iron in geophysically relevant materials (McCammon, 2021). The radioactive isotope ^{57}Co is used for lab sources, which decays to an excited state of ^{57}Fe that then emits gamma-rays during the transition to its ground state. Subtle variations in absorption energy for a particular isotope relate to various nuclear interactions, including isomeric shift due to differences in nearby electron densities, quadrupole splitting due to atomic-scale electric field gradients, and hyperfine splitting of nuclear levels due to local magnetic fields. For ^{57}Fe, these interactions relate to important properties such as coordination environment, oxidation state, spin state, and magnetic ordering (Nasu, 2013; McCammon, 2021). For lab-based Mössbauer spectroscopy the gamma-ray source is rapidly oscillated (i.e., physically accelerated back and forth) to scan through a range of energies via the Doppler effect. The extremely narrow line widths of nuclear gamma rays result in very high energy resolution, making Mössbauer spectroscopy a particularly sensitive technique, and

a useful probe of iron valence and spin state at high-pressure (e.g., McCammon et al., 1997; Frost et al., 2004; Lin et al., 2004a; McCammon et al., 2008; Kupenko et al., 2015; Zhang et al., 2016; Dorfman et al., 2020). However, the low natural abundance of ^{57}Fe ($\sim$2%) in samples and the low brilliance of lab sources means that long collection times of several days are often required. This makes lab-based Mössbauer spectroscopy prohibitively difficult to interface with laser-heating due to the poor temperature stability and constant user input. Furthermore, the difficulty in focusing gamma-rays emitted by lab sources prohibits Mössbauer studies at pressures over $\sim$100 GPa, due to the small culet (and sample) sizes required (McCammon, 2021).

In contrast, synchrotron Mössbauer sources (SMS) provide radiation that is significantly more intense, and can focused to spot sizes $\sim$10 μm in diameter (Potapkin et al., 2012). SMS typically uses a crystal of $^{57}FeBO_3$ (which allows pure nuclear diffraction of the synchrotron radiation beam at specific Bragg reflections) as a nuclear resonant monochromator, with single-line nuclear resonance achieved by applying an external magnetic field and a specific temperature (close to the Néel temperature; Smirnov et al., 1997). A motor is typically used to provide the velocity oscillations of the crystal in the same way as a lab-source (Potapkin et al., 2012). The intensity and fine focus of Mössbauer gamma-radiation produced in this way allows high quality measurements of samples at high-pressure in the DAC, and significantly reduces collection times (e.g., McCammon et al., 2013; Cerantola et al., 2017; Kiseeva et al., 2018; Dorfman et al., 2020). Nevertheless, laser-heating is still difficult to interface with SMS, and collection times can still be up to several hours (Kupenko et al., 2012; Cerantola et al., 2017).

1.3 High *P*-*T* Experimental Techniques: The Diamond Anvil Cell

1.3.1 Diamond Anvil Cell Design and Pressure Generation

Pressures encompassing mantle conditions can be generated routinely in the diamond anvil cell (DAC). Pressure is generated in the diamond anvil cell by compressing the sample between the tips of two opposed diamonds. Cut, gem-quality diamonds are used, with the culet tip polished flat to form an anvil surface typically <1 mm in diameter. The anvils are mounted on ceramic seats and held in a cell body to ensure they remain perfectly aligned and parallel, and force is then applied by squeezing the anvils together. Since $P = F/A$, the DAC can subject sub-millimetre samples to megabar pressures with only moderate forces that can be handled by the strong diamonds. Combined with resistive or laser heating techniques, the DAC can simultaneously generate sample temperatures of many thousand kelvin at high pressure, and cooling down to the millikelvin range is achievable using a cryostat (Palmer et al., 2015; Anzellini & Boccato, 2020). The transparency of diamond across a wide frequency range offers optical access to the sample, allowing *in situ* analysis by optical microscopy, spectroscopy, or x-ray scattering techniques. Interfacing the DAC with this wide range of techniques in labs or at synchrotron beamlines is also greatly simplified by their compact and portable nature (Shen & Mao, 2016; Anzellini & Boccato, 2020). An excellent historical review of the diamond anvil cell and its development can be found in the paper by Bassett (2009).

A wide variety of designs for the DAC cell body exist, including many commercially available options. The form factor is generally designed to suit specific purposes or experimental set-ups, such as maximising the opening angle for x-ray diffraction experiments, interfacing with a particular analysis technique, or combining with methods of sample heating or cooling. Achievable pressure is mainly limited by the anvils, but the cell body itself must be sufficiently strong to withstand the forces applied, and is typically made from high-strength steel or nickel super-alloys (e.g., nimonic and inconel; Kantor et al., 2012). Force is applied by simply squeezing the anvils together, either by tightening spring-loaded screws, or using an inflatable metallic membrane. Screw-driven DACs are much simpler, and the pressure generated is usually more stable over long time periods. However, membrane-driven designs offer more precise control over the pressure and the possibility of remote operation, making them particularly well suited for compression experiments at synchrotron beamlines (Jayaraman, 1986; Letoullec et al., 1988; Kantor et al., 2012).

The backing plates are usually made from tungsten carbide (WC), although for magnetic measurements, other (non-magnetic) materials such as SiC are sometimes used (Pugh, 2016), and (relatively) x-ray transparent materials such as cubic boron nitride (cBN) are sometimes used for diffraction ex-

periments (Shen et al., 2003). The seats have a small hole to allow optical access to the sample through the back of the diamonds. As WC is not x-ray transparent, the backing plates will limit the accessible scattering angle for measurements. A large hole will reduce the mechanical strength of the seats and so a conical design is generally used to maximise the opening angle. In the Boehler-Almax anvil-seat design, the anvil is recessed in the seat slightly to maximise the opening angle (Boehler & De Hantsetters, 2004).

Natural, gem-quality and inclusion-free diamonds are typically used for the anvils, although for some specific applications, such as XAS, nano-polycrystalline diamonds may be used instead to avoid sharp Bragg peaks from the anvils in collected data (Ishimatsu et al., 2012; Rosa et al., 2020). Sintered nano-polycrystalline diamonds may also be beneficial for wider applications due to their higher strength and lower thermal conductivity (Irifune et al., 2003b,a; Ohfuji et al., 2010). For optical spectroscopy, diamonds with negligible impurities (mainly nitrogen) may also be selected for a low fluorescence background (Adams & Sharma, 1977). The most commonly used anvil shape is the jeweller's round brilliant cut (or a modified version of this) but other designs (such as Boehler-Almax anvils) are also used, often to reduce anvil thickness and increase opening angle for spectroscopic or x-ray scattering measurements (Boehler & De Hantsetters, 2004; Bassett, 2009). During polishing, the diamonds are also commonly oriented so that the culet face is cut parallel to a specific crystallographic plane, usually the (100) plane. This increases anvil strength and reduces the complexity of background peaks from the anvils in x-ray diffraction experiments (Bassett, 2009; Bassett & Skalwold, 2017). In x-ray scattering experiments a broad background arising from incoherent Compton scattering of the diamond is also present. For experiments where the background can obscure the signal, such as x-ray diffraction of amorphous or low-Z materials, this can be reduced by using thinner or partially perforated anvils (Dadashev et al., 2001; Soignard et al., 2010; Drewitt, 2021). The culet itself is typically a few 10s to a few hundred microns in diameters, with smaller culets able to access higher pressures. Single or double bevelled culet designs are commonly used to increase the achievable pressure for a given culet size, as they can deform further before breaking while cupping under pressure (Mao et al., 1979; Hemley et al., 1997; Li et al., 2018; O'Bannon III et al., 2018). Toroidal anvil geometries based on this concept have also been developed, and can access multi-megabar pressures (Dewaele et al., 2018; Jenei et al., 2018).

A thin gasket is used to separate the anvils and confine the sample to a pressure chamber. The gasket is made by compressing a thin metal foil in the DAC to leave an indentation of the culet tips. The pressure chamber can then be made by drilling a circular hole in the centre of the indentation by laser-ablation, spark-erosion, or mechanical micro-drilling. A single pressure chamber is the most common geometry, but multi-chamber experiments can also be performed (e.g., Walter et al., 2015). Rhenium is the most commonly used gasket material due to its hardness, with stainless steel a common low-cost alternative for experiments at lower pressures. Other materials can be used

for specific use cases, such as non-conductive composite gaskets for electrical measurements (e.g., Reichlin, 1983), or x-ray transparent materials such as beryllium, amorphous boron, or Kapton-boron-epoxy composite for radial x-ray diffraction measurements (e.g., Hemley et al., 1997; Lin et al., 2003; Merkel & Yagi, 2005). The indentation pressure will control the original thickness of the sample chamber and the deformation of the gasket during an experiment, and so can be tuned to the loading procedure or experimental conditions.

The sample is typically loaded into the pressure chamber along with a pressure transmitting medium that (combined with the radial confinement of the gasket) transforms the uniaxial compression from the anvils into a quasi-hydrostatic pressure. Hydrostaticity is important for many DAC experiments. Under deviatoric stress the quality of optical spectra deteriorate (Piermarini et al., 1973) and for x-ray diffraction experiments anisotropic and inhomogeneous stress can affect volume measurements, and pressures obtained from a calibrant will be biased and contain greater uncertainty (Meng et al., 1993; Chai & Michael Brown, 1996). This has a significant impact on the fine volume and pressure measurements required for precise determinations of equations of state. Pressure media are generally fluids or soft solids chosen for their low shear strength. Fluids offer a purely hydrostatic sample environment as they can freely deform without exerting shear stress on the sample, and are fairly simple to load. A wide variety of fluids are used as pressure media in DAC experiments, including alcohol mixtures (such as ethanol, methanol, and propanol), mineral oils (such as silicone oil or paraffin), and water (Angel et al., 2007; Klotz et al., 2009). However, fluid pressure media generally solidify at fairly low pressures ($<$10 GPa) and the solid phase can result in significant non-hydrostaticity (Angel et al., 2007; Takemura, 2021). It is therefore preferable to use noble (rare) gases which only become fluids at a few hundred MPa at room temperature, and although only remain stable in the fluid phase to several GPa, remain extremely soft throughout the solid phase (Klotz et al., 2009; Takemura, 2021). The noble gases are also chemically inert, which prevents reaction with the sample, and are optically transparent. The light noble gases also have small x-ray scattering factors which results in low backgrounds for x-ray diffraction experiments. Helium is generally considered to be the best pressure medium for maintaining hydrostatic conditions as it has the highest freezing pressure (11.6 GPa at 300 K), and the solid phase has extremely low shear strength and can release stress through re-crystallisation (Besson & Pinceaux, 1979; Mao et al., 1988; Takemura, 2001). Helium appears to remain completely hydrostatic up to 50 GPa, and offers the best performance beyond this up to at least 100 GPa (Takemura, 2021). However, the extreme compressibility of helium (and other gas pressure media) results in more significant radial collapse of the pressure chamber. With a solidified pressure medium, irregular deformation of the sample chamber can impose stress states (Takemura, 2021). Furthermore, gas loading requires more complicated procedures as the gas must be loaded under compression so that it remains in the fluid phase. Nevertheless, gas loading apparatus have become fairly widespread in university labs and central facilities (e.g., Kenichi et al., 2001; Kurnosov et al., 2008; Rivers et al., 2008). The use of solid pressure media greatly simplifies the loading procedure, and soft solids such as NaCl or KCl generally remain fairly

hydrostatic, particularly at high temperature (Anzellini & Boccato, 2020). The degree of sample pressure non-hydrostaticity can be investigated and quantified by several methods, including peak broadening of the R-line fluorescence of a ruby pressure calibrant (Piermarini et al., 1973; Chai & Michael Brown, 1996), or the effect of deviatoric stress on the different lattice planes of the sample, pressure media, or pressure calibrant (Singh & Kenichi, 2001; Takemura & Dewaele, 2008). Beyond using a soft pressure medium, non-hydrostatic stress can be reduced by annealing the sample at high temperature and minimising anisotropic deformation of the sample chamber (Anzellini & Boccato, 2020; Takemura, 2021).

As there is such a wide variety of options for the pressure medium, it is generally chosen to suit the specific experiment. Important considerations include possible chemical reactions with the sample, pressure calibrant or gasket, and mechanical limitations such as needing to prevent gasket deformation and maintain sample geometry. At high temperatures, a further consideration is the insulating properties of the pressure medium. High temperature techniques where heat is generated inside the sample chamber require adequate thermal insulation due to the extremely high thermal conductivity of the diamond anvils (Boehler, 2000; Anzellini & Boccato, 2020). While many noble gases are excellent insulators, their highly compressible nature results in significant thinning of the insulation layer at high pressure (Boehler, 2000; Takemura, 2021). Good sample confinement is also more important due to increased chemical reactivity at high temperature (Sinmyo & Hirose, 2010). For melting experiments (such as melting curve determinations or liquid structure measurements) additional care must be taken to ensure good sample confinement and prevent diffusion of the molten sample (Drewitt, 2021). The chosen pressure medium should therefore remain solid and be chemically unreactive with the sample at the target P-T conditions. Materials with high melting points and low thermal conductivities such as salt (KCl, NaCl, etc.) and ceramics (MgO, Al_2O_3, ZrO_2, etc.) are common options.

1.3.2 Pressure Measurement

1.3.2.1 XRD of Internal Calibrant

High pressure experiments obviously require a method of measuring the sample pressure. Unlike the MAP, there is no simple relation between the applied force and resulting pressure for a DAC experiment. As a result, calibrations based on the change in physical properties of an internal standard with P are used to measure pressure. The most accurate method is to use x-ray diffraction to measure the volume of a material with a well known equation of state. However, constructing a pressure scale by determining an equation of state in the way described in section 1.2.4 requires an already existing pressure scale. Such secondary scales will inherit uncertainty from the calibration

used, and so primary pressure scales are generally constructed instead by deriving an equation of state using another method. A common method is to use data from shock-wave experiments from which an EOS can be directly derived via the Hugoniot-Rankine equations (Takeuchi & Kanamori, 1966; McQueen et al., 1970; Morris, 1991). An alternative approach is to use simultaneous measurements of density (i.e., volume) and elasticity (e.g., from ultrasonics or Brillouin spectroscopy) under compression. The isentropic bulk modulus, K_S, can be directly calculated as an average from elasticity measurements (section 1.2.1), and an EOS constrained by fitting an equivalent (finite strain) equation of state in terms of $K(P)$ and V to obtain K_{T0} and K'_{T0} (e.g., Zha et al., 1998, 2000; Li et al., 2005; Murakami & Takata, 2019). However, external thermodynamic parameters (mainly the Grüneisen parameter) are required to both convert a reduced shock-wave EOS to a 300 K isotherm, and convert measured K_S to K_T (see equation 1.2). The resulting uncertainties can lead to inconsistencies between pressure scales constructed from one set of data for different materials (e.g., Fei et al., 2004; Dorogokupets & Oganov, 2007). Pressure scales are therefore typically constructed by combining multiple data sets and comparing static compression data for different materials (e.g., Dewaele et al., 2004; Dorogokupets & Dewaele, 2007; Fei et al., 2007; Dewaele, 2019).

To achieve the best accuracy, an ideal XRD pressure calibrant material will have low chemical reactivity (with the sample), high crystal symmetry, intense diffraction peaks, high compressibility, and low thermal expansion. Satisfying all these requirements is difficult, and so the calibrant is usually chosen based on the particular experiment. Typical pressure calibrants are platinum, gold, KCl, NaCl, MgO and neon. The use of an internal pressure calibrant also relies on the assumption that the calibrant and sample are experiencing the same conditions of pressure, temperature, and stress. In DAC experiments the pressure medium itself is commonly used as the calibrant, ensuring the two materials are in the same region of the pressure chamber while also reducing the amount of data that needs to be collected. However, as the pressure medium often doubles as thermal insulation in high-T DAC experiments, this can lead to large pressure uncertainties or systematic errors due to strong axial thermal gradients across the insulation thickness.

While this method of measuring pressure is generally the most accurate, it requires access to synchrotron facilities for x-ray diffraction, and so other pressure scales (such as using spectroscopic methods) are used for in-house experiments.

1.3.2.2 Ruby Pressure Scale

The most widely used gauge of pressure in DAC experiments is the scale based on the red-shift of the characteristic R-line fluorescence of ruby (α-Al_2O_3 corundum doped with Cr^{3+}) as a function of pressure (Forman et al., 1972; Piermarini et al., 1975; Mao et al., 1986; Shen et al., 2020). Cr^{3+} substitution on the Al^{3+}-site induces trigonal distortion from the octahedral oxygen coordination

environment and results in additional crystal field split states of the Cr^{3+} ion (Sugano & Tanabe, 1958; Powell, 1966). Absorption of light in the blue-green region leads to temporary electronic excitations of the Cr^{3+} ion (primarily ${}^4A_2 \rightarrow {}^4F_2$ in the U band ~550 nm and ${}^4A_2 \rightarrow {}^4F_1$ in the Y band ~400 nm). The energy state relaxes via fast, nonradiative decay to an intermediate metastable energy state, ${}^2E$, before radiative transfer to the ground state, ${}^4A_2$. The metastable ${}^2E$ state is itself split by trigonal distortions and spin-orbit interactions into two states, $\overline{E}({}^2E)$ and $2\overline{A}({}^2E)$, resulting in stimulated emission at ~694.3 nm (R_1-line) and ~692.9 nm (R_2-line) respectively (Sugano & Tanabe, 1958; Powell, 1966; Eggert et al., 1989b).

This fluorescence makes ruby a convenient pressure gauge as measurements of the R-line ruby shift can be easily made in-house with a simple spectroscopic setup. The position of both R-lines shift to longer wavelengths with pressure and have been used as reliable pressure indicators in DAC experiments (e.g., Forman et al., 1972; Eggert et al., 1989a; Gupta & Shen, 1991), but the R_1-line is typically used due its greater intensity (Powell, 1966; Mao et al., 1986; Shen et al., 2020). While the intensity of the R_1-line increases with Cr^{3+} concentration, rubies with low chromium concentrations (i.e., pink rubies) are preferred as pressure markers because the line width also increases (and so reduces precision; Chervin et al., 2001; Shen et al., 2020). Furthermore, Cr^{3+} concentrations above 0.6% lead to interactions between Cr^{3+} ions that result in additional fluorescence lines, the N-lines, that can confuse the spectra, particularly at high pressures where the N-lines are more intense than the R-lines (Powell, 1966; Chervin et al., 2001). Chervin et al. (2001) found a Cr^{3+} concentration of 0.3% provided the best compromise between line width and intensity. Temperature has a considerable effect on the wavelength and line-width of the R lines, and for room temperature experiments, the power of the excitation laser should be <10 mW to avoid the effects of local heating (Chervin et al., 2001; Shen et al., 2020). For most experiments, a spectrometer with a wavelength resolution of ~0.05 nm typically corresponds to a precision of ~0.05 GPa in the pressure measurement (Shen et al., 2020), although this will also be limited by the ambient pressure width of the R_1-line (~0.6 nm; Cook & Michaels, 2017). The accuracy of the R-line technique is generally much worse, mainly arising from uncertainties in the calibration of the ruby scale, including those inherited from the pressure standard chosen as a calibrant (Shen et al., 2020).

Below ~20 GPa, the shift of the R_1-line can be closely approximated by a linear relationship with pressure (e.g., Piermarini et al., 1975), but the relationship becomes strongly non-linear at higher pressures (e.g., Mao et al., 1986). A wide range of calibrations and revisions exist in the literature, often with discrepancies between calibrations of ~3–5% up to pressures of 100 GPa due to the variety of assumptions and approximations made (Shen et al., 2020). Calibrations have been made against a variety of primary pressure scales for metallic, ionic, and covalent materials that have been derived using different techniques and data-types, including isotherms calculated from reduced shock-wave data (e.g., Mao et al., 1978, 1986; Dewaele et al., 2004; Holzapfel, 2003; Silvera

et al., 2007), theoretical and *ab initio* studies (e.g., Holzapfel, 2003; Kunc et al., 2003, 2004), and phonon or direct elasticity measurements (e.g., Aleksandrov et al., 1987; Zha et al., 2000; Holzapfel, 2003). Multiple metastudies that consider a range of approaches and/or use recalibrations of existing datasets have also been made (e.g., Dorogokupets & Oganov, 2003, 2006; Dorogokupets & Dewaele, 2007; Chijioke et al., 2005; Silvera et al., 2007; Lei et al., 2013; Shen et al., 2020), and calibration measurements have been made using a range of pressure media (approximating quasi-hydrostatic to strongly non-hydrostatic conditions) to investigate the effect of hydrostaticity (e.g. Mao et al., 1986; Lei et al., 2013; Shen et al., 2020).

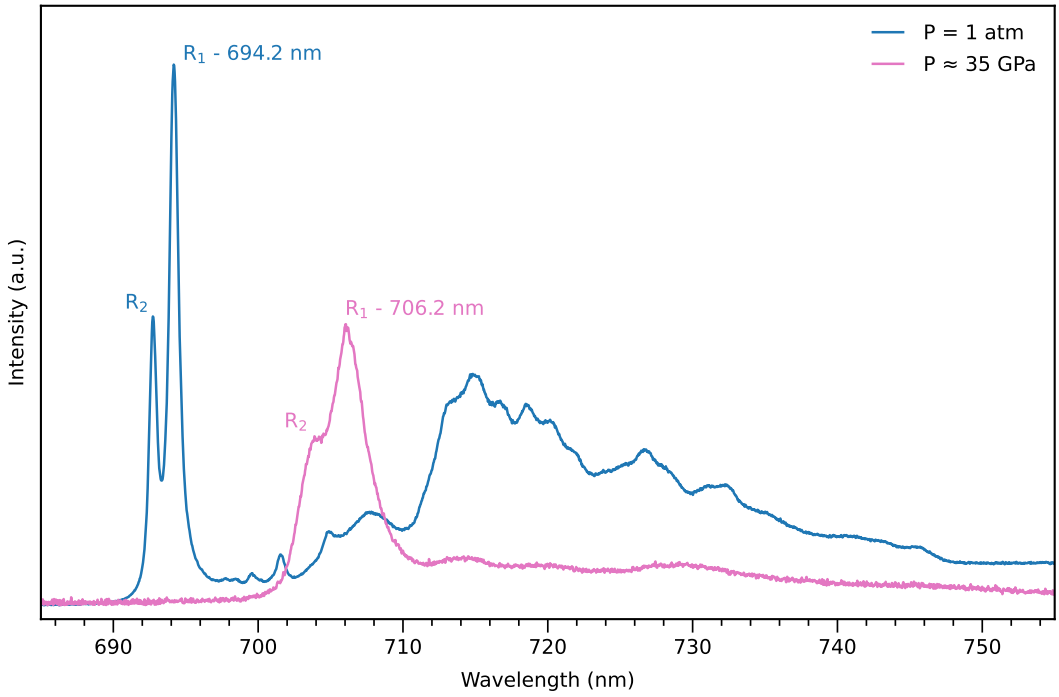

Figure 1.6: *Example fluorescence spectra of ruby at ambient conditions (blue line) and at ~35 GPa in the DAC. The pressure is calculated from the shift of the R_1 peak. At high pressure in the DAC the intensity is reduced and uniaxial stress results in peak broadening which makes the R_2 peak harder to resolve and reduces precision in the location of the R_1 peak.*

Data has also been fit to a variety of functional forms. The most commonly used equation is (e.g., Mao et al., 1978, 1986; Zha et al., 2000; Dewaele et al., 2004; Dorogokupets & Oganov, 2003, 2006):

$$P = \frac{A}{B}\left\{\left[1+\left(\frac{\lambda-\lambda_0}{\lambda_0}\right)\right]^B - 1\right\} = \frac{A}{B}\left[\left(\frac{\lambda}{\lambda_0}\right)^B - 1\right], \tag{1.48}$$

where A and B are the fitting parameters, λ is the wavelength of the R_1-line at elevated pressure, and λ_0 is the wavelength of the R_1-line at ambient pressure.

Alternatively, a quadratic form is sometimes used (Aleksandrov et al., 1987; Syassen, 2008; Shen et al., 2020), which can be expressed in two ways:

$$P = A\left(\frac{\lambda-\lambda_0}{\lambda_0}\right)\left[1+B\left(\frac{\lambda-\lambda_0}{\lambda_0}\right)\right] = A\left[\left(\frac{\lambda-\lambda_0}{\lambda_0}\right)+B\left(\frac{\lambda-\lambda_0}{\lambda_0}\right)^2\right]. \tag{1.49}$$

Some authors (Chijioke et al., 2005; Silvera et al., 2007) prefer the form:

$$P = A\left(\frac{\lambda-\lambda_0}{\lambda}\right)\left[1+B\left(\frac{\lambda-\lambda_0}{\lambda}\right)\right] = a\left[\left(\frac{\lambda-\lambda_0}{\lambda}\right)+b\left(\frac{\lambda-\lambda_0}{\lambda}\right)^2\right]. \tag{1.50}$$

Note the different denominators in equations 1.49 and 1.50, and that the parameters A and B are not equivalent between the different forms. Equation 1.50 is constructed by normalising to the ambient pressure frequency (ν) of the R_1-line, rather than wavelength, and can be equivalently expressed as (Kunc et al., 2003, 2004):

$$P = A\left(\frac{|\nu-\nu_0|}{\nu_0}\right)\left[1+B\left(\frac{|\nu-\nu_0|}{\nu_0}\right)\right]. \tag{1.51}$$

In addition, Holzapfel (2003) proposed a three term form (with an additional parameter, C), to resolve discrepancies in calibration datasets:

$$P = \frac{A}{B+C}\left(\exp\left\{\frac{B+C}{C}\left[1-\left(\frac{\lambda}{\lambda_0}\right)^{-C}\right]\right\}-1\right). \tag{1.52}$$

Recently, a proposal for a standardised ruby calibration (an international practical pressure scale, IPPS-Ruby2020; Shen et al., 2020) was made based on traceable data for a variety of materials constrained by multiple approaches to pressure-scale construction, and quasi-hydrostatic ruby measurements. The fit of the recalibrated data by Shen et al. (2020) to equation 1.49 yielded parameters $A = 1870 \pm 10$ and $B = 5.63 \pm 0.03$, with a maximum uncertainty in pressure of ±2.5% (in the range 0 to 150 GPa) based on a full assessment of inherited uncertainties and assumptions in the data.

1.3.2.3 Raman Pressure Scale

Although Ruby is the most widely used optical pressure gauge, other optical scales have been proposed, including the pressure dependence on the fluorescence lines of SrB_4O_7:Sm^{2+} (Lacam & Chateau, 1989; Datchi et al., 1997; Jing et al., 2013; Romanenko et al., 2018) and Sm^{3+}:YAG (Hess & Exarhos, 1989; Hess & Schiferl, 1992; Liu & Vohra, 1993; Trots et al., 2013), and on the Raman spectra of cubic boron nitride (cBN; Kawamoto et al., 2004; Datchi & Canny, 2004; Ono et al., 2015) and diamond (e.g., Hanfland et al., 1985, 1986; Eremets, 2003; Sun et al., 2005; Baer et al., 2008; Akahama & Kawamura, 2004, 2006, 2007, 2010; Dubrovinskaia et al., 2010; Ono et al., 2014). Of these scales the Raman spectra of diamond is the most convenient for DAC experiments, as the signal from the anvils themselves can be used as a reliable pressure indicator, removing the need for a calibrant inside the pressure chamber (e.g., Eremets, 2003; Akahama & Kawamura, 2004; Baer et al., 2008). The first order Raman mode of diamond can be seen as a single sharp peak in the spectra, with an ambient pressure value of $\sim$1333 cm^{-1}. The mode is triply degenerate (in the absence of stress), corresponding to vibrations of the two Bravais lattices of carbon atoms with respect to each other (Krishnan, 1945; Hanfland et al., 1985; Occelli et al., 2003). The diamond peak shifts to higher frequency as a near-linear function of pressure with a slope $\sim$0.5 GPa/cm^{-1} (e.g., Hanfland et al., 1985, 1986; Walter et al., 2015), allowing pressure measurements with a precision of <0.5 GPa (given typical precision in peak location of <1 cm^{-1}), and unlike ruby fluorescence, the Raman signal from the diamond typically remains strong and resolvable even into the multi-megabar range (e.g. Eremets, 2003; Sun et al., 2005; Baer et al., 2008; Akahama & Kawamura, 2010). However, the Raman signal from the anvils in high-pressure experiments is generally observed as a broad band, which results from stress inhomogeneity in the scattering volume and background scattering along the laser path in the [100] direction (i.e., along the compression axis in (100) cut anvils) from the table face (back) of the anvil at near ambient pressures, to the culet surface at the sample-anvil interface (Hanfland et al., 1986; Popov, 2004; Baer et al., 2008; Ono et al., 2014). At high pressure, sharp edges to the Raman band are commonly observed on the low- and high-frequency sides, and should correspond to the spectra of the table face and the culet face respectively (e.g., Hanfland et al., 1986; Baer et al., 2008; Akahama & Kawamura, 2010). Uniaxial loading of the anvil in the [100] direction (and associated non-hydrostaticity) also lifts the mode degeneracy of the diamond peak and results in splitting into a high frequency singlet and lower frequency doublet mode (Hanfland et al., 1985, 1986; Popov, 2004; Akahama & Kawamura, 2004, 2005, 2006), although this is not always observed (Baer et al., 2008; Ono et al., 2014). Mode splitting can be used to evaluate stresses in the sample (Popov, 2004).

The peak of the singlet mode has been used to construct a pressure scale, relying on highly confocal measurements to filter scattering from the anvil body and resolve the spectra at the culet surface (Walter et al., 2015). However, the singlet peak is not always resolvable or may be obscured by fluorescence (particularly at pressures $\gtrsim$30 GPa; Baer et al., 2008; Ono et al., 2014; Edwards, 2020),

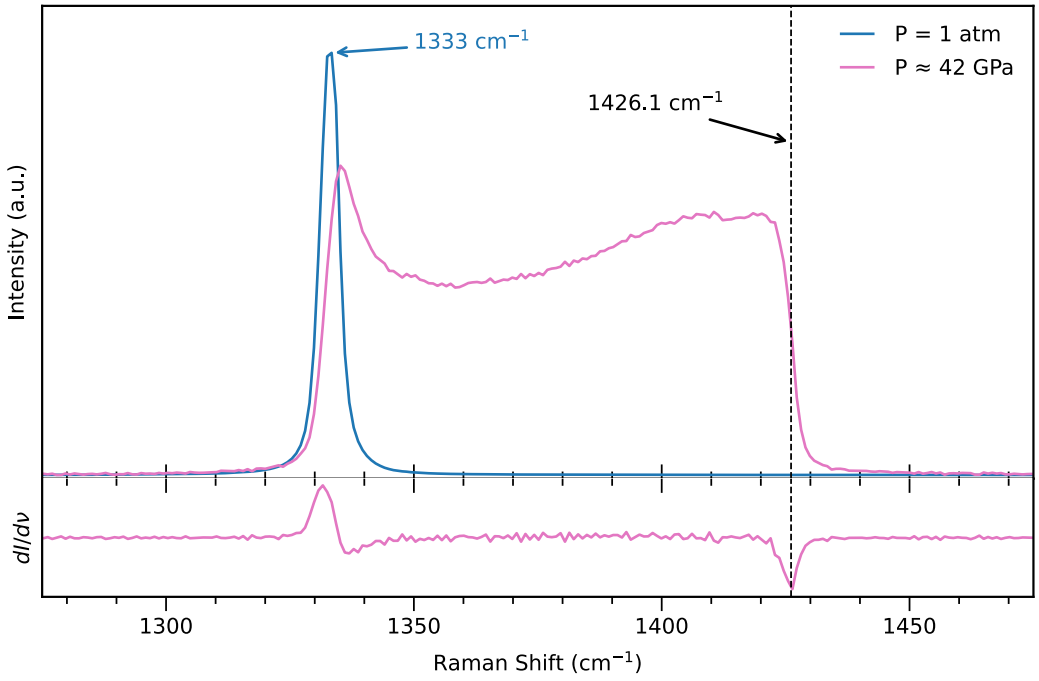

Figure 1.7: *Example Raman spectra of diamond at ambient conditions (blue line) and from the culet tip of a diamond anvil with the cell compressed to ∼42 GPa (pink line). In cases such as this, where the singlet mode is not well resolved at high pressure, the high-frequency edge can be determined from the minimum in the differential spectrum, $dI/d\nu$ (dashed black line). The intensity of the ambient spectra has been scaled down to fit on the same plot. The low frequency edge of the high pressure spectrum does not match the ambient peak position due to the confocal nature of the measurements (and possibly stress on the table face).*

and this method is sensitive to focus and potentially more sensitive to deviatoric stresses, and as a result, to the anvil geometry and sample environment (Popov, 2004; Baer et al., 2008; Walter et al., 2015; Liu et al., 2021a). As a result, the high-frequency edge of the whole Raman spectrum is generally used to construct a pressure scale (e.g., Akahama & Kawamura, 2004; Ono et al., 2014), although using the singlet peak is typically the most robust method at lower pressures (Walter et al., 2015; Edwards, 2020). The high-frequency edge is typically defined as the minimum of the differential spectrum ($dI/d\nu$) across the sharp edge (e.g. Akahama & Kawamura, 2004, 2010; Ono et al., 2014). The shift in the high-frequency edge of the diamond Raman spectra in the centre zone of the culet has been calibrated against the secondary ruby gauge (Hanfland et al., 1986; Popov, 2004; Akahama & Kawamura, 2004; Walter et al., 2015), the raman shift of hydrogen (Baer et al., 2008), and primary pressure scales constructed from reduced shock-wave data of metals (Sun et al., 2005; Akahama & Kawamura, 2004, 2005, 2006, 2007, 2010; Ono et al., 2014) up to 400 GPa (Akahama & Kawamura, 2010). Calibrations have also been performed for anvils with different crystallographic orientations (Akahama & Kawamura, 2005, 2007). The existing calibrations agree well at pressures below ∼50 GPa (e.g., see the review in Ono et al., 2014), but significant discrepancies exist from ∼60 GPa (Popov, 2004; Akahama & Kawamura, 2004; Sun et al., 2005; Ono et al., 2014; Walter

et al., 2015). This has been attributed to differential stress influenced by anvil orientation, culet geometry, and sample environment (Baer et al., 2008; Ono et al., 2014; Walter et al., 2015), although this can be minimised by annealing at high temperature (Ono et al., 2014). Nevertheless, the Raman spectra of the diamond anvils remains a convenient lab-based method to determine pressure, and simplifies experimental procedure by removing the need for a calibrant material inside the pressure chamber.

1.3.3 Temperature Generation

Studies replicating lower mantle conditions typically employ laser heating to reach the required temperatures in the DAC, and advances since the early 1970s have resulted in an accessible temperature range of over 5000 K (Ming & Bassett, 1974; Bassett, 2001; Anzellini & Boccato, 2020). Near-IR lasers ($\lambda \sim 1\,\mu m$) with powers of 50 to 200 W are typically used. For iron-free samples, which do not absorb the IR radiation, a metallic absorber must be mixed with the sample. Nevertheless, the IR radiation is generally only weakly absorbed, and so tight focusing of the laser beams is required. This can result in large radial and axial temperature gradients due to the small spot size and minimal penetration depth of the laser (Anzellini & Boccato, 2020). CO_2 lasers operating at longer wavelengths ($\sim$10 μm) that are directly absorbed by iron free compositions can be used instead, and are typically applied when optical transparency is necessitated by the experiment. CO_2 lasers also have a much greater penetration depth into the sample, significantly reducing axial temperature gradients. However, CO_2 lasers are more expensive, require specialist optics, are less stable, and are harder to align (Kurnosov et al., 2019; Anzellini & Boccato, 2020). Heterogeneous temperature during laser heating results in large uncertainties, and can lead to overestimates of temperature (Walter & Koga, 2004) and cause diffusion of elements along thermal gradients (Soret diffusion; Sinmyo & Hirose, 2010). Axial temperature gradients can be reduced by simultaneous laser heating on both sides of the sample and by surrounding the sample with equal thicknesses of thermal insulation. Radial gradients can be reduced by improvements in the optical components of the system, such as the use of beam shaping (e.g., π-shapers) to flatten the raw gaussian intensity profile of the laser beam (Prakapenka et al., 2008; Lord et al., 2014a). The temperature relies not only on the spot size and intensity profile of the heating laser but, critically, the geometry and absorbance characteristics of the sample itself which can vary significantly both spatially and with time. These combined spatial and temporal fluctuations in temperature over the duration of an experiment lead to uncertainties that are typically 100 K or more (Walter et al., 2015). Heating instability poses a particular problem for techniques requiring long data acquisition times. Techniques such as Brillouin spectroscopy, IXS, and Mössbauer spectroscopy require collection times of several hours or more (Fukui et al., 2008; Kurnosov et al., 2017; McCammon, 2021), and heating periods of less than an hour may be insufficient for the sample to reach thermodynamic equilibrium (Dorfman, 2016), but heating over

these timescales is difficult (often prohibitively) to achieve with laser heating. In addition, the small spot size of the laser relative to the sample can result in analysis of unheated regions (if particular care is not given to alignment), and generally prohibits melting of the entire sample.

Resistive heating techniques provide significantly improved temperature stability, more precise control, reduced thermal gradients, and uncertainties that are an order of magnitude smaller compared to laser heating (Dubrovinskaia & Dubrovinsky, 2003). In addition, resistive heating enables melting of the entire sample, which is particularly important for liquid structure measurements (Louvel et al., 2020; Drewitt et al., 2020).

External resistive heating, in which a heater surrounds the anvil assembly or entire DAC, is a commonly used technique. A wide range of designs exist, including commercially available options (e.g., Dubrovinskaia & Dubrovinsky, 2003; Jenei et al., 2013; Louvel et al., 2020). However, external heating techniques are typically limited to < ∼1300 K, beyond which the unpressurised parts of the diamond anvils begin to graphitise, and the other components of the cell deform. The temperature limit can be extended through the use of small metal or graphite micro-heaters which limit heading to near the anvil tips, innovative cooling systems, and vacuum chambers that minimise oxidation (Immoor et al., 2020; Méndez et al., 2020). Nevertheless, heating above ∼1500 K presents significant experimental difficulty, and routine experiments replicating lower mantle conditions are not feasible using external resistive heating techniques.

Internal resistive heating, in which heat is generated only within the pressure chamber and isolated from the diamonds, can extend the accessible temperature range drastically. Internal resistive heating techniques are commonly used in the study of metals at high pressure and temperature, by electrically heating a fine wire, compressed between the anvils, which serves as both heating element and sample. This method, termed 'fine-wire heating', was first pioneered by Liu & Bassett (1975) and is now well established for studies of the melting and resistivity of metals (e.g., Boehler, 1986; Boehler et al., 1986; Dubrovinsky et al., 2007; Komabayashi et al., 2009; Sinmyo et al., 2019; Suehiro et al., 2019). However, the study of Earth materials requires heating of non-metallic, insulating materials. Some limited application of internal resistive heating to non-metallic samples has been previously reported (Zha & Bassett, 2003; Zha et al., 2008). However, existing designs rely on complex experimental geometry and composite gaskets that present significant technological difficulties. As a result, the technique has not been adopted for further studies. Furthermore, the temperature range is limited to <1900 K above 10 GPa, insufficient for reproducing deep lower mantle conditions (Zha & Bassett, 2003; Zha et al., 2008). As such, there is a clear need for the development of resistive heating techniques that can be used to study lower mantle phases *in situ* at the relevant *P*-*T* conditions.

1.3.4 Temperature Measurement

Several techniques are available to measure temperature in diamond anvil cell experiments. Thermocouples are commonly employed for external resistive heating experiments. Thermocouple measurements are based on the Seebeck effect, where a temperature dependent voltage is produced at an electrical junction formed by two wires with differing resistivities. Standardised alloy combinations (thermocouple types) are generally used, with the particular type chosen to suit the temperature range of the experiment, and desired precision. These are commercially available and inexpensive, making thermocouples a convenient choice for temperature measurement. In the temperature range of external resistive heating (up to $\sim$1500 K), the accuracy of thermocouple measurements is typically $\sim$2 K, which, combined with the stability of external resistive heaters, allows fine control of temperature during experiments. However, the placement of a thermocouple is naturally important, and assumptions about the temperature gradients between the sample and thermocouple location can lead to systematic errors. Thermocouples are typically placed adjacent to the WC seats, or close to the tip of the anvils. Designs where the heater surrounds the entire cell or anvil assembly typically create very uniform heating over a large area that includes the thermocouples, allowing accurate temperature measurement, but gradients between the thermocouple and sample are more significant in designs pushing the temperature limits of external heating, as the heated region is generally limited to the gasket and anvil tips.

Direct physical access to the heated volume in laser- or internal resistive-heated experiments is not possible, and so thermocouples cannot be used. However, since the spectral intensity (energy density) of the thermal emission from the heated sample is explicitly related to temperature via Planck's law (Planck, 1914), sample temperature can be measured by spectroradiometry instead. This is done by collecting the radiation emitted from the heated volume, measuring the wavelength distribution with a spectrograph, and fitting the calibrated spectral radiant exitance to a blackbody function (Heinz & Jeanloz, 1987; Walter & Koga, 2004). For accurate measurement of high temperatures, spectroradiometric set-ups usually employ a detector in the visible range, but this limits the lowest measurable temperatures to $\sim$1200 K. Detectors sensitive to near-IR radiation (e.g., InGaAs detectors) can be used to measure temperature down to $\sim$500 K, but are not accurate at very high temperatures (Shen et al., 2010).

Planck's law is formulated for a perfect blackbody, with emissivity $\epsilon = 1$, but in DAC experiments emissivities are typically < 0.1 (Heinz & Jeanloz, 1987). The spectral radiant exitance of a real material (M) is the product of its spectral hemispherical emissivity (ϵ_λ) and the spectral radiant exitance of a blackbody emitter with the same temperature (M_{BB}), i.e.:

$$\epsilon_\lambda = \frac{M(\lambda, T)}{M_{BB}(\lambda, T)}. \tag{1.53}$$

Taking the greybody approximation that emissivity is independent of wavelength, Planck's law for spectral radiant exitance can then be written:

$$M(\lambda, \epsilon, T) = \epsilon M_{BB}(\lambda, T) = \epsilon \frac{c_1}{\lambda^5} \frac{1}{\exp\left(c_2/\lambda T\right) - 1}, \tag{1.54}$$

where T is temperature, λ is the wavelength of the measured signal, ϵ is the emissivity, and M is the radiant exitance. c_1 and c_2 are the radiation constants: $c_1 = 2\pi hc^2$ and $c_2 = hc/k_\mathrm{B}$, where h is Planck's constant, k_B is Boltzmann's constant, and c is the speed of light. Further discussion of equations 1.53 and 1.54 can be found in (for example) Boyd (1983) and McCluney (2014).

The measured spectral response of the detector to the sample radiance, $I_\mathrm{measured}(\lambda, \epsilon, T)$, is distorted relative to the actual spectral radiant exitance of the sample, $M(\lambda, \epsilon, T)$, by interference in the optical pathway and wavelength dependent detector efficiency (Walter & Koga, 2004). These distortions can be considered the optical response of the specific system, $S(\lambda)$, i.e.:

$$I_\mathrm{measured}(\lambda, \epsilon, T) = S(\lambda) M(\lambda, \epsilon, T). \tag{1.55}$$

The distortion effects of the specific optical pathway must be taken into account to obtain $M(\lambda, \epsilon, T)$ (and hence accurate temperatures) using spectroradiometry. This is typically done by calibrating the system using a standard of known, calibrated spectral radiance ($M_\mathrm{standard}(\lambda, T_0)$) at a specific temperature (T_0), such as a NIST calibrated tungsten ribbon-filament lamp (e.g., Walter & Koga, 2004; Lord et al., 2014a). A spectra collected through the optical pathway with the lamp placed at the sample position, $I_\mathrm{standard}(\lambda, T_0)$, can then be used to obtain the unknown sample $M(\lambda, \epsilon, T)$ in an experiment:

$$M(\lambda, \epsilon, T) = \frac{I_{\text{measured}}(\lambda, \epsilon, T)}{I_{\text{standard}}(\lambda, T_0)} \times M_{\text{standard}}(\lambda, T_0). \tag{1.56}$$

The two unknown quantities, temperature (T) and emissivity (ϵ), can then be obtained by fitting equation 1.54 to the (calibration corrected) $M(\lambda, \epsilon, T)$. In practice, however, it is more common to use Wien's distribution law rather than the full form of Planck's law. Wien's approximation for spectral radiant exitance is given by:

$$M(\lambda, \epsilon, T) = \epsilon \frac{c_1}{\lambda^5} \exp\left(-\frac{c_2}{\lambda T}\right). \tag{1.57}$$

Wien's approximation holds true in the short wavelength or low temperature limit, and is accurate to within 1% when $\lambda T \lesssim 3100\,\mu\text{m K}$ (Stewart & Johnson, 2016). For typical DAC experiments Wien's approximation is almost exact to 3000 K, beyond which it gives progressively lower values, with ~1% difference at 5000 K (Walter & Koga, 2004). Wien's approximation is convenient as it can be easily linearised, allowing simpler extraction of temperature and assessment of the fit reliability:

$$J = \ln(\epsilon) - \frac{\omega}{T}, \tag{1.58}$$

where the normalised intensity, $J = \ln\left(\lambda^5 c_1^{-1} M_{\lambda,\epsilon,T}\right)$ and the normalised wavelength, $\omega = c_2 \lambda^{-1}$ (Heinz & Jeanloz, 1987). A calibrated spectrum can be easily transformed to coordinates of J and ω, and a simple linear fit used to extract the temperature (inverse gradient) and emissivity (y-intercept). The analytical precision on temperature extracted from a fit to either Planck's law or the Wien approximation is typically a few K (Heinz & Jeanloz, 1987; Walter & Koga, 2004). However, several other sources of uncertainty can lead to combined systematic or random errors of up to several hundred Kelvin. Spectral sampling of thermal gradients, along with chromatic aberrations caused by refractive optics in the system, can lead to large systematic errors, although this can be mitigated by careful choice of optical components (Walter & Koga, 2004). An additional source of uncertainty, and one that is poorly constrained, is the validity of the greybody approximation. Spectroradiometric measurements of the well-known melting points of metals at ambient conditions suggest the approximation holds true for some materials, but may deviate significantly for others and lead to systematic overestimations in temperature of 50 to 200 K (Lord et al., 2009). Measurements of absorption at ambient conditions and modelling of optical characteristics at elevated P and T suggest that lower mantle phases may deviate significantly from greybody behaviour and that spectroradiometry may under- or over-estimate temperatures by several hundred Kelvin (e.g., Deng et al.,

2017; Lobanov & Speziale, 2019; Lobanov et al., 2021b,a; Andrault et al., 2022). This may be particularly true for Fe-bearing samples which all have absorption bands in the visible range (Lobanov & Speziale, 2019; Lobanov et al., 2021b), or polycrystalline samples where grain boundary scattering may impact emissivity (Lobanov et al., 2021a). Nevertheless, the optical properties of most materials at high-P-T conditions are poorly constrained, making the greybody approximation necessary in most cases.

In addition to these considerations, spatial thermal gradients can lead to underestimations of temperature if spectral data is not collected from the hotspot. Traditionally, thermal emission is selected from a region of interest on the sample using a pinhole (e.g. Bassett & Weathers, 1987; Anzellini et al., 2018). However, when the system geometry allows it, a slit spectrometer can be used instead, with the light dispersed onto a 2D detector, with one dimension corresponding to wavelength and the other a spatial dimension where each row of pixels corresponds to a point along a cross-section of the sample surface (e.g. Shen et al., 2001; Lord et al., 2014a). Extraction of a 1D temperature profile in this manner helps to quantify radial thermal gradients in the sample, however hot spots outside the section line will not be mapped. In most real experiments the heated region is not radially symmetric, and so a 1D profile can lead to inaccurate temperature estimates (Campbell, 2008; Lord et al., 2014a).

Because the Wien approximation can be reduced to a linear form (equation 1.58), data at only two wavelengths are required to extract temperature. The two wavelengths must be close enough that the wavelength dependence of ϵ is negligible, but far enough for a measurable difference in intensity to exist. Such two-colour radiometry is prone to errors due to a lack of redundancy, but accurate temperature measurements can be made with data collected at only four or more spectral bands (Campbell, 2008). This provides the possibility to select wavelengths (or narrow spectral bands) from the thermal emission using optical components (i.e., monochromatic filters) rather than with a spectrometer. A separate 2D image can be obtained at each wavelength, and after spatial correlation, full 2D maps of temperature and emissivity generated, with only a slight reduction in radiometric precision. Furthermore, the ability to independently focus each image reduces chromatic aberration, which is a potentially significant source of uncertainty in spectroradiometric temperature measurements (Walter & Koga, 2004; Lord & Wang, 2018). Multispectral (generally four-colour) imaging radiometry (MIR) can therefore reduce errors in estimates of peak sample temperature and fully quantify radial thermal gradients across the heated region (e.g. Campbell, 2008; Du et al., 2013; Lord et al., 2014b; Lord & Wang, 2018; Heinen et al., 2021). In contrast to other methods of estimating 2D temperature gradients such as scanning the spectrometer pinhole across the sample or the peak-scaling method (Kavner & Nugent, 2008; Rainey & Kavner, 2014), MIR allows simultaneous collection of spectral data across the whole hotspot and does not require theoretical data corrections to be applied.

While thermocouples and spectroradiometric methods are the most commonly used techniques to measure temperature, other procedures can be used. One example is the ratio of Stokes to anti-Stokes inelastic scattering intensity ($I_{\mathrm{Stokes}}/I_{\mathrm{anti-Stokes}}$), which can be measured using Raman spectroscopy (Long, 1977; Lin et al., 2004b). The method is based on the principle of detailed balance, where the intensity asymmetry is controlled by the Boltzmann factor, using the relation:

$$\frac{I_{\mathrm{Stokes}}}{I_{\mathrm{anti-Stokes}}} = \frac{(\nu_0 - \nu_i)^4}{(\nu_0 + \nu_i)^4} f(\nu) \exp\left(\frac{hc\nu_i}{k_{\mathrm{B}}T}\right), \tag{1.59}$$

where T is temperature, ν_0 is the Rayleigh line wavenumber, ν_i is the wavenumber of the ith Raman mode, h is Planck's constant, k_{B} is Boltzmann's constant, c is the speed of light, and $f(\nu)$ is the spectral response of the system which can be calibrated in a similar way to spectroradiometric systems using a standard tungsten ribbon-filament lamp. Only the sample contributes to the Raman modes used and the intensity ratio is dependent only on temperature, and so this method does not require assumptions or approximations about other values (such as emissivity) or thermal gradients within the insulation. An additional benefit is that (particularly in transmission) temperature derived in this way is a representative average of the sample volume and not just a surface measurement (Lin et al., 2004b). However, difficulty in spectral discrimination of the Raman signal from the intense thermal emission (see section 1.2.6) has limited the application of this method, particularly at high temperature. Furthermore, the sensitivity of this technique is significantly reduced at high temperature ($>\sim$1800 K), particularly for low-frequency modes (Lin et al., 2004b). Nevertheless, Stokes–anti-Stokes intensity asymmetry can be a useful method for direct temperature measurement at low temperatures (i.e., below the thermal limit of spectroradiometry).

1.4 Thesis Overview

For many important Earth materials there is a lack of mineral physics data at the high temperatures that are applicable to the lower mantle, or the uncertainties on such high-T data are significant. While laser-heating techniques can generate temperatures of many thousand Kelvin, the large thermal gradients and poor temperature stability limits the accuracy of measured data and often prohibits analyses requiring long acquisition times. Resistive heating offers clear advantages in these regards. However, external heating techniques are limited to <1500 K and internal resistive heating techniques applicable to non-metallic samples are currently limited to <1900 K at lower mantle pressures as the filaments used in 'fine-wire' designs that can surpass these conditions are too small to contain a distinct sample chamber. There is therefore a clear need to develop new heating methods that can provide an alternative to laser heating for experiments at lower mantle conditions.

Minimising uncertainty in the determination of thermal EOS parameters requires the collection of dense P-V-T datasets across a large P-T range with minimal temperature uncertainties at all conditions. Similarly, delineation of phase relations requires precise and stable temperature control along with reduced thermal gradients to more accurately constrain phase boundaries. Measurements of liquid structure and density principally require low thermal gradients to allow melting of the entire sample, but will also benefit from stable heating over the longer acquisition times required for low-Z materials. Mössbauer spectroscopy, and sound velocity measurements via Brillouin and IXS would similarly benefit from reduced thermal gradients and temperature uncertainties, although the primary concern is the ability to stably heat over the duration of the long acquisition times. Based on these considerations we can define several ideal characteristics of a resistive heating system:

1) Large temperature range encompassing lower mantle conditions (1500 to 3000 K)
2) Stable heating over timescales of several hours
3) Precise control over temperature
4) Low spatial thermal gradients
5) Allow whole melting of the sample
6) Sample independent (i.e., applicable to metallic/non-metallic, opaque/transparent samples)

One of the main benefits of laser-heating is that it is relatively easy to perform an experiment, and laser-heating set-ups already exist at many facilities including synchrotron beamlines. Therefore, in addition to the above characteristics of an ideal design, it should not be prohibitively difficult to assemble or conduct an experiment, or require extensive modifications to existing analytical equipment in order to interface the design, i.e.:

8) Simple to use
9) Relatively easy to manufacture/assemble
10) Simple to interface with existing analytical equipment (e.g., at a beamline)

The primary aims of this project were to 1) develop an internal resistive heating technique to study both crystalline phases and melts at lower mantle conditions in the DAC, and 2) further develop analytical techniques for characterising these materials at extreme conditions.

Chapter 2 details the experimental design developed over the course of the project, and reports on the stable heating of non-metallic materials up to *P*-*T* conditions of 3000 K and 64 GPa.

Chapter 3 describes the development of new analytical tools for liquid structure characterisation and density measurement at extreme conditions, synthesising analytical methods from the literature in the form of open source computer software.

Chapter 4 describes preliminary experiments in the application of the developed IRH experimental framework to metallic materials. It explores the use of the IRH design for lab-based determinations of metal melting temperatures, with titianium as a case study, and to stabilise metallic melts of sufficient volumes for liquid diffuse scattering measurements.

Chapter 5 summarises the impact of the research presented here, and contains a description of current and ongoing work, as well as a discussion of future research directions and possible applications of the techniques developed here.

Chapter 2

Internal Resistive Heating of Non-Metallic Samples to 3000 K and >60 GPa in the Diamond Anvil Cell

Author contributions and declaration: Part of this chapter has been published in Review of Scientific Instruments: **Heinen, B. J.**, Drewitt, J. W. E., Walter, M. J., Clapham, C., Qin, F., Kleppe, A. K., and Lord, O. T. (2021). Internal resistive heating of non-metallic samples to 3000 K and >60 GPa in the diamond anvil cell. *Review of Scientific Instruments*, **92**(6):063904. Benedict Heinen developed the IRH design under the supervision of Oliver Lord. Some early prototyping of the IRH concept was performed by James Drewitt. Benedict Heinen designed and manufactured the laser-processed IRH components. Benedict Heinen and Charles Clapham designed the PEEK gasket holders, which were then manufactured by Charles Clapham in the Bristol Earth Sciences workshop. Additional technical assistance during the prototyping phase was provided by Gerald Mwale. Annette Kleppe provided assistance to Benedict Heinen, Oliver Lord, James Drewitt, and Fei Qin in collecting synchrotron x-ray data at beamline I15 of Diamond Light Source, UK (proposal number CY21972). Additional x-ray data (used to generate Fig. 2.21) was collected at I15 under proposal number CY28995 with the assistance of Simone Anzellini. Data processing was performed by Benedict Heinen, who also wrote the initial draft of the manuscript. The manuscript was improved by feedback from Oliver Lord, James Drewitt, and Mike Walter. Further improvements were made during the publication process as a result of careful reviews from two anonymous reviewers.

Abstract

High pressure-temperature experiments provide information on the phase diagrams and physical characteristics of matter at extreme conditions and offer a synthesis pathway for novel materials with useful properties. Experiments recreating the conditions of planetary interiors provide important constraints on the physical properties of constituent phases and are key to developing models of planetary processes and interpreting geophysical observations. The laser-heated diamond anvil cell (DAC) is currently the only technique capable of routinely accessing the Earth's lower-mantle geotherm for experiments on non-metallic samples, but large temperature uncertainties and poor temperature stability limits the accuracy of measured data and prohibits analyses requiring long acquisition times. We have developed a novel internal resistive heating (IRH) technique for the DAC and demonstrate stable heating of non-metallic samples up to 3000 K and 64 GPa, as confirmed by *in situ* synchrotron x-ray diffraction and simultaneous spectroradiometric temperature measurement. Temperature generated in our IRH-DAC can be precisely controlled and is extremely stable, with less than 20 K variation over several hours without any user intervention, resulting in temperature uncertainties an order of magnitude smaller than those in typical laser-heating experiments. Our IRH-DAC design, with its simple geometry, provides a new and highly accessible tool for investigating materials at extreme conditions. It is well suited for the rapid collection of high-resolution *P-V-T* data, precise demarcation of phase boundaries, and for experiments requiring long acquisition times at high temperature. Our IRH technique is ideally placed to exploit the move toward coherent nano-focused x-ray beams at next-generation synchrotron sources.

2.1 Introduction

High pressure research is a rapidly advancing field. High pressure causes materials to undergo structural and electronic changes, affects the chemical reactivity of elements and gives rise to a wide variety of exotic physical phenomena such as liquid–liquid (polyamorphic) transitions (Henry et al., 2020; Tanaka, 2020; Walton et al., 2020), metallisation (Akahama et al., 1995; Dias & Silvera, 2017), and superionic (Millot et al., 2018) and superconducting (Snider et al., 2020) behaviour. The phase diagrams of materials are important to fundamental condensed matter physics, and even the high-pressure behaviour of elements and simple systems is an area of frontier research (Laniel et al., 2020; Drewitt et al., 2020). The application of pressure can stabilise exotic materials with unprecedented stoichiometries, chemical activity, bonding or physical properties. Therefore pressure (P) provides a powerful tuning parameter or synthesis pathway for a vast array of materials with desirable properties. These include superhard materials with a wealth of industrial uses (Huang et al., 2014; Solozhenko et al., 2019; Bykov et al., 2019), novel superionic phases and high entropy oxides with important applications in next-generation battery technology (Wang et al., 2018; Huang et al., 2019; Cheng et al., 2020), high-energy-density materials for propellants (Tomasino et al., 2014; Wang et al., 2015a), novel polymorphs of pharmaceutical molecules (Guerain, 2020), electrides (Dong et al., 2017), hydrogen storage materials (Li et al., 2011), and superconductors (Snider et al., 2020). The addition of temperature (T) as another parameter expands the phase space for materials discovery or novel phenomena even further (Zaghoo & Silvera, 2017; Fedotenko et al., 2019; Nakao et al., 2019; Robinson & Hermann, 2020; Solozhenko et al., 2019). High temperature techniques can provide alternative synthesis pathways for materials similar to those with recently reported room temperature superconducting properties (Nakao et al., 2019; Fedotenko et al., 2019; Snider et al., 2020). The metallisation of hydrogen at extreme pressures has been reported (Dias & Silvera, 2017; Loubeyre et al., 2020), as has an analogous liquid metallic state of hydrogen stable at megabar pressures and temperatures over 1800 K that is thought to be the main constituent of gas giant planets (Weir et al., 1996; Zaghoo & Silvera, 2017). Superionic states in hot, dense molecular compounds such as solid H_2O, NH_3–H_2O, and NH_3–He mixtures have been created at high P-T conditions and are likely to be present in the interiors of icy giant planets (Sugimura et al., 2012; Millot et al., 2018; Liu et al., 2020; Robinson & Hermann, 2020).

Recreating the extreme conditions of planetary interiors can provide the phase assemblage for a given bulk composition (Ricolleau et al., 2010; Dorfman, 2016; Xu & Inoue, 2019). For the Earth, experimental constraints on the thermoelastic parameters of deep Earth materials are vital for the correct interpretation of observed seismic structure, but significant uncertainties currently exist for many of these parameters (Marquardt & Thomson, 2020). The lower mantle is of particular interest as it is the largest reservoir for many elements, stores a record of both planetary formation processes and the exchange of materials between the exosphere and deep interior over the course of Earth's

history, and has seismic features that are still poorly understood (French & Romanowicz, 2015; Kurnosov et al., 2017; Thomson et al., 2019; Tkalčić et al., 2015; McNamara et al., 2010; Walter et al., 2015). Knowledge of the physical and chemical characteristics of the lower mantle therefore provides important constraints on the evolution of our planet.

There are many experimental techniques for generating high pressure and temperature conditions in the laboratory, but the extreme conditions required to study the lower mantle (∼24 to 130 GPa, ∼1900 to 3000 K) and to synthesise many of the novel materials described above present significant experimental difficulty. The primary apparatuses used for static pressure generation at these conditions are the Kawai-type multi anvil press (MAP) and the diamond anvil cell (DAC).

MAP apparatus are typically limited to ∼20 to 30 GPa for routine experiments. Advances in experimental techniques, such as innovative anvil truncation designs, and the use of sintered diamond anvils instead of the typical WC cubes, have pushed the MAP pressure limit well into the range of lower mantle conditions for some experimental setups, and pressures above 100 GPa have been reported, though are far from routine (Liebermann, 2011; Ishii et al., 2019; Yamazaki et al., 2019). High temperatures are generated through the use of a resistive heater surrounding the sample assembly, and are typically very stable, with precise measurements made via a thermocouple. However, temperature generation in MAP experiments above 30 GPa has typically been limited to <1500 K (Tange et al., 2008; Yamazaki et al., 2014; Kunimoto et al., 2016), although a recent study reported stable heating at 2000 K and 50 GPa (Ishii et al., 2019). Nevertheless, much of the pressure-temperature (*P-T*) range of the lower mantle remains outside the capabilities of MAP techniques. Furthermore, the size of MAP apparatus makes them difficult to interface with *in situ* analysis techniques such as x-ray diffraction (XRD), and impractical to conduct multiple analyses using different techniques on the same sample.

In contrast, pressures encompassing the mantle can be generated routinely in the DAC. Unlike MAPs, the transparency of diamond anvils allows *in situ* optical analysis such as Raman, Fourier-transform infrared (FTIR) and Brillouin spectroscopy, and the portability of DACs mean that they can be easily interfaced with a wide range of synchrotron x-ray techniques including XRD, inelastic x-ray scattering (IXS), x-ray fluorescence (XRF), and x-ray absorption spectroscopy (XAS). Combined with laser heating, DACs can easily access the whole of the lower mantle geotherm. Typically, heating lasers operate at near-IR wavelengths (∼1 μm) that are not absorbed by iron free compositions, necessitating the mixing of the sample with a metallic absorber, which can lead to significant thermal gradients (Sinmyo & Hirose, 2010). CO_2 lasers that operate at much longer wavelengths (∼10 μm) can be directly absorbed by iron free compositions and have a greater penetration depth into the sample (thereby lessening axial temperature gradients; Anzellini & Boccato, 2020). However, CO_2 lasers are more expensive, require specialist optics, are less stable, and are harder to align

(Anzellini & Boccato, 2020; Kurnosov et al., 2019). Compared to near-IR lasers, CO_2 lasers are also harder to interface with fibre-optics, which facilitate the design of more portable and flexible setups (Kurnosov et al., 2019). Temperatures are measured in laser-heated DAC experiments spectroradiometrically, which involves fitting a Wien function to the thermal emission collected from the heated region, often with an analytical precision of a few K on a single measurement (Walter & Koga, 2004; Lord et al., 2014a). However, the true uncertainty in the temperature of the analysed sample volume over the timescale of the laser heating experiment is controlled by the size and intensity profile of the heating laser and, most importantly, the geometry and absorbance characteristics of the sample itself which can vary significantly both spatially and with time. Heterogeneous temperature during laser heating can cause diffusion of elements along thermal gradients (Sinmyo & Hirose, 2010). Axial temperature gradients can be reduced by simultaneous laser-heating of both sides of the sample and by surrounding the sample with a thermal insulator, while improvements in laser heating optics, including the use of beam shaping to flatten the gaussian intensity profile of the heating laser, can reduce radial temperature gradients (Prakapenka et al., 2008; Lord et al., 2014a). Nevertheless, spatial and temporal fluctuations in temperature over the duration of an experiment lead to uncertainties that are typically 100 K or more (Walter et al., 2015). Heating instability poses a particular problem for techniques requiring long data acquisition times, such as Brillouin spectroscopy and IXS (Ohtani et al., 2015; Ohira et al., 2016), and heating periods of less than an hour may be insufficient for the sample to reach thermodynamic equilibrium (Dorfman, 2016).

Resistive heating techniques provide greater temperature stability, more precise control, reduced thermal gradients, and uncertainties that are an order of magnitude smaller (Dubrovinskaia & Dubrovinsky, 2003). External resistive heating, in which a heater surrounds the anvil assembly or entire DAC, is a commonly used technique. A wide range of designs exist, including commercially available options (e.g., Dubrovinskaia & Dubrovinsky, 2003; Jenei et al., 2013; Louvel et al., 2020). Designs often incorporate the use of thermocouples, which allows temperature measurement below the typical limit of spectroradiometry ($\sim$1200 K). Resistive heating techniques also enable melting of the entire sample, which is difficult to achieve with laser heating (Louvel et al., 2020; Drewitt et al., 2020). However, external heating techniques are typically limited to $< \sim$1300 K, beyond which the unpressurised parts of the diamond anvils begin to graphitise, and the other components of the cell deform. Several recently reported designs have pushed this limit to $\sim$1500 K through the use of graphite heaters in combination with vacuum chambers and innovative cooling systems (Immoor et al., 2020; Méndez et al., 2020). One successful run with a reported peak temperature of 1900 K also demonstrates the possibility for advancement of these techniques (Immoor et al., 2020), but significant experimental difficulty remains. Routine experiments replicating the conditions of the lower mantle are therefore not feasible with external resistive heating.

Internal resistive heating, in which heat is generated only within the pressure chamber and isolated from the diamonds, can extend the accessible temperature range drastically. Internal resistive heating techniques have previously been successful in the study of metals at high pressure and temperature, by electrically heating a fine wire, compressed between the anvils, which serves as both heating element and sample. This technique (often termed 'fine-wire heating') was first pioneered by Liu & Bassett (1975) and is now well established (e.g., Boehler, 1986; Boehler et al., 1986; Dubrovinsky et al., 2007; Komabayashi et al., 2009). Recent experimental advances in this technique have proved useful in the study of melting (Sinmyo et al., 2019) and resistivity (Suehiro et al., 2019) of metals, however the application of internal resistive heating to non-metallic samples has been limited (Zha & Bassett, 2003; Zha et al., 2008).

To achieve resistive heating inside a DAC pressure chamber, the electrical circuit must be carefully designed so that it runs through the heating filament and is not broken as the cell is compressed. This is typically done by running distinct electrodes into the pressure chamber, necessitating electrical isolation of the electrodes from other metallic components (i.e., the gasket) to prevent a short. Existing designs rely on a composite gasket to do this, employing a layered (Boehler et al., 1986; Dubrovinsky et al., 2001a; Dubrovinskaia & Dubrovinsky, 2005; Dubrovinsky et al., 2007), concentric (Komabayashi et al., 2009; Sinmyo et al., 2019; Suehiro et al., 2019; Inoue et al., 2020) or combined design (Zha & Bassett, 2003; Ozawa et al., 2018). The use of a composite gasket introduces significant manufacturing complexity, and can lead to pressure limitations due to reduced structural integrity (Zha & Bassett, 2003). Furthermore, in these designs, the heater cannot be completely isolated from the diamonds, and the filament or electrodes must directly contact diamond along the electrical pathway into the pressure chamber. This can create a temperature limit as heating outside of the insulated sample chamber can lead to failure of the anvils due to thermal weakening and/or graphitisation, or draw heat away from the sample due to the unusually high thermal conductivity of diamond (Zha et al., 2008). One solution is to design the heater such that the insulated portion of the filament has a much greater electrical resistance relative to the external leads. This is commonly achieved by reducing the cross-sectional area of the filament. Several designs using this approach are capable of generating temperatures of several thousand K at multi-megabar pressures, but employ filaments too small to accommodate a separate sample (Sinmyo et al., 2019; Suehiro et al., 2019).

An alternative approach is to use a material with a much greater intrinsic resistivity. Ozawa et al. (2018) recently suggested boron-doped diamond (BDD) as a promising candidate material, as its resistivity is around five orders of magnitude greater than the Pt or W electrical leads used in their design (depending on Boron content). While this strategy achieved maximum heater temperatures of 3580 K at 28 GPa and 2580 K at 43 GPa, it has not yet been adapted to contain a distinct sample chamber and relies on surrounding the heater with a silicate sample material that also acts as the pressure medium, leading to maximum sample temperatures much lower than those of the hottest

part of the heater, and introducing large temperature gradients. The use of BDD also introduces significant fabrication complexity, necessitating a MAP apparatus to synthesise the heater material and the use of an argon ion beam to prepare the filament (Ozawa et al., 2018).

Zha & Bassett (2003) and Zha et al. (2008) previously reported x-ray diffraction and Raman scattering measurements of non-metallic materials measured in an internally resistive heated DAC. The design of Zha & Bassett (2003) employed a combined composite gasket approach, with an outer layered composite gasket and an inner (concentric) solid gasket. The outer gasket consisted of an insulation layer sandwiched between two stainless steel supporting gaskets to which the electrical leads were welded, and the inner gasket was composed of a fine grained (1 μm) mixture of diamond (30 vol. %) and MgO (70 vol. %) powders compressed in the outer gasket (with the entire culet region drilled out) for more than one hour at > 5 GPa. The pressure chamber was drilled into the inner gasket and a rhenium heating filament threaded through the chamber to connect the upper and lower outer gaskets and form a circuit. In this geometry, only the central region of the filament could be thermally isolated and most of the filament was in direct contact with the diamond anvils above and below the inner gasket. As a result, the design of Zha & Bassett (2003) relied on the high thermal conductivities of the diamond anvils and inner gasket material to keep the regions outside the insulated pressure chamber cool. Furthermore, the complex experimental geometry presents significant manufacturing difficulty. The heater was able to achieve a maximum reported temperature of 2800 K, but due to the use of a non-metallic inner gasket achievable pressure was limited to < 10 GPa. Zha et al. (2008) reported a modified version of this design in which the non-metallic inner gasket was replaced by rhenium that was layered between the insulation layer and lower supporting gasket and had a slot cut into one side (through which the heating filament runs) to maintain electrical isolation. This modification extended the achievable pressure range to 77 GPa, but the differences in insulation geometry and gasket material reduced the maximum temperature that could be reached to 1900 K (Zha et al., 2008). As such, IRH designs capable of heating non-metallic samples are currently limited to 1900 K above 10 GPa, insufficient for reproducing deep lower mantle conditions.

In this chapter, we present a new method designed to avoid the complexities and issues described above, and to achieve resistive heating of non-metallic samples at lower mantle conditions. A novel 'split-gasket' design is employed, in which we cut a typical metal DAC gasket in half and place a resistive heating filament inside the pressure chamber to bridge the gap and form a circuit. This approach completely isolates the electrical filament from the diamonds, eliminates the need for a composite gasket, allows the heater to be made from commonly available materials, and maintains gasket support during compression. In contrast to previous IRH designs (Zha & Bassett, 2003; Zha et al., 2008), our experimental geometry is greatly simplified, enabling efficient and reproducible generation of high *P-T* conditions beyond the limits of other IRH designs. We believe that our new

IRH-DAC design provides an important tool for investigations of materials at extreme conditions and is a significant step forward in heating techniques for the diamond anvil cell. It is particularly suited to the study of non-metallic and refractory materials, such as lower mantle minerals.

2.2 Methods

2.2.1 Laser Micromachining

We found it necessary to use a specialist laser micromachining system to fabricate the sub-millimetre components of the IRH experiments. All laser machining procedures were performed using an Oxford Lasers A-Series Laser Micromachining System equipped with a pulsed 1064 nm Neodymium-doped yttrium orthovanadate ($Nd:YVO_4$) solid state laser, frequency doubled to 532 nm (Innolas NANIO 521-10-V). The nominal power output is 11.4 W at 40 kHz, with a pulse width of < 30 ns and a pulse to pulse stability of < 1%. The precision of the x-y stage is $\sim$1 µm, and the focused spot size is $\sim$3 µm. The pulse energy is 250 µJ at 40 kHz, giving a peak power of > 8.3 kW.

Due to the small part size and low tolerances of the IRH design, it was necessary to optimise the machining quality of each component. In the laser micromachining method, laser ablation will occur when laser fluence (energy density) is above a threshold level for the material and is sufficient to result in vaporisation (Jandeleit et al., 1997). The mechanism and characteristics of laser ablation will depend on the properties of both the material and laser. The energy delivered by each laser pulse is absorbed directly by electrons at the material surface, with the energy then first propagating through the electron subsystem before being transferred to the lattice. The time required for complete energy propagation and for the system to reach thermodynamic equilibrium is controlled by the electron cooling time and lattice heating time of the material (which depends on the electron-phonon relaxation time; e.g., Chichkov et al., 1996; Von der Linde & Sokolowski-Tinten, 2000). If the laser pulse duration is significantly shorter than the time required to reach thermodynamic equilibrium, laser ablation will take the form of direct vaporisation (i.e., sublimation) of the material (Fig. 2.1; e.g., Petkov et al., 2008). This is the case for pulsed lasers in the femtosecond range, where ablation mechanisms become mostly material independent as the pulse duration is always shorter than the electron cooling time, which for most materials is in the picosecond range (Petkov et al., 2008). In addition, the energy density in femtosecond pulses is sufficient to form solid plasma which is ejected by self-expansion following the pulse, and assisted by the repulsion between charged particles (Kautek & Krüger, 1994; Von der Linde & Sokolowski-Tinten, 2000; Petkov et al., 2008). For pulse durations in the nanosecond range (such as for the laser used in this study), there is generally sufficient time for the electrons and lattice to reach thermal equilibrium, resulting in several effects.

Firstly, the timescale is long enough to melt the material, with further heating resulting in vaporisation from the intermediate liquid state. Material (both molten and vaporised) is then ejected due to the vapour/plasma pressure in the ablation cavity. In contrast to direct vaporisation, in this regime some material is retained due to the surface tension of the liquid, forming a recast layer (Fig. 2.1; Kautek & Krüger, 1994; Petkov et al., 2008). This process will be strongly controlled by both laser and material properties, primarily the melting point of the material, the energy distribution in the laser pulse, and the absorption characteristics of the material at the specific laser wavelength (which is also temperature dependent). For most metals, there is an abrupt increase in laser absorption at the melting point, resulting in a thermal run-away effect and more efficient vaporisation (and therefore ablation) compared to other materials. In addition to the melting effect, nanosecond scale laser pulses result in a thermal shock wave. This results in a heat affected zone, sub-surface micro-cracks, surface damage and ejected solid (and usually oxidised) debris that forms a layer surrounding the ablation spot (Fig. 2.1; e.g., Petkov et al., 2008; Tański & Mizeraczyk, 2016). For a set pulse width, the extent of these unwanted effected will be strongly material dependent. However, even within the nanosecond regime, the extent of thermal damage can be reduced by using shorter laser pulses (Chichkov et al., 1996).

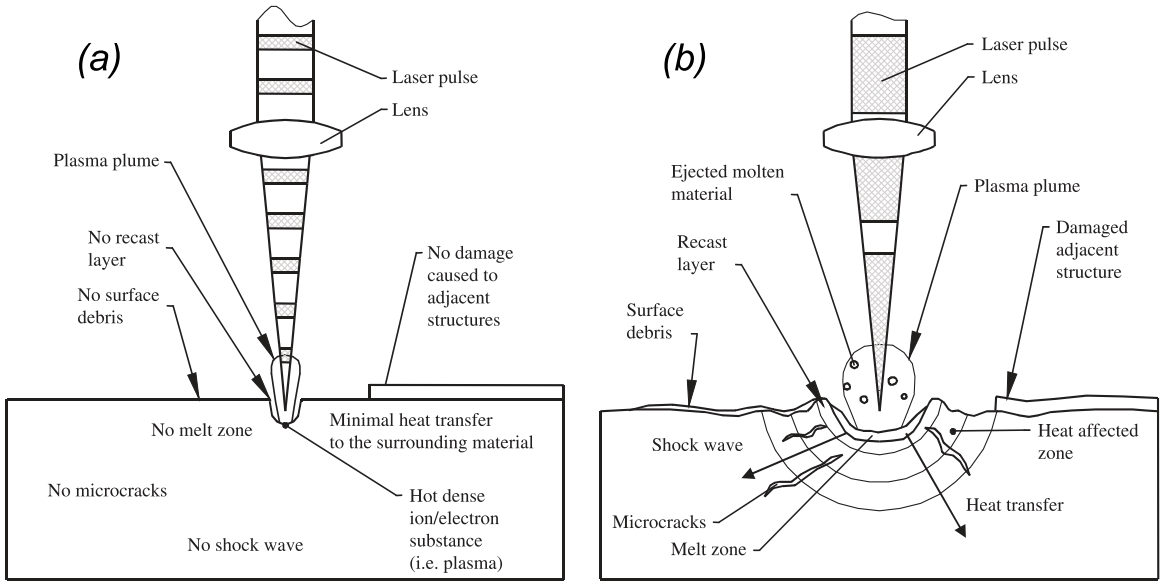

Figure 2.1: *Schematic diagram of laser ablation regimes and associated effects for femtosecond (a) and nanosecond (b) pulse widths. Ultra-short (femto- or picosecond) pulse widths result in direct vaporisation of material, minimal thermal damage, and decoupling of ablation regime and material absorption characteristics (a). Nanosecond pulses result in melting and thermal shock, causing micro-cracks, surface damage, increased debris deposition, and forming a recast layer. The extent of thermal damage, and which of these effects occur, will depend strongly on material properties, but can be mitigated by optimising process parameters. Figure reprinted with permission from Petkov et al. (2008). © 2008 IMechE.*

Laser micro-machining relies on repeated laser pulses to progressively remove material. This allows for several modes of operation and associated process parameters that can be modified to optimise the machining and reduce thermal damage. The modes of operation are percussion drilling, cutting, and milling. Percussion drilling (repeated laser firing in one spot) can be used to drill holes with a diameter of the same order of magnitude as the focused laser spot size. For laser cutting, the workpiece is moved underneath the laser beam to create tracks of ablation spots (i.e., grooves). Laser milling then simply overlaps parallel grooves to form a milled 2D area. Repeated passes over the milled region, with the focus readjusted to account for the material ablated in each pass, allows the milling of 3D topography. While most of the laser characteristics are fixed properties, several parameters can be modified to increase machining efficiency and/or quality. The focus can be offset from the material surface to increase spot size and decrease laser fluence, and/or to improve laser coupling by accounting for beam distorting optical effects in transparent materials. The laser power can be modified by the use of an attenuator, with higher power typically increasing ablation efficiency but also thermal damage. This effect may be significantly non-linear for some materials (particularly transparent materials).

The laser pulse repetition rate (pulse frequency) and workpiece track speed can also be varied. This will principally affect the overlap between ablation pits, given as a percentage by:

$$overlap = \left(1 - \frac{v}{fd}\right) \times 100, \tag{2.1}$$

where v is the scanning speed, f is the pulse frequency, and d is the spot diameter. A low overlap will result in high surface roughness due to incomplete removal of material along the track. However, a high overlap can significantly increase thermal damage due to the increase in delivered energy per unit of surface area (i.e., increased fluence at the same location). As the dissipation of the energy depends on the material properties, the optimum overlap will also be material dependent, but generally falls in the region of 65 to 95% (Jandeleit et al., 1997; Yasa & Kruth, 2010). For milling, the overlap between parallel tracks (hatch pitch) is similarly important, although for large areas there is generally enough time between adjacent spots in different tracks for thermal effects to be less important (Williams et al., 2014). The analogous adjustment in focus between each pass (the z-step) can also be adjusted. This is ideally simply based on the per pass ablation rate, but as the ablation properties depend on surface morphology the ideal z-step can change throughout the machining process. For milling, the beam divergence should also be considered, as this angle will limit the maximum possible depth of a milled recess for a specific width, and can change the ablation properties within the recess.

The limitations of the stage motors must also be considered for both cutting and milling. The ramp rate of the motors as they slow down or speed up at the end of cutting tracks will alter the overlap, and may reduce process quality for small parts. At high scan speeds, the motors will also overshoot on tight curves, limiting the maximum scan speed for particularly small parts with curves or complex geometry. As a result, the optimal machining parameters will often be part-dependent as well as material dependent.

The pulse frequency will also affect ablation characteristics independent of overlap affects. For example, high repetition rates may result in laser-plasma interactions that shield the material surface and causes re-deposition of ablated material. Re-deposition of material can be mitigated somewhat by air-assisted machining or flowing gas through a workpiece containment chamber. The use of an inert gas flowing through such a chamber can also prevent oxidation. However, non-linear optical effects of the chamber window and the gas can lead to wavefront disruption and distortion of the laser profile, meaning that a different set of parameters will generally be optimal. In addition, the average laser power will also vary with repetition rate (Fig. 2.2), further coupling the machining parameters. This means it is a non-trivial task to find the optimal set of process parameters for a particular component, and the various tradeoffs between different parameters must be considered. There is also typically a tradeoff between machining efficiency (i.e., time) and quality (i.e., surface roughness, thermal damage, geometric accuracy, etc.). The optimised process parameters for the different IRH components described in the next section can be found in appendix B.

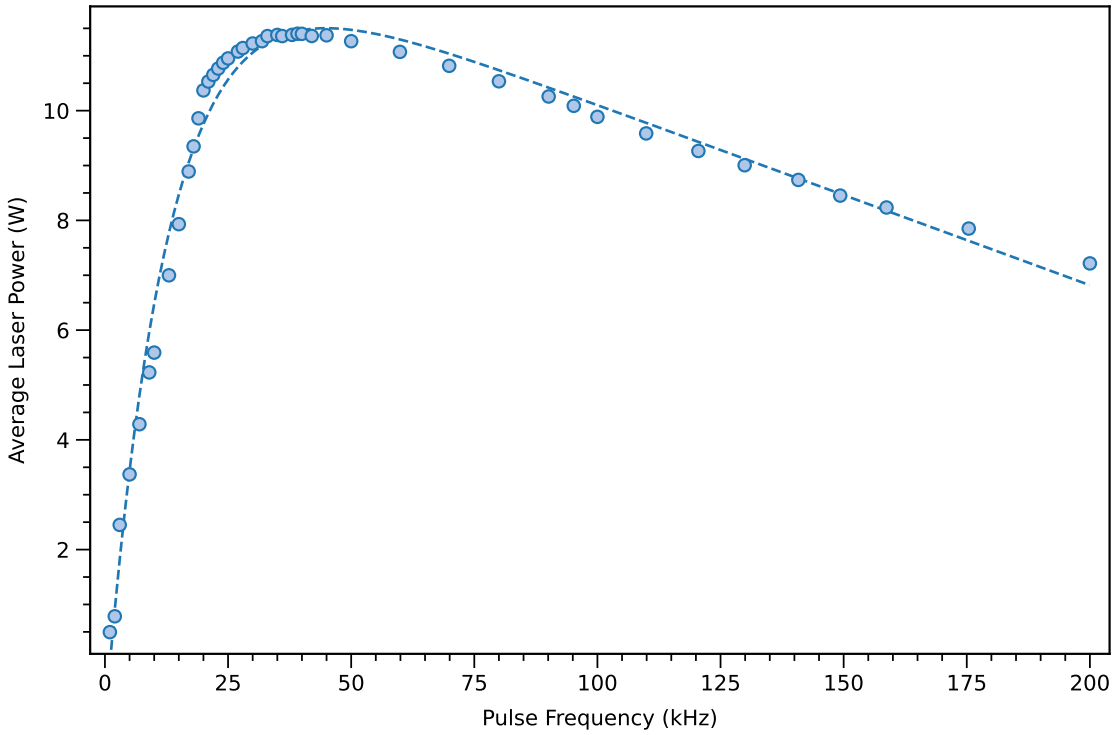

Figure 2.2: *Variation in measured average laser power with repetition rate (pulse frequency) for the Oxford Lasers micromachining system used to prepare IRH components. Peak average power is obtained at ∼40 kHz, dropping off rapidly at lower repetition rates but more gently at higher repetition rates. The operating range of the system is 0.2 kHz to 200 kHz. The power variation is not easily modelled, but the dashed line shows a fit to an exponential function of the form* $f(x) = d\left[c - \exp\left(ab - ax\right) - \left(ax - ab\right)\right]$ *(a modified linex), with* a *= 0.079,* b *= 44.87,* c *= 28.75, and* d *= 0.41.*

2.2.2 IRH Experimental Technique

The IRH gaskets must be held in place as an experiment is prepared to avoid any relative movement between the two sides when the gasket is cut. We used reuseable custom holders for this purpose (Fig. 2.3 and 2.5). The holders were machined from polyether ether ketone (PEEK), a thermoplastic with excellent mechanical properties, which is resistant to temperatures up to several hundred °C. Two brass electrodes clamp the gasket into a slot in the body of the holder and extend beyond the DAC body so that electrical connectors can be attached. The gasket holder was designed to fit tightly into a BX90 DAC (Kantor et al., 2012) so that the position of the diamonds relative to the gasket remained constant as an experiment was assembled. Long rectangular gaskets were used to maximise the clamped surface area and provide a good electrical contact to the brass electrodes (see Fig. 2.5). We used gaskets laser cut from 250 μm thick stainless steel sheet for these experiments, but any electrically conductive material can be used (e.g., rhenium). After clamping into a holder, each gasket was pre-indented by compression in a DAC to 15 GPa, resulting in a gasket thickness of ∼70 μm in the culet region. The gasket is then partially split, leaving just the culet region intact. This was achieved by milling 100 μm wide slots up to the edge of the culet on both sides using a laser milling routine designed to minimise thermal distortion near the thin culet region, and minimise the amount of conductive debris left in the slots. The slots were cleaned by flushing with acetone and then filled with a temperature resistant, non-conductive two-part epoxy (Loctite Stycast 2850FT). A circular hole with a diameter of 150 μm was then laser-drilled in the centre of the culet region to form a pressure chamber to accommodate the heating filament. The electrical isolation of the two sides of the gasket was completed by laser-milling two 80 μm wide slots that extend from the central chamber to the Stycast filled slots at the edge of the culet. The culet region is cleaned with a fine needle and placed in an ultra-sonic bath with acetone to remove any debris. The resistive heating filaments were machined from 12.5 μm thick rolled rhenium foil (GoodFellow). First, a 10 μm diameter sample chamber with vertical sides was created by laser percussion drilling. Next, the filament shape was cut out around the pre-drilled hole. The 'bow tie' shape of the filament was designed to maximise the area of the electrical contact between the filament and the steel gasket whilst creating a well-defined hot region in the centre of the filament by reducing the cross-sectional area (thereby increasing resistance; Fig. 2.4).

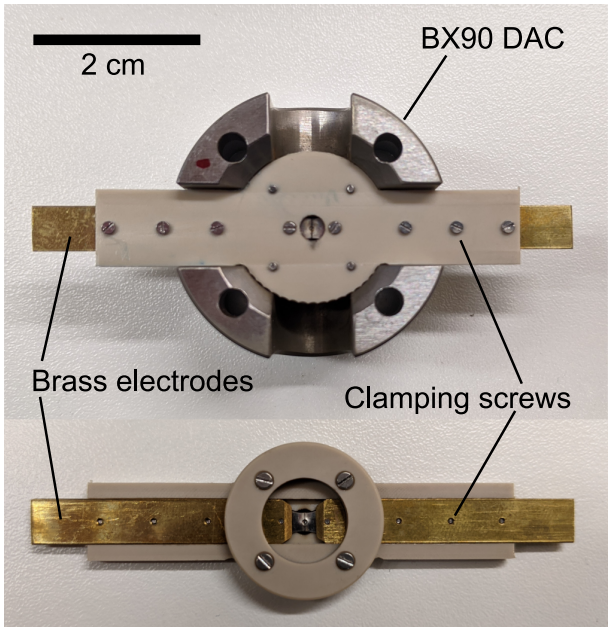

Figure 2.3: *Photograph of an IRH gasket holder mounted in the bottom half of a BX90 DAC along with the reverse side of the holder. The body of the holders are machined from polyether ether ketone (PEEK), with brass electrodes and stainless steel clamping screws. Full technical drawings of the holder are shown in figure 2.5.*

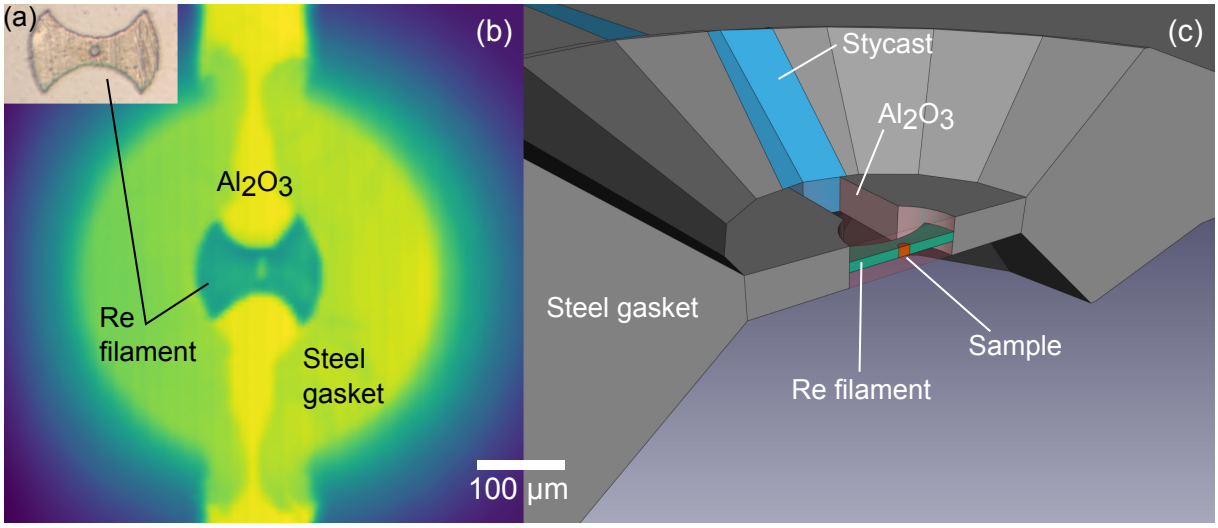

Figure 2.4: *(a) Photomicrograph of a rhenium IRH filament prior to loading. The sample chamber is 10 µm in diameter and the filament thickness is 12.5 µm. (b) Synchrotron x-radiograph of experiment #5b showing the IRH system at pressure (17 GPa). (c) 3D CAD model showing a cross section of the IRH sample environment.*

Next, the experimental sample is pre-loaded into the IRH filament. We found the simplest procedure for this is to place a small piece of sample material roughly the same size as the sample chamber directly on top of it, and then use a DAC with a pair of large diameter diamonds to gently press the sample into the hole (Fig. 2.6). To assemble an experiment, the gasket holder is placed in a BX90 DAC and seated on the lower anvil. The filament assembly is then placed in the central hole sandwiched between layers of Al_2O_3 that fill both the sample chamber and the slots in the culet region (Fig. 2.4 and 2.6). This material provides thermal insulation for the diamonds as well as mechanical support for the gasket so that the slots remain open as the cell is compressed. In these experiments we used Al_2O_3 as the insulating material, but other similarly hard ceramics could be chosen to suit the experiment (such as MgO, SiO_2 or ZrO_2), provided they are unreactive with the sample at the target *P-T* conditions, are optically transparent, and have relatively low thermal conductivity. As loose alumina powder is fairly compressible and the slots need to be braced open, we pre-compressed alumina nano-powder (<50 nm, Sigma-Aldrich) into densified plates using a hydraulic hand press. These plates were then broken up into form-fitting pieces to fit into the milled region of the culet. Each filament was carefully loaded into the central hole, orientated so that it bridges the gap between the two halves of the gasket, and seated horizontally within the chamber (Fig. 2.6). Careful orientation of the filament is important to avoid any rotation or shearing during compression. A small amount of loose alumina nano-powder was added along with the plates above the filament to fill in any remaining void spaces. If the sample is expected to react with the chosen insulating medium during an experiment, discs of another material that is unreactive with the sample can be placed above and below the filament to chemically isolate the sample. The only limitation is that the majority of the pressure transmitting medium must be a hard ceramic capable of maintaining the mechanical strength of the assembly.

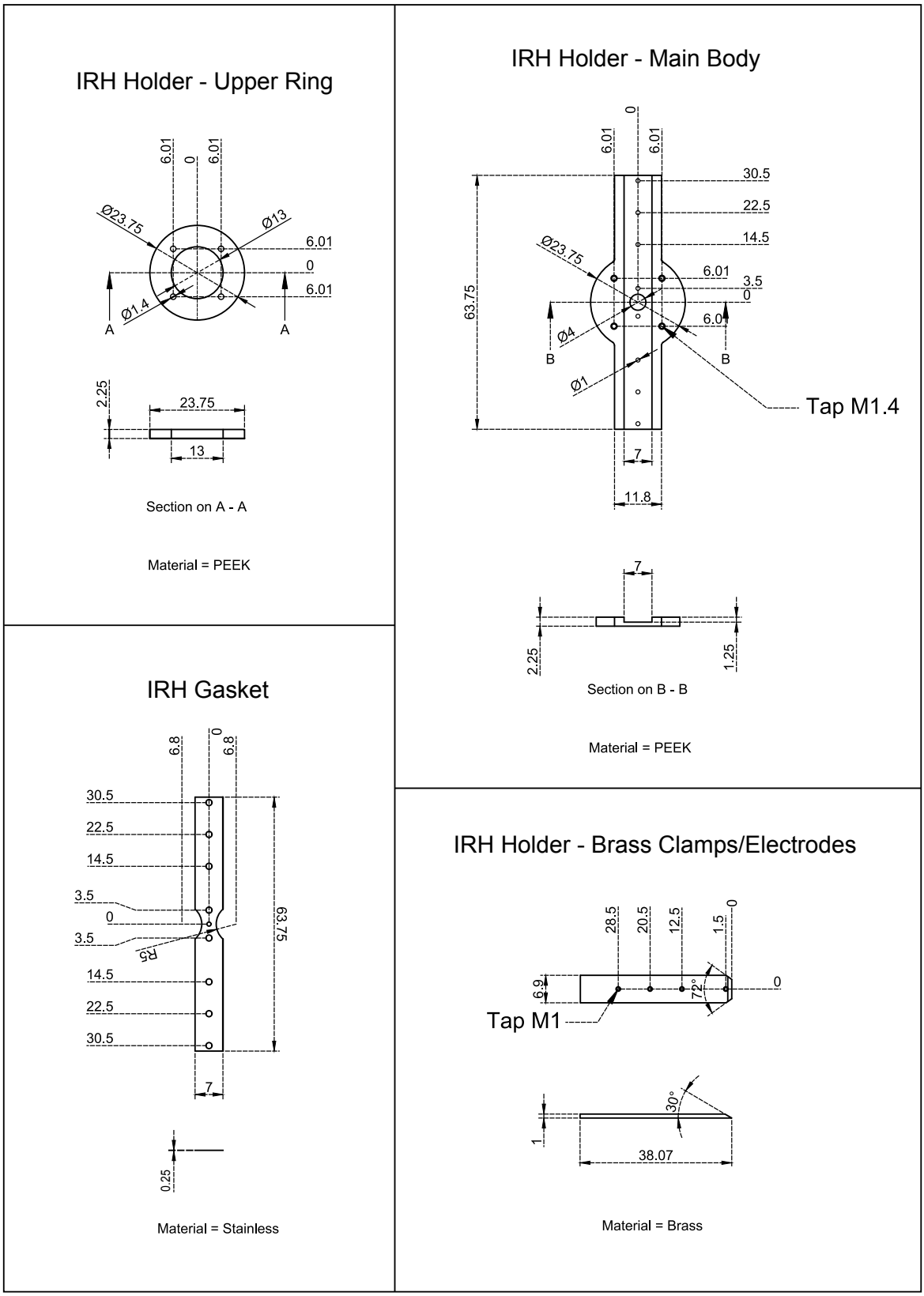

Figure 2.5: *Technical drawings of the IRH gasket and gasket holder. All units are in mm. The gaskets are cut using laser machining methods, while all other components are machined conventionally. Slightly countersunk, low profile screws were used for the two M1 screws nearest the anvils so that they do not touch the diamonds as the cell is compressed.*

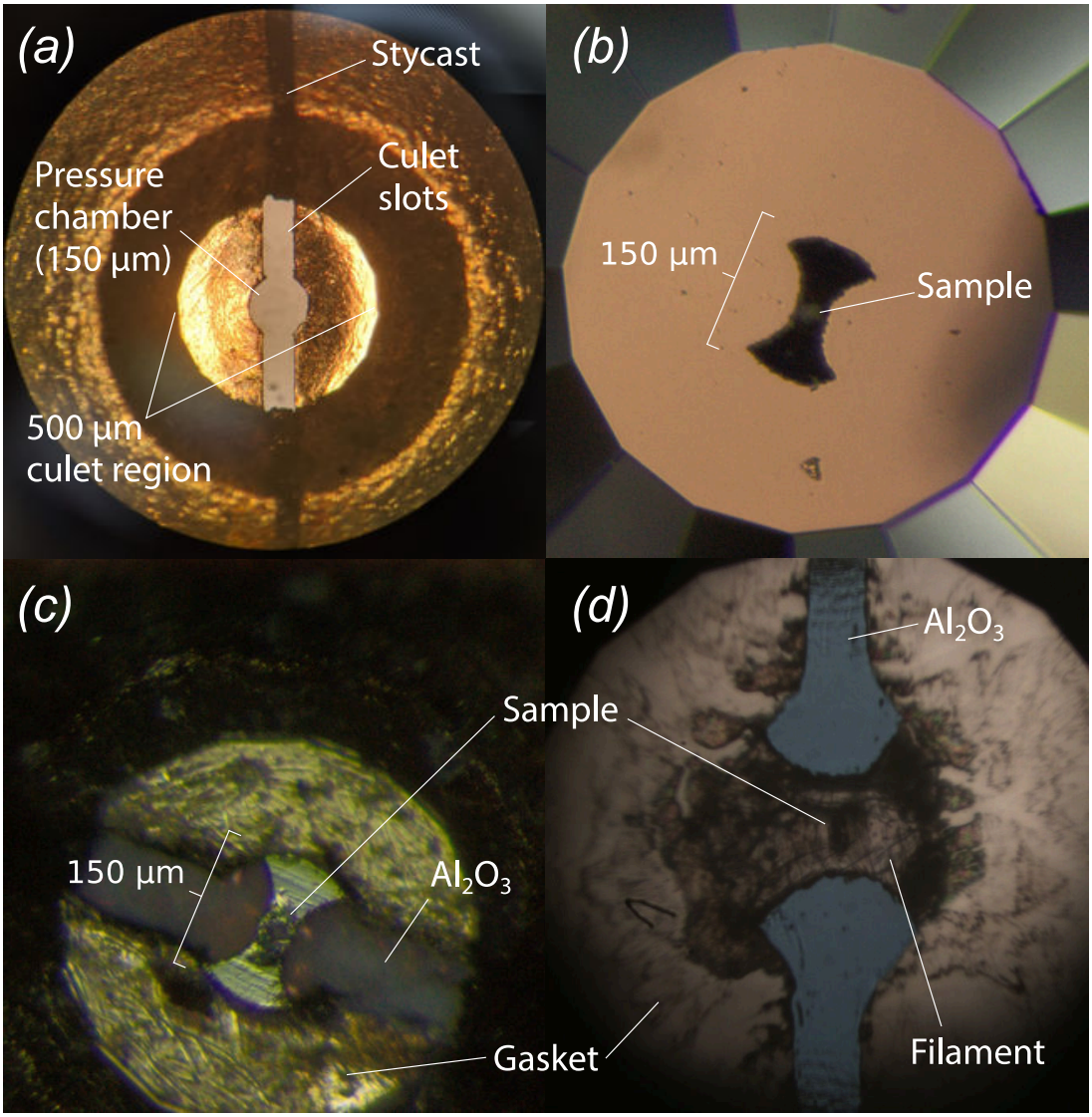

Figure 2.6: *Photomicrographs of the IRH culet geometry design and loading procedure. (a) The pressure chamber is formed from a 150 µm hole in the centre of the culet, with 80 µm wide slots extending to the culet edges to complete the splitting of each side of the gasket. The Stycast epoxy filling in the slots beyond the culet region can also be seen. (b) Photomicrograph of an IRH filament on an anvil tip after loading a small piece of material into the ∼15 µm sample chamber within the filament. (c) Photomicrograph of an IRH experiment part-way through the loading procedure. Careful orientation of the filament is important. The filament is loaded over the top of compressed plates of alumina nano-powder. More alumina is added on top of the filament before the cell is compressed. (d) Photomicrograph of IRH experiment #5c at ∼32 GPa prior to heating. The alumina nanopowder becomes transparent as the cell is compressed. The deformation of the sample chamber can also be seen, elongated in the y-direction (parallel to the slots).*

2.2.3 Temperature Generation and Measurement

To illustrate the efficacy of our IRH-DAC design in performing high *P-T* experiments with *in situ* x-ray diffraction measurements, four cells were heated at beamline I15, Diamond Light Source, UK. After the initial heating runs, each of the cells was compressed further and reheated at a higher pressure. One of the cells was heated three times to make a total of nine experiments (*#3a* to *#6b*). Two further off-line heating experiments were made in the Diamond Anvil Cell Laboratory at Bristol (*#7a/b*). The details of the experimental runs are presented in Table 2.1.

To conduct a heating run, electrical leads were attached to the brass electrodes of the gasket holder with crocodile clips and a programmable DC power supply used to supply current. We used an Aim-TTi EX2020R 400 W power supply for experiments performed at Diamond Light Source and an Elektro-Automatik 5040-40-A power supply for experiments performed at Bristol. During experiments, the IRH-DAC was placed in a water-cooled copper jacket to ensure the gasket holder and cell itself did not suffer any thermal distortion, although any warming of the DAC body was minimal.

Temperatures during experimental runs at Diamond Light Source were measured spectroradiometrically using the system in place on the laser-heating stage at I15 (Anzellini et al., 2018). The system collects thermal emission from a region ∼3 μm in diameter, with the aperture pre-aligned to the position of the x-ray beam (with an accuracy of ∼1 μm) and periodically checked for drift throughout the experiments (Anzellini et al., 2018). For experiments performed at Bristol, four-colour multispectral imaging radiometry was used to allow us to illustrate the temperature gradients within an IRH experiment. This system has previously been described in detail by Lord & Wang (2018).

2.2.4 Synchrotron X-Ray Diffraction

In situ angle-dispersive x-ray powder diffraction measurements were made using an x-ray beam with a wavelength of λ = 0.4246 Å, which was micro-focused to a nominal beam dimension of 6×4 μm^2 (full width at half maximum) to minimise scattering from the rhenium filament surrounding the sample chamber. Diffraction patterns were collected with a Pilatus 2M detector and a typical acquisition time of 30 seconds. The sample to detector distance was calibrated using a CeO_2 standard. As the sample material was only present inside the sample chamber, which was similar in diameter (∼10 μm) to the x-ray beam, we were able to precisely locate the sample by maximising its XRD signal in a 2D scan across the pressure chamber, which was first located using an optical image centered on the x-ray beam. The x-ray diffraction images were integrated to one-dimensional spectra and the

Table 2.1: *Starting materials and P-T conditions of IRH experiments.*[†]

Run	Sample	P_{pre} (GPa)		P_{post} (GPa)		P_{max} (GPa)		T_{max} (K)
		P_{Mo}	P_{KCl}	P_{Mo}	P_{KCl}	P_{Mo}	P_{KCl}	
#3a	KCl + Mo	3.0(1)	3.5(1)	···	···	···	<2[*]	1167(5)
#3b	KCl + Mo	10.7(2)	···	11.9(1)	···	22.7(1)	···	2059(1)
#4a	KCl + Mo	···	4.1(0)	···	4.1(0)	···	···	<1150
#4b	KCl + Mo	···	5.1(0)	···	···	···	···	<1150
#5a	KCl + Mo	17.0(1)	···	17.7(3)	···	···	···	<1150
#5b	KCl + Mo	16.6(2)	···	25.9(4)	···	42.4(4)	39.6(3)	2002(60)
#5c	KCl + Mo	33.7(2)	30.1(8)	···	29.7(5)	64.2(2)	62.6(3)	3059(1)
		P_{Pt}		P_{Pt}				
#6a	Ti35[**] + Pt	1.6(1)		12.2(1)		20.4(3)		1941(36)
#6b	Ti35[**] + Pt	16.7(1)		26.8(1)		40.1(6)		2337(72)
		P_{Raman}						
#5d	KCl + Mo	43(1)						
#7a/b	Al_2O_3	25(1)						

[†]Uncertainties on *P-T* conditions in parentheses are 1σ on the last digit
[*]Pressure dropped below the B1-B2 KCl transition at ∼2 GPa (Pistorius, 1965)
[**]$Ca(Si_{0.65},Ti_{0.35})O_3$ glass

peaks indexed using the *GSAS-II* software (Toby & Von Dreele, 2013). The background, fitted as a cubic spline, was subtracted from each pattern and diffraction peaks attributed to the pressure calibrants (Mo, B2 KCl, or Pt) were individually fit to pseudo-voigt profiles using the program *fityk* (Wojdyr, 2010). Uncertainties in the peak parameters, including position, were estimated from the fitting procedure. As all of the pressure calibrants used were cubic, a lattice parameter, $a(hkl)$, was calculated directly from each present reflection and a weighted arithmetic average, $\bar{a}_m$, used to determine unit cell volumes. Pressure was determined from the unit cell volumes of the calibrants and their known thermal equations of state (Dorogokupets & Dewaele, 2007; Litasov et al., 2013; Tateno et al., 2019). For experiments performed at Bristol, pressure was determined from the Raman shift of the singlet peak of the diamond anvil at the culet surface, using the calibration of Walter et al. (2015).

2.3 Results and Discussion

2.3.1 Heater Performance

Our IRH-DAC design enables remarkably precise and stable power generation over the duration of long experiments. Temperatures up to 3000 K were generated within the sample chamber, with no apparent temperature limit imposed by increasing pressure, as is common with other resistive heating techniques. During initial compression, the alumina filled slots typically contracted unevenly and began to pinch at the edges of the culet, but we found that heating improved the geometry of the slots, which became increasingly parallel after heating. This allowed cells to be compressed further and re-heated at higher pressures, making a large *P-T* region accessible with a single loading.

2.3.1.1 Electrical Behaviour

The measured resistance across the whole circuit of an IRH cell was typically ∼0.9 Ω (Fig. 2.7). In some runs the measured resistance prior to heating was extremely high (kΩ) or no circuit was detected with a multimeter, due to poor contact between the filament and steel gasket. In all cases, this was solved by applying a current of 4 A across the circuit. This was most likely due to local heating at contact points and thermal annealing of the filament-gasket contact. The power-temperature relationship was very linear across the whole range of measured temperatures in our experiments, and was in the range of 7.3 to 15.3 K/W (Fig. 2.8). This ratio was different for each run, which can be explained by slight differences in mechanical deformation of the filament during compression, variations in insulation thickness, and differences in resistivity with varying pressure between runs.

The power required to achieve a given temperature is higher in the experiments reported here than those reported by Zha & Bassett (2003) due to differences in the thermal conductivity and thickness of the insulation material and the geometry of the filament. Nevertheless, we successfully heated to sample temperatures of 3000 K with no damage to the diamond anvils or other components and the power required was in the normal range that commonly available power supplies can provide. The precision of commonly available programmable DC power supplies is typically ∼0.1 W, giving our IRH-DAC a theoretical precision of ∼1 K, which is similar to the analytical precision of spectroradiometric temperature measurements (Walter & Koga, 2004). A rigorous linear relationship between power and temperature is useful as it provides the possibility to use an extrapolation from a linear regression of the power-temperature relationship to estimate temperature when no spectroradiometric temperature measurement is available, or below the thermal limit of spectroradiometry. The average 95% prediction interval of the linear fits to the power-temperature relationship was 5.5% of the temperature (Fig. 2.8). However, the period of decreasing circuit resistance observed at the start of several experiments suggests that the linear relationship does not hold down to room temperature (Fig. 2.7). This is also evident from the fact that the zero power intercepts of the fits are offset from room temperature (Fig. 2.8). The performance of the heater in this region should be investigated further before a power-temperature calibration below 1200 K can be reliably established or deemed feasible. A spectrometer with sensitivity in the near-IR spectral range (such as an InGaAs detector) could be used to measure spectroradiometric temperature down to 500 K (Shen et al., 2010).

During runs where the temperature was slowly increased and decreased to and from a maximum, the temperature achieved at a set electrical power was also observed to be lower on cooling. This can also be seen as a reduction in measured resistance of the whole circuit after heating (Fig. 2.7). We assume that this is due to the improvement of the contact between the gasket and filament during heating, and the removal of distortion induced by cold compression. Previous studies of Joule heating inside a DAC sample chamber found that multiple temperature cycles were necessary to achieve a linear power-temperature relationship and achieve stable temperature generation (Zha & Bassett, 2003), but this is unnecessary with our design, and the heater appears to stabilise during the first 40 W of power application (Fig. 2.7).

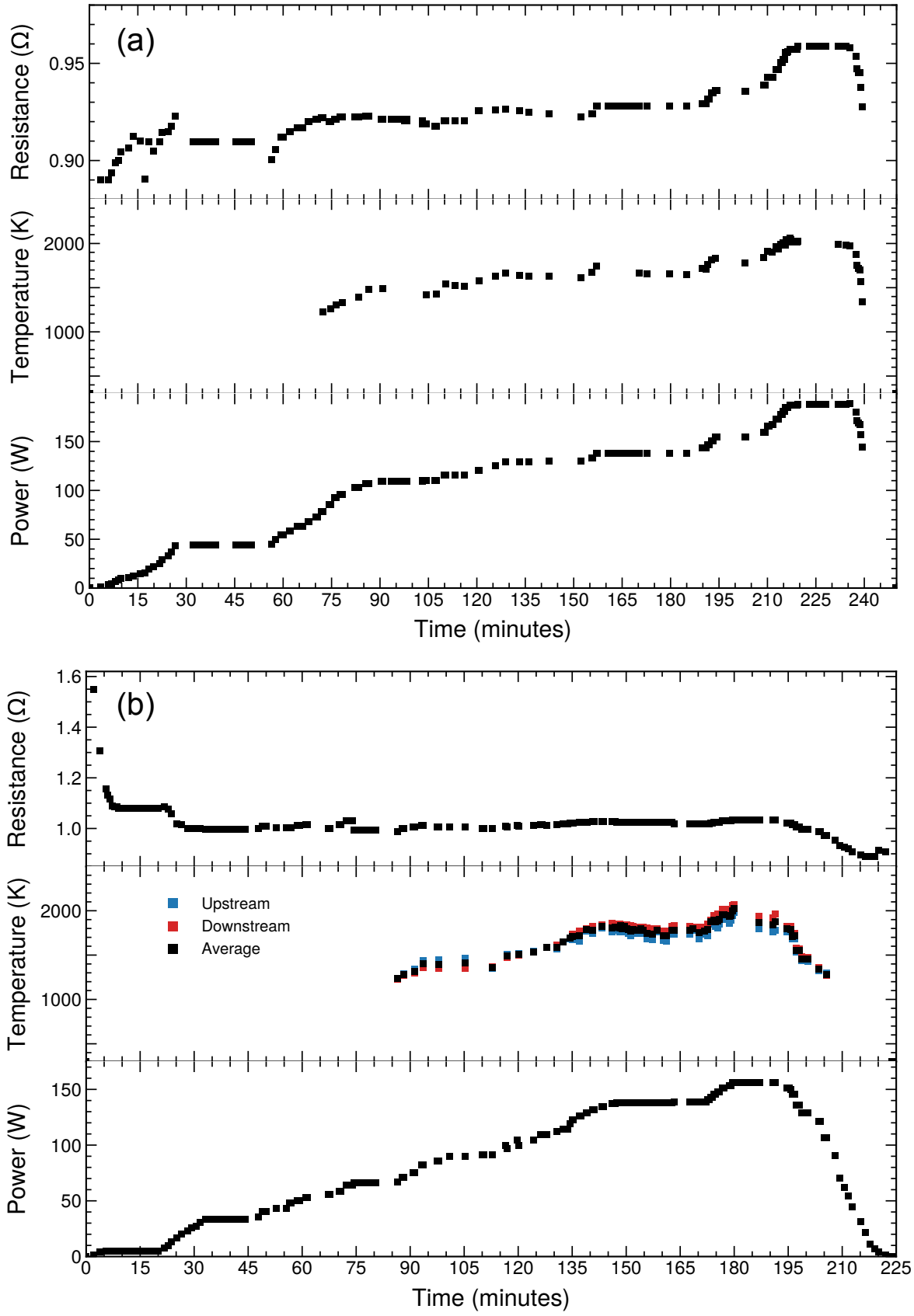

Figure 2.7: *Plots of electrical power, measured sample temperature, and circuit resistance over the duration of experiments (a) #3b and (b) #5b. Data from other experiments can be found in appendix A.*

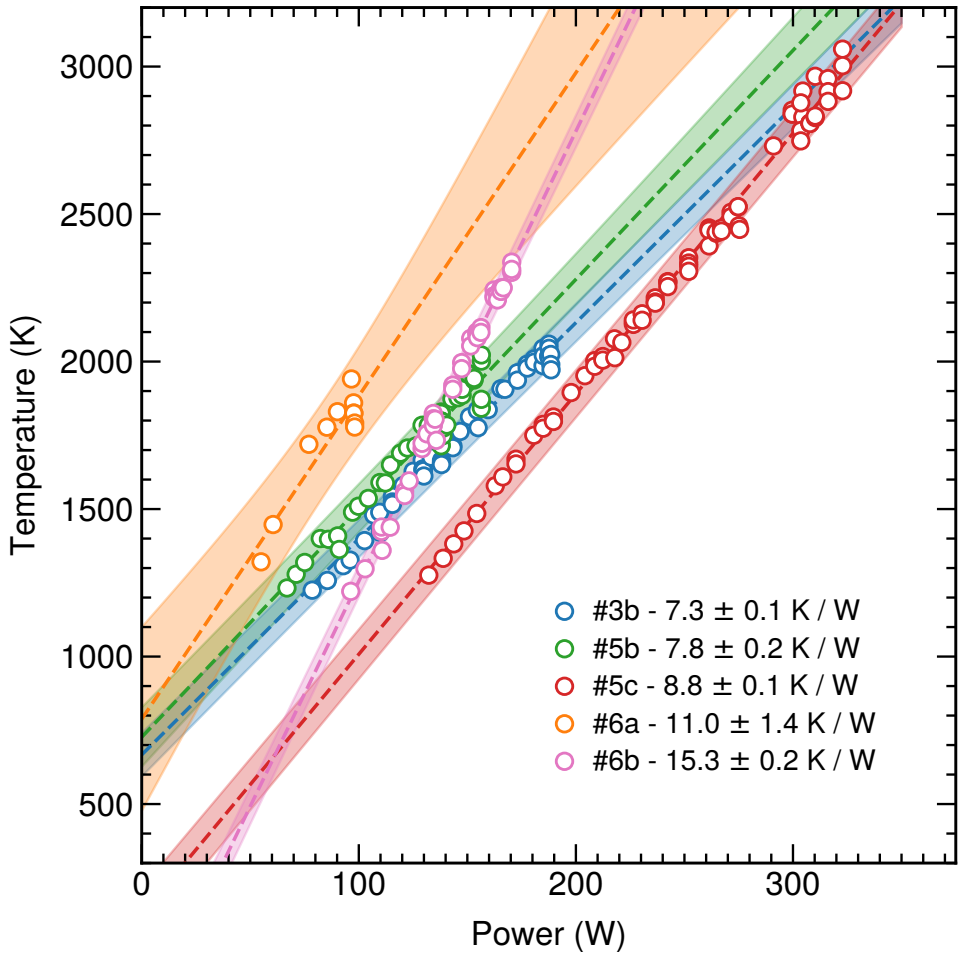

Figure 2.8: *Plots of sample temperature vs electrical power during temperature increase. Temperatures below ~1200 K were too low to measure with spectroradiometry. The analytical uncertainties on individual temperature measurements were typically < 1 K and are smaller than the scale of the data points, although the real uncertainty (e.g., taking into account the greybody approximation) is likely to be larger as discussed in section 1.3.4. Dashed lines show linear fits to the data and the shaded regions show 95% prediction intervals. The linear fits and 95% prediction intervals (which show where a future temperature measurement would be statistically expected to fall at a set power) have been extrapolated down to zero power to demonstrate the difficulty in using electrical power to estimate temperature below the thermal limit of spectroradiometry.*

2.3.1.2 Temperature Stability

The resistance of the heater can change with temperature and pressure or as a result of mechanical deformation. This can lead to temperature instability over the duration of an experiment. Applying a constant current during a resistive heating experiment may lead to unstable temperature generation and even cause a run-away temperature increase. This is because the resistance of a metal filament will increase with temperature, and so more electrical power is needed to maintain the current as the temperature increases. To avoid this issue, we used a regulated constant voltage mode in experiments performed at Diamond.

During experiment *#5b*, we measured the temperature at a constant voltage of 11.9 V over a 20 minute period, a timescale typical of a laser heating experiment. The sample temperature decreased slowly, at a constant rate of 5 K/min, while the measured resistance of the circuit remained stable, suggesting that the temperature decrease was caused by heat loss from the sample to the diamond anvils or that any decrease in electrical power was below the precision of the power supply readout. This temperature change could be easily controlled with only minor adjustments to the electrical power, as the rate is constant and slow.

To further investigate the stability of our IRH-DAC over longer time periods, and the dependency on the power supply regulation mode, we conducted two additional heating runs at Bristol using regulated constant voltage (*#7a*) and constant power (*#7b*) modes. The temperature was passively monitored, and no manual adjustments to the voltage or power were made during these experiments. In contrast to experiment *#5b*, the voltage control test conducted at Bristol (*#7a*) showed an increase in temperature over the duration of the experiment (Fig. 2.9). This opposite behaviour could be explained by differences in the sample environment, such as insulation thickness, or by a different method of voltage regulation used by the power supply. Nevertheless, the rate of temperature change was also extremely low and could be easily controlled by compensating for the power increase, which rose 4 W over the four hour test. Although the temperature change appears to be nonlinear, we found the behaviour to be best fit by two periods of linear temperature increase — initially a rate of 1 K/min over a 30 minute period, followed by a rate of 0.16 K/min for the remaining 3.5 hours of the test. In a 90 minute stability test of their design, Zha & Bassett (2003) similarly found an initial 30 minute period of faster warming, which they attributed to thermal equilibration of the heater with the body of the DAC. The temperature increase during the first 30 minutes of their test was much greater than ours ($\sim$250 K), likely due to the larger heated region in their design and thermal equilibration with more thermally conductive components due to heating outside the insulated pressure chamber (Zha & Bassett, 2003). However, the stability test performed by Zha & Bassett (2003) was conducted in a constant current mode, which may account for some of the differences in performance.

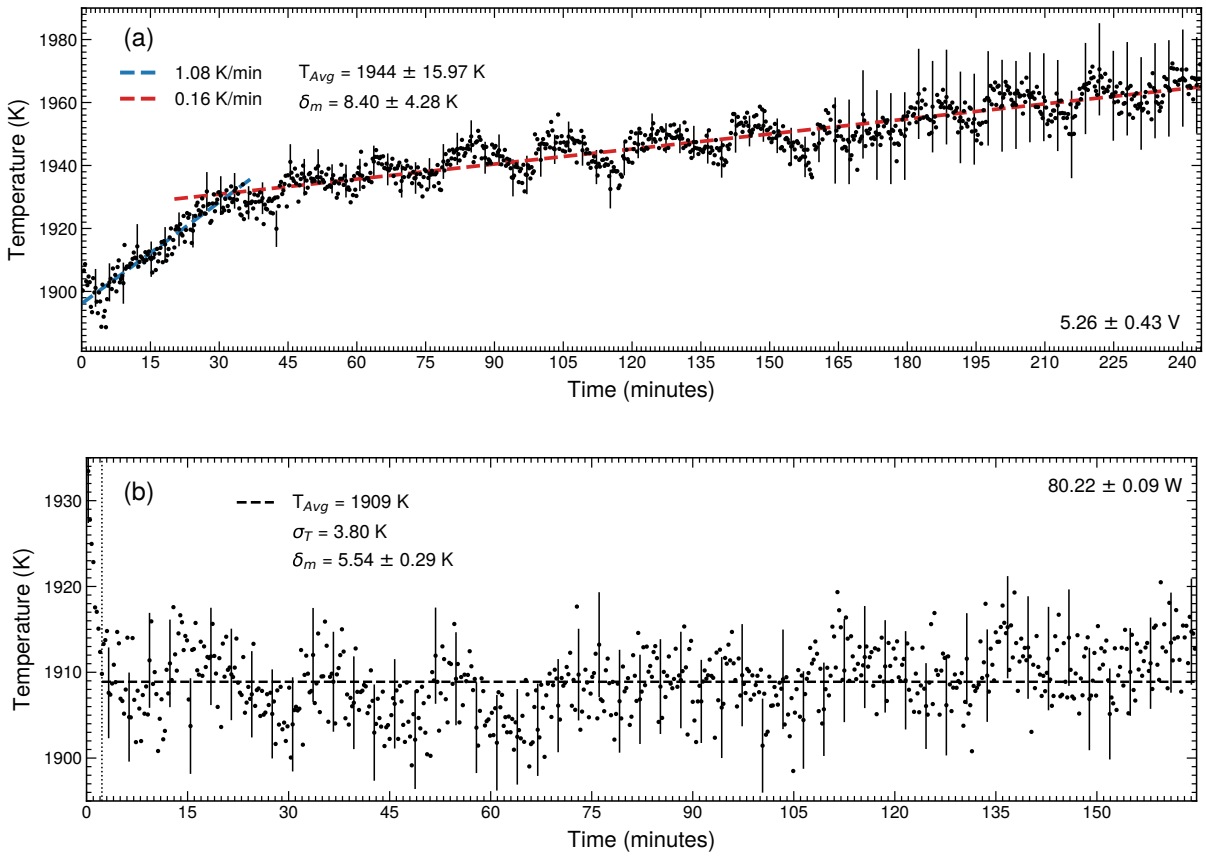

Figure 2.9: *(a) Sample temperature measured over a 4 hour period with a constant voltage of 5.3 V. The temperature rises ∼60 K over the four hour experiment. This can be characterised as two periods of linear increase, shown by the dashed lines. (b) Sample temperature measured over a 2.75 hour period with an electrical power of 80 W. A 2 minute stabilisation period can be observed at the start of the test. The average temperature (T_{Avg}) is 1909 K for the remainder of the test with a standard deviation (σ_T) of 3.80 K. The average measurement uncertainty (δ_m) was 5.54 ± 0.29 K. Statistical analysis suggests (with >99% certainty) that the observed scatter is stationary (Augmented Dickey-Fuller (Dickey & Fuller, 1981; MacKinnon, 2010) test statistic = −4.024, p=0.001), and is normally distributed (Shapiro-Wilk (Shapiro & Wilk, 1965) test statistic = 0.998, p=0.560). For both (a) and (b) errorbars represent 1σ uncertainty in the temperature measurement and are only plotted for every twelfth measurement so that the scatter can be seen.*

We conducted a subsequent test using automatic power regulation that demonstrates that any average temperature change when using a constant voltage mode is a result of compensation by the power supply and is not intrinsic to our IRH-DAC design (experiment *#7b*, Fig. 2.9b). After a short stabilisation period of <2 minutes, during which the sample temperature fell by 20 K, the temperature was stationary. The average measured temperature over a period of 2.75 hours was 1909 ± 3.8 K, and the standard deviation (3.8 K) was < 0.2% of the temperature and smaller than the average analytical precision in the temperature measurements (5.54 ± 0.29 K). It is statistically likely that the measured temperature variation is simply a result of the analytical uncertainty on the temperature measurement as the scatter in the measured temperatures is Gaussian (Shapiro-Wilk (Shapiro & Wilk, 1965) test statistic = 0.998, p=0.560) and occurs as a stationary process with no trend (Augmented Dickey-Fuller (Dickey & Fuller, 1981; MacKinnon, 2010) test statistic = −4.024, p=0.001), although we note a slight instability in the power regulation (σ = 0.09 W), suggesting that the performance of our IRH-DAC could be increased even further by a more stable power supply. Temperature during IRH-DAC experiments using our design can therefore be controlled to an accuracy of < ± 10 K over the duration of long experiments lasting multiple hours. Although the stability test was stopped after nearly three hours, there was no indication that any significant temperature fluctuations would be observed during longer experiments.

2.3.1.3 Quench Rates

The sample was quenched at the end of experiment *#7b* by switching off the power supply. As the heated region is so small, this was likely to be almost instantaneous. The pressure chamber geometry remained stable, and the cell could be successfully reheated after quench. Potential applications of these rapid quench rates include the deep supercooling of molten materials to by-pass crystallisation for the synthesis of novel solid-state amorphous phases at high-pressure (Drewitt et al., 2020).

2.3.1.4 Temperature Gradients

Two-dimensional temperature maps of the IRH-DAC made using four-colour multi-spectral imaging radiometry illustrate the radial temperature gradients within the cell and sample chamber. The maximum measured temperature of the filament was typically ∼300 to 400 K hotter than the sample. However, as the sample chamber is so small (∼10 μm diameter) the gradients within the sample are minimal (less than 10 K/μm in the central region, but larger near the edges closest to the filament hotspots, Fig. 2.10). This is lower than the typical temperature gradients across a laser heating spot of a comparable size (Anzellini & Boccato, 2020), and as the entire sample is heated, there is no risk of analysing an unheated portion of the sample. The temperature gradients along the y-axis are steeper than along the x-axis due to the location of the hotspots. The radial temperature gradients

in our design appear to be slightly higher than the previous IRH design of Zha & Bassett (2003). Zha & Bassett reported a difference of 51 K between a temperature measured in the centre of the sample and at a point near the edge of the sample chamber, whereas the difference (in the same direction) measured in experiment *#5d* was ∼80 K (Fig. 2.10). This is because of the smaller heated region in our design. Nevertheless, the temperature variation across the whole analysed volume will determine the temperature uncertainty in scattering measurements. The standard deviation of temperature across the sample volume in our experiments was <35 K (Fig. 2.10). The radial temperature gradients could also be reduced by future refinement of the filament shape. The temperature gradients in the axial direction are not measured, but are likely to be lower than those in an equivalent laser-heating experiment. This is because heat is generated internally throughout the filament thickness, unlike a laser-heating experiment where the laser power is absorbed at the surface (Campbell et al., 2007). The average difference in measured temperature based on the radiation from the sample surface on either side of the cell was 31 K for runs performed at Diamond, although this rose to a maximum of 86 K in experiment *#6b*. This is due to differences in the thickness of insulation either side of the filament, and could be improved by laser milling form-fitting pieces of single crystal insulation to an exact and equal thickness. Reduced temperature gradients will also lead to reduced thermal pressure gradients, which in the laser-heated DAC can reach 1 GPa/μm (Yen et al., 2020).

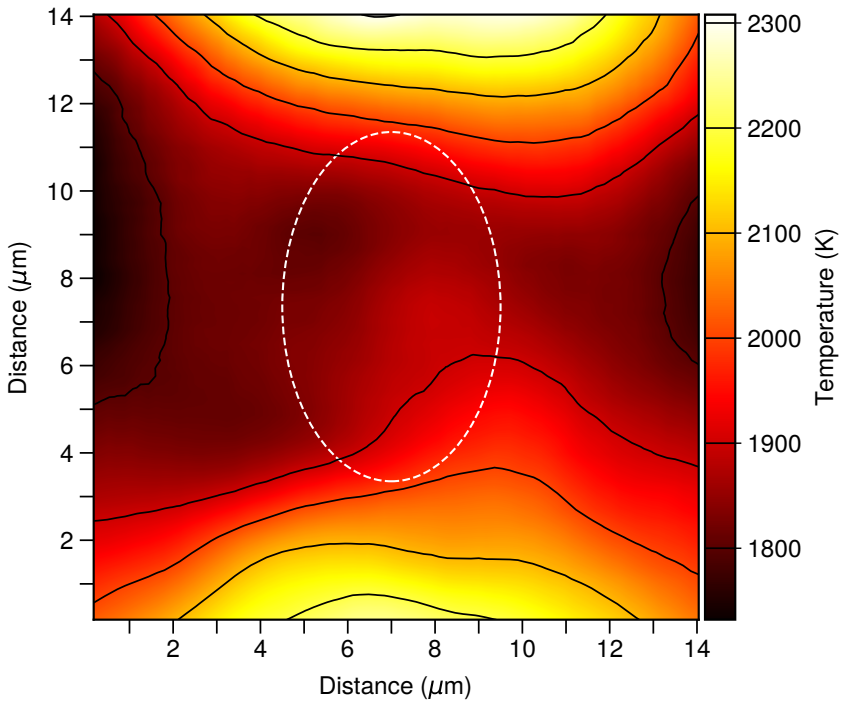

Figure 2.10: *2D temperature map of an IRH heating experiment (#5d) made using four-colour imaging radiometry. The pressure prior to heating was ∼43 GPa. The dashed white line shows the outline of the sample chamber, which had compressed and deformed during previous runs. The mean temperature inside the sample region was 1872 ± 34 K, though the absolute range of temperatures inside the sample chamber was 178 K. The filament hotspots either side of the sample chamber are typically 300 to 400 K hotter than the sample.*

2.3.2 X-Ray Diffraction

During nine heating experiments, we were able to obtain *in situ* XRD measurements across a large *P*-*T* range that would otherwise only be accessible with laser heating (Table 2.1, Fig. 2.11). This shows that our IRH-DAC is not only capable of performing long, stable heating experiments at lower mantle conditions, but is a useful tool for rapid acquisition of the high-resolution *P*-*V*-*T* datasets required for constraining the thermoelastic parameters of minerals in the deep Earth. One of the heated cells (*#6a/b*) was loaded with a glass with the stoichiometric composition $Ca(Si_{0.65},Ti_{0.35})O_3$, which should form a stable perovskite phase at P > 10 GPa and T > 1500 K (Kubo et al., 1997). Titanium bearing calcium perovskite is likely to be an important phase in the lower mantle, and its physical properties are relevant to the interpretation of inclusions found in 'super-deep' diamonds, the seismic structure of the deep Earth, and the freezing of magma oceans present during early Earth history (Thomson et al., 2016b, 2019; Braithwaite & Stixrude, 2019). Figure 2.12 shows a contoured waterfall plot of patterns collected during experiment *#6a* and *#6b*. Corundum peaks can be seen to appear during initial heating as the alumina nano-powder recrystallises. Sample peaks appear from 1450 K as the $Ca(Si_{0.65},Ti_{0.35})O_3$ glass begins to crystallise, and remain present in all further diffraction patterns. The sample peaks can be explained by an orthorhombic unit cell with space group *Pbnm* as expected for this composition. However, refinement of the unit cell yielded lattice parameters a = 4.57(1), b = 4.32(1), c = 6.56(1) at 12.2 GPa (run *#6a*) and a = 4.51(1), b = 4.27(1), c = 6.47(1) at 26.8 GPa (run *#6b*) after quenching to room temperature, which gives volumes that are much lower than expected at these pressures (Kubo et al., 1997; Thomson et al., 2019). This is probably due to a reaction with the alumina pressure medium. The effect of thermal pressure during the experiments is apparent as peaks shift towards higher 2θ angles during heating (Fig. 2.12).

2.3.2.1 Thermal Pressure and Nonhydrostaticity

An increase in pressure during heating is inevitable in a volumetrically constrained sample chamber. As a result, pressure should be monitored during experiments. We found a near-linear pressure dependency on temperature, with a typical increase of 0.5 to 1 GPa/100 K. Total thermal pressure during experiments was 50–100 % of the pressure measured after heating. IRH experiments differ from laser heating experiments in that the sample is heated from the outside, rather than from within. The thermal expansion of the filament surrounding the sample compresses the sample as the experiment is heated. This is consistent with our observation of a linear reduction in unit cell volume as a function of temperature (see appendix A). Some changes in pressure will also result from the thermal relaxation of the IRH assembly. Pressures measured after heating were higher than those measured prior to heating (Table 2.1, Fig. 2.13).

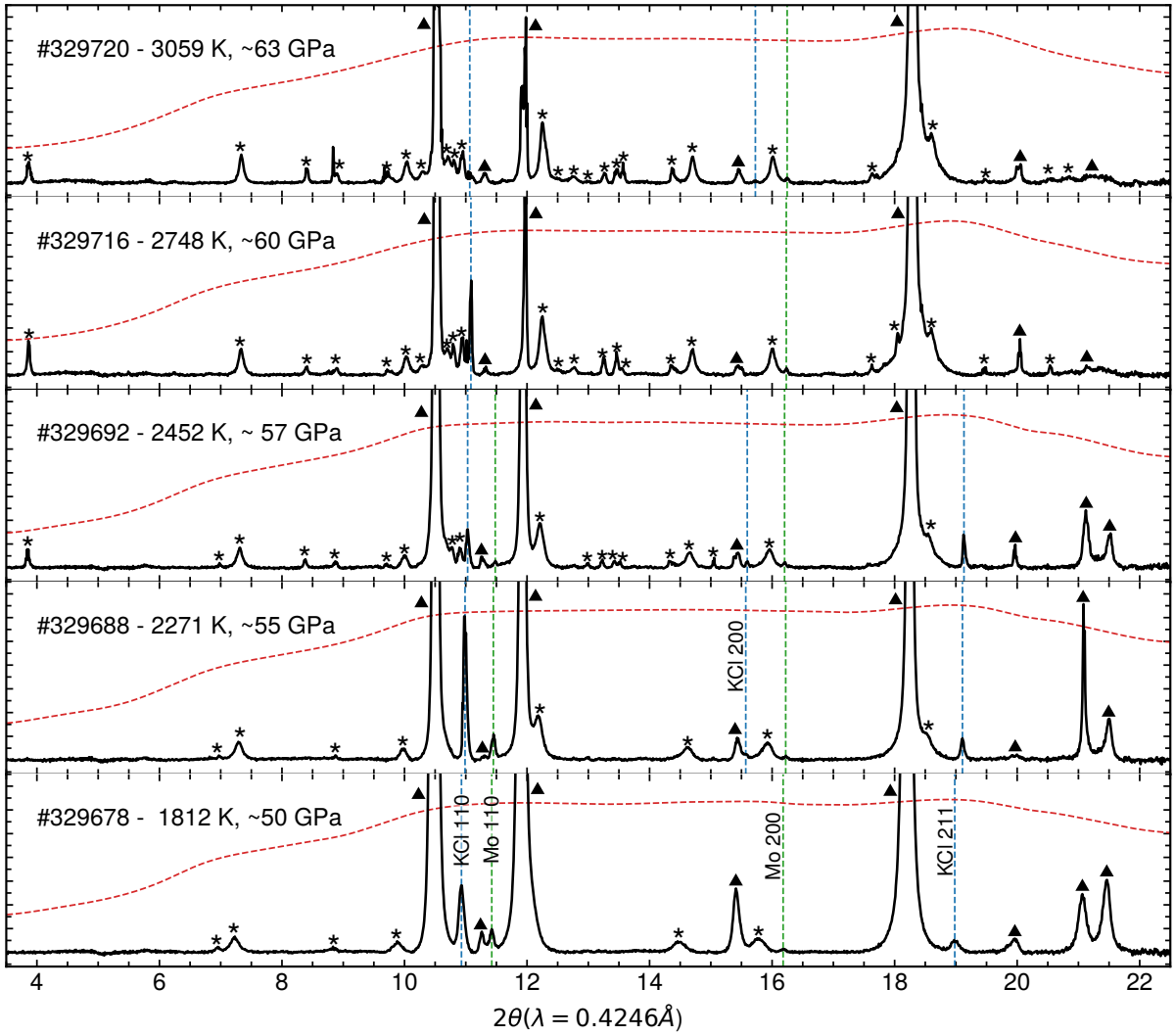

Figure 2.11: *Representative 1D background-subtracted XRD spectra from experiment #5c. The subtracted backgrounds are shown by the dashed lines (red). Vertical dashed lines show refined peak centres of pseudo-voigt fits to KCl (blue) and Mo (green) peaks. Peaks attributed to Al_2O_3 are denoted by asterisks (*), and rhenium by triangles (▲). The signal-to-noise ratio of sample peaks was reduced at higher temperatures due to grain growth which resulted in 'spottier' diffraction patterns.*

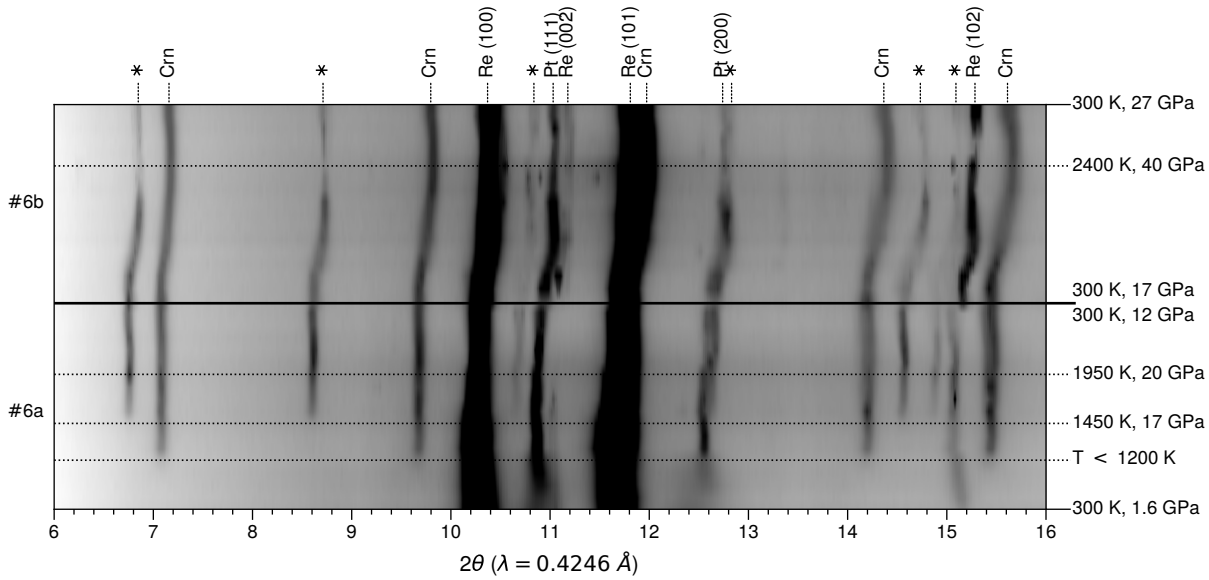

Figure 2.12: *Contoured waterfall plot of 1D x-ray diffraction patterns collected during experiment #6a and #6b. Peaks attributed to Pt, Re, Corundum (Crd), and the sample (*) are indicated, as are P-T conditions of selected patterns throughout the experiments.*

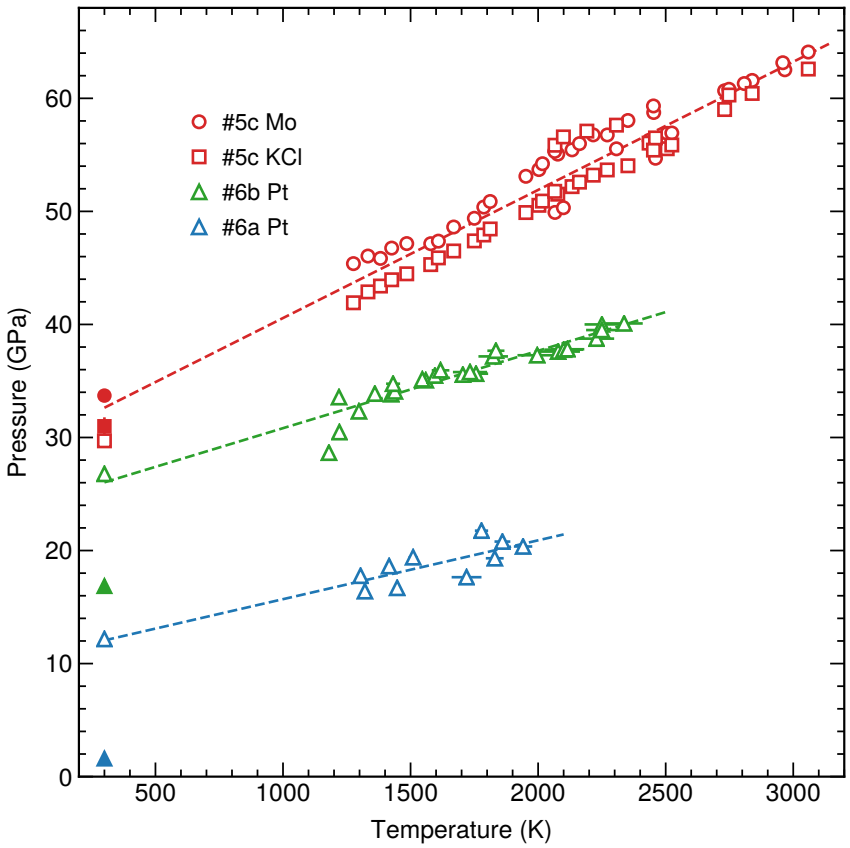

Figure 2.13: *Plots of the dependency of pressure on temperature in our IRH-DAC for experiments #5c, 6b & 6a. Closed symbols show pressures measured prior to heating. Dashed lines show linear fits to the data.*

Pressures in the DAC commonly deviate from hydrostatic, as uniaxial compression can increase the differential stress, t, between the axial and radial directions. Soft or fluid pressure transmitting media are commonly used to reduce differential stress in DAC experiments (Klotz et al., 2009); however, the IRH-DAC design relies on a very incompressible pressure medium to keep the cell geometry stable. As non-hydrostatic stress affects each (hkl) reflection to a varying degree, the axial stress condition, t, can be estimated from a 'gamma plot' — a plot of the measured lattice parameters for a given reflection, $a_m(hkl)$, against $3\left(1-3\sin^2\theta\right)\Gamma(hkl)$, where θ is the diffraction angle and $\Gamma(hkl) = (h^2k^2+k^2l^2+l^2h^2)/(h^2+k^2+l^2)^2$ (Singh & Kenichi, 2001). The St value is derived from the intercept (M_0) and slope (M_1) of the gamma plot: $St = -3M_1/M_0$, where S is the single crystal elastic compliance: $S = (S_{11} - S_{12} - S_{44}/2)$. As only two or three reflections from each pressure calibrant were present in the diffraction patterns (Fig. 2.11), gamma plots were only made when the (200) reflection was present, which is most sensitive to deviatoric stress for cubic materials with a positive elastic anisotropy parameter S (such as Pt) in DAC experiments (Takemura & Dewaele, 2008; Dorfman et al., 2012). The elastic anisotropy of Pt and Mo under pressure was calculated from data available in the literature (Menéndez-Proupin & Singh, 2007; Zeng et al., 2010), and t calculated for experiments before and after heating (Table 2.2). As S of B2 KCl under pressure, and S of Pt and Mo at high temperature are not available, the St value was used as a stress indicator for all other experiments and during heating runs. The measured t of Pt in experiments *#6a* and *#6b* was less than 1.5 GPa after heating (Table 2.2), which is comparable to cold compression in a Neon pressure medium (t = 1 to 4 GPa in Dorfman et al., 2012), and only slightly elevated compared to laser annealed samples in NaCl (t < 1 GPa in Dorfman et al., 2010). The axial stress is noticeably lower after heating due to thermal annealing and relaxation in the pressure chamber. A reversible component to the change in axial stress was also observed during heating (Fig. 2.14). St was observed to decrease with temperature, and in many runs became negative. Negative axial stress (where the radial stress component, σ_3, is larger than the axial stress component, σ_1) has been observed in diamond anvil cell experiments with highly compressible pressure media and is attributed to the radial collapse of the sample chamber (Takemura & Dewaele, 2008). In our experiments, it is likely that the additional hard components (i.e., the filament) within the pressure chamber impose radial pressure on the sample as they thermally expand during heating. This appears to have the affect of counteracting some of the axial stress caused by the uniaxial compression of the DAC and likely results in lower axial stress than laser heating experiments performed with a similarly hard pressure medium.

For experiments loaded with two calibrants, we observed a systematic offset between the pressures measured from the volume of Mo and from the volume of KCl. The offset was present down to room temperature, so is not only a thermal effect, and was noticeable in post-heating pressures with low measured t, so is unlikely to be a result of deviatoric stress in the sample chamber. Although the estimated uncertainty on our pressure measurements using Mo and KCl calibrants do not overlap, the true uncertainty is likely to be much larger as studies reporting equations of state typically do not

publish the full covariance matrix required to propagate the uncertainty in fitted parameters which arises from scatter in the *P-V-T* dataset. There are several sources that can introduce uncertainty or systematic errors to an equation of state, including its analytical form, the choice of pressure scale, and most importantly, measurement uncertainty in the *P-V-T* dataset, with temperature being the largest contributor. Temperature uncertainty is important even in studies of processes that are relatively insensitive to temperature (e.g., mapping phase boundaries with very low Clapeyron slopes) because the error in pressure is largely dependent on the error in temperature due to its much higher relative uncertainty compared to the uncertainty in the volumetric measurement of the pressure calibrant. New techniques, such as our IRH-DAC design, that can reduce the temperature uncertainty in high pressure experiments are therefore key to improving our understanding of the physical and chemical characteristics of the deep Earth.

Table 2.2: *Axial stress (t) and pressure (P) before and after heating.*[†]

Run	Calibrant	Pre-heating		Post-heating	
		P (GPa)	t (GPa)	P (GPa)	t (GPa)
#5a	Mo	17.02(7)	3.24(0)	17.66(30)	−2.72(3)
#5b	Mo	16.60(19)	−4.12(3)	25.86(39)	···
#5c	Mo	33.71(18)	−1.35(1)	29.70(52)	···
#6a	Pt	1.61(8)	6.83(1)	12.17(6)	1.42(0)
#6b	Pt	16.86(6)	−1.24(0)	26.78(7)	−0.72(0)
			St		St
#3a	KCl	3.55(6)	−0.0008	···	···
#4a	KCl	4.09(1)	0.0052	4.07(1)	0.0007
#4b	KCl	5.12(2)	0.0381	···	···

[†]Uncertainties in parentheses are on the last digit and are 1σ

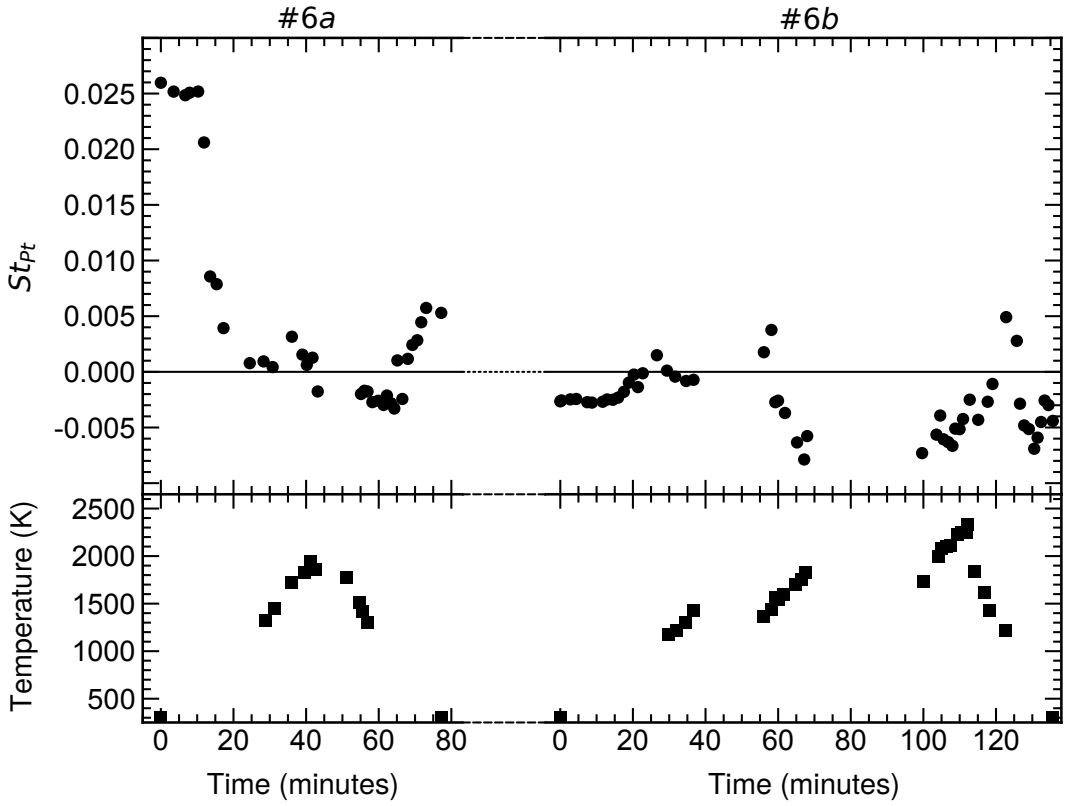

Figure 2.14: *Stress indicator values, St, of Pt derived from gamma plots for experiment #6a and #6b along with measured temperature plotted as a function of experiment duration. Data from other experiments can be found in appendix A.*

2.3.3 Potential Improvements

Our 'split gasket' approach provides a simple design framework for performing IRH experiments. In the present study, we have demonstrated its efficacy with a 150 μm 'bow-tie' Re filament, a ∼10 μm diameter sample chamber, an Al_2O_3 nano-powder pressure medium/thermal insulation, and 500 μm culet diameter anvils to *P-T* conditions of ∼3000 K and ∼60 GPa. However, as the filament material/shape and insulation material/geometry are not the limiting features of the design, our IRH technique could be improved by refinement of these components. The use of different filament materials may improve heater performance, and alternative materials for thermal insulation may improve temperature homogeneity and/or stability. Finite element modelling could help quantify the thermal gradients along the compression axis and inform refinement of the filament shape to reduce both axial and radial temperature gradients, although it should be noted that there are mechanical and geometric constraints on the filament shape (Fig. 2.15). Although high quality machining results were achieved with the nano-second range laser used to fabricate the IRH filaments, the use of a shorter pulse laser (e.g., pico- or femto-second laser micromachining) may improve axial thermal gradients by reducing the heat-affected zone around the drilled sample chamber on the machined surface, and reducing the slight conical shape to the sample chamber walls (Fig. 2.16. The deformation of the sample chamber at high pressure that results in an elongated shape parallel to the gasket slots can be reduced by drilling overlapping holes to form an oval shaped sample chamber that becomes circular at high pressure (Fig. 2.17). The sample chamber loading procedure can also be optimised for the specific experiment, either loading the pressure calibrant in the centre of a soft sample/pressure medium to minimise axial stress as performed in this study, or at the edges of the sample chamber to maximise the scattering signal from the sample when irradiating the central portion of the sample chamber (Fig. 2.18). Thermal gradients and heating efficiency are strongly controlled by the insulation geometry. More advanced micro-fabrication techniques such as femtosecond laser micromachining (Gattass & Mazur, 2008; Pfeifenberger et al., 2017) or xenon plasma focused ion beam milling (Xe^+-FIB; Smith et al., 2019) will allow fabrication of form-fitting single crystal insulation, reducing axial gradients by ensuring equal insulation thickness on either side of the filament. Form-fitting pieces of insulation with a milled depression to hold the filament could also improve the efficiency of the loading procedure, potentially allowing the sample, filament, and insulation components to be assembled outside the cell and loaded into the pressure chamber as a single piece. Discs of a material unreactive with the sample could be incorporated into the design above and below the filament to chemically isolate the sample from the insulation material if necessary. Precisely milled annuli placed above and below the central portion of the filament would also allow for gas loading of a fluid pressure medium around the sample chamber itself.

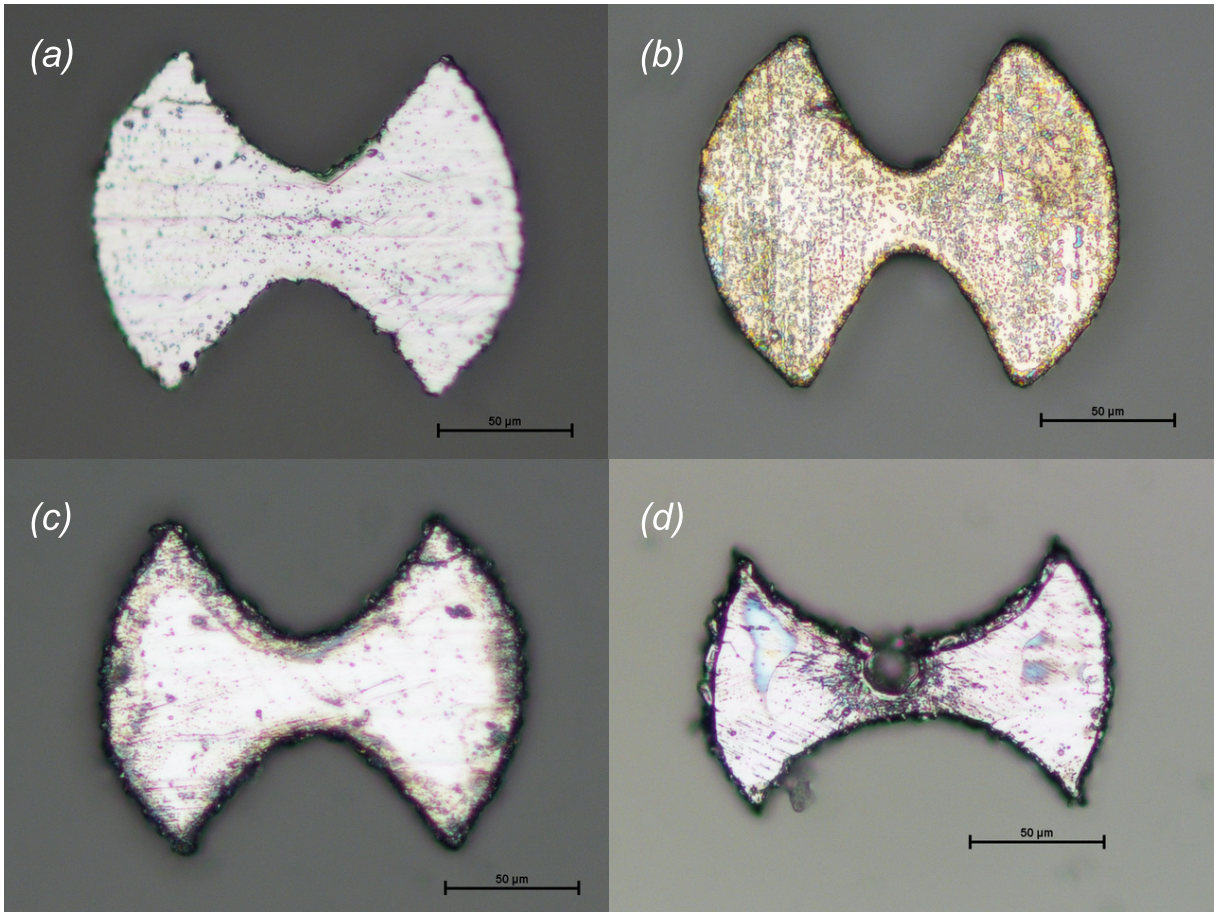

Figure 2.15: *Photomicrographs of selected IRH filament shapes that were tested. (a) A wide (in the y-direction) central portion does not provide enough resistance contrast for efficient temperature generation around the sample chamber. (b) A large contrast between the width (in the y-direction) at the filament edges and centre results in significant deformation as the cell is compressed, with shearing of the filament and/or extrusion into the slots more commonplace. (c) Reducing the width (in the y-direction) of the curve sector at the filament edges helps stabilise the geometry but the resistance contrast must still be considered to promote efficient heating and prevent high temperature gradients in the x-direction. (d) A design with more moderate curves is easier to machine accurately, is more geometrically stable under compression, allows for poorer accuracy in loading orientation, and has lesser thermal gradients. The curve is still necessary to create a good contact between the gasket and filament, and to localise heating to the centre surrounding the sample chamber. However, greater precision in the drilling of the sample chamber is required to prevent chamber blowouts as seen here.*

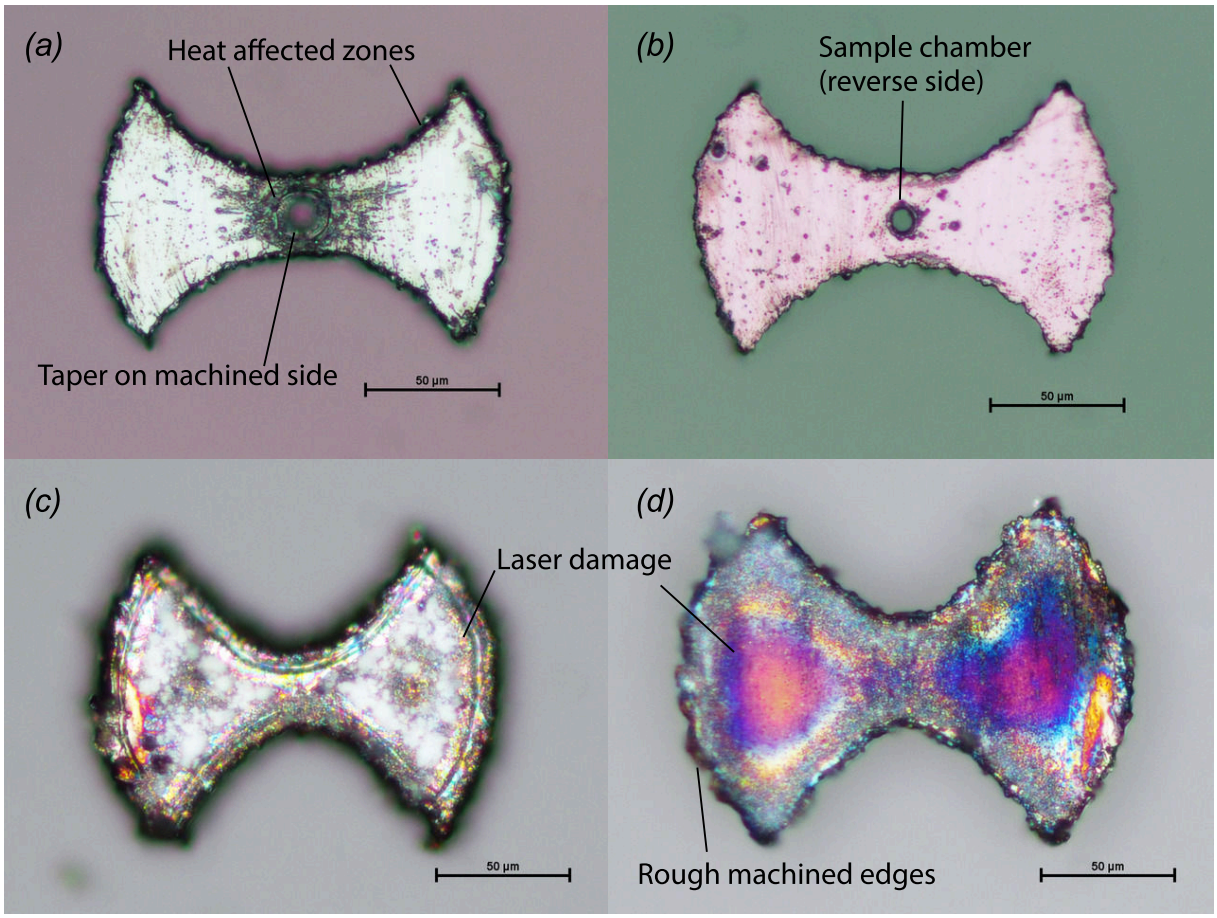

Figure 2.16: *Photomicrogaphs of an IRH filament on the machined side (a) and reverse side (b). The entry side of the percussion drilled sample chamber is somewhat funnel shaped and there is a slight ring of a heat-affected zone a few microns wide. The exit hole is much cleaner. A heat affected zone with some oxidation is also apparent around the machined edges of the filament. Material on the filament faces is mostly surface dirt that was already on the metal foil prior to machining (and is difficult to clean off). Examples of surface laser-damage from poorly optimised process parameters can be seen in (c) and (d). High surface roughness on the machined edges (e.g., d) also worsens the filament-gasket contact. The optimised process parameters provide improved results.*

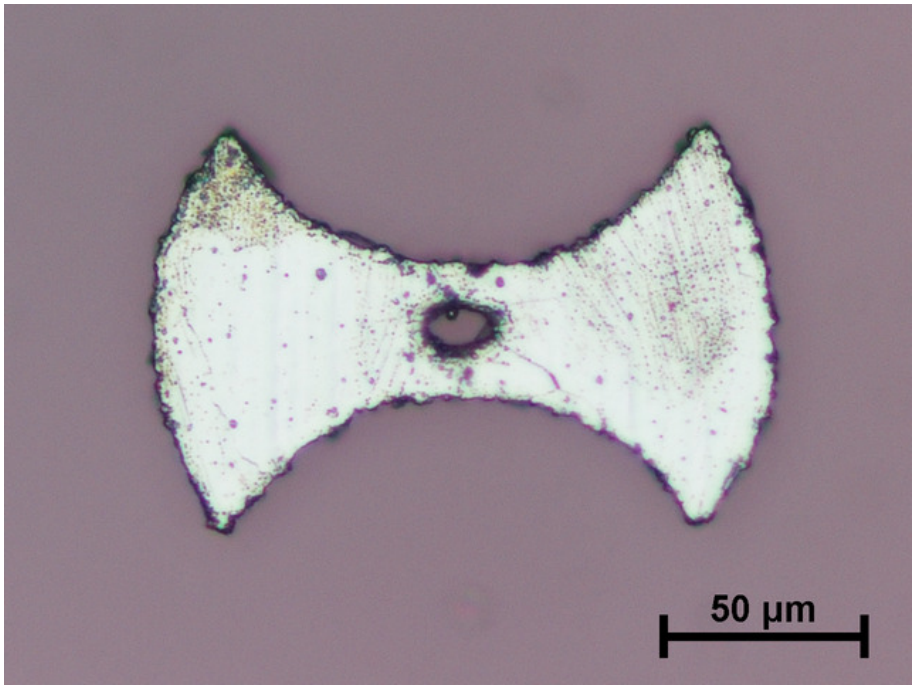

Figure 2.17: *Photomicrograph of a rhenium IRH filament drilled with three overlapping holes to create an oval sample chamber. This allows the sample chamber to take a more circular shape as it deforms at high pressure.*

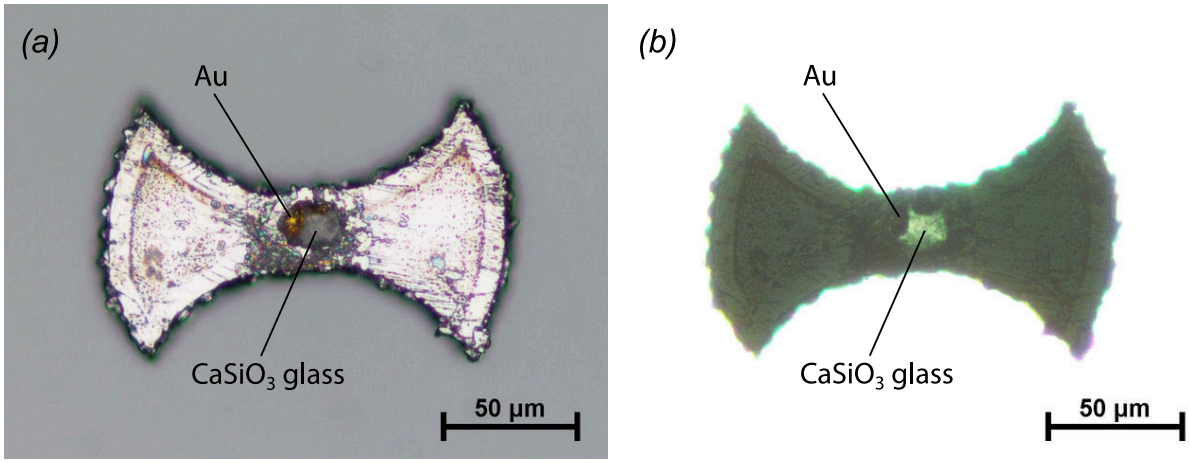

Figure 2.18: *Photomicrographs in reflected (a) and transmitted (b) light of a rhenium IRH filament loaded with Au and $CaSiO_3$ glass. The position of material within the sample chamber can be controlled somewhat, even at this small scale. The small pieces of Au (the pressure marker) are placed at the edge of the sample chamber (though still wholly within it) to allow for a cleaner sample signal in the centre of the chamber.*

To test such potential improvements to the design we fabricated form-fitting pieces of alumina insulation. While we found accurate part shapes could be cut from single-crystal ceramics using our laser micromachining system, we could not obtain single-crystal ceramic plates of the right thickness. We were also unable to fabricate plates of the right thickness ($\sim$25 μm for the insulation either side of the filament) using mechanical polishing or laser-milling techniques. We therefore used plates of polycrystalline alumina to fabricate the components. Form-fitting blocks that precisely fit into the culet slots were cut from $\sim$75 μm thick polished polycrystalline alumina plate (Fig. 2.19. The use of such blocks greatly simplifies the loading procedure, but does affect the deformation characteristics of the culet geometry under compression. We found the blocks should be machined smaller than the slots to allow for deformation in the culet region to be taken up by the slots narrowing rather than deformation of the filament. Polycrystalline alumina annuli (doughnut shaped pieces) were also fabricated by laser-milling $\sim$50 μm thick alumina plate to a thickness of $\sim$20 μm, before cutting out an inner hole $\sim$135 μm in diameter and an outer ring the same diameter as the central pressure chamber. We found we were unable to mill a recess the same shape as the filament into the alumina doughnuts, although simpler shaped recesses could be milled. As a result we loaded the filament between the flat surfaces of the alumina doughnuts, with KCl loaded into both central holes to fully isolate the sample from the insulation material. We found that use of this design significantly impeded the mechanical stability of the culet geometry, and prevented efficient heating. An x-radiograph of such an experiment shows that under compression the filament conforms to the milled topography of the insulation (even though the filament was loaded between the polished surfaces), resulting in uneven thickness (Fig. 2.21). Furthermore, the combination of increased strain on the filament when bracing the slots open with form-fitting insulation and the use of soft insulation above and below the pressure chamber resulted in thickening around the sample chamber and extrusion of the filament into the central holes in the insulation (Fig. 2.21). This behaviour prevented efficient heating. To solve these issues, it is likely that a shorter pulse laser is required, either to mill a filament-shaped recess or to reduce the surface topography enough to prevent such deformation.

The pressures reached in this study (up to $\sim$63 GPa) were limited by the relatively large culet diameter of the diamonds used (500 μm in the highest pressure run), which is itself limited by the size of the heating filament and diameter of the pressure chamber (150 μm). It is likely that smaller anvils down to $\sim$300 μm in diameter could be used with little or no adaption of the heating filament to extend the pressure range to $\sim$80 GPa (O'Bannon III et al., 2018). Extending the pressure range further is conceivable but would require further miniaturisation of the filament and sample assembly. In this study, we used spectroradiometric temperature measurement in the visible range, which limited the minimum measurable temperature to $\sim$1200 K. The use of an InGaAs detector sensitive to near-IR radiation would extend the temperature measurement range down to 500 K (Shen et al., 2010). The full isolation of the heating filament enabled by our novel 'split-gasket' approach significantly extends the *P-T* range accessible to IRH techniques and improves temperature stability. However, because the shorter filament must also be narrower to compensate for the reduction in

resistance, the sample chamber in our design is smaller in diameter compared to previous IRH designs (Zha & Bassett, 2003; Zha et al., 2008). The small diameter of the sample chamber (∼10 µm) in our design presents the possible issue of unwanted scattering by the filament material adversely affecting diffraction data. The diameter of the sample chamber could be increased by using a correspondingly thinner filament in future studies. Nevertheless, we were able to obtain usable XRD data using an uncollimated micro-focused x-ray beam (6×4 μm^2 full width at half maximum) in this study. Our IRH technique is ideally placed to exploit the outstanding coherence properties and sub-micron focusing of x-ray beams at fourth-generation synchrotron sources being developed now, increasing data quality and the range of techniques with which it can be interfaced (Pacchioni, 2019; Khubbutdinov et al., 2019).

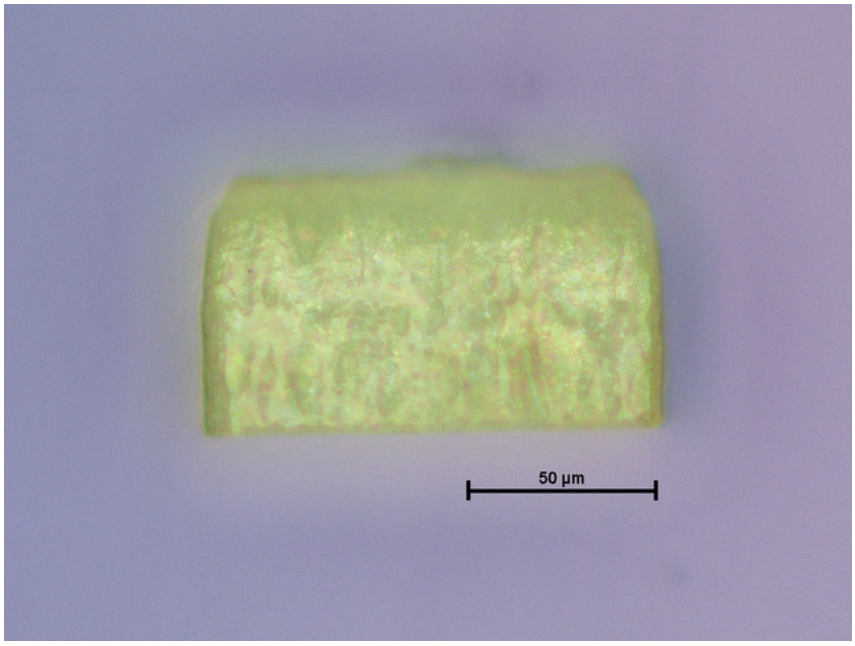

Figure 2.19: *Photomicrograph of laser-fabricated single-piece polycrystalline alumina blocks for the culet slots in the IRH design. The block shown here is the design for 400 µm culets, 120 × 65 × 75 µm. For the 500 µm culet design the blocks are 170 µm long. The block shown here is at a slight angle, allowing the flat top surface and slight rough topography on the cut side surface to be seen.*

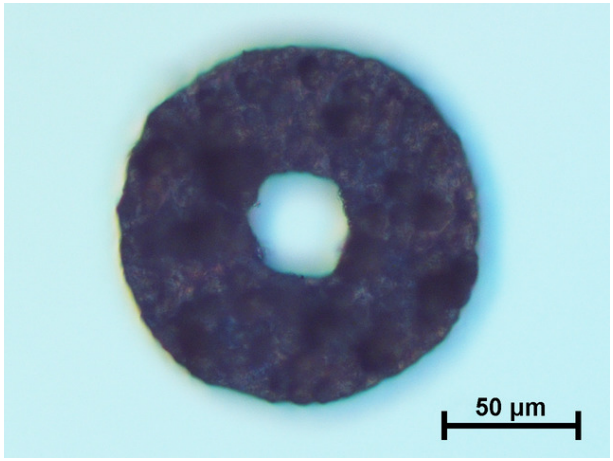

Figure 2.20: *Photomicrograph of a doughnut shaped insulation piece for the IRH design, milled from polycrystalline alumina. The outer diameter is ∼135 µm and the inner diameter ∼30 µm, designed to fit precisely into the ∼150 µm pressure chamber, with the central hole over the ∼15 µm sample chamber. The central hole is loaded with a salt (KCl or NaCl) that completely isolates the sample from the alumina insulation. The pieces are made from ∼50 µm thick polished polycrystalline alumina plate that is laser-milled to a thickness of ∼25 µm before cutting out the pieces. The milled topography can be seen in the photograph, the reverse side is smooth.*

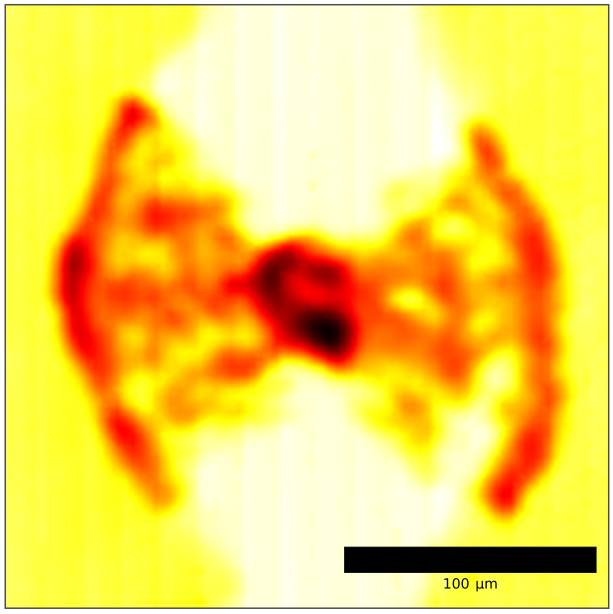

Figure 2.21: *Synchrotron x-radiograph of an IRH experiment loaded with polycrystalline alumina annuli (doughnuts; as in Fig. 2.20) above and below the filament, with KCl discs directly above and below the sample chamber. Under compression the filament conforms to the milled topography of the insulation, resulting in uneven thickness. This can be seen from the patchy appearance of the radiograph. Additionally, the softer material (KCl) in the centre hole of the insulation allows the filament to 'bunch-up' in this region. The filament is also thicker at the edge where it extends slightly beyond the insulation pieces. Data for this figure was collected at beamline I15 of Diamond Light Source, UK (proposal no. CY28995).*

2.4 Conclusions

Our new IRH-DAC design significantly extends the *P-T* range accessible to resistive heating techniques, easily encompassing the mantle geotherm to 1500 km depth. The temperature range of our IRH design is also sufficient to recreate the conditions of a hotter Archean mantle (Herzberg et al., 2010). While recent advances have been made in MAP techniques, our IRH-DAC design provides a much more accessible alternative for performing resistive heating experiments at lower mantle conditions. The 'split-gasket' approach adopted in our IRH design provides several benefits over existing IRH techniques applicable to non-metallic samples (Zha & Bassett, 2003; Zha et al., 2008): the experimental design is much simpler, and the geometry allows for the heating filament to be completely isolated within the insulated pressure chamber. These features enable more reproducible, efficient, and routine generation of high *P-T* conditions beyond the limits of other IRH designs. Our IRH-DAC technique is cost effective and time efficient. Fabrication of the filament and gasket geometry requires a precise laser mill, and a programmable DC power supply is needed for heating, but no other specialist equipment is required and the materials used are commonly available and relatively cheap. Experiments take under two days to prepare, with most of that time required for the epoxy glue to cure, and a single cell can be reheated at several different pressures for efficient data collection over a large *P-T* range. We also found the experiment failure rate of our IRH design to be remarkably low (with no diamonds broken during the runs performed at Diamond Light Source) in comparison to experiments pushing the limits of MAP techniques, where 'blow-outs' of the expensive WC or sintered diamond cubes are common (Ishii et al., 2019). Our IRH-DAC design provides an important new tool for investigating materials at extreme conditions. The excellent temperature stability during experiments lasting many hours, reduced thermal gradients, elimination of the requirement for a metallic absorber to be mixed with the sample, and precise temperature control are significant improvements over laser heating techniques in this *P-T* range. These advantages make our IRH-DAC design well suited for studies requiring stable homogeneous heating, including the collection of high-resolution, accurate *P-V-T* data, the precise demarcation of phase boundaries, making liquid state measurements of wholly molten samples, and heating experiments over the long acquisition times required for techniques such as Brillouin spectroscopy and IXS. Our IRH-DAC technique is ideally placed to exploit the highly coherent nano-focused x-ray beams in development at current and next-generation synchrotron sources.

Chapter 3

LiquidDiffract: Software for Liquid Total Scattering Analysis

Author contributions and declaration: This chapter has been accepted for publication in Physics and Chemistry of Minerals: Heinen, B. J. & Drewitt, J. W. E. (2022). LiquidDiffract: Software for Liquid Total Scattering Analysis. *Physics and Chemistry of Minerals*, (accepted). Benedict Heinen designed and wrote the software, *LiquidDiffract*, which is available from a public github repository (`https://github.com/bjheinen/LiquidDiffract`), with releases distributed via PyPI (`https://pypi.org/project/LiquidDiffract/`). LiquidDiffract v1.1.8 can be directly accessed at `https://doi.org/10.5281/zenodo.5796187`. James Drewitt provided guidance on best practices for total scattering data analysis and user-tested the software. Data used in the examples (Figures 3.3 and 3.4) were background corrected by James Drewitt. Data analyses were performed by Benedict Heinen. The data of liquid gallium at ambient conditions used to generate Figure 3.3 was previously published in Physical Review Letters: Drewitt, J. W. E., Turci, F., **Heinen, B. J.**, Macleod, S. G., Qin, F., Kleppe, A. K., & Lord, O. T. (2020). Structural ordering in liquid gallium under extreme conditions. *Physical Review Letters*, **124**(14). Louis Hennet (CEMHTI, Orléans) and Daniel Neuville (IPGP, Paris) provided assistance to James Drewitt in collecting the synchrotron x-ray diffraction measurements of liquid $MgSiO_3$ and $CaSiO_3$ glass (ESRF proposal No. HD517) used to generate Fig. 3.4. Benedict Heinen wrote the initial draft of the manuscript and James Drewitt provided feedback. The careful comments of two anonymous reviewers helped improve and clarify the manuscript during the publication process.

Abstract

LiquidDiffract is an open source, Python-based graphical application for x-ray total scattering analysis of liquids and disordered solids. The software implements procedures to obtain information on macroscopic bulk properties and local atomic-scale structure of monatomic or polyatomic samples from x-ray total scattering data. LiquidDiffract provides an easy to use interface with tools to perform background subtraction; calculation, normalisation, and refinement of the reciprocal-space structure factor and real-space correlation functions; and the extraction of structural information such as bond lengths, coordination number, and bulk density. The software is well suited to investigations of amorphous materials at extreme conditions, such as studies of high-pressure melt structure, polyamorphic phase transitions, and liquid equations of state. The open-source distribution and graphical interface will be of particular benefit to researchers who are new to the field. In this chapter we describe the distribution, system requirements, and installation of LiquidDiffract, and detail the data processing workflow and underlying numerical methods.

3.1 Introduction

Despite a lack of long-range order, the structure of liquids and glasses exhibit a high-degree of ordering on short- to medium-range length scales, originating from chemical interactions that lead to arrangements of local structural motifs (Kitaigorodskiy & Chomet, 1967). The study of liquid and glass structure provides insight into the behaviour and physical properties of amorphous materials that is important in many fields of research. At extreme conditions of high temperature (T) and pressure (p) an understanding of liquid structure and polyamorphic (liquid–liquid) phase transitions has important industrial applications, including novel phase discovery, and modelling of industrial melt processes (Drewitt, 2021). Fluids and melts are also key to our understanding of the dynamic Earth, occurring from the crust to the core and controlling mass transfer in the deep interior, and geothermal, volcanic, and ore-forming processes at the near surface.

For liquids and disordered solids, X-ray diffraction provides direct information on the average atomistic structure. The total intensity of scattered radiation arises from coherent, incoherent (Compton), and self-scattering effects. These components can be separated out, and the structure factor, $S(Q)$, extracted following a normalisation procedure. The structure factor is a measure of the coherent scattering by atoms found at different positions in the sample, and hence contains the useful structural information about the material. $S(Q)$ is a reciprocal-space function, where Q is the scattering vector, usually measured in Å^{-1}, which is related to the wavelength of the incident radiation, λ, and the scattering angle, 2θ, by:

$$Q = \frac{4\pi \sin\theta}{\lambda}. \tag{3.1}$$

It is generally more useful to interpret the structure of disordered materials by considering correlation functions in real-space, the primary example being the pair distribution function, $g(r)$, which describes variations in the microscopic pair density of a sample with distance, $\rho(r)$, proportional to the average (bulk) number density (ρ_0):

$$g(r) = \frac{\rho(r)}{\rho_0}. \tag{3.2}$$

These variations arise when correlations between pairs of atoms are more likely to occur at a specific separation distance r. Peaks in the $g(r)$ are therefore centered around the average bond lengths

of coordination shells, and the $g(r)$ approaches 1 at high r as variations from the bulk density become negligible. The pair distribution function is related to the structure factor via a sine Fourier transform:

$$g(r) = 1 + \frac{1}{2\pi^2 r \rho_0} \int_0^\infty Q\,[i(Q)] \sin(Qr) dQ, \tag{3.3}$$

where the interference function, $i(Q)$, is a simple transformation of the structure factor such that $\lim_{Q\to\infty} i(Q) = 0$ (Equation 3.20).

LiquidDiffract is a data analysis application that computes these functions from x-ray diffraction data, and provides a range of tools to extract structural information in an easy to use, graphical interface. It can be used to obtain information on macroscopic bulk properties and local atomic-scale structure of monatomic or polyatomic samples from x-ray total scattering data.

While there is a wealth of tools available to analyse liquid structures obtained from simulations (e.g., ISAACS, Le Roux & Petkov, 2010; MDAnalysis, Michaud-Agrawal et al., 2011; STRFACT, Bernardes, 2021; Correlation, Rodríguez et al., 2021; POLYANA, Dimitroulis et al., 2015; GROMACS, Van Der Spoel et al., 2005), there is not a wide range of software available for total x-ray scattering analysis. Some of the tools available as part of XPDFSuite (e.g., PDFXgetX3; Juhás et al., 2013) may provide similar functionality to LiquidDiffract, however this is non-free software. XPDFSuite is also optimised for disordered crystalline materials, and does not implement correct normalisation of the $S(Q)/g(r)$ for liquids or amorphous solids. The software RAD and RAD-2 (Petkov, 1989) may similarly provide some overlapping functionality, but is also non-free and appears obsolete, with binaries only available for the Windows 7 operating system. The software GudrunX (Soper, 2017) provides routines for data reduction from 2D diffraction images, complex background refinement, and calculation of PDF functions, but is also distributed under a non-free license. It does not implement methods for extracting density or methods of optimising the $S(Q)$ normalisation that are suitable for high-pressure experimental data. GudrunX is also not particularly accessible, as binaries are only available for Windows operating systems, and the code is difficult to install on other platforms. Briggs et al. (2019) and Yu et al. (2019) cite the use of the program Glassure in their data analysis. Glassure (Prescher, 2017) is *libre*, fairly simple to install (it is also python-based) and can be used to calculate and properly normalise the $S(Q)$ and $g(r)$ from diffraction data. However, some features, such as density refinement, are not fully functional in the latest available version. Unlike LiquidDiffract, Glassure also does not implement methods to investigate the radial distribution function, $RDF(r)$, or extract estimates of coordination number and bond-length.

There is a clear need for software such as LiquidDiffract, which provides an open-source and *libre* tool for x-ray total scattering analysis of liquids and disordered solids. The procedures implemented to extract bulk liquid number density will be of particular benefit to researchers performing experiments at extreme conditions, as the equations of state of many liquids and glasses at high-p are poorly known (Drewitt, 2021). The efficacy of LiquidDiffract to produce accurate structure factors and equation of state data of liquids under extreme conditions has been successfully demonstrated in published studies of liquid gallium to 25 GPa (Drewitt et al., 2020), and liquid tantalum shock-released from several hundred GPa (Katagiri et al., 2021). We hope that the accessible distribution and simple graphical interface of LiquidDiffract will be of particular benefit to researchers who are new to the field.

3.2 Distribution, Licence, Installation, and Dependencies

LiquidDiffract is a pure-Python application, ensuring that installation requires no compiling by the user, and that the software is platform-independent. A Python version ≥ 3.5 is required. LiquidDiffract makes use of the open source scientific Python ecosystem for data processing and numerical operations, including the SciPy (Virtanen et al., 2020) and NumPy (Harris et al., 2020) libraries. 'lmfit', an extension package to the curve-fitting functionality in SciPy, is used for curve-fitting procedures as it provides a higher-level interface to minimisation routines that promotes easier extensibility, either in future versions of LiquidDiffract, or user defined code that makes use of LiquidDiffract's core functionality (Newville et al., 2014). The graphical user interface (GUI) is written using the PyQt5 library (`https://www.riverbankcomputing.com/software/pyqt/`), which provides Python bindings for version 5 of the Qt C++ cross-platform application framework. The PyQtGraph library (`http://www.pyqtgraph.org/`) is used to display and plot data. PyQtGraph is a pure-python graphics library built on PyQt that is intended for scientific use cases, and achieves fast updating of displays due to its heavy leverage of NumPy arrays and Qt's GraphicsView framework. PyQtGraph was chosen for this speed performance, as well as for the in-built collection of tools to provide intuitive interaction controls to the user. In addition, the importlib_resources package (a backport of the Python 3.9 standard library module importlib.resources) is required for Python versions < 3.7).

LiquidDiffract is freely available and distributed under the GNU General Public License v3.0 (GPLv3). The source-code is hosted on a public GitHub repository located at `https://github.com/bjheinen/LiquidDiffract`, and the package is primarily distributed via The Python Package Index, PyPI (`https://pypi.org/project/LiquidDiffract/`). Python's standard package installer, pip, automatically tracks the PyPI so this allows users to install LiquidDiffract from any computer with a Python installation and an internet connection with the command:

```
$ pip install LiquidDiffract.
```

Alternatively, pip can also be used to install LiquidDiffract from the source code downloaded to a local directory. All of the dependencies are automatically handled and installed by pip when installing LiquidDiffract.

3.3 Application Description and Workflow

The user interface of LiquidDiffract is designed around the normal steps and procedures in an experimental data processing pipeline to enable an efficient workflow. The interface is organised into four main tabs which each provide a selection of toolboxes for data operations at sequential stages of the workflow. These are: 1) Background subtraction, 2) Data operations and structure factor refinement, 3) Calculation and output of PDF functions, and 4) Extraction of coordination numbers. The data are automatically visualised graphically and the tabs updated as operations are made through the workflow (Fig. 3.1).

3.3.1 Background Scaling and Subtraction

The first tab allows data and optional background files to be loaded in to the software and inspected. LiquidDiffract expects Q-space diffraction data but a toolbox is provided to convert experimental files saved with 2θ values to Q-space. The measured or background intensity profile, $I_{\mathrm{Measured}}(Q)$ or $I_{\mathrm{Background}}(Q)$, is uniformly sampled from a cubic spline interpolation of the raw data, which is also used to extrapolate low-Q values to $Q = 0$. The sampling rate (Q-step) can be set by the user and the background profile scaled and subtracted if present. A background auto-scale feature (that roughly scales the background to match the data profile) is provided to speed up workflow but is not recommended for a close fit. Subtracting a scaled background pattern from the measured intensity gives the scattering intensity of the sample, $I_{\mathrm{Sample}}(Q)$:

$$I_{\mathrm{Sample}}(Q) = I_{\mathrm{Measured}}(Q) - bI_{\mathrm{Background}}(Q). \tag{3.4}$$

More complex Q-dependent background corrections that are sometimes required for high-pressure experiments and other complex sample environments are not currently implemented. In these cases pre-processed, background corrected data can be loaded in.

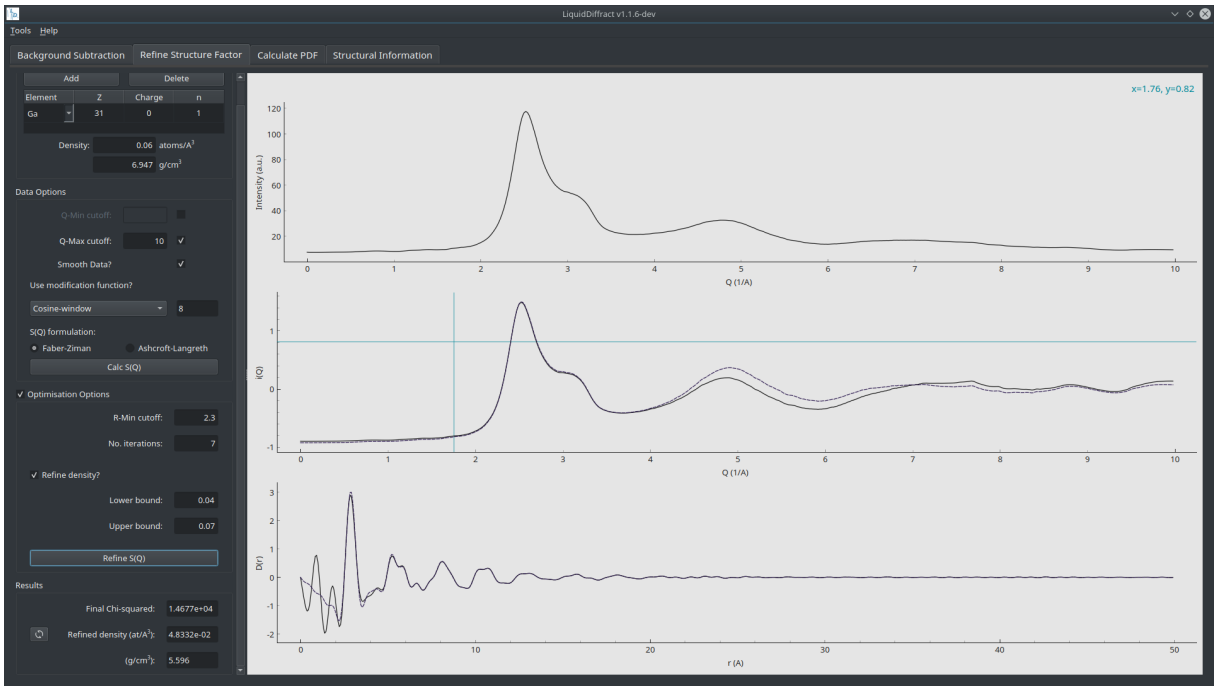

Figure 3.1: *The user interface of LiquidDiffract showing data operations being made on sample data in the refinement tab.*

3.3.2 Data Operations and *S(Q)* Refinement

The second tab is where most of the data processing is performed. The sample composition and data processing options can be set to calculate the structure factor $S(Q)$ and corresponding real-space $g(r)$ function. This tab also offers an option for numerical refinement of both the $S(Q)$ normalisation and average sample density. Functionality is provided by several toolboxes which group operations for different stages of the workflow.

The *Composition Toolbox* allows the user to set the atomic species present in the sample, and set the atomic number density, ρ_0. If the user later chooses to refine the sample density then this value of ρ_0 is also passed to the solver as an initial estimate.

The *Data Options Toolbox* then allows the user to set the majority of important options for data pre-processing and calculation of the normalised total structure factor, $S(Q)$. An option is provided to smooth noise in the data, which applies a Savitzky-Golay filter. The length of the filter window and order of the polynomial used to fit samples can be set in an *Additional Preferences* dialog, accessible from the *Tools* menu.

The Q_{min} cut-off setting allows the user to mask spurious peaks or oscillations in the low-Q region of the data which can arise from the experimental set-up (e.g., from a slightly mislocated beam stop). Toggling this option sets $I(Q < Q_{\mathrm{min}}) = I(Q_{\mathrm{min}})$.

The Q_{max} cut-off setting allows the user to truncate the data at high-Q. At high Q-values experimental data often becomes increasingly noisy because the relative contribution of coherent scattering to the experimental signal is inversely related to the scattering vector. The increasingly noisy signal can lead to dramatic and anomalous oscillations near the first peak in the real space correlation functions. It can therefore be beneficial to truncate experimental data at high-Q.

Irrespective of the Q_{max} value chosen by the user, experimental data is always effectively truncated due to the finite Q-range available to experimental measurements. This truncation is essentially an ideal low-pass brick-wall filter, and so results in spurious oscillations in the real-space correlation function via the Gibbs phenomenon. The effect corresponds to the time-domain 'ringing' artifacts seen in signal processing, and is equivalent to convolution of the real-space correlation function with the impulse response of the filter - the real space peak function $P(r)$. For a simple truncation the $P(r)$ is a normalised sinc function, i.e.:

$$P(r; Q_{\mathrm{max}}) = 2Q_{\mathrm{max}} \frac{\sin\left(2\pi r Q_{\mathrm{max}}\right)}{2\pi r Q_{\mathrm{max}}}. \tag{3.5}$$

The interference function, $i(Q)$, tends to zero at $Q = \infty$, so the effect of truncating at very high-Q ($\gtrsim 30\,\text{Å}^{-1}$) is often negligible. However, the effect is much more significant for high-pressure studies due to the limited accessible scattering angle when working with high-pressure instruments (Drewitt, 2021). Furthermore, truncating at a lower Q_{max} corresponds to a broadening of the sinc function, and these broader oscillations are often difficult to distinguish from real structural information (Lorch, 1969; Shen et al., 2004).

A filter with a smoother roll-off can be used to suppress FT artifacts in the real-space functions. This is done by applying a window function to the low-pass filter, equivalent to multiplying the Q-space data by a modification function, $M(Q)$, which damps the data cut-off at $Q_{\max}$ (i.e., reduces the amplitude of the discontinuity). Two window functions are available in LiquidDiffract: the Lanczos (1966) window proposed by Lorch (1969, commonly called the Lorch function in total scattering literature):

$$M(Q) = \begin{cases} \frac{\sin\left(\frac{\pi Q}{Q_{\max}}\right)}{\left(\frac{\pi Q}{Q_{\max}}\right)} & \text{if } Q < Q_{\max} \\ 0 & \text{if } Q > Q_{\max} \end{cases} \tag{3.6}$$

and a cosine window function (i.e., a Hann window; Blackman & Tukey, 1958; Drewitt et al., 2013):

$$M(Q) = \begin{cases} 1 & \text{if } Q < Q_{\text{Window}} \\ 0.5\left[1 + \cos\left(\frac{x\pi}{N-1}\right)\right] & \text{if } Q_{\text{Window}} < Q < Q_{\max} \\ 0 & \text{if } Q > Q_{\max} \end{cases} \tag{3.7}$$

where N is width of the window function and x is an integer with values from 0 to $(N-1)$ across the window.

After setting these options, the *'Calculate $S(Q)$'* button will calculate the total structure factor, $S(Q)$, and display the interference function, $i(Q)$, and the differential correlation function, $D(r)$, to the user. LiquidDiffract provides the option to use either the Faber-Ziman (FZ; Faber & Ziman, 1965) or Ashcroft-Langreth (AL; Ashcroft & Langreth, 1967) formalisms of the total structure factor ($S^{\text{FZ}}(Q)$ and $S^{\text{AL}}(Q)$ respectively; see also: Keen, 2001).

In both cases, the total molecular structure factor is converted to normalised (atomic) units using the method of Krogh-Moe (1956) and Norman (1957). For both formalisms the scattering intensity from the sample, $I_{\text{Sample}}(Q)$, is first extracted from the measured intensity by subtracting a background pattern with a scaling factor applied as in equation 3.4.

The Faber-Ziman total structure factor is then defined as:

$$S^{\mathrm{FZ}}(Q) = \frac{I^{\mathrm{Coh}}(Q) - (\langle f^2 \rangle - \langle f \rangle^2)}{\langle f \rangle^2}. \tag{3.8}$$

In the above equation $I^{\mathrm{Coh}}(Q)$ is the coherent scattering from the sample, defined as:

$$I^{\mathrm{Coh}}(Q) = \alpha^{\mathrm{FZ}} I^{\mathrm{Sample}}(Q) - \frac{1}{N} \sum_p I_p^{\mathrm{Incoh}}(Q), \tag{3.9}$$

where α^{FZ} is the Krogh-Moe-Norman normalisation factor that converts the signal into atomic units, N is the total number of atoms in the compositional unit, and $\sum_p I_p^{\mathrm{Incoh}}(Q)$ is the sum of the Q-dependent incoherent (Compton) scattering signals from each atom p in the compositional unit. In LiquidDiffract $I^{\mathrm{Incoh}}(Q)$ is interpolated from the analytical tabulations of Hubbell et al. (1975). The normalisation factor α^{FZ} is defined as:

$$\alpha^{\mathrm{FZ}} = \frac{-2\pi^2 \rho_0 + \int_0^{Q_{\max}} \frac{\sum_p I_p^{\mathrm{Incoh}}(Q) + \langle f^2 \rangle}{\langle f \rangle^2} Q^2 dQ}{\int_0^{Q_{\max}} \frac{Q^2 I^{\mathrm{Samp}}(Q)}{\langle f \rangle^2} dQ}, \tag{3.10}$$

where $Q_{\max}$ is the maximum scattering momentum and ρ_0 is the average atomic number density of the sample. The Q-dependent functions $\langle f^2 \rangle$ and $\langle f \rangle^2$ are the average scattering functions:

$$\langle f^2 \rangle = \frac{1}{N} \sum_p \left(f_p(Q)\right)^2 \tag{3.11}$$

$$\langle f \rangle^2 = \frac{1}{N^2} \sum_p \sum_q f_p(Q) f_q(Q), \tag{3.12}$$

where $f_p(Q)$ are the atomic form factors for each atom p in the compositional unit. The atomic form factors are taken from the analytic tabulation published in the International Tables of Crystallography (Brown et al., 2006). For a monatomic sample $\langle f^2 \rangle = \langle f \rangle^2$.

The Ashcroft-Langreth total structure factor is defined as:

$$S^{\mathrm{FZ}}(Q) = \frac{I^{\mathrm{Coh}}(Q)}{N Z_{\mathrm{tot}}^2 f_e^2(Q)}, \tag{3.13}$$

where N is the number of atoms in the compositional unit, Z_{tot} is the total atomic number of the compositional unit (i.e., $\sum_p Z_p$), and $f_e(Q)$ is an effective electronic form factor. The coherent scattering from the sample $I^{\mathrm{Coh}}(Q)$ is here defined as:

$$I^{\mathrm{Coh}}(Q) = N \left[\alpha^{\mathrm{AL}} I^{\mathrm{Samp}}(Q) - \sum_p I_p^{\mathrm{Incoh}}(Q) \right]. \tag{3.14}$$

The incoherent scattering signals are calculated in the same way as equation 3.9, but here the normalisation factor α^{AL} is defined as:

$$\alpha^{\mathrm{AL}} = Z_{\mathrm{tot}}^2 \frac{-2\pi^2\rho_0 + \int_0^{Q_{\max}} \left[J(Q) + S_\infty\right] Q^2 dQ}{\int_0^{Q_{\max}} \frac{I^{\mathrm{Samp}}(Q)}{f_e^2(Q)} Q^2 dQ}. \tag{3.15}$$

The effective electronic form factor for the sample, $f_e(Q)$, is defined as:

$$f_e(Q) = \frac{\sum_p f_p(Q)}{Z_{\mathrm{tot}}}. \tag{3.16}$$

The function $J(Q)$ is then defined by:

$$J(Q) = \frac{\sum_p I_p^{\mathrm{Incoh}}(Q)}{Z_{\mathrm{tot}}^2 f_e^2(Q)}, \tag{3.17}$$

and the value S_∞ by:

$$S_\infty = \frac{\sum_p K_p^2}{Z_{\text{tot}}^2}, \tag{3.18}$$

where K_p is the Warren-Krutter-Morningstar approximation for the effective atomic number of each atom (Warren et al., 1936). This is calculated by:

$$K_p = \left\langle \frac{f_p(Q)}{f_e(Q)} \right\rangle_Q, \tag{3.19}$$

where the angled brackets denote an average over the Q-range of the data.

The interference function, $i(Q)$, is simply related to $S(Q)$:

$$i(Q) = S(Q) - S_\infty, \tag{3.20}$$

with $S_\infty = 1$ for all samples in the FZ formalism and for monatomic samples in the AL formalism (Equation 3.18). The differential correlation function, $D(r)$, describes the difference between the (local) microscopic pair density and the average density:

$$D(r) = 4\pi r \left[\rho(r) - \rho_0\right]. \tag{3.21}$$

It is related to $g(r)$, the pair-distribution function (Equation 3.2), by:

$$D(r) = 4\pi r \rho_0 \left[g(r) - 1\right], \tag{3.22}$$

or, following from equation 3.3:

$$D(r) = \frac{2}{\pi} \int_0^{Q_{\max}} Q i(Q) \sin\left(Qr\right) dQ. \tag{3.23}$$

In LiquidDiffract, $D(r)$ is computed from the sine Fourier transform of $Qi(Q)$ using a standard FFT algorithm. As the transform is sine-only, the Q-space function, $Qi(Q)$, is mirrored with its odd image and the imaginary components of the Fourier transform used. $Qi(Q)$ is also zero-padded for computational efficiency and interpolation in real-space. The length of the transformed array, 2^N, can be set by the user via the *Additional Preferences* dialog. Increasing N increases the density of points in the real-space array, which may be necessary when using a large Q-range, which, for the same value of N, would otherwise give a lower real-space resolution.

An option is then provided to optimise the calculated $i(Q)$ and $g(r)$ through the numerical iterative procedure developed by Eggert et al. (2002), that follows from the work of Kaplow et al. (1965). The procedure is based on the assumption that, in real-space, a minimum distance, $r_{\min}$, can be defined, which represents the largest distance ($r = 0$ to $r = r_{\min}$) where no atoms can be found. In a liquid, this corresponds to the region below the first interatomic distance in the 1st coordination shell. Correspondingly, no oscillations or peaks should be observed in the real-space correlation functions within this region. As a result, the function $D(r) = -4\pi r\rho_0$ for $r < r_{\min}$. However, oscillations are commonly observed in this region, due to the effects of Fourier transforming finite Q-space data described above, along with systematic errors in the scattering factors and the normalisation factor, α. These errors can be minimised by taking the difference between the observed and modelled behaviour of $D(r)$ below $r_{\min}$, Fourier transforming this difference to reciprocal space, and subtracting from the $i(Q)$ (with a scaling factor applied based on the definition of $S(Q)$ used) to compute a refined $i(Q)$. This refined $i(Q)$ can then be fed back into equation 3.24, and the final refined $i(Q)$ computed after a set number of iterations, n_{iter}. A minimum of 3 iterations is normally required for convergence. The value of $r_{\min}$ used in the refinement should be set carefully, as it exerts a strong influence (Shen et al., 2004). This value should correspond to the minimum preceding the first *physical* peak in $D(r)$, which is generally obvious in the preliminary $D(r)$ (prior to optimisation), particularly when using a modification function to suppress FT artifacts (i.e., unphysical peaks). In some cases the user may need additional knowledge of their sample or its structure to set the $r_{\min}$ correctly. The iterative procedure is as follows:

$$(1) \quad D_{(n)}(r) = \frac{2}{\pi}\int_0^{Q_{\max}} Qi_{(n)}(Q)\sin(Qr)\,dQ \tag{3.24}$$

$$(2) \quad \Delta D_{(n)}(r) = D_{(n)}(r) - S_\infty\left(-4\pi\rho_0 r\right), \text{ for } r < r_{\min} \tag{3.25}$$

$$(3) \quad i_{(n+1)}(Q) = i_{(n)}(Q) - \frac{1}{Q}\left[\frac{i_{(n)}(Q)}{z(Q)} + 1\right] \times \int_0^{r_{\min}} \Delta D_{(n)}(r)\sin(Qr)dr \tag{3.26}$$

where for the Ashcroft-Langreth formalism:

$$z^{\mathrm{AL}}(Q) = S_\infty + J_0(Q) \tag{3.27}$$

and for the Faber-Ziman formalism:

$$z^{\mathrm{FZ}}(Q) = 1. \tag{3.28}$$

$J(Q)$ and S_∞ are defined in equations 3.17 and 3.18 respectively.

LiquidDiffract also provides the option to use this refinement procedure to extract the average number density of the sample, ρ_0. As ρ_0 is an independent variable in the refinement procedure its optimum value can be found by minimising a χ^2 figure of merit, defined as a function of ρ_0:

$$\chi^2_{(n)}(\rho_0) = \int_0^{r_{\min}} \left[\Delta D_{(n)}(r)\right]^2 dr. \tag{3.29}$$

LiquidDiffract supports several solvers implemented in the SciPy libraries to do this minimisation. The solver to be used, along with specific options like convergence criteria and number of function iterations can be set from the *Additional Preferences* dialog. The solvers currently supported by LiquidDiffract are L-BFGS-B (Byrd et al., 1995; Zhu et al., 1997), SLSQP (Kraft, 1988) and COBYLA (Powell, 1994, 1998, 2007), which are fast, robust, and represent a good cross-section of the different derivative-free and gradient-based approaches available in the SciPy library. All solvers require upper and lower bounds on the density to be set. The optimisation is typically very fast ($\sim$0.05 seconds on a mid-range laptop), although the accuracy of the result depends on the initial estimate of ρ_0 and the range of the limits used. A useful recipe to use if a good initial estimate of ρ_0 cannot be made is to first run the optimisation with only 1 iteration in the refinement procedure to extract a better

initial estimate of ρ_0. The optimisation can then be run again using a higher number of iterations that provides full convergence. The bounds on ρ_0 can also be progressively narrowed to encourage true convergence. Alternatively, a global minimisation option is provided. This is a basin-hopping algorithm which runs the optimisation several times, randomly perturbing the initial estimate of ρ_0 between each run, and accepting or rejecting each minimisation based on the standard Metropolis criterion (Li & Scheraga, 1987; Wales & Doye, 1997). This option can be useful in some cases of otherwise poor convergence, but is much slower.

The density, ρ_0, is the only optimisation parameter in the refinement procedure implemented in LiquidDiffract, however the χ^2 figure of merit can be used to simultaneously refine the background scaling factor, b, alongside ρ_0 (Eggert et al., 2002). In high-pressure experiments additional care in the background scaling (such as Q-dependent scaling functions) is often required, and in these cases naive optimisation of both ρ_0 and b can lead to unphysical results. As LiquidDiffract was primarily designed for data collected at extreme conditions, simultaneous refinement of ρ_0 and b is not currently implemented, but this is a planned feature for future releases of the software. Nevertheless, as b and ρ_0 are not strongly correlated (Eggert et al., 2002), the background can be independently scaled by other methods prior to refinement of ρ_0, which is equivalent to a step-wise optimisation across the full b-ρ_0 parameter space.

It is also important to note that a well defined minimum in $\chi^2_{(n)}(\rho_0)$ relating to the sample density only exists for $n < \Xi$, where Ξ is typically ~ 10. This is a result of the way the iterative procedure works, and the definition of $\chi^2_{(n)}(\rho_0)$. After a large number of iterations the refinement procedure can always force the data to closely fit the modelled slope through unreasonable manipulation (e.g., by massively inflating low-Q values). This results in a drastically reduced χ^2 at large values of n. Furthermore, at values of $n > \Xi$, $\chi^2_{(n)}(\rho_0)$ will decrease with decreasing ρ_0 because the absolute values used to calculate $\chi^2_{(n)}(\rho_0)$ are smaller as the magnitude of the model slope decreases. However, a minimum generally exists at $\rho_0 > 0$ because the iterative procedure struggles to force the $D(r)$ to the horizontal. Computing the function $\chi^2(\rho_0; n)$ illustrates that above Ξ iterations a well defined minimum in $\chi^2(\rho_0)$ no longer exists, and the density region in which the iterative procedure can fit the data rapidly increases (Fig. 3.2).

The value of Ξ will depend on the data and the value of $r_{\min}$. The change in behaviour of $\chi^2(\rho_0; n)$ above and below Ξ can be illustrated by plotting a map of the function (Fig. 3.2c). The rapid asymptotic convergence in just a few iterations to the true minimum in χ^2 can be seen, as can the sharp shelf in the function at $n = \Xi$. Above $n = \Xi$ the true density minimum is briefly preserved as a local minimum in the function, with the global minimum at lower ρ_0 physically meaningless (Fig. 3.2b,d). Care must be taken in the density refinement to ensure that $n < \Xi$, as any solver would naively find the physically meaningless minimum at $n > \Xi$. Prior to the $n = \Xi$ limit

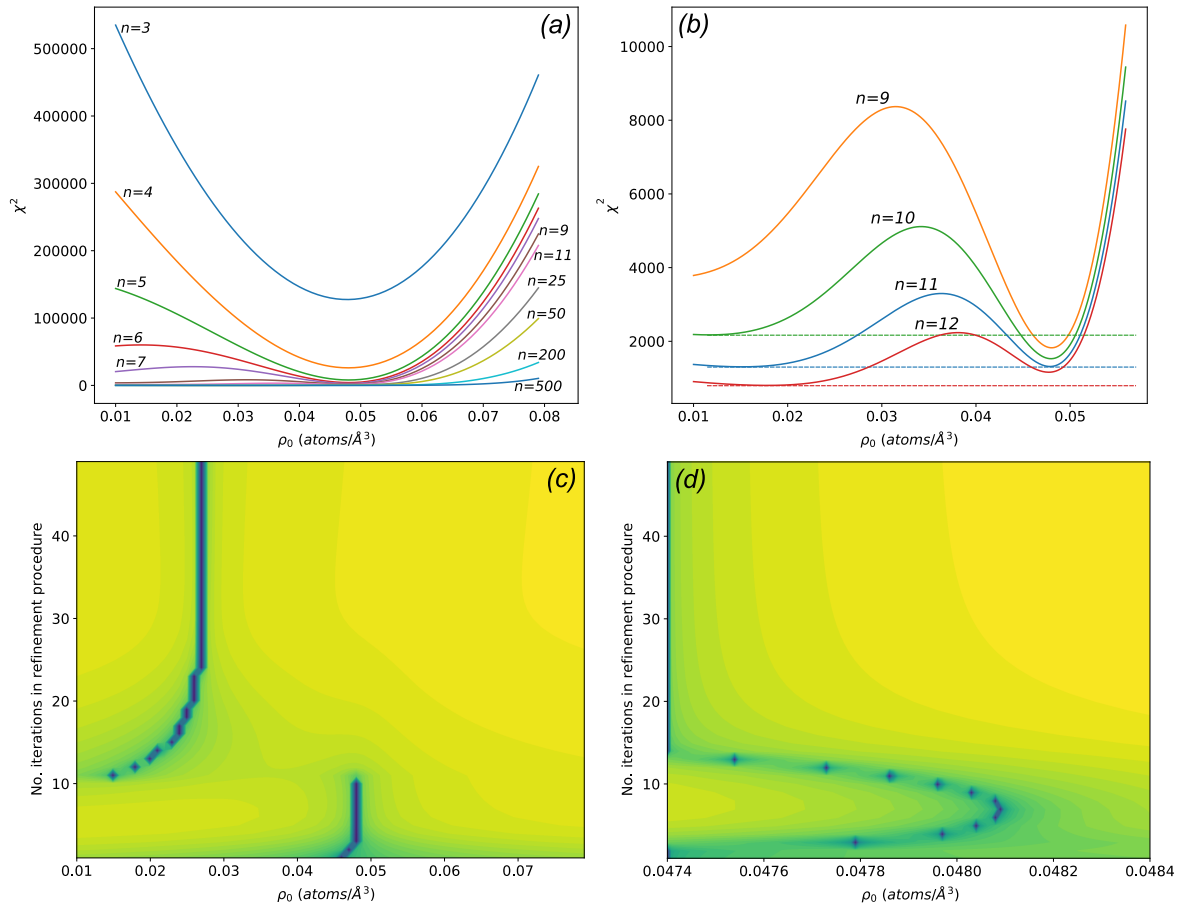

Figure 3.2: *(a) Function $\chi^2(\rho_0;n)$ computed for sample data at increasing values of n. The lack of a well-defined minimum at high values of n can be seen, as can the increasing density region in which the iterative procedure can fit the data, but the sharp change in behaviour at $n \geq \Xi$ is not obvious. The minimum within the widening plateau region at $\rho_0 \sim 0.027$ that exists at high values of n is also not obvious. (b) Close up of the function $\chi^2(\rho_0;n)$ across the limit $\Xi = 11$. At $n = 11$ the local minimum towards $\rho_0 = 0$ becomes the global minimum. Immediately beyond the $n = \Xi$ limit the local minimum is still well-defined enough to find with a solver, given a bound-constrained minimisation that excludes the new global minimum from the search space. (c) Map of the function $\chi^2(\rho_0;n)$ computed for the same sample data. The colour scaling shows the log-scale value of the χ^2 function, so that the minima above and below $n = \Xi$ are obvious, despite the difference in scale. For this data, more than 3 iterations are required for convergence and above 10 iterations a density refinement procedure would fail. More iterations can be used to optimise the $S(Q)/g(r)$ but the value of χ^2 used to extract density becomes meaningless. (d) Close-up of the function $\chi^2(\rho_0;n)$ computed with increased resolution in ρ_0. The colour scaling shows the log-scale value of the χ^2 function, so that the minima at low and high n are obvious, despite the difference in scale. The density minimum persists as a local minimum beyond $n = \Xi$ until $n = 14$, although the minimum begins to be shifted to lower values of ρ_0. The optimum number of iterations can be seen as a local maximum in the value of ρ_0 along the minimum in $\chi^2(\rho_0;n)$.*

the density minimum already begins to be shifted away from the true value of ρ_0 by the widening plateau at low ρ_0 (Fig. 3.2d). At high enough ρ_0 resolution the number of iterations itself can be optimised, as this is seen as a maximum in the value of ρ_0 along the minimum in $\chi^2(\rho_0; n)$ (Fig. 3.2d). This is a result of the trade-off between the minimum asymptotically approaching the true value of ρ_0 with increasing number of iterations, and the shift of the minimum towards lower ρ_0 as n approaches Ξ. An example script to compute maps of the $\chi^2(\rho_0; n)$ function is provided with the LiquidDiffract source code. Greater values of n can be used to optimise the $S(Q)$ and real-space correlation functions at a set density, but the value of χ^2 used to extract density becomes meaningless.

The next workflow tabs are automatically updated with the resulting PDF functions after the refinement of $i(Q)$ has run, or after the initial calculation of $i(Q)$ if the $S(Q)$ pass-through option is selected. If a modification function is selected the default behaviour is to only apply this to display the initial $i(Q)$ and to calculate the final $g(r)$ after the refinement procedure has completed. An option is provided to use the modification function within the refinement procedure, although this is not recommended for most use cases. Figure 3.3 shows an example of using the iterative refinement procedure in LiquidDiffract to obtain a properly normalised $S(Q)$ and $g(r)$.

3.3.3 PDF Output

This tab displays the optimised structure factor, $S(Q)$, pair distribution function, $g(r)$, and radial distribution function, $RDF(r)$, following operations made in the refinement tab. The functions can be inspected within the software, or output to text files for further analysis or graphing by the user. If a modification function has been used in the data treatment then information on this is saved along with the raw $S(Q)$. Information on the sample composition and density is also saved automatically. The $S(Q)$ is defined as in equations 3.8 and 3.13, and the $g(r)$ as the finite integral version of equation 3.2:

$$g(r) - 1 = \frac{1}{2\pi^2 r \rho_0} \int_0^{Q_{\max}} Q i(Q) \sin(Qr) dQ. \tag{3.30}$$

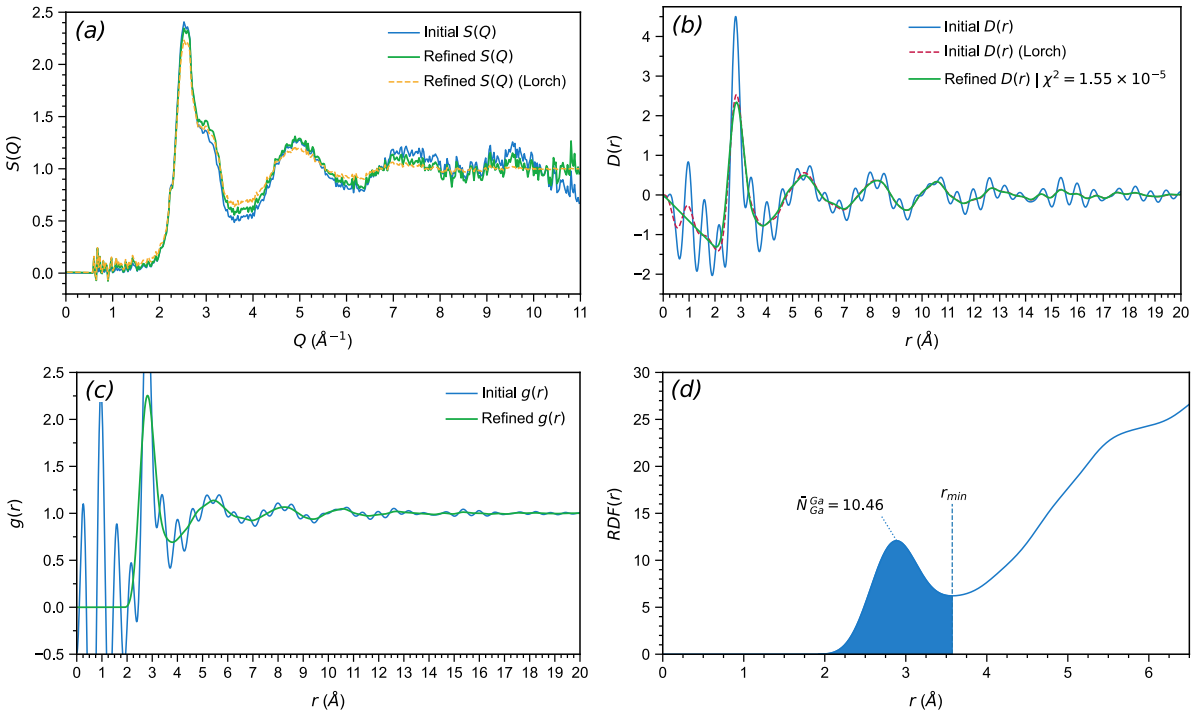

Figure 3.3: *Reciprocal-space structure factor and real-space correlation functions of liquid gallium as processed through LiquidDiffract from synchrotron x-ray diffraction data measured at 0.1 GPa in a diamond anvil cell (Drewitt et al., 2020). (a) Initial $S(Q)$ and optimised $S(Q)$ after refinement of the normalisation using the iterative procedure ($Q_{\min}$ = 0.54, $Q_{\max}$ = 11, $r_{\min}$ = 2.2, n_{iter} = 50) at ρ_0 = 0.05256 atoms/Å^3 (6.085 g/cm^3). The dashed orange line shows the optimised $S(Q)$ modified with a Lorch function. (b) Initial differential correlation function, $D(r)$ (blue line). Applying a Lorch function prior to the Fourier transform suppresses some of the FT artifacts (red dashed line). The green line shows the optimised $D(r)$. (c) Initial $g(r)$ (blue line) and resulting optimised $g(r)$ (green line) at ρ_0 = 6.085 g/cm^3 with a Lorch function applied prior to the Fourier transform. (d) Integration across the first peak in the resulting $RDF(r)$ to $r_{\min}$ = 3.57 (automatically located by the Integration Toolbox) gives an average coordination number, $\bar{N}_{\text{Ga-Ga}}$, of 10.46, with the position of the $T(r)$ peak maximum, $r_{\text{Ga-Ga}}$, at 2.83 Å, which is consistent with previously reported values of coordination number and bond-length in liquid gallium (Waseda & Suzuki, 1972; Yagafarov et al., 2012; Drewitt et al., 2020). The first peak is asymmetric, and can also be fitted with a skewed gaussian using the Curve-fitting Toolbox, yielding $\bar{N}_{\text{Ga-Ga}}$ = 10.53 ± 0.04 and $r_{\text{Ga-Ga}}$ = 2.615 ± 0.002 with σ = 0.509 ± 0.004 and ξ = 1.91 ± 0.03.*

The $RDF(r)$ describes the average number of particles that can be found within a sphere of radius r. It is defined as:

$$RDF(r) = 4\pi r^2 \rho(r) = 4\pi r^2 \rho_0 g(r) \tag{3.31}$$

or, by combining with equation 3.30:

$$RDF(r) = \left[\frac{2r}{\pi}\int_0^{Q_{\max}} Qi(Q)\sin(Qr)dQ\right] + 4\pi r^2\rho_0. \tag{3.32}$$

The Faber-Ziman $S(Q)$ is normalised to unity at infinite Q (i.e., $\lim_{Q\to\infty} S^{\mathrm{FZ}}(Q) = 1$), but for the Ashcroft-Langreth formalism $\lim_{Q\to\infty} S^{\mathrm{AL}}(Q) = S_\infty$. For monatomic samples the value $S_\infty = 1$, but for multi-component (polyatomic) samples $0 < S_\infty < 1$. This means that the $g(r)$ approaches $1 - S_\infty$ rather than 0 at $r = 0$, and the $D(r)$ and $RDF(r)$ are similarly scaled. An option is provided in the Additional Preferences dialog to either plot the Ashcroft-Langreth $S(Q)$ and $g(r)$ as calculated, or re-scaled to match the conventional scaling of the Faber-Ziman functions. The re-scaling of the $RDF(r)$ is always performed to allow the same fitting routines to be used in the structural information tab.

The re-scaled functions are calculated by:

$$S'(Q) = \frac{S^{\mathrm{AL}}(Q)}{S_\infty}, \tag{3.33}$$

$$g'(r) = \frac{g^{\mathrm{AL}}(r) - 1}{S_\infty} + 1, \tag{3.34}$$

and

$$RDF'(r) = \frac{RDF^{\mathrm{AL}}(r) - 4\pi\rho_0 r^2}{S_\infty} + 4\pi\rho_0 r^2. \tag{3.35}$$

3.3.4 Structural Information: Integration and Curve Fitting

The final tab provides several methods of extracting average coordination numbers of atomic pairs from the calculated radial distribution functions. Two toolboxes are provided: an *Integration Toolbox* (which is generally used for monatomic samples), and a *Curve-fitting Toolbox* (which is generally used for polyatomic samples).

An average coordination number, $\bar{N}_{\alpha\beta}$, can be defined as the average number of atoms β around an atom α. This can be calculated by integrating the pair-distribution function, $g(r)$, over a spherical shell defined by an inner and outer radius, r_1 and r_2, and multiplying by the bulk density:

$$\bar{N}_{\alpha\beta} = \int_{r1}^{r2} 4\pi\rho_0 c_\beta g_{\alpha\beta}(r) r^2 dr, \tag{3.36}$$

where c_β is the atomic concentration of species β in the sample and $g_{\alpha\beta}(r)$ is the partial pair distribution function for the $\alpha-\beta$ pair. For a monatomic sample this is equivalent to simply integrating over the $RDF(r)$. LiquidDiffract provides a toolbox to extract the first coordination number, N_1, by computing this integral across the first peak in $RDF(r)$. Three alternative methods are implemented based on commonly used methods in the literature (Waseda, 1980).

The first method is based on the assumption that the quantity $rg(r)$ is symmetrical for a coordination shell about its average position. This is computed by integrating over $RDF(r)$ from the leading edge of the first peak in $rg(r)$ (equivalently, $T(r)$, equation 3.42), r'_0, to its maximum $r'_{\max}$, and doubling the result:

$$\bar{N}_A = 2\int_{r'_0}^{r'_{\max}} 4\pi\rho_0 r \left[rg(r)\right]_{\text{sym}} dr. \tag{3.37}$$

The second method is based on the assumption that the coordination shell is instead symmetrical about a radius which defines the maximum in the $r^2g(r)$ curve. This is computed in a similar way, integrating over $RDF(r)$ from the leading edge of the first peak in $r^2g(r)$ (equivalently, the $RDF(r)$), r_0, to its maximum $r_{\max}$ and doubling:

$$\bar{N}_B = 2\int_{r_0}^{r_{\max}} 4\pi\rho_0 \left[r^2 g(r)\right]_{\text{sym}} dr. \tag{3.38}$$

Since the first peak is not truly symmetrical $\bar{N}_A$ and $\bar{N}_B$ can be considered estimates of the lower bound on the average coordination number. Typically it also the case that $\bar{N}_A < \bar{N}_B$. This consideration of asymmetry leads to the third method, which involves integrating $RDF(r)$ from the leading edge of the first peak r_0 to first minimum following it, $r_{\min}$:

$$\bar{N}_C = \int_{r_0}^{r_{\min}} 4\pi\rho_0 r^2 g(r) dr. \tag{3.39}$$

An auto-refine button is provided to quickly find the positions of r_0, $r'_{\max}$, $r_{\max}$ and $r_{\min}$ using a root-finding and minimisation procedure. The user can also set the limits manually via a spinbox or by dragging the limits on the data plot. In particular, careful setting of $r_{\min}$ may be required as its apparent value can fluctuate due to errors in $RDF(r)$, and with changes in p-T conditions (e.g. Yagafarov et al., 2012). An example of coordination number extraction for a monatomic sample using the *Integration Toolbox* is illustrated in Figure 3.3d.

For polyatomic samples it is more useful to fit the $RDF(r)$ with a number of peaks so that the individual contributions from different α-β pairs can be investigated. LiquidDiffract provides a curve-fitting toolbox to do this. For each individual peak attributed to an α-β pair the coordination number can be calculated by (Petkov, 2012):

$$\bar{N}_{\alpha\beta} = \frac{c_\beta}{W'^{\text{x-ray}}_{\alpha\beta}} \times Respective\ RDF\ Peak\ Area, \tag{3.40}$$

where c_β is the atomic proportion of β in the composition, and $W'^{x\text{-}ray}_{\alpha\beta}$ is the x-ray weighting factor for the α-β pair, given by (Faber & Ziman, 1965):

$$W'^{\text{x-ray}}_{\alpha\beta} = \frac{c_\alpha c_\beta K_\alpha K_\beta \left(2 - \delta_{\alpha\beta}\right)}{\left(\sum_\alpha c_\alpha K_\alpha\right)^2}, \tag{3.41}$$

where c_p is the atomic fraction of species p, δ is the Kronecker delta ($\delta_{\alpha\beta} = 0$ if $\alpha \neq \beta$ and $\delta_{\alpha\beta} = 1$ if $\alpha = \beta$), and K_p is the effective atomic number of species p given by the Warren-Krutter-Morningstar approximation specifically at $Q = 0$ (an option is provided in the *Additional Preferences* dialog to use the data Q-range instead; equation 3.19; Warren et al., 1936).

It is generally preferable to fit the $T(r)$ instead of $RDF(r)$ as the peaks are symmetrically broadened and gaussian in shape (Waseda, 1980), with:

$$T(r) = \frac{RDF(r)}{r}. \tag{3.42}$$

The gaussian peak function is defined as:

$$Gauss(r) = \frac{A}{\sigma\sqrt{2\pi}} \exp\left[\frac{-(r-\mu)^2}{2\sigma^2}\right] \tag{3.43}$$

with μ the peak centre, σ describing the width of the peak, and A the area under the curve. In many cases prior knowledge of the coordination number or average bond length for an α-β pair may be available so it is more useful to redefine the peak function with $\bar{N}_{\alpha\beta}$ as a fitting parameter. Combining equation 3.43 with equation 3.40 and the definition of $T(r)$ from equation 3.42 we can find:

$$T(r) = \sum_{\alpha\beta}\left[\frac{\bar{N}_{\alpha\beta}W'^{\text{x-ray}}_{\alpha\beta}}{c_\beta\sigma_{\alpha\beta}r\sqrt{2\pi}} \exp\left[\frac{-(r-r_{\alpha\beta})^2}{2\sigma^2_{\alpha\beta}}\right]\right] \tag{3.44}$$

with the peak centre, μ, equivalent to the average $\alpha-\beta$ bond length, $r_{\alpha\beta}$, and $\sigma_{\alpha\beta}$ a measure of the distribution of interatomic distances arising from thermal and static structural disorder.

In LiquidDiffract the user can add an arbitrary number of peaks and fix or refine any combination of the parameters ($\bar{N}_{\alpha\beta}$, $r_{\alpha\beta}$ and $\sigma_{\alpha\beta}$) for each peak individually or simultaneously. The data range to fit can also be selected by the user, and residuals are plotted alongside the fits.

In some cases the peaks in the radial distribution function may have significant asymmetry. Sukhomlinov & Müser (2017, 2020) noted that for some samples and conditions the interatomic distances may form a skewed distribution, and that a skew-normal distribution provides a closer fit to the

$RDF(r)$ than a pure gaussian. The skew-normal distribution is a pure gaussian multiplied by a skewness coefficient defined as:

$$1 + \mathrm{erf}\left(\xi \frac{x-\mu}{\sigma\sqrt{2}}\right) \tag{3.45}$$

where ξ is an additional fitting parameter describing the skew. By analogy with equation 3.44 we can then instead fit:

$$T(r) = \sum_{\alpha\beta} \left[\frac{\bar{N}_{\alpha\beta} W'^{\text{x-ray}}_{\alpha\beta}}{c_\beta \sigma_{\alpha\beta} r\sqrt{2\pi}} \exp\left[\frac{-(r-r_{\alpha\beta})^2}{2\sigma^2_{\alpha\beta}}\right] \times \left[1 + \mathrm{erf}\left(\xi_{\alpha\beta}\frac{r-r_{\alpha\beta}}{\sigma_{\alpha\beta}\sqrt{2}}\right)\right]\right] \tag{3.46}$$

When $\xi_{\alpha\beta} = 0$ equation 3.46 is identical to 3.44. LiquidDiffract provides the option to individually toggle this additional skewness parameter for any of the peaks in the fit.

It is important to note that naively fitting multiple Gaussians to the $RDF(r)$ or $T(r)$ can sometimes lead to unphysical results (Cristiglio et al., 2009; Petkov, 2012). Peaks must be correctly assigned to specific pair correlations, which requires additional structural information. Strongly overlapping peaks may also result in non-unique solutions to the fit, and additional structural constraints from theory, modelling, or complementary experimental data (such as neutron diffraction with isotope substitution or extended x-ray absorption fine structure spectroscopy) may be required to fix one or more values in the fit and obtain sensible estimates of the remaining structural parameters (Figure 3.4b; Cristiglio et al., 2009). As $\bar{N}_{\alpha\beta}$ and $r_{\alpha\beta}$ are both fitting parameters in the *Curve-fitting Toolbox*, and any combination of parameters can be fixed or refined, this process is simple in LiquidDiffract. Nevertheless, structural parameters of multiple correlations can still often be extracted directly from partially overlapping peaks without prior knowledge of any parameters (Figure 3.4a; Petkov, 2012). An example of using the *Curve-fitting Toolbox* to extract structural parameters from the $T(r)$ functions of polyatomic samples is shown in Figure 3.4.

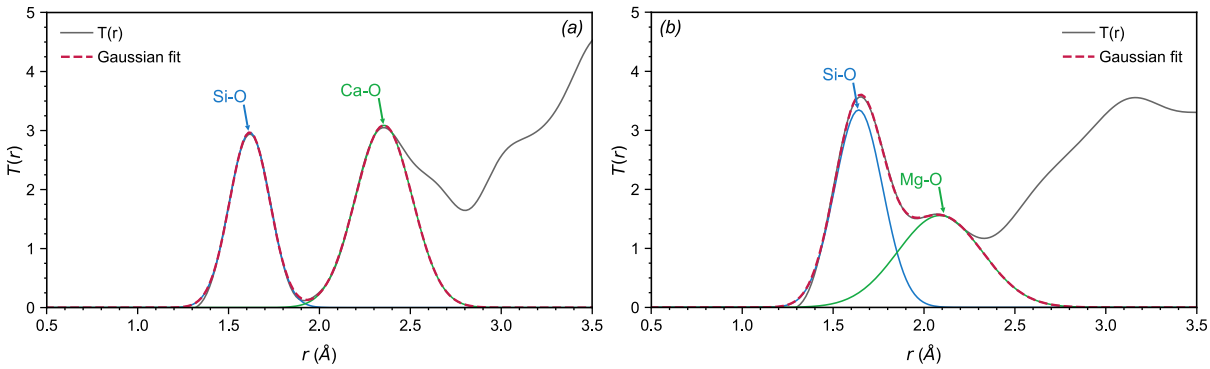

Figure 3.4: *Example usage of the Curve-fitting Toolbox to extract structural information in LiquidDiffract. Gaussian fits (red dashed lines) to the refined $T(r)$ (grey lines) of two samples are shown: (a) $CaSiO_3$ glass and (b) $MgSiO_3$ liquid. The blue and green lines show the individual gaussians that contribute to the summed models. Data was obtained from in situ synchrotron x-ray diffraction with aerodynamic levitation and CO_2 laser-heating at beamline ID11 of the European Synchrotron Radiation Facility (ESRF), Grenoble, France. (a) The $T(r)$ of $CaSiO_3$ glass at ambient conditions was calculated by LiquidDiffract with ρ_0 = 0.0749 atoms/Å^3 (2.89 g/cm^3). The correlation function was refined using the iterative procedure (with Q_{min} = 1.25, Q_{max} = 26, r_{min} = 1.25 and n_{iter} = 1000) and a Lorch function was applied prior to the final Fourier transform. The first two peaks in the $T(r)$ can be attributed to the nearest-neighbour Si-O and Ca-O correlations respectively, with a high-r contribution from O-O correlations overlapping the second peak (Waseda & Toguri, 1977; Taniguchi et al., 1997; Benmore et al., 2010). As the Si-O and Ca-O correlations do not overlap significantly, both peaks could be fitted simultaneously and all parameters allowed to vary in the fit. This yielded parameters for the Si-O correlation of $\bar{N}_{\mathrm{Si-O}}$ = 4.00 ± 0.01, $r_{\mathrm{Si-O}}$ = 1.624 ± 0.001 and $\sigma_{\mathrm{Si-O}}$ = 0.110 ± 0.001 ($\xi_{\mathrm{Si-O}}$ = 0), and parameters for the Ca-O correlation of $\bar{N}_{\mathrm{Ca-O}}$ = 6.06 ± 0.04, $r_{\mathrm{Ca-O}}$ = 2.367 ± 0.001 and $\sigma_{\mathrm{Ca-O}}$ = 0.157 ± 0.001 ($\xi_{\mathrm{Ca-O}}$ = 0). The obtained structural parameters are consistent with previously reported values derived from both simulations (Mead & Mountjoy, 2006; Lan et al., 2017b) and experimental studies (Yin et al., 1986; Eckersley et al., 1988; Gaskell et al., 1991; Taniguchi et al., 1997; Benmore et al., 2010; Skinner et al., 2012; Salmon et al., 2019). (b) The $T(r)$ of $MgSiO_3$ liquid at ambient pressure was calculated by LiquidDiffract at ρ_0 = 0.07816 atoms/Å^3 (2.606 g/cm^3, with ρ_0 extracted using the density refinement feature. The refined density is consistent with previously reported estimates (Nomura et al., 2017; Kim et al., 2019). The correlation function was refined using the iterative procedure (with Q_{min} = 0.3, Q_{max} = 24, r_{min} = 1.34 and n_{iter} = 1000) and a Lorch function was applied prior to the final Fourier transform. The first two peaks in the $T(r)$ are attributed to the nearest-neighbour Si-O and Mg-O correlations respectively (Waseda & Toguri, 1977; Wilding et al., 2008). The Si-O coordination number was fixed to 4.0 in the fit (Wilding et al., 2008) due to the overlapping nature of the two peaks. A simultaneous fit of the remaining structural parameters yielded $r_{\mathrm{Si-O}}$ = 1.651 ± 0.001, $\sigma_{\mathrm{Si-O}}$ = 0.132 ± 0.001 ($\xi_{\mathrm{Si-O}}$ = 0), $\bar{N}_{\mathrm{Mg-O}}$ = 5.08 ± 0.06, $r_{\mathrm{Mg-O}}$ = 2.114 ± 0.003 and $\sigma_{\mathrm{Mg-O}}$ = 0.232 ± 0.003 ($\xi_{\mathrm{Mg-O}}$ = 0). These structural parameters are also consistent with previously reported values derived from both simulations (Lan et al., 2017a; Kim et al., 2019) and experimental studies (Funamori et al., 2004; Wilding et al., 2008).*

3.4 Further Development

The features and capabilities of LiquidDiffract described here relate to version 1.1.8 of the software. Planned features include the option to use neutron scattering data, improvements to the *Curve-fitting Toolbox* such as convolution with modification functions to account for FT artifacts in the $RDF(r)$, support for saving data options set in the GUI to a configuration file, and better support for working with multiple data sets simultaneously. LiquidDiffract also assumes there is no intramolecular contribution to the $D(r)$, but this is only strictly true for some compositions (e.g., monatomic metallic liquids; Eggert et al., 2002). Support for including intramolecular forces may be added in future releases however. The current version of LiquidDiffract does not implement simultaneous refinement of the background scaling factor, b along with density, which is a method commonly employed in the literature Eggert et al. (2002). LiquidDiffract was primarily designed for analysis of data collected in high-pressure experiments. In these cases additional care in the background scaling is often required, and naive optimisation of b along with density can lead to unphysical results. Nevertheless, this is a planned feature for future releases of LiquidDiffract, as is support for more complex background scaling such as Q-dependent background corrections. We also welcome feature requests or bug reports via the github issue tracker (`https://github.com/bjheinen/LiquidDiffract/issues`), or directed to the corresponding author.

Chapter 4

Internal Resistive Heating for Metallic Melting Experiments at Extreme Conditions

4.1 Introduction

The high-pressure melting behaviour of transition metals is an important topic in condensed-matter physics, and in geophysics the accurate determination of high-pressure melting curves (for Fe and Ni in particular) helps place important constraints on the structure, composition, and temperature profiles of planetary cores (e.g., Boehler, 1993; Anzellini et al., 2013; Lord et al., 2014b). However, the high pressure melting curves of many transition metals are controversial, largely as a result of the significant disparity between curves determined by static experiments, and those determined by shock-wave (SW) melting experiments or molecular dynamics (MD) simulations (e.g., see Brown & McQueen, 1986; Boehler, 1993; Errandonea et al., 2001; Errandonea, 2005; Japel et al., 2005; Alfè, 2009; Dai et al., 2009; Belonoshko & Rosengren, 2012; Errandonea, 2013; Lord et al., 2014b; Akin et al., 2019; Parisiades, 2021). The high melting points of most transition metals preclude the use of external resistive heating, and so static pressure experiments are generally performed in the laser-heated diamond anvil cell (LH-DAC). The most extensively used criterion for the onset of melting in LH-DAC experiments has been the visual observation of motion, usually aided by the speckle (interference) pattern produced by illuminating the sample with a green laser (the laser speckle method; Boehler, 1993, 1996; Lazor et al., 1993; Errandonea et al., 2001; Japel et al., 2005; Errandonea, 2013). However, the melting curves of many elements determined by the laser speckle method are significantly shallower than SW or MD data would suggest, with differences of up to 3000 K at 100 GPa (Errandonea et al., 2001). *In situ* x-ray diffraction (XRD) experiments have shown that melting points based on the laser speckle method often coincide with the onset of dynamic fast recrystallisation, a phenomenon reported to occur between 100 K and 1200 K below the

melting point depending on the sample material and experimental conditions (Santamaría-Pérez et al., 2009; Anzellini et al., 2013; Lord et al., 2014b). This suggests that the visual observation of motion may misinterpret sub-solidus recrystallisation as melting.

The use of *in situ* XRD allows direct observation of melt based on the appearance of liquid diffuse scattering in the XRD signal (Dewaele et al., 2007, 2010; Morard et al., 2011; Anzellini et al., 2013; Lord et al., 2014b; Stutzmann et al., 2015; Anzellini et al., 2019; Errandonea et al., 2019; Weck et al., 2020). In LH-DAC melting experiments the liquid diffuse signal typically appears gradually as temperature is increased, coexisting with Bragg peaks that only disappear at significantly higher temperatures, thus indicating partial melting of sample. The first appearance of liquid diffuse scattering is therefore interpreted as the onset of melting and used as the melt criterion. High pressure melting curves determined in this way are in much better agreement with with SW and MD studies (e.g, Dewaele et al., 2010; Anzellini et al., 2013; Lord et al., 2014b; Briggs et al., 2017; Parisiades, 2021). For several elements this has also been corroborated by XANES measurements (Aquilanti et al., 2015; Boccato et al., 2017, e.g., Fe and Ni:), and, for Fe, by changes in the mean square displacement at the melting point measured by synchrotron Mössbauer spectroscopy or nuclear resonant inelastic x-ray scattering (e.g., Murphy et al., 2011; Jackson et al., 2013). These studies are similarly backed up by post-heating analyses (such as *ex situ* SEM analysis) that show changes in microstructure, sample morphology, or texture that are indicative of melting (Yang et al., 2012; Karandikar & Boehler, 2016; Hrubiak et al., 2017). However, the uncertainties in melting curves determined by XRD measurements are still significant, primarily as a result of the large temperature uncertainties inherent to laser heating techniques (Parisiades, 2021). Furthermore, as the liquid signal scales with melt volume, the first appearance of diffuse scattering is extremely weak and can be masked by Compton scattering from the diamond anvils. As a result, there is a potential to overestimate melting temperature with this method. Nevertheless, the appearance of liquid diffuse scattering is likely the most reliable melting criterion in DAC experiments.

An alternative lab-based melting criterion for LH-DAC experiments is the appearance of a plateau in laser power vs temperature functions (e.g., Lord et al., 2009). This was initially interpreted as a result of the laser power providing the latent heat of melting at an endothermic invariant melting point, leading to an increase in melt volume (rather than an increase in temperature) as the laser power is increased until a specific melt threshold is reached (Lord et al., 2009). However, due to the small magnitude of latent heat in the melting of small DAC samples compared to the magnitude of heat provided by the laser, the exact mechanism of plateau formation has been debated (Geballe & Jeanloz, 2012; Lord et al., 2014a). Several mechanisms may lead to a plateau, including discontinuities in absorbance at the heating laser wavelength or thermal conductivity across phase transitions (including melting; e.g., Santamaría-Pérez et al., 2009; Geballe & Jeanloz, 2012), changes in thickness or geometry of the thermal insulation (e.g., Stutzmann et al., 2015), and thermal convection in

a liquid phase moving heat away from the laser spot to the solid-liquid boundary where it promotes further melting (Lord et al., 2014a). The laser power plateau method has been successfully applied to a range of materials, including Ni (Lord et al., 2014b), Pt, Pb (Lord et al., 2009), Sn (Briggs et al., 2017), Ca (Anzellini et al., 2021), FeSi (Lord et al., 2010; Asanuma et al., 2010; Fischer et al., 2013), NiSi (Lord et al., 2014b), Fe_3C, Fe_7C_3, the Fe–Fe_3C eutectic (Lord et al., 2009), along with various mantle silicates (Shen & Lazor, 1995), and the MgO–SiO_2 (Baron et al., 2017), silicate–water (Walter et al., 2015), $MgCO_3$–$CaCO_3$, and $MgCO_3$–$MgSiO_3$ systems (Thomson et al., 2014). For many materials the melting curves obtained using this criterion agree well with those determined by the onset of liquid diffuse scattering in the DAC and, at lower pressures, *ex situ* analysis of melt texture in multi-anvil experiments (Lord et al., 2010, 2014a,b; Morard et al., 2011; Errandonea et al., 2019). Simultaneous measurements of liquid diffuse scattering at the onset of a laser power–temperature plateau have also been reported in several studies (e.g., Lord et al., 2014a,b; Anzellini et al., 2021). However, as this method is also based on laser heating, the temperature uncertainties are similarly large, often several hundred Kelvin. Additionally, a plateau in the laser power vs temperature function may result from processes other than sample melting (which several authors have reported to occur concurrent with a plateau), such as solid–solid phase transitions and sub-solidus fast recrystallisation (Errandonea et al., 2020), melting of the pressure medium (Dewaele et al., 2010), or decreased heating efficiency coupled with thinning of the pressure media at high pressure (Stutzmann et al., 2015). However, these causes are difficult (or often impossible) to distinguish without simultaneous XRD measurements. The reliability of a power–temperature plateau as a melting criterion appears strongly dependent on the sample material and experimental conditions. For example, Parisiades et al. (2019) reported that for Zr melting experiments a plateau in the laser power temperature function appeared concurrently with the onset of liquid diffuse scattering in some runs, but in other runs appeared below the melting point (though also not concurrent with the onset of fast recrystallisation either) or was completely absent. Additionally, *in situ* XRD measurements made by Stutzmann et al. (2015) suggest that in the case of titanium, a plateau in the laser power temperature function can appear up to 1000 K above the onset of a diffuse scattering signal, and so may be a similarly unreliable melting criterion. The melting curve determined by Stutzmann et al. on the basis of a liquid diffuse scattering signal is higher than previously reported curves using the laser-speckle method (Errandonea et al., 2001), but still significantly shallower than curves based on SW data or MD simulations (Kerley, 2003; Zeng et al., 2011).

As discussed in previous chapters, internal resistive heating techniques can provide greatly improved temperature stability and precision, along with reduced thermal gradients that result in temperature uncertainties often an order of magnitude smaller than those in laser heating experiments. However, the necessarily small sample volume in fine-wire or thin-film heating techniques generally precludes the detection of melting by XRD (e.g., Boehler, 1986; Weir et al., 2012; Sinmyo et al., 2019; Suehiro et al., 2019). Melting can instead be determined from changes in resistivity at the melting point. In metals, lattice irregularities and disorder impede conductance. This is why resistivity increases

with temperature, as there is increased thermal disorder. Consequently, the loss of long-range order on melting (but retention of strong short-range order) results in a sharp increase in resistivity (Faber, 1972). Changes in resistivity can be deduced from resistance measurements, either of the metal sample itself using a four-terminal technique (e.g., Weir et al., 2012), or of the entire heating circuit including the lead resistance and influence of contact resistance (e.g., Boehler, 1986; Sinmyo et al., 2019). The use of resistance measurements as a melting criterion is similarly complicated by the variety of other factors that can affect resistance. These include the positive temperature dependence on resistivity, the negative pressure dependence on resistivity for most metals (Bridgman, 1949, chap. 9; Bridgman, 1952), resistivity changes across solid–solid phase transitions, the effect of changes in sample dimensions or morphology on resistance, oxidation of the filament or reaction with the pressure medium (Boehler et al., 1986), and high-pressure resistivity saturation (Kiarasi & Secco, 2015; Ohta et al., 2016; Pozzo & Alfè, 2016; Sundqvist & Tolpygo, 2018; Inoue et al., 2020). Nevertheless, changes in resistance have been used as a reliable melting criterion in internal resistive heating experiments on several metals, including Fe (Boehler, 1986; Sinmyo et al., 2019), Li (Schaeffer et al., 2012) and Sn (Weir et al., 2012).

The larger filament used in our IRH design (chapter 2) may provide the possibility to detect melting via *in situ* observation of liquid diffuse scattering. This would allow corroboration of any resistance changes detected at the filament melting point, and support the use of resistance measurements using our design as a lab-based melting criterion with potentially significantly reduced temperature uncertainties compared to laser heating techniques. Furthermore, if the temperature stability of our IRH design is maintained above the filament melting point, it may provide a useful technique for obtaining structural measurements of metallic liquids at extreme conditions. In this chapter we investigate the effect of filament melting on the electrical and temperature characteristics of our IRH design, taking the melting curve of titanium as a case study. Titanium is a useful candidate material to study as its resistivity is higher than that of rhenium (allowing efficient heating), only one solid phase is stable along the melting curve (bcc β-Ti; Dewaele et al., 2015), and its melting curve (based on XRD measurements) falls well within the range of experimental conditions accessible with our IRH design (1941 K at ambient pressure, ∼2600 K at 50 GPa; Rumble, 2021; Stutzmann et al., 2015).

4.2 Methods

4.2.1 Preliminary Experiments

To test the behaviour of our 'split-gasket' IRH design as it is heated across the melting point of the filament we first manufactured titanium 'bow-tie' shaped filaments and prepared an experiment in the same manner as described in chapter 2. The filament was laser-machined from 15 μm thick rolled titanium foil (99.99% purity, GoodFellow TI000232) to the same specifications as the rhenium filaments used previously. A different set of optimised process parameters were used (appendix B) with lower power to prevent increased thermal damage and oxidation due to the different machining properties compared to the rhenium filaments. The Ti filament was loaded into a 150 μm pressure chamber in a stainless steel IRH split-gasket, with compressed plates of Al_2O_3 nanopowder as the thermal insulation. Slight shearing of the filament was observed on compression, most likely as a result of a slight mis-orientation during the loading. Nevertheless, a complete circuit was formed, with a measured resistance across the gasket holder prior to heating of ∼4 Ω. To monitor any warming of the cell body during an IRH experiment, a type-K thermocouple was placed at the base of the WC seat on one side of the DAC. The power supply was operated in power-control mode, with the power manually increased to a maximum of ∼115 W over a period of around 70 minutes, resulting in a peak temperature of ∼2400 K. Temperature across the filament hotspot was measured spectroradiometrically using the system in place at Bristol, and electrical data from the power supply was automatically logged throughout the experiment. The maximum measured temperature within the cell body at the thermocouple junction was 107 °C. The filament temperature at a set power is greater than that for a rhenium filament (chapter 2) as expected for the higher resistivity of titanium (172 nΩ·m for Re at 273 K and 390 nΩ·m for Ti at 273 K; Rumble, 2021), although this is likely offset slightly by the slightly thicker Ti filament (12.5 μm thick for the Re filaments), explaining why the difference is not very large. A linear fit to the power–temperature relationship in the region below 61 W yields a slope of 13.7 ± 0.3 K/W (Fig. 4.1), which is the range observed for rhenium filaments of similar dimensions (chapter 2). This suggests that the heating efficiency of the IRH design is strongly controlled by the thermal insulation as well as the filament material. A post-heating pressure of 22.1 ± 0.7 GPa was estimated from the shift in the Raman spectra of the diamond anvil measured at the culet surface using the calibration of Akahama & Kawamura (2010). The experiment was monitored visually throughout, and at a temperature of ∼2360 K a region of melt clearly began to form, rapidly fluctuating in brightness and at several points appearing to flow around the filament region of the pressure chamber. There were repeated instances of melt blob formation, fluctuation, and movement as the power was further increased. The measured temperature of the first melt 'blob' to appear (2360 K) is within error of the melting point predicted by Stutzmann et al. (2015) for titanium at 22 GPa. It is important to note that these

visual observations are much more reliable indicators that melting has occurred than the subtle observations of motion used in the laser-speckle method. However, it is not necessarily a useful criterion to determine the melting point as a significant volume of melt may be needed before movement is observed, and the actual melting point may be lower.

A plot of the filament temperature against electrical power shows a change in slope during the experiment (Fig. 4.1). A linear fit to the data below 61 W yields a slope of 13.7 ± 0.3 K/W, and a fit to the data above 84 W yields a slope of 6.1 ± 0.4 K/W. The intersection of the two fits is at 2096 K (61.04 W). However, it is not clear where the change of slope actually occurs as there is a region of significant scatter between ∼50 W and ∼84 W. The power–temperature curve appears to first plateau at ∼1980 K from ∼50 W, before moving in a step like fashion to ∼2220 K. After this there is a sharp drop in temperature as the power is increased beyond 70 W, along with significant temperature fluctuations before the temperature stabilises and begins to linearly rise with power again beyond 84 W (and 2240 K).

The electrical resistance data may provide a better constraint on the melting temperature as a discontinuity (i.e., a resistance jump) would be expected to occur across the melting point. This criterion has been applied by other authors to the melting curve of iron, and may be sensitive to very small volume fractions of melt (e.g., Sinmyo et al., 2019; Basu et al., 2020; Hou et al., 2021). A plot of the power–resistance relationship (Fig. 4.2) reveals two resistance jumps during the experiment. The second jump at ∼78 W appears to correlate with the change in slope of the power–temperature plot, with an average temperature at the discontinuity of 2104 ± 35 K. The first jump at ∼55 W occurs at a lower temperature of 2001 ± 31 K. Multiple instances of rapid resistance increase as significant fractions of melt form would be consistent with the repeated short bursts of rapid temperature fluctuation and movement observed visually during the experiment. If these resistance jumps do correlate with the onset of melting then the first resistance discontinuity would represent the melting temperature. However, it is difficult to assign physical mechanisms to any of these observed features as they do not occur at the same time as other indicators of melting such as a plateau in the power–temperature relationship or the visual observation of melt motion. There is also significant scatter in the measured data which is likely due to the stepped and somewhat inconsistent manual increase of power during the experiment. Deformation (including sub-solidus deformation) of the filament (as well as changes in contact and lead resistance) will also lead to changes in the power–resistance relationship. It is interesting to note that beyond ∼10 W the circuit resistance decreases with increasing power (and therefore temperature), rather than an expected monotonic increase (Fig. 4.2). This is likely due to deformation of the filament, although improvement of the filament-gasket contact and the effect of thermal pressure may also play a role.

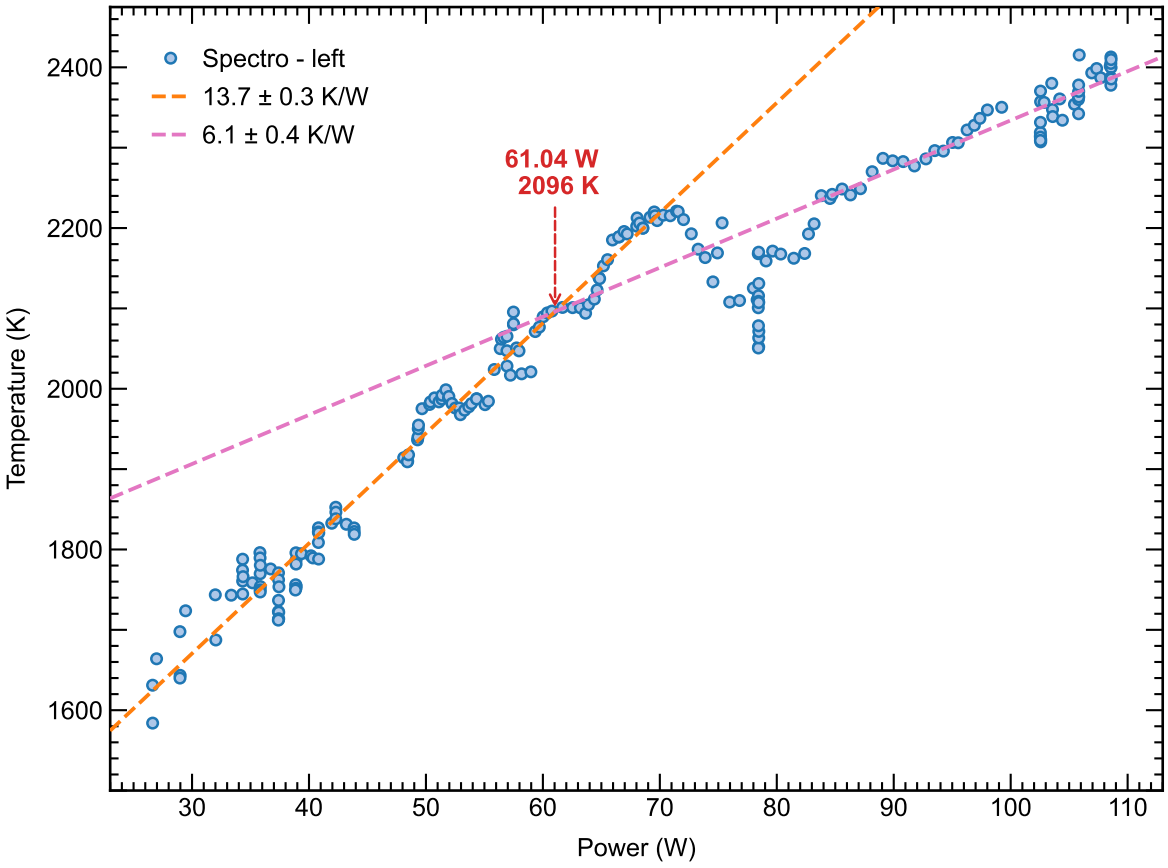

Figure 4.1: *Power–temperature relationship during experiment #1 at ∼22.1 GPa. A 'bow-tie' style filament was used and the power increased incrementally and manually. Significant scatter results from the manual power supply operation. No clear power–temperature plateau is observed, but there is a change in slope during the experiment. The intersection of linear fits to the data below 61 W (orange dashed line) and above 84 W (pink dashed line) is at 2096 K. The temperature points are the maximum value along a 1D profile. The uncertainty in individual measurements is smaller than the scale of the markers.*

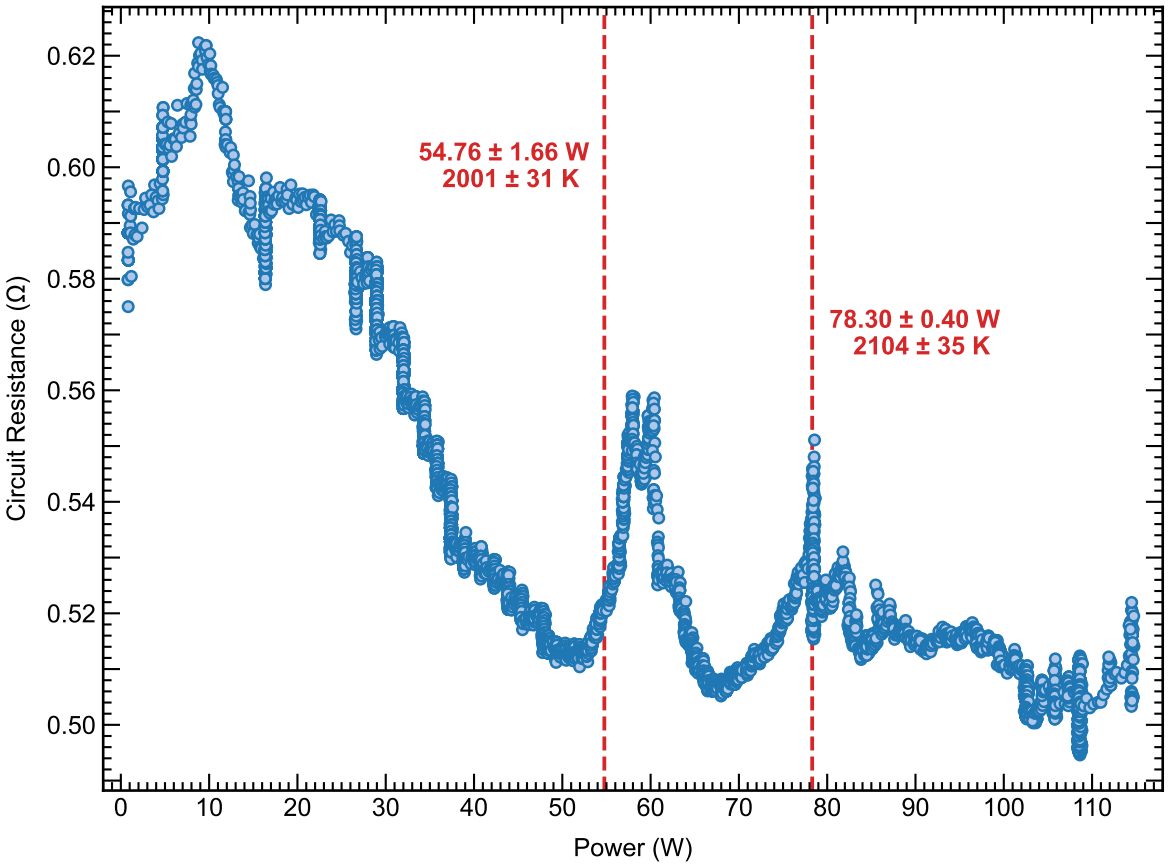

Figure 4.2: *Circuit resistance against electrical power during experiment #1 at ∼22.1 GPa. A 'bow-tie' style filament was used and the power increased incrementally and manually. The downward trend of the circuit resistance may be a result of filament deformation, the effect of increasing thermal pressure on resistivity, or changes in the contact resistance (e.g., at the filament-gasket contact). Two significant discontinuities are apparent in the circuit resistance at high-temperature. The first resistance jump is interpreted as an indicator of the onset of melting. The average temperature across the resistance discontinuity is 2001 K.*

4.2.2 Experiments Using Rectangular 'Ribbon' Filaments

The scatter in the data, temporal fluctuations in temperature and resistance at a set power, and the complex geometry of the 'bow-tie' filaments makes it difficult to untangle the effects of melting, sub-solidus phase transitions, and changes in filament shape and morphology. To better constrain or reduce the number of these factors the filament shape should be simplified, filament confinement improved, and the power increased at a constant rate throughout the experiment.

To simplify the filament geometry we machined rectangular ribbon filaments 20 μm wide and 150 μm long from the same 15 μm thick rolled titanium foil. Single pieces of form-fitting insulation may also improve confinement of the thin ribbon filaments and help to maintain the geometry and stabilise any melt that forms. To test this we manufactured single-pieces of insulation from ∼50 μm thick polished Al_2O_3 polycrystalline plate. A 30 μm wide region was first laser milled to a thickness of ∼20 μm, and 140 μm diameter discs cut out around this (Fig. 4.3). This allowed the titanium filaments to be loaded into the depression in the disc of insulation, with ∼5 μm extending beyond the insulation on either side to promote better contact between the filament and gasket during loading. A flat disc of polycrystalline Al_2O_3 laser milled to a thickness of ∼25 μm was loaded above the filament. Compressed plates of alumina nanopowder were used to fill the slots in the culet region. This was done to allow the deformation as the cell was compressed to be taken up by the slots rather than the thin filament. However, we found that the loading procedure was complicated by the brittle nature of the alumina insulation, with the pieces commonly splitting in half on loading, leading to insufficient insulation below the filament, or significant misalignment that prevented a contact. As a result, the Ti ribbon filaments were loaded directly onto compressed plates of alumina nanopowder in the same manner as described in chapter 2. Slight rotation of several filaments occurred as the cells were closed and initially compressed, but no significant shearing was observed on compression and the filament geometry remained stable in all the cells, with no significant deformation from the rectangular shape. Figure 4.4a shows a photomicrograph of a cell compressed to ∼30 GPa.

We conducted four heating runs using cells compressed to between 13 and 40 GPa. The pressure was measured before and after heating using the shift in the high-frequency edge of the Raman spectra at the culet surface and the calibration of Akahama & Kawamura (2010). The power supply was again operated in power control mode, but, unlike the previous manually controlled experiment, we automated the procedure so that the set power was steadily increased at a constant rate of 0.1 W every 8 seconds (0.75 W/min). This was done to reduce scatter in the data and make any changes in electrical characteristic easier to identify. In each run the power was increased to a point well beyond the onset of visual melt motion to ensure the electrical characteristics above the melting point were measured. At the maximum power the experiments were quenched to room temperature

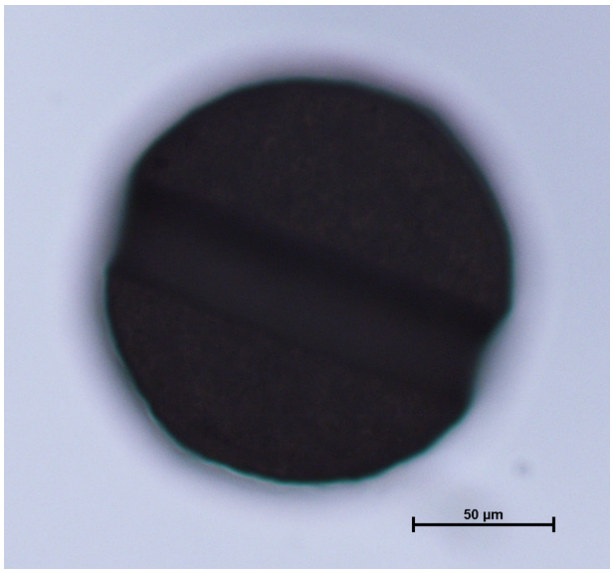

Figure 4.3: *Photomicrograph of single-piece polycrystalline Al_2O_3 insulation that was initially tested. The total piece is ∼50 µm thick. The central slot, designed to fit the rectangular ribbon filament, is 30 µm wide and milled down to a thickness of 20 µm. Further development is needed before such pieces can be used, as during preliminary testing the pieces tended to break along the slot due to their brittle nature. This resulted in significant filament deformation and thinning on the insulation below the filament. Compressed plates of alumina nano-powder were used instead.*

by switching off the power supply, except in one experiment (run #5) where the anvils failed. This anvil failure was likely due to mobile metallic melt coming into contact with the anvil surface and causing thermal damage and/or reaction with the diamond to form titanium carbide. The details of each experiment run are presented in Table 4.1.

The temperature was again measured spectroradiometrically using the system in place at Bristol. In addition, four-colour multi-spectral imaging radiometry (MIR) was used to measure temperature on one side. This allowed the 2D spatial temperature gradients to be measured, and ensured the hotspot could always be measured. This is important because a 1D spectroradiometric temperature profile may underestimate the peak temperature if not perfectly aligned with the hottest part of the sample.

No correction is made for the thermal pressure in each experiment as this would require *in situ* data for the specific experimental geometry. It is likely that thermal pressure is not as high as observed in chapter 2 due to the different sample geometry, which in these experiments is more similar to laser heating. However, laser-heating experiments using similarly hard pressure media such as MgO exhibit thermal pressures up to ∼10 GPa across a similar P-T range, suggesting it will be significant in these experiment (e.g., Lord et al., 2014b).

Table 4.1: *Experimental conditions of Ti melting experiments. Pressure was measured from the Raman shift of the diamond anvil measured at the culet surface using the calibration of Akahama & Kawamura (2010).*[†]

Exp	Max Power (W)	P (GPa)	
		Pre-heating	Post-heating
#1[‡]	114.7	···	22.1(7)
#2	95.1	19.7(6)	23.5(7)
#3	26.4	13.8(4)	12.5(4)
#4	44.7	29.6(9)	31.1(9)
#5	72.9	39.1(12)	···[*]

[†]Uncertainties in parentheses are on the last digit and are 1σ
[‡]Preliminary experiment with 'bow-tie' filament and manual power control
[*]Experiment ended with anvil failure

4.3 Results

Figure 4.5 shows a plot of temperature against electrical power during experiment *#4*, performed at ∼30 GPa. The temperature, measured from ∼1500 K, initially increases linearly with power, although we observe a change in slope at ∼12 W. This kink in the power–temperature relationship is mirrored by a kink and down-turn in the power–resistance plot at a similar power (Fig. 4.6). This feature may be a result of deformation, or a sub-solidus phase transformation: i.e., the expected high-T transition from ω-Ti to bcc β-Ti. A sharp drop in resistivity does occur across the α-β transition at ambient pressure (Maglić & Pavičić, 2001; Bel'skaya & Kulyamina, 2007), but to our knowledge the high pressure resistivity across the ω-β transition has not been measured. The linear increase in temperature continues up to ∼19 W and ∼2300 K. Figure 4.7 shows a selection of snapshots from a video recording of the experiment. In this linear region the heating can be seen to be very even, with the heated region symmetrical and the same shape as the rectangular filament, and with the hotspot located in the centre (Fig. 4.7, marks A to D). At a power of ∼20 W the hotspot was observed to migrate towards the edge of the filament, accompanied by fluctuation in hotspot shape and temperature (mark E), which may be a result of incipient melting or sub-solidus deformation. The power–temperature plot shows that at ∼20.9 W the temperature drops suddenly, and a stable plateau then forms, with the temperature remaining extremely stable for a period of 15 to 20 minutes as the power is increased further to ∼35 W (Fig. 4.5). The video recording shows that the hotspot shape and location also remains stable during the plateau (Fig. 4.7, mark F), although several sharp spikes in temperature do occur, which may be a result of localised run-away flash heating (Fig. 4.5). The plateau in the power–temperature relationship is interpreted as melting, with the temperature remaining stable as the melt fraction increases with power. The average hotspot temperature across the plateau is 2196 K, with a standard deviation of 50 K. The plateau can also be seen in a plot of the circuit resistance against temperature (Fig. 4.8), with the marked changed in behaviour at the melting point particularly obvious. An average of the cluster in this plot yields an identical melting temperature. The start of the temperature plateau correlates with a sharp discontinuity at 20.88 ± 0.06 W in a plot of circuit resistance against power (Fig. 4.6). This jump in resistance provides another condition for the onset of melting, as the resistivity of the liquid phase should be considerably higher than that of the solid. The mean of the temperatures measured during the resistance jump was 2237 ± 17 K, within error of the plateau temperature. The sharpness of the resistance discontinuity likely makes this a tighter constraint on the melting temperature. The end of the temperature plateau is characterised by increased fluctuations in temperature, and rapid fluctuations in the hotspot change as well as moving 'blobs' and 'arcs' of hot material we presume to be localised mobile pockets of melt (Fig. 4.5; Fig. 4.7, mark G and H). A larger channel of hot material (that we presume to be a channel of melt) then forms and migrates away from the original filament location as the temperature rapidly increases (Fig. 4.7, mark H). The rapid temperature increases is presumably due to the higher resistivity of the melt channel now

conducting the electricity, and a run-away heating effect as an increase in both the volume of melt fraction and temperature will increase the resistivity further. The snapshots in figure 4.7 (marks I and J) show that the geometry of this apparent melt channel remains remarkably stable for some time, despite the high temperature which suggests it is wholly molten. The formation and migration of this melt channel is associated with a sharp drop in the circuit resistance (Fig. 4.6). This resistance drop is most likely due to the migration of the melt to form a shorter electrical path length. This is corroborated by the post-heating observation that metallic material migrated out of the central pressure chamber and into the alumina filled slots during the experiment (Fig. 4.4b). Although there is a lot of scatter in the data due to temperature fluctuations, the temperature appears to plateau a second time between ~38 W and ~43 W rather than continuing to rise. This may represent a thermal limit to the heating efficiency of the experiment, or the onset of melting of the alumina pressure medium. The temperature of this plateau, 3914 ± 158 K, is consistent with the expected melting temperature of Al_2O_3 (Shen & Lazor, 1995; Wang et al., 2000). The end of the experiment is characterised by further fluctuations in temperature and migration of melt before the experiment was quenched (Fig. 4.7), mark K).

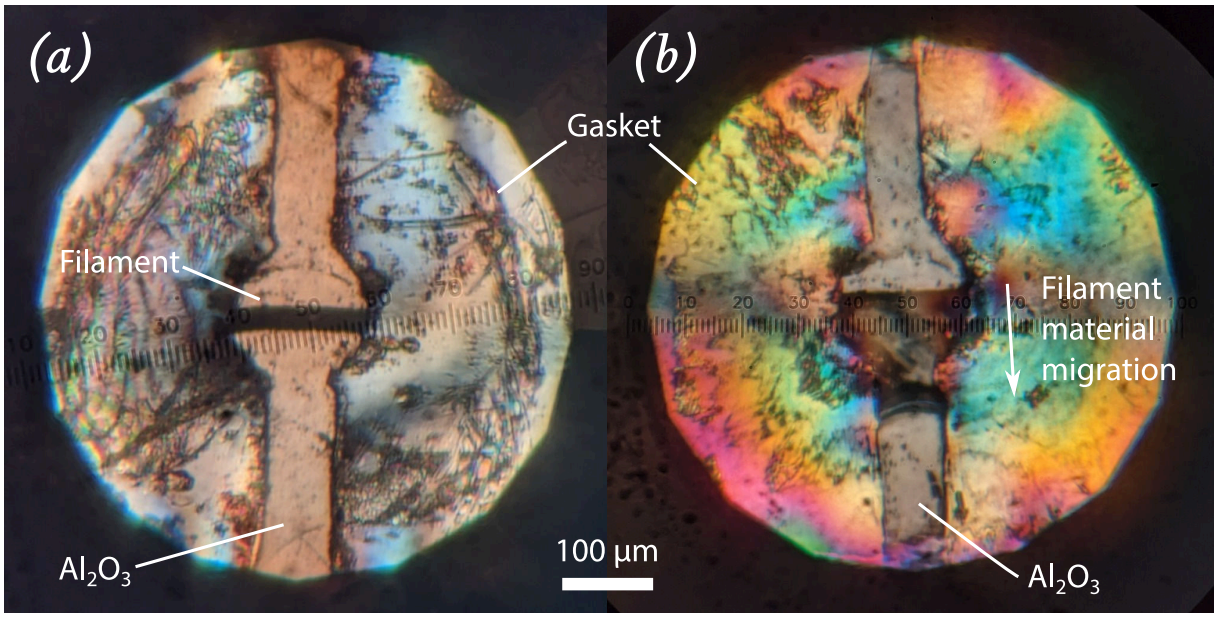

Figure 4.4: *(a) Photomicrograph of experiment #4 prior to heating at 29.6 GPa (pre-heating pressure). No significant deformation of the rectangular filament is apparent. (b) Photomicrograph of experiment #4 after heating at 31.1 GPa (post-heating pressure). Migration of the molten filament into the alumina filled slots is clear. Some material is left in the original filament position, but a large area in the central region is now transparent. The shorter path length results in a lower overall circuit resistance.*

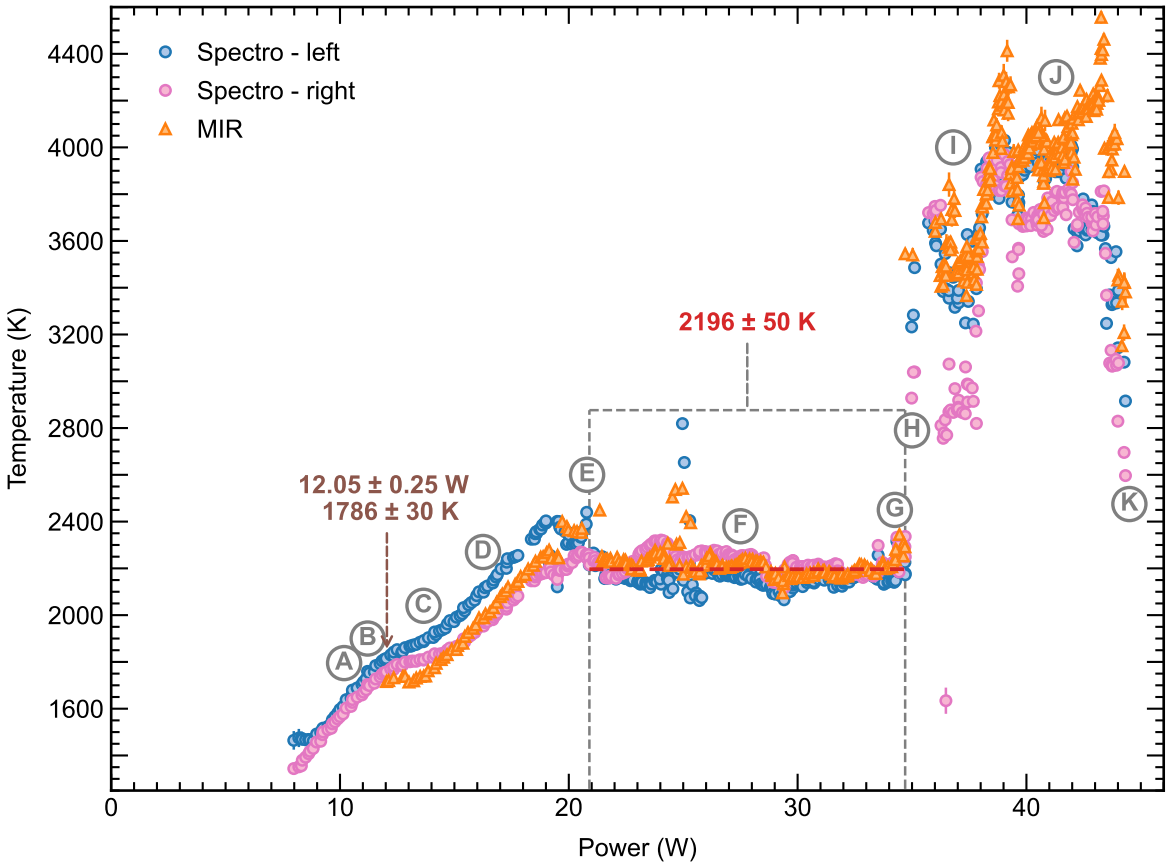

Figure 4.5: *Power–temperature relationship during experiment #4 at ∼31 GPa. The temperatures are the maximum recorded values across 1D profiles (for spectroradiometry) or 2D maps (for MIR). Plotted uncertainties on individual data points are 1σ and are smaller than the scale of most markers. A kink in the power–temperature relationship occurs at 12.05 W and 1786 K. A temperature plateau appears from around 20.9 W. The average temperature of the plateau (red dashed line) is 2196 ± 50 K. The letter marks correspond to the video snapshots captured throughout the experiment shown in figure 4.7.*

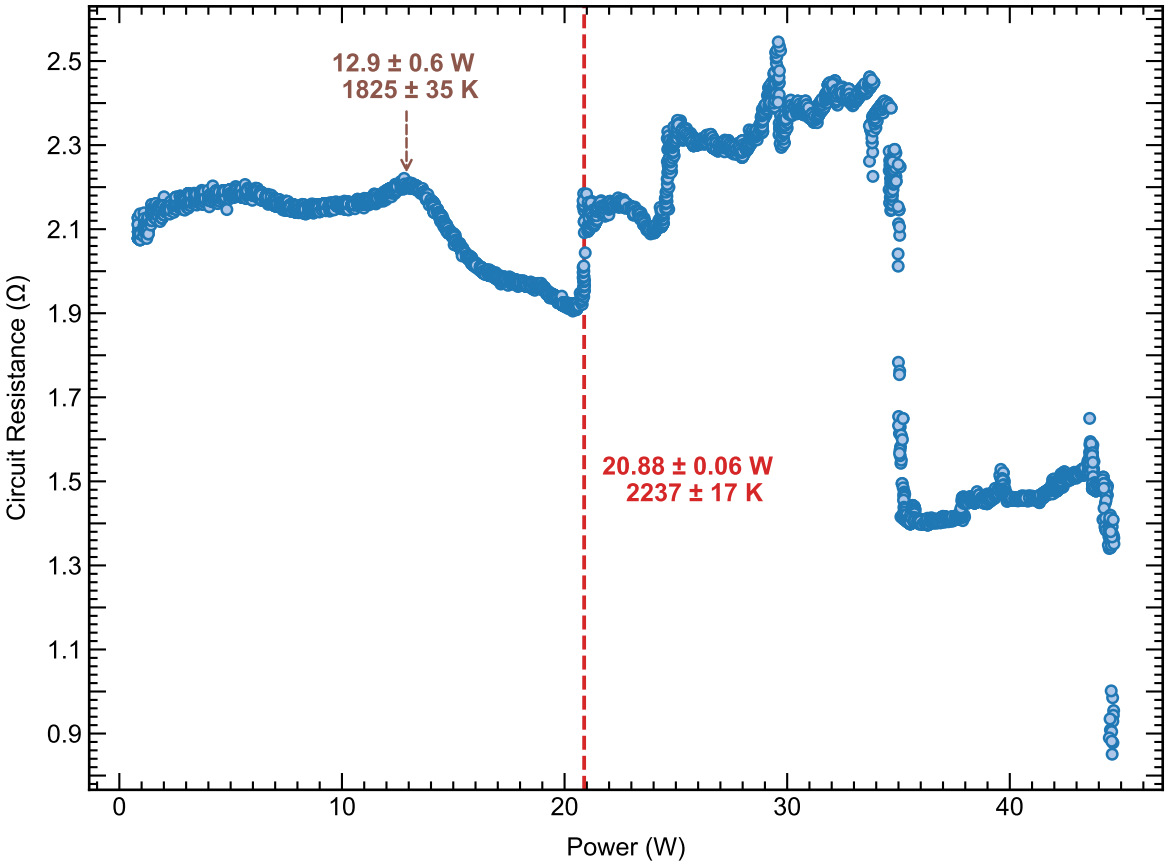

Figure 4.6: *Variation in circuit resistance against electrical power during experiment #4 at ∼31 GPa. The change in slope at 12.9 W corresponds to the change in slope in the power–temperature relationship ∼12 W. The jump in resistance at 20.88 W is interpreted as the onset of melting and coincides with the start of a power–temperature plateau. The average temperature across the resistance discontinuity is 2237 ± 17K. The drops in circuit resistance beyond the melting point are interpreted as due to the migration of melt into the culet slots.*

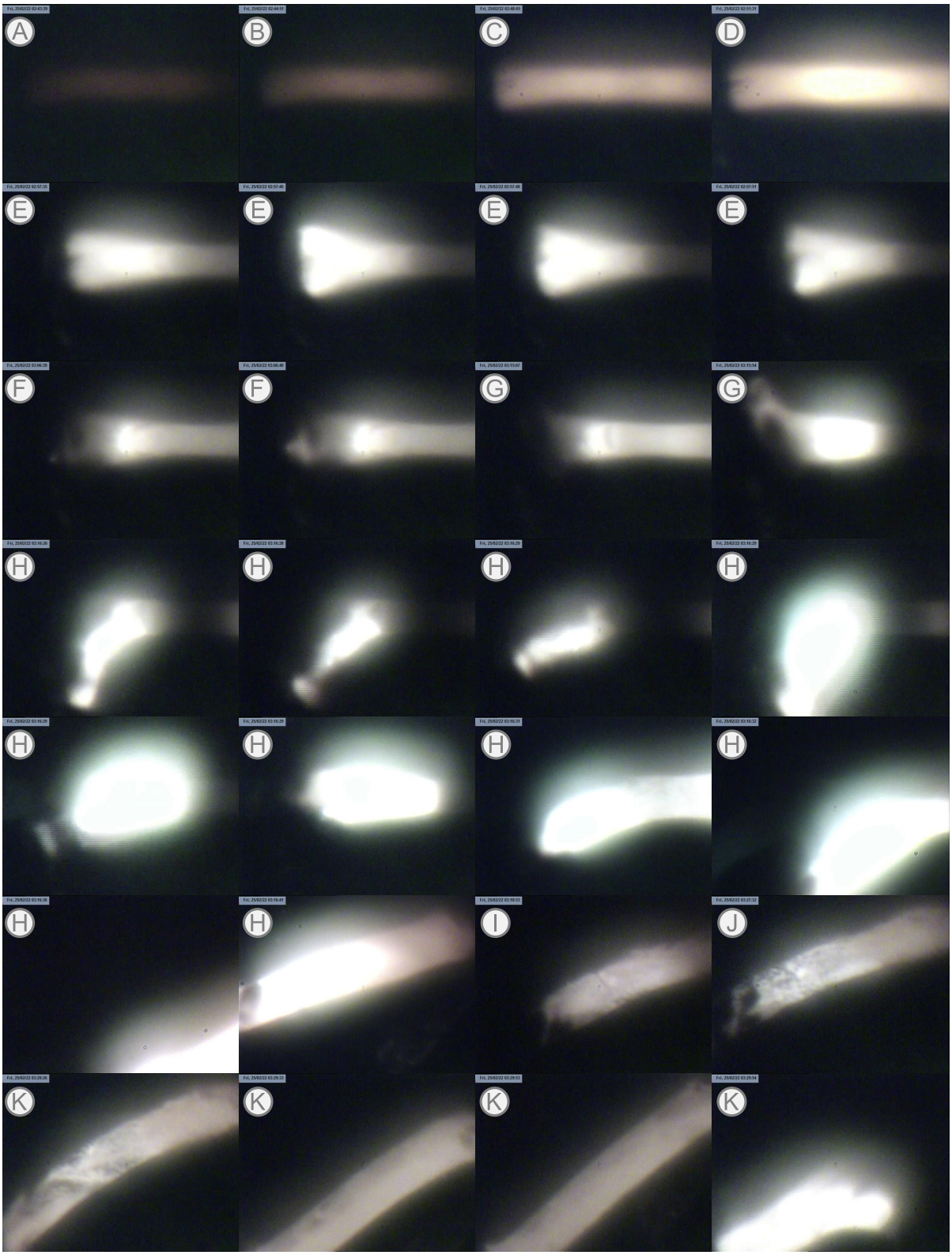

Figure 4.7: *Video frames captured during experiment #4 (caption continued on following page).*

Figure 4.7: ***(Previous page)*** *Video frames captured during experiment #4 on one side. The letter marks correspond to points in the power–temperature curve plotted in figure 4.5. A to D: The rectangular filament heats evenly across its length, with the hotpot located centrally. E: The hotspot migrates to an edge contacting the gasket and fluctuates in shape and brightness. F: No significant changes occur and the hotspot appears stable. G: Fluctuations in shape and brightness begin again. H: Rapid fluctuations in the hotspot brightness and shape continue along with apparent movement. Several 'arcs' of molten material briefly form before the entire filament appears to melt and migrate out of frame. I to J: The tube of melt appears to stabilise in a new position. Apparent movement and flow is observed within the heated region. K: The material begins to migrate again before the experiment is quenched.*

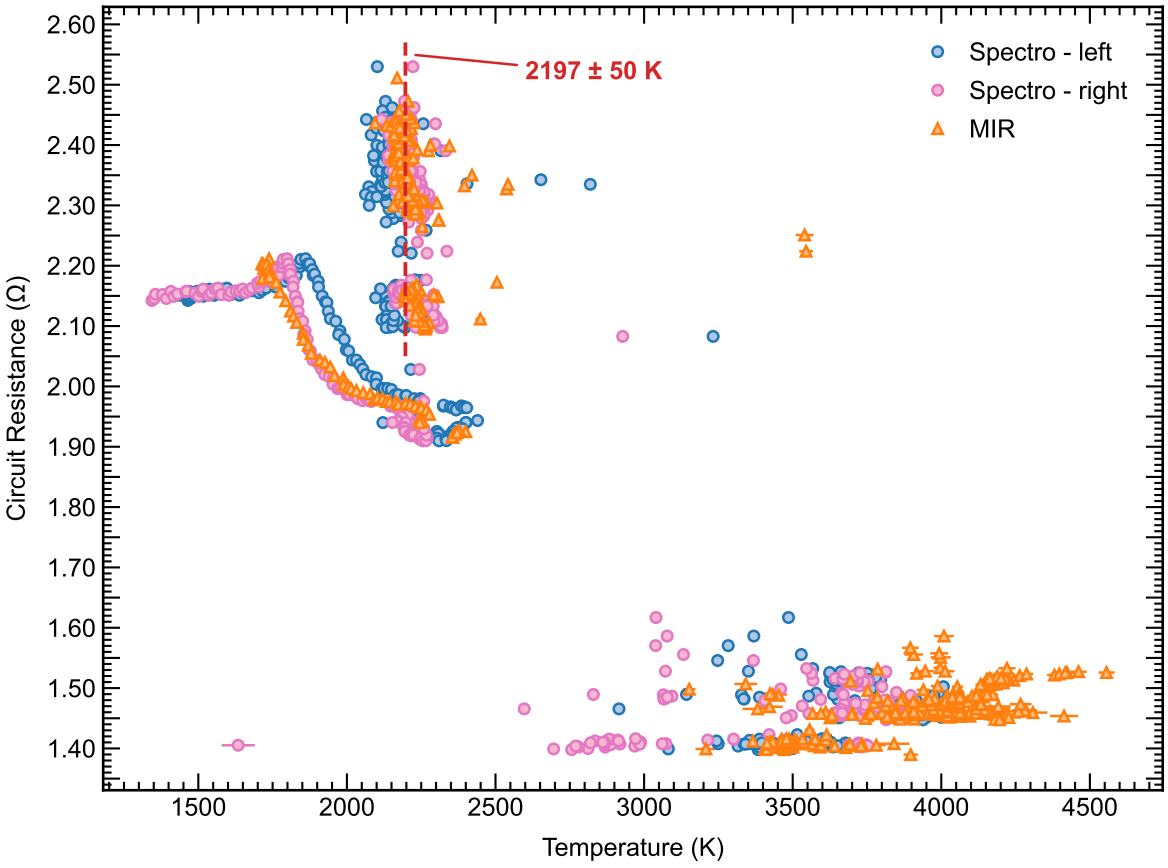

Figure 4.8: *Circuit resistance plotted against temperature for experiment #4. The cluster of data around 2200 K corresponds to the plateau seen in the power–temperature relationship. The cluster of data at high temperature is presumed to result from high resistivity melt migrating into the filament slots, resulting in lower overall circuit resistance (due to the shorter path length).*

Similar features can be seen in the other three experiments. Figures 4.9 to 4.14 show plots of temperature and circuit resistance against electrical power during these experiments. A kink in both the power–temperature and power–resistance plots during the period of initial warming is apparent in all experiments. The average temperature at the inflection point in the power–temperature curve is similar to the temperature at the inflection point in the power–resistance curve for all experiments. A resistance discontinuity was also observed in all three experiments, and the temperatures at these points was similarly extracted. Visual observations of melt motion were similar to that described for run *#4* previously.

Power–temperature plateaus were also observed in experiments *#3* and *#5*, and the average temperature during both plateaus were within error of the temperatures measured at the resistance jump concurrent with their onset (run *#5*, Figs. 4.9 and 4.10; run *#3*, Figs. 4.13 and 4.14.) No plateau in the power–temperature relationship during experiment *#2* was observed (Fig. 4.11). It is not clear that a plateau did not form in this experiment, as from ∼31 W the filament hotspot became very mobile and migrated out of the field of view, which was not fully corrected until ∼39 W. A change in slope is apparent either side of this region, suggesting it bounds the melting temperature. The resistance jump occurred at ∼38 W (Fig. 4.12), which confirms this, but the average temperature at this point (2015 ± 48 K) may underestimate the melting temperature if the real hotspot was not captured. Nevertheless, this temperature is within error of the temperature at the resistance jump in run *#1*, which was conducted at a similar pressure. In all other runs the filament hotspot was carefully tracked by moving the cell to ensure it always remained within the field of view.

The plateau in run *#3*, which was conducted at the lowest pressure (12.5 GPa after heating), displays much more scatter than the other experiments, resulting in a much greater uncertainty on the plateau temperature. The more significant temperature fluctuations are likely to be a result of greater melt mobility due to poorer confinement at lower pressures. Visual observations throughout the experiment also suggest increased mobility of produced melt. In contrast, much less movement was observed in the highest pressure run (*#5* at ∼40 GPa), suggesting increased pressure helps stabilise the sample geometry and better confine melt products. This can also be seen in the power–resistance data from run *#5* (Fig. 4.10), where the circuit resistance increases throughout the experiment with no sharp drops. Sharp drops in the circuit resistance were observed beyond the melting point in all other experiments and are presumed to result from mobile melt migrating towards or into the slots where the circuit path length is shorter. As a result the power–resistance relationship in run *#5* is much simpler, with three distinct domains apparent, bounded by changes in slope at the sub-solidus inflection point and at the presumed melting temperature.

The power and temperature conditions of each of these key features (resistance discontinuities and temperature plateaus) for each experiment are summarised in table 4.2.

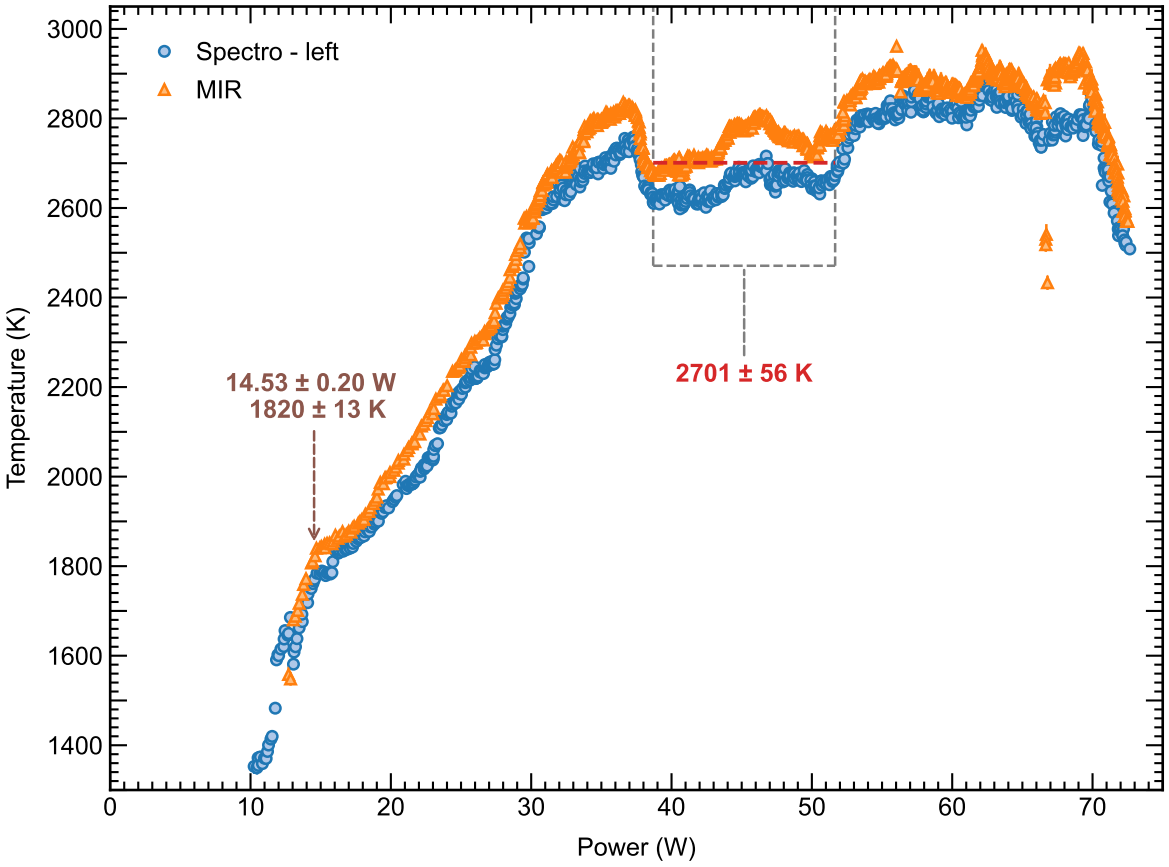

Figure 4.9: *Power–temperature relationship during experiment #5 at ∼39 GPa. The temperatures are the maximum recorded values across 1D profiles (for spectroradiometry) or 2D maps (for MIR). Spectroradiometric temperature data is only shown for one side due to issues with the optical system. Plotted uncertainties on individual data points are 1σ and are smaller than the scale of most markers. A kink in the power–temperature relationship occurs at 14.53 W and 1820 K. A temperature plateau appears from around 38 W. The average temperature of the plateau (red dashed line) is 2701 ± 56 K. Only average of the first portion of the plateau is fitted as the temperature continues to rise in a stepped fashion. This corresponds to the monotonic increase in circuit resistance throughout this period.*

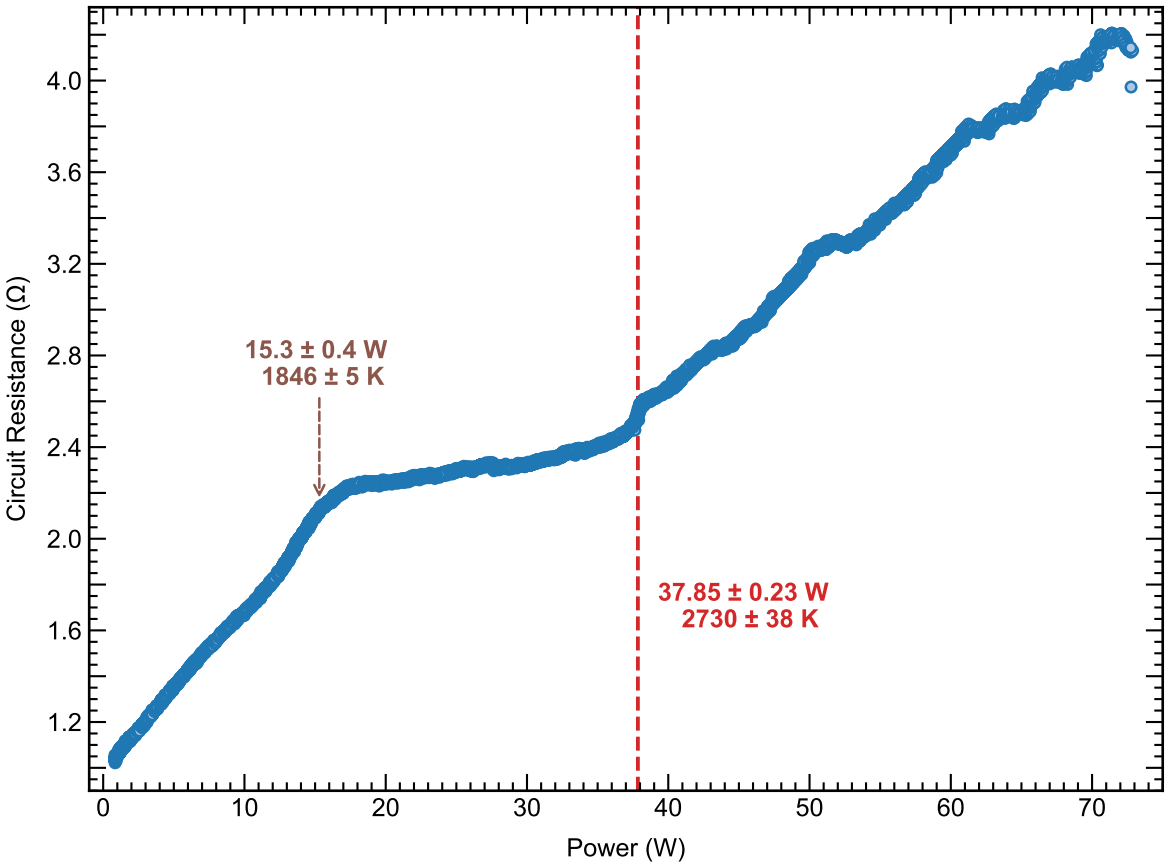

Figure 4.10: *Variation in circuit resistance against electrical power during experiment #5 at ∼39 GPa. Two changes in slope are obvious. The first change in slope at 15.3 W corresponds to the change in slope in the power–temperature relationship ∼14.5 W. The second change in slope is interpreted to be a melting signature. The initial jump in resistance at 37.85 W is taken to indicate the onset of melting and coincides with the start of a power–temperature plateau. The average temperature across the resistance discontinuity is 2730 ± 38K. The increase in circuit resistance with power is due to the positive effect of temperature on resistivity, with an increased dependence above the melting point. In contrast to other experiment no large fluctuations or drops in resistance are observed. This is presumed to be due to improved sample confinement and more limited melt mobility at the higher pressure of this experiment.*

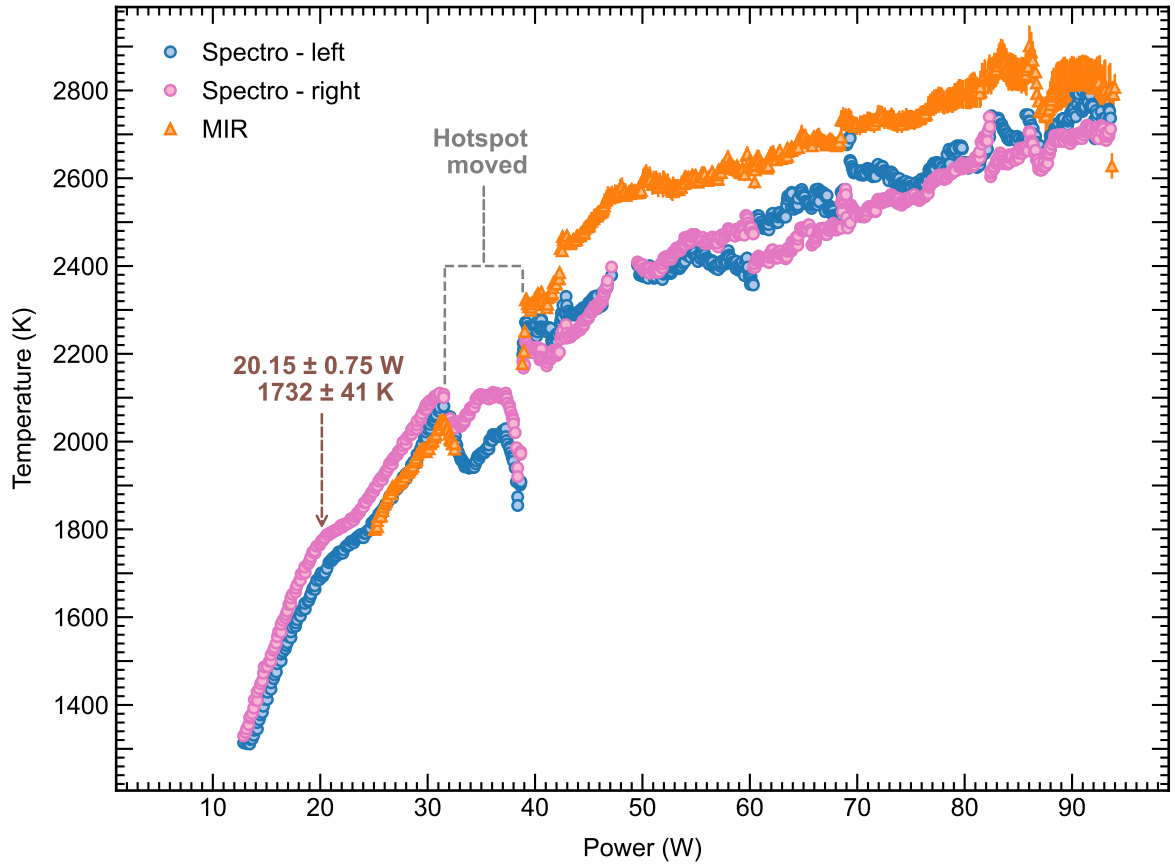

Figure 4.11: *Power–temperature relationship during experiment #2 at ∼23.5 GPa. The temperatures are the maximum recorded values across 1D profiles (for spectroradiometry) or 2D maps (for MIR). Spectroradiometric temperature data is only shown for one side due to issues with the optical system. Plotted uncertainties on individual data points are 1σ and are smaller than the scale of most markers. A kink in the power–temperature relationship occurs at ∼20.15 W and 1732 K. A change in slope between ∼30 W and 50 W is apparent. The hotspot migrated out of the field of view in the range indicated.*

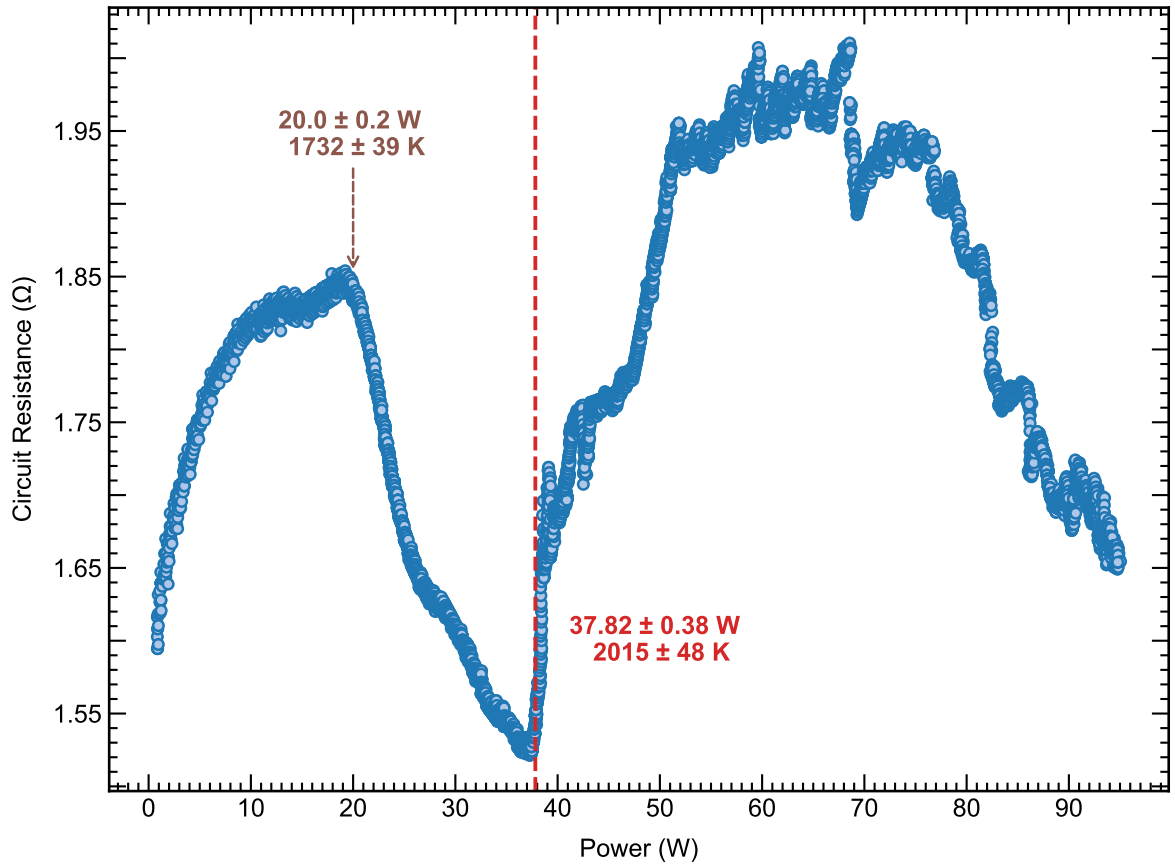

Figure 4.12: *Variation in circuit resistance against electrical power during experiment #2 at ∼23.5 GPa. Fluctuations and drops in resistance are likely due to sub-solidus deformation of the filament and melt migration. The discontinuity at 20 W corresponds to the change in slope in the power–temperature relationship 20.15 W. The sharp discontinuity at 37.82 W is taken to indicate the onset of melting. The average temperature across the initial jump in resistance is 2015 ± 48K.*

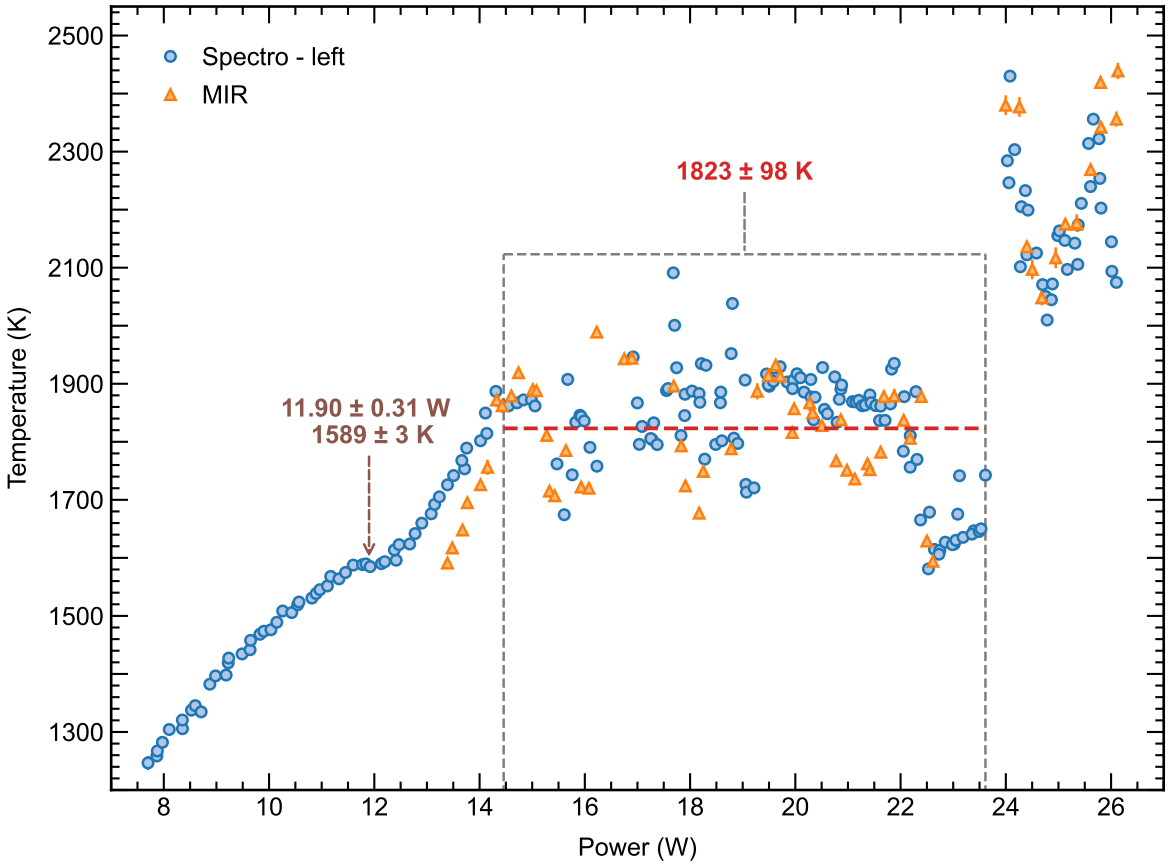

Figure 4.13: *Power–temperature relationship during experiment #3 at ~12.5 GPa. The temperatures are the maximum recorded values across 1D profiles (for spectroradiometry) or 2D maps (for MIR). Spectroradiometric temperature data is only shown for one side due to issues with the optical system. Plotted uncertainties on individual data points are 1σ and are smaller than the scale of most markers. A kink in the power–temperature relationship occurs at 11.9 W and 1589 K. A temperature plateau appears from around 14 W. The average temperature of the plateau (red dashed line) is 1823 ± 98 K. The increased scatter and temperature fluctuations in this experiment is presumed to be due to increased melt mobility and poorer sample confinement at the lower pressure of this experiment.*

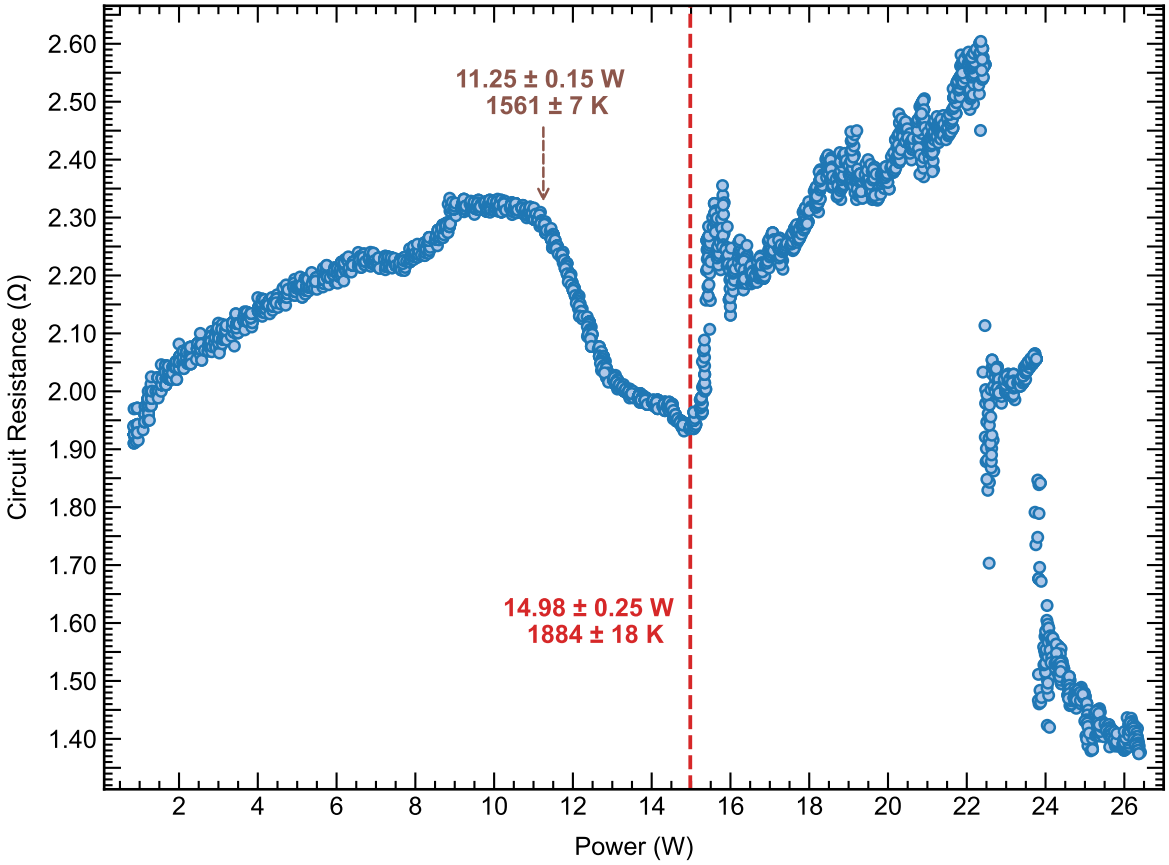

Figure 4.14: *Variation in circuit resistance against electrical power during experiment #3 at ∼12.5 GPa. The change in slope at 11.25 W corresponds to the change in slope in the power–temperature relationship ∼11.9 W. The resistance discontinuity at ∼15 W is interpreted as the onset of melting and coincides with the start of a power–temperature plateau. Significant fluctuations in resistance occur across the discontinuity, likely due to increased mobility of produced melt. The average temperature, 1884 ± 18K is therefore taken only across the initial jump in resistivity, interpreted to indicate the first onset of melting. The drop in circuit resistance beyond ∼22 W is interpreted as due to the migration of melt into the culet slots.*

Table 4.2: *Summary of power (P) and temperature (T) conditions of features observed in Ti melting experiments.*[†]

Exp	P-T Kink		P-R Kink		Resistance Jump		T Plateau (K)
	P (W)	T (K)	P (W)	T (K)	P (W)	T (K)	
#1[‡]	···	···	···	···	54.76(166)	2001(31)	···[*]
#2	20.15(75)	1732(41)	20.00(20)	1732(39)	37.82(38)	2015(48)	···[*]
#3	11.90(31)	1589(3)	11.25(15)	1561(7)	14.98(25)	1884(18)	1823(98)
#4	12.05(25)	1786(30)	12.90(60)	1825(35)	20.88(6)	2237(17)	2196(50)
#5	14.53(20)	1820(13)	15.30(40)	1846(5)	37.85(23)	2730(38)	2701(56)

[†]Uncertainties in parentheses are on the last digit and are 1σ

[‡]Preliminary experiment with 'bow-tie' filament and manual power control

[*]No power–temperature plateau apparent

4.4 Discussion

Fig. 4.15 shows a pressure–temperature (P–T) diagram with the temperatures of each of the features described in section 4.3. The melting temperatures and curves previously reported by Errandonea et al. (2001) based on the laser-speckle method and by Stutzmann et al. (2015) based on the onset of a liquid diffuse scattering signal are shown for comparison. The sub-solidus phase boundaries from Dewaele et al. (2015) are also shown for reference. The P–T slope defined by the kinks in the power–temperature and power–resistance curves follows that of the ω–β transition reported by Dewaele et al. (2015) very closely, but occurs at temperatures ∼550 K higher. The equilibrium position of the ω–β boundary is not well constrained (Kerley, 2003; Velisavljevic et al., 2012; Dewaele et al., 2015), and the transition displays significant hysteresis, with Dewaele et al. (2015) recording the persistence of ω-Ti up to ∼500 K above the determined phase boundary. This transition therefore represents the most likely cause of the feature in our data, although it clearly does not reflect the equilibrium position of the phase boundary. Reversal experiments, or a stepped heating approach with long periods of heating at subsequent temperatures may be able to determine the phase boundary, although at lower pressures it may be below the limit of spectroradiometry in the visible range. Additionally, we do not know what percentage of the titanium filament has to undergo the phase transition for it to be detectable in the electrical data. The temperatures reported here are the maximum of the filament hotspot, and the average temperature of the bulk of the filament will be significantly lower. This will be important if a large fraction of the titanium must convert to β-Ti to manifest in the electrical data, because the average temperature of the entire filament is difficult to measure due to its large size. X-ray diffraction measurements would confirm any correlation between such features in the electrical data and subsolidus phase transitions.

Our melting temperatures, determined from the resistance jumps and power–temperature plateaus (when present), are somewhat surprising and yield a clearly unphysical trend for the melting curve. The melting temperature at 39 GPa (cold pressure; run *#5*) is greater than that predicted by Stutzmann et al. (2015), suggesting that the Ti melting curve is higher than previously reported. Stutzmann et al. (2015) reported significant temperature errors (of ± 300 K), and only measured melting temperature above 47 GPa, with the melting curve partly determined by ab initio calculations. Our determined melting temperature at 39 GPa nevertheless suggests a significantly shallower curve than those reported by Kerley (2003) and Zeng et al. (2011). In contrast, the melting temperature determined in our experiments between 10 and 30 GPa (runs *#1* to *#4*) are anomalously low. Although the melting temperatures in runs *#1*, *#2* and *#4* fall within error of the data reported by Errandonea et al. (2001), they define a clearly unphysical trend. This is clear from the temperature of both the plateau and resistance jump in run *#3* (12.5 GPa post-heating), which is lower than the well-defined ambient pressure melting point of titanium (1941 K; Rumble, 2021).

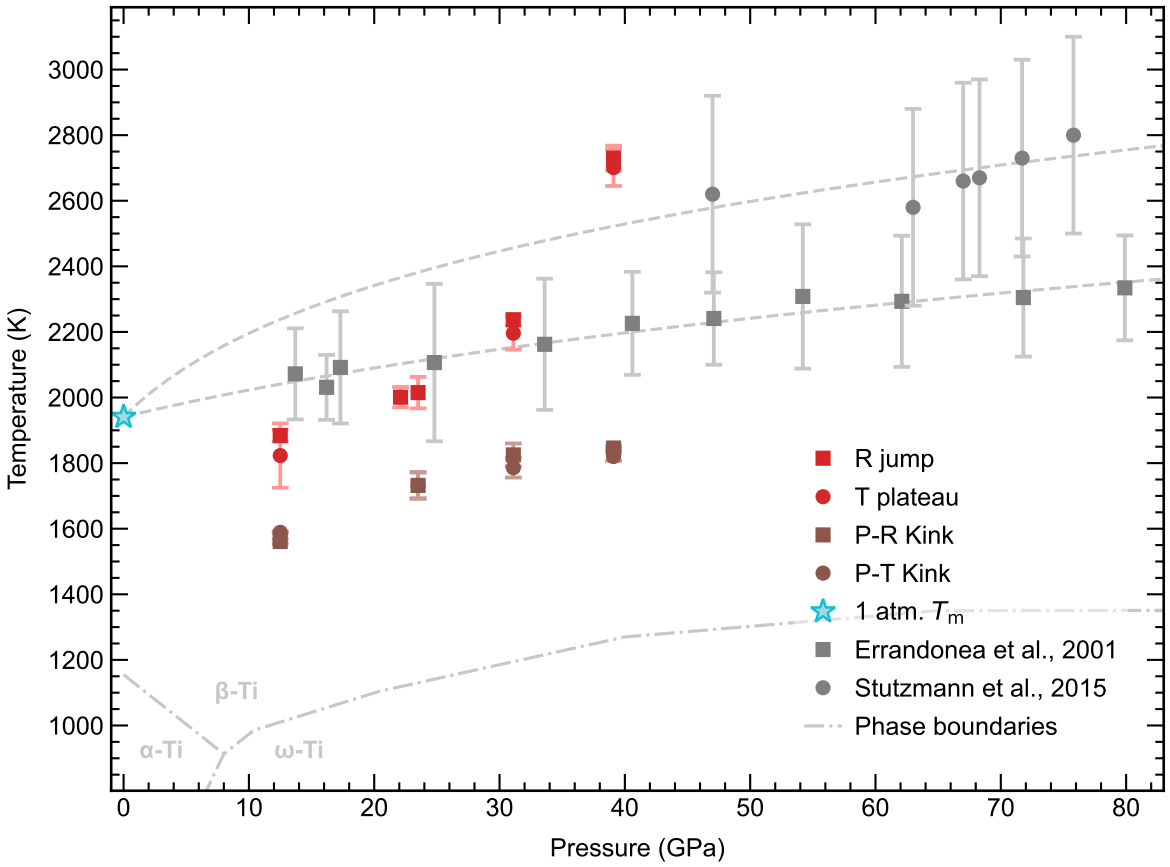

Figure 4.15: *P-T diagram summarising the conditions of features observed in Ti melting experiments. The error bars shown are 1σ. The uncertainty on pressure measurements is 3%. No correction is made for thermal pressure, which may be significant due to the hard Al_2O_3 pressure medium. Melting temperatures derived from resistance discontinuities (red squares) and power–temperature plateaus (red circles) are within error. The trend defined by the melting conditions is clearly unphysical, so no fit is attempted. The trend defined by the kinks in power–resistance (brown squares) and power–temperature (brown circles) curves follows the slope of the ω–β transition, although at temperatures ∼550 K hotter. The ambient melting point (blue star) is at 1941 K (Rumble, 2021). The data of Errandonea et al. (2001) and Stutzmann et al. (2015) are shown for comparison. The titanium phase boundaries (grey dash-dotted lines) are from Dewaele et al. (2015).*

There are several possible causes of such an anomalous melting temperature. The greater temperature fluctuations in run *#3* may have led to an underestimate of the plateau temperature if the temperature drops below the melting point more than it rises above it. Additionally, the lower temperatures in the lower pressure runs required longer exposure times for the temperature measurement, and this may lead to erroneous temperatures if the frequency of temperature fluctuations is faster than the exposure time. However, both of these possibilities are likely to only apply to the lowest pressure run (*#3*). We have previously observed the pressure to drop during heating for IRH experiments at low starting pressures (<5 GPa) due to expansion of the alumina pressure medium into the gasket slots (chapter 2). However, the measured melting temperature in run *#3* is still anomalously low even if the pressure dropped to zero during heating, which is also unlikely given the post-heating pressure. Some minor reaction between the mobile melt fraction and the Al_2O_3 insulation is also expected, similar to the reaction between metallic melt and MgO pressure media observed in Ni melting experiments (Lord et al., 2014b), but this should have a systematic effect on all data. Deviations from the greybody approximation may result in systematic errors of several hundred Kelvin in spectroradiometric temperature measurements (see chapter 1, section 1.3.4; e.g., Deng et al., 2017; Andrault et al., 2022). However, this is unlikely in this case as both previous studies used similar spectroradiometric techniques. The validity of the greybody approximation in the case of Ti could be confirmed by an ambient pressure melting experiment. In lower pressure experiments we observed the melt to be much more mobile compared to the highest pressure run. This could be seen visually, as well as from the sharp drops in circuit resistance above the melting point in all experiments apart from *#5*. The use of MIR to track the hostpot and measure temperature, as well as the consistency of the two experiments at ∼20 GPa (*#1* and *#2*) suggests that it is unlikely that movement of melt away from the region in which temperature was measured is responsible for the anomalously low melting temperatures. However, in all experiments apart from *#5*, we observed the hotspot to migrate towards an edge of the filament (at the gasket contact) just prior to melting. It is therefore possible that alloying between the filament and gasket resulted in the depression of the melting point in these experiments. Incorporation of ∼5 wt. % Fe may depress the ambient pressure melting point by several hundred Kelvin, which may be enough to explain these results (Okamoto, 2010). Stainless steel gaskets were used in these experiments primarily for cost reasons. Replicate experiments with other gasket materials may help determine the effect of alloying in filament melting experiments, and the use of titanium gaskets may be necessary, although the experimental design has not been tested with this. Alternatively, alloying between the filament and gasket could be detected by *ex situ* analysis of recovered experiments to determine iron content. Similarly, any offset in the post-quench unit cell volume of the titanium at ambient temperature measured by x-ray diffraction would reveal any influence of alloying on the melting temperature. Spatial x-ray diffraction maps in particular could help quantify alloying at the filament-gasket contact. Improvement of the sample confinement through re-design of the thermal insulation may help prevent migration of hotspot melting to the filament edges in lower-pressure experiments, but ruling out any alloying effects will still be important.

4.5 Conclusions

These experiments provide useful preliminary results that demonstrate the potential of our IRH design for studies of metallic materials. It is clear that a metallic filament can be heated to well above its melting point, and temperature of up to at least 4000 K can be achieved using compressed alumina nano-powder as the thermal insulation. If this technique is combined with synchrotron x-ray diffraction, and the onset of liquid diffuse scattering used as a melting criterion, it would offer clear benefits over laser-heated DAC experiments, as well as a complementary technique. The reduced thermal gradients, improved temperature stability, and more precise temperature control could allow tighter constraints on high-pressure melting temperatures with significantly reduced uncertainties. Additionally, we have shown that in lab-based experiments signatures of melting can be detected in electrical and temperature data. The appearance of a power–temperature plateau appears to provide a reliable indicator of melting in most experiments, and a discontinuity in circuit resistance at the melting point appears to be a consistent feature in all experiments. The onset of melting at these features should be corroborated with *in situ* x-ray diffraction data, but may provide a useful lab-based melting criterion in future studies. The continued heating of filament well above their melting point also allows for the generation of significant volumes of melt, with wholly molten regions larger than 100 µm × 25 µm apparent in most experiments (e.g., run *#4*), much larger than possible in typical laser-heating experiments. The generation of stable, large volumes of melt may allow for x-ray diffraction measurements with a clean, liquid diffuse signal that could allow structural analysis of metallic melts at extreme conditions, although characterisation of the background signal from the alumina pressure media would require a careful experimental approach. *In situ* x-ray diffraction should also be used to quantify thermal pressure, which was poorly constrained in this study. This could then be used to more accurately correct for thermal pressure in lab-based experiments with no *in situ* XRD data. Confinement of the produced melt volume is clearly improved at higher pressure, with a marked difference between experiment at pressure below ∼30 GPa, and the run performed at ∼40 GPa. While the experiment geometry was essentially stable at all pressures, migration of melt into the culet slots complicates the interpretation of electrical data. In addition, alloying between the filament and gasket may influence melting behaviour and should be further investigated with *in situ* measurements in future studies. Further experimental development of single-piece thermal insulation should be investigated to improve sample confinement. Our obtained data suggest that the electrical characteristics of the design are also sensitive to sub-solidus phase transitions. This provides a promising possibility to map sub-solidus phase boundaries using a solely lab-based technique. Nevertheless, the thermal pressure in such experiments would need to be well constrained, and the position of phase transitions at the electrical features we observed should be corroborated with *in situ* XRD measurements. Reversal experiments and stepped heating profiles should also be used in future studies to constrain the equilibrium positions of phase boundaries.

Chapter 5

Conclusions

The primary aim of this project was to develop new heating techniques to study both solid and liquid phases at lower mantle conditions in the diamond anvil cell. In chapter 1 I defined several ideal characteristics of a resistive heating system suited to the investigation of a wide range of important material properties. These characteristics were:

1) Large temperature range encompassing lower mantle conditions (1500 to 3000 K)
2) Stable heating over timescales of several hours
3) Precise control over temperature
4) Low spatial thermal gradients
5) Allow whole melting of the sample
6) Sample independent (i.e., applicable to metallic/non-metallic, opaque/transparent samples)
7) Simple to use
8) Relatively easy to manufacture/assemble
9) Simple to interface with existing analytical equipment (e.g., at a beamline)

The internal resistive heating (IRH) design developed during the course of this project achieves many of these goals, and the preliminary experiments reported in this thesis demonstrate the potential of our 'split-gasket' approach for investigations of material properties at extreme conditions. As discussed in chapter 2, the design is capable of heating non-metallic or metallic materials contained in a distinct sample chamber to temperatures of 3000 K at pressures up to 64 GPa. Further

experiments reported in chapter 4 using the heating filament as the sample show that temperatures in excess of 4000 K can be sustained with this experimental approach. The temperature range of our design far exceeds that of other resistive heating techniques applicable to non-metallic samples, and so provides a complementary method to laser-heating across a pressure range equivalent to ∼1000 km depth within the Earth. As detailed in chapter 2, the design also offers precise control over temperature by making small variations to the applied electrical power, and the generated sample temperature is extremely stable. Experiments lasting many hours can be performed routinely, with variations of less than 20 K over the duration of a typical experiment. Spatial temperature gradients are also lower compared to typical laser-heating experiments, although the IRH design does not offer a completely flat thermal profile. Possible modifications to the design that could reduce thermal gradients were discussed in chapter 2. The experiments described in chapter 4 in which the filament itself was melted demonstrate the stability of melt produced in the IRH assembly, which should cross-over to melting of non-metallic materials within a sample chamber. Those experiments also demonstrated the ability to detecting melting signatures from the electrical data, suggesting the design can be a useful tool for constraining the high-pressure melting curves of metals. Complete sample isolation is still an issue in the design, with reaction between the sample and alumina pressure media observed in the experiments described in chapter 2, and melt migration an issue in the experiments described in chapter 4. Capping the sample chamber with discs of salt is likely to prevent unwanted reactions, and we are undergoing work to test this further. The possibility of using machined single pieces of form-fitting insulation was also investigated in chapters 2 and 4. The tests we conducted were hampered by mechanical issues, but is the subject of ongoing technical development. If the issue are overcome, form-fitting insulation could improve the design by simplifying the loading procedure, reducing thermal gradients, and improving sample confinement. Similarly, work to further miniaturise the design and increase the accessible pressure range is ongoing. One of the main benefits of out IRH design over existing IRH techniques applicable to non-metallic samples is the relative simplicity of our 'split-gasket' approach, and the complete isolation of the filament within the insulated pressure chamber – enabling more reproducible, efficient, and routine generation of high *P-T* conditions beyond the limits of other resistive heating techniques. Experiments can be prepared rapidly using commonly available materials and the failure rate is extremely low, making it a cost-effective and time-efficient approach. A fairly advanced laser micro-machining system with a pulse width in the nano-second range or shorter is required to machine the components, but these are available at most institutions (if not individual lab facilities). Finally, the form-factor of the IRH cell is essentially the same as a standard DAC. As a result, when combined with a standard bench-top power supply the IRH system provides a fully portable heating system which can be easily integrated with existing analytical equipment.

The main limitation of the IRH design is the small sample chamber, which is only ∼10 μm in diameter. This means that internal resistive heating is best suited to analyses utilising synchrotron techniques. In chapter 2 we showed that it is already possible to obtain usable x-ray diffraction

data with a micro-focused beam. Micro-focus configurations, such as the one we used at Diamond Light Source, are widely available at synchrotron facilities. However, IRH will greatly benefit from the coherent nano-focused x-ray beams provided by next-generation synchrotron sources, such as is already available at the newly upgraded ESRF. With nano-focus x-ray diffraction a wide range of IRH applications are already well within experimental capabilities. These include determining phase relations, mapping phase diagrams and melting curves, and collecting dense *P*-*V*-*T* datasets with minimal uncertainties to accurately constrain equations of state. Liquid state measurements of wholly molten samples are also already likely feasible, although the small sample volume will pose some difficulty (particularly for low-Z materials) and careful characterisation of the background will be necessary. As described in chapter 3, structural information can be extracted from total x-ray scattering data of liquid samples, extending the phase mapping and EOS applications of IRH to fluid phases that may be present within the deep Earth. Internal resistive heating should also be well suited to performing synchrotron Mössbauer spectroscopy at high *P*-*T* conditions, as SMS radiation can be focused to spot sizes of $\sim$10 μm. This provides a method to constrain the *P*-*T* conditions of the spin transition in lower mantle minerals, which, with laser heating, is a technologically challenging endeavour. One of the most exciting future applications of IRH is heating samples over the long timescales required to make elasticity measurements of lower mantle phases at high *P* and *T*. Currently, IXS beamlines available at the ESRF, APS, and Spring-8 do not have the focusing capabilities required by the small IRH sample size, but this is likely to change in the future. Indeed, the development of next-generation light sources will massively increase the spatial resolution of most synchrotron techniques, and IRH is ideally placed to exploit this. Although more development of IRH is needed, and this project was just a preliminary exploration of its capabilities, it is my hope that internal resistive heating will become a useful and widely used tool for Earth Scientists and the wider high-pressure community.

References

Abe, R., Shibazaki, Y., Ozawa, S., Ohira, I., Tobe, H., & Suzuki, A. (2018). In situ X–ray diffraction studies of hydrous aluminosilicate at high pressure and temperature. *Journal of Mineralogical and Petrological Sciences*, **113**:106–111. doi:10.2465/jmps.170714.

Adams, D. M. & Sharma, S. K. (1977). Selection of diamonds for infrared and Raman spectroscopy. *Journal of Physics E: Scientific Instruments*, **10**(7):680.

Akahama, Y. & Kawamura, H. (2004). High-pressure Raman spectroscopy of diamond anvils to 250 GPa: Method for pressure determination in the multimegabar pressure range. *Journal of Applied Physics*, **96**(7):3748–3751.

Akahama, Y. & Kawamura, H. (2005). Raman study on the stress state of [111] diamond anvils at multimegabar pressure. *Journal of Applied Physics*, **98**(8):083523.

Akahama, Y. & Kawamura, H. (2006). Pressure calibration of diamond anvil Raman gauge to 310 GPa. *Journal of Applied Physics*, **100**(4):043516.

Akahama, Y. & Kawamura, H. (2007). Diamond anvil Raman gauge in multimegabar pressure range. *High Pressure Research*, **27**(4):473–482.

Akahama, Y. & Kawamura, H. (2010). Pressure calibration of diamond anvil Raman gauge to 410 GPa. *Journal of Physics: Conference Series*, **215**(1):012195.

Akahama, Y., Kawamura, H., Häusermann, D., Hanfland, M., & Shimomura, O. (1995). New high-pressure structural transition of oxygen at 96 GPa associated with metallization in a molecular solid. *Physical Review Letters*, **74**(23):4690.

Akin, M. C., Nguyen, J. H., Beckwith, M. A., Chau, R., Ambrose, W. P., Fat'yanov, O. V., Asimow, P. D., & Holmes, N. C. (2019). Tantalum sound velocity under shock compression. *Journal of Applied Physics*, **125**(14):145903.

Aleksandrov, I., Goncharov, A. F., Zisman, A., & Stishov, S. M. (1987). Diamond at high pressures: Raman scattering of light, equation of state, and high pressure scale. *Journal of Experimental and Theoretical Physics, JETP*, **66**(2):384. Russian original: (1987) *Zhurnal Éksperimental'noĭ Teroeticheskoĭ Fiziki*, **93**(2):680.

Alfè, D. (2009). Temperature of the inner-core boundary of the Earth: Melting of iron at high pressure from first-principles coexistence simulations. *Physical Review B*, **79**(6):060101.

Allègre, C. J., Staudacher, T., & Sarda, P. (1987). Rare gas systematics: Formation of the atmosphere, evolution and structure of the Earth's mantle. *Earth and Planetary Science Letters*, **81**(2-3):127–150.

Anderson, D. L. (1967). The anelasticity of the mantle. *Geophysical Journal International*, **14**(1-4):135–163.

Anderson, O. L. (1984). A universal thermal equation-of-state. *Journal of Geodynamics*, **1**(2):185–214.

Anderson, O. L. (1995). *Equations of State of Solids for Geophysics and Ceramic Science*, *Oxford Monographs on Geology and Geophysics*, vol. 31. Oxford University Press, Oxford.

Andrault, D., Angel, R. J., Mosenfelder, J. L., & Le Bihan, T. (2003). Equation of state of stishovite to lower mantle pressures. *American Mineralogist*, **88**(2-3):301–307.

Andrault, D., Bolfan-Casanova, N., Bouhifd, M. A., Guignot, N., & Kawamoto, T. (2007). The role of Al-defects on the equation of state of Al–(Mg, Fe)SiO3 perovskite. *Earth and Planetary Science Letters*, **263**(3-4):167–179.

Andrault, D., Bolfan-Casanova, N., & Guignot, N. (2001). Equation of state of lower mantle (Al,Fe)-MgSiO3 perovskite. *Earth and Planetary Science Letters*, **193**(3-4):501–508.

Andrault, D. & Fiquet, G. (2001). Synchrotron radiation and laser heating in a diamond anvil cell. *Review of Scientific Instruments*, **72**(2):1283–1288.

Andrault, D., Fiquet, G., Guyot, F., & Hanfland, M. (1998). Pressure-induced Landau-type transition in stishovite. *Science*, **282**(5389):720–724.

Andrault, D., Pesce, G., Bouhifd, M. A., Bolfan-Casanova, N., Hénot, J.-M., & Mezouar, M. (2014a). Melting of subducted basalt at the core-mantle boundary. *Science*, **344**(6186):892–895.

Andrault, D., Pison, L., Morard, G., Garbarino, G., Mezouar, M., Bouhifd, M., & Kawamoto, T. (2022). Comment on: Melting behavior of SiO2 up to 120 GPa (Andrault et al. 2020). *Physics and Chemistry of Minerals*, **49**(2):1–6.

Andrault, D., Trønnes, R. G., Konôpková, Z., Morgenroth, W., Liermann, H. P., Morard, G., & Mezouar, M. (2014b). Phase diagram and PVT equation of state of Al-bearing seifertite at lowermost mantle conditions. *American mineralogist*, **99**(10):2035–2042.

Angel, R. J. (2000). Equations of State. *In:* Hazen, R. M. & Downs, R. T. (eds.), *High-Temperature and High Pressure Crystal Chemistry*, *Reviews in Mineralogy and Geochemistry*, vol. 41, chap. 2, pp. 35–59. Mineralogical Society of America. ISBN 978-0-939950-53-9.

Angel, R. J., Bujak, M., Zhao, J., Gatta, G. D., & Jacobsen, S. D. (2007). Effective hydrostatic limits of pressure media for high-pressure crystallographic studies. *Journal of Applied Crystallography*, **40**(1):26–32.

Antonangeli, D., Siebert, J., Aracne, C. M., Farber, D. L., Bosak, A., Hoesch, M., Krisch, M., Ryerson, F. J., Fiquet, G., & Badro, J. (2011). Spin crossover in ferropericlase at high pressure: A seismologically transparent transition? *Science*, **331**(6013):64–67.

Anzellini, S., Alfé, D., Pozzo, M., & Errandonea, D. (2021). Melting line of calcium characterized by in situ LH-DAC XRD and first-principles calculations. *Scientific Reports*, **11**(1):1–9.

Anzellini, S. & Boccato, S. (2020). A practical review of the laser-heated diamond anvil cell for university laboratories and synchrotron applications. *Crystals*, **10**(6):459.

Anzellini, S., Dewaele, A., Mezouar, M., Loubeyre, P., & Morard, G. (2013). Melting of iron at Earth's inner core boundary based on fast X-ray diffraction. *Science*, **340**(6131):464–466.

Anzellini, S., Kleppe, A. K., Daisenberger, D., Wharmby, M. T., Giampaoli, R., Boccato, S., Baron, M. A., Miozzi, F., Keeble, D. S., Ross, A., Gurney, S., Thompson, J., Knap, G., Booth, M., Hudson, L., Hawkins, D., Walter, M. J., & Wilhelm, H. (2018). Laser-heating system for high-pressure X-ray diffraction at the Extreme Conditions beamline I15 at Diamond Light Source. *Journal of Synchrotron Radiation*, **25**(6):1860–1868.

Anzellini, S., Monteseguro, V., Bandiello, E., Dewaele, A., Burakovsky, L., & Errandonea, D. (2019). In situ characterization of the high pressure–high temperature melting curve of platinum. *Scientific Reports*, **9**(1):1–10.

Aquilanti, G., Trapananti, A., Karandikar, A., Kantor, I., Marini, C., Mathon, O., Pascarelli, S., & Boehler, R. (2015). Melting of iron determined by X-ray absorption spectroscopy to 100 GPa. *Proceedings of the National Academy of Sciences*, **112**(39):12042–12045.

Asahara, Y., Hirose, K., Ohishi, Y., Hirao, N., Ozawa, H., & Murakami, M. (2013). Acoustic velocity measurements for stishovite across the post-stishovite phase transition under deviatoric stress: Implications for the seismic features of subducting slabs in the mid-mantle. *American Mineralogist*, **98**(11-12):2053–2062.

Asanuma, H., Ohtani, E., Sakai, T., Terasaki, H., Kamada, S., Kondo, T., & Kikegawa, T. (2010). Melting of iron–silicon alloy up to the core–mantle boundary pressure: implications to the thermal structure of the Earth's core. *Physics and Chemistry of Minerals*, **37**(6):353–359.

Ashcroft, N. W. & Langreth, D. C. (1967). Structure of binary liquid mixtures. I. *Physical Review*, **156**(3):685.

Auld, B. A. (1973). *Acoustic Fields and Waves in Solids: Volume I*. John Wiley & Sons, New York. ISBN 0-471-03700-1.

Austermann, J., Kaye, B. T., Mitrovica, J. X., & Huybers, P. (2014). A statistical analysis of the correlation between large igneous provinces and lower mantle seismic structure. *Geophysical Journal International*, **197**(1):1–9.

Ayrinhac, S., Gauthier, M., Le Marchand, G., Morand, M., Bergame, F., & Decremps, F. (2015). Thermodynamic properties of liquid gallium from picosecond acoustic velocity measurements. *Journal of Physics: Condensed Matter*, **27**(27):275103.

Badro, J. (2014). Spin transitions in mantle minerals. *Annual Review of Earth and Planetary Sciences*, **42**:231–248.

Badro, J., Fiquet, G., Guyot, F., Rueff, J.-P., Struzhkin, V. V., Vankó, G., & Monaco, G. (2003). Iron partitioning in Earth's mantle: toward a deep lower mantle discontinuity. *Science*, **300**(5620):789–791.

Baer, B. J., Chang, M. E., & Evans, W. J. (2008). Raman shift of stressed diamond anvils: Pressure calibration and culet geometry dependence. *Journal of Applied Physics*, **104**(3):034504.

Ballaran, T. B., Kurnosov, A., Glazyrin, K., Frost, D. J., Merlini, M., Hanfland, M., & Caracas, R. (2012). Effect of chemistry on the compressibility of silicate perovskite in the lower mantle. *Earth and Planetary Science Letters*, **333**:181–190.

Ballmer, M. D., Houser, C., Hernlund, J. W., Wentzcovitch, R. M., & Hirose, K. (2017). Persistence of strong silica-enriched domains in the Earth's lower mantle. *Nature Geoscience*, **10**(3):236–240.

Ballmer, M. D., Schmerr, N. C., Nakagawa, T., & Ritsema, J. (2015). Compositional mantle layering revealed by slab stagnation at~ 1000-km depth. *Science Advances*, **1**(11):e1500815.

Baron, A. Q. R. (2016a). High-Resolution Inelastic X-Ray Scattering I: Context, Spectrometers, Samples, and Superconductors. *In:* Jaeschke, E. J., Khan, S., Schneider, J. R., & Hastings, J. B. (eds.), *Synchrotron Light Sources and Free-Electron Lasers: Accelerator Physics, Instrumentation and Science Applications*, pp. 1643–1719. Springer International Publishing, Cham, Switzerland. ISBN 978-3-319-14394-1. doi:10.1007/978-3-319-14394-1_41.

Baron, A. Q. R. (2016b). High-Resolution Inelastic X-Ray Scattering II: Scattering Theory, Harmonic Phonons, and Calculations. *In:* Jaeschke, E. J., Khan, S., Schneider, J. R., & Hastings, J. B. (eds.), *Synchrotron Light Sources and Free-Electron Lasers: Accelerator Physics, Instrumentation and Science Applications*, pp. 1721–1757. Springer International Publishing, Cham, Switzerland. ISBN 978-3-319-14394-1. doi:10.1007/978-3-319-14394-1_52.

Baron, M. A., Lord, O. T., Myhill, R., Thomson, A. R., Wang, W., Trønnes, R. G., & Walter, M. J. (2017). Experimental constraints on melting temperatures in the MgO–SiO2 system at lower mantle pressures. *Earth and Planetary Science Letters*, **472**:186–196.

Bassett, W. A. (2001). The birth and development of laser heating in diamond anvil cells. *Review of Scientific Instruments*, **72**(2):1270–1272.

Bassett, W. A. (2009). Diamond anvil cell, 50th birthday. *High Pressure Research*, **29**(2):163–186.

Bassett, W. A. & Brown Jr, G. E. (1990). Synchrotron radiation: applications in the earth sciences. *Annual Review of Earth and Planetary Sciences*, **18**(1):387–447.

Bassett, W. A. & Skalwold, E. A. (2017). Diamond cleavage: importance to high pressure research. *High Pressure Research*, **37**(1):46–58.

Bassett, W. A. & Weathers, M. S. (1987). Temperature Measurements in a Laser-Heated Diamond Cell. *In:* Manghnani, M. H. & Syono, Y. (eds.), *High-Pressure Research in Mineral Physics: A Volume in Honor of Syun-iti Akimoto*, *Geophysical Monograph Series*, vol. 39, pp. 129–133. American Geophysical Union, Washington, DC. ISBN 9781118664124. doi:10.1029/GM039p0129.

Basu, A., Field, M. R., McCulloch, D. G., & Boehler, R. (2020). New measurement of melting and thermal conductivity of iron close to outer core conditions. *Geoscience Frontiers*, **11**(2):565–568.

Bell, D. R., Ihinger, P. D., & Rossman, G. R. (1995). Quantitative analysis of trace OH in garnet and pyroxenes. *American Mineralogist*, **80**(5-6):465–474.

Bell, D. R. & Rossman, G. R. (1992). Water in Earth's mantle: The role of nominally anhydrous minerals. *Science*, **255**(5050):1391–1397.

Bell, D. R., Rossman, G. R., Maldener, J., Endisch, D., & Rauch, F. (2003). Hydroxide in olivine: A quantitative determination of the absolute amount and calibration of the IR spectrum. *Journal of Geophysical Research: Solid Earth*, **108**(B2).

Bell, D. R., Rossman, G. R., Maldener, J., Endisch, D., & Rauch, F. (2004). Hydroxide in kyanite: A quantitative determination of the absolute amount and calibration of the IR spectrum. *American Mineralogist*, **89**(7):998–1003.

Belonoshko, A. B. & Rosengren, A. (2012). High-pressure melting curve of platinum from ab initio Z method. *Physical Review B*, **85**(17):174104.

Bel'skaya, E. A. & Kulyamina, E. Y. (2007). Electrical resistivity of titanium in the temperature range from 290 to 1800 K. *High Temperature*, **45**(6):785–796.

Benmore, C. J. (2012). A review of high-energy X-ray diffraction from glasses and liquids. *International Scholarly Research Notices*, **2012**.

Benmore, C. J., Weber, J. K. R., Wilding, M. C., Du, J., & Parise, J. B. (2010). Temperature-dependent structural heterogeneity in calcium silicate liquids. *Physical Review B*, **82**(22):224202.

Bercovici, D. & Karato, S.-i. (2003). Whole-mantle convection and the transition-zone water filter. *Nature*, **425**(6953):39–44.

Bernardes, C. E. S. (2021). STRFACT: Determining X-Ray Total Scattering Factors from Molecular Dynamics Simulation Data. Version 1.2. doi:10.5281/zenodo.4762008.

Berry, A. J., Hermann, J., O'Neill, H. S. C., & Foran, G. J. (2005). Fingerprinting the water site in mantle olivine. *Geology*, **33**(11):869–872.

Besson, J. M. & Pinceaux, J. P. (1979). Melting of helium at room temperature and high pressure. *Science*, **206**(4422):1073–1075.

Bina, C. R. & Helffrich, G. (2014). Geophysical Constraints on Mantle Composition. *In:* Holland, H. D. & Turekian, K. K. (eds.), *Treatise on Geochemistry*, chap. 3.2, pp. 41–65. Elsevier, Oxford, 2nd edn. ISBN 978-0-08-098300-4. doi:10.1016/B978-0-08-095975-7.00202-3.

Bindi, L., Nishi, M., Tsuchiya, J., & Irifune, T. (2014). Crystal chemistry of dense hydrous magnesium silicates: The structure of phase H, MgSiH2O4, synthesized at 45 GPa and 1000 C. *American Mineralogist*, **99**(8-9):1802–1805.

Birch, F. (1947). Finite elastic strain of cubic crystals. *Physical Review*, **71**(11):809.

Blackman, R. B. & Tukey, J. W. (1958). The measurement of power spectra from the point of view of communications engineering—Part I. *Bell System Technical Journal*, **37**(1):185–282.

Boccato, S., Torchio, R., Kantor, I., Morard, G., Anzellini, S., Giampaoli, R., Briggs, R., Smareglia, A., Irifune, T., & Pascarelli, S. (2017). The melting curve of nickel up to 100 GPa explored by XAS. *Journal of Geophysical Research: Solid Earth*, **122**(12):9921–9930.

Boehler, R. (1986). The phase diagram of iron to 430 kbar. *Geophysical Research Letters*, **13**(11):1153–1156.

Boehler, R. (1993). Temperatures in the Earth's core from melting-point measurements of iron at high static pressures. *Nature*, **363**(6429):534–536.

Boehler, R. (1996). Fe–FeS eutectic temperatures to 620 kbar. *Physics of the Earth and Planetary Interiors*, **96**(2-3):181–186.

Boehler, R. (2000). Laser heating in the diamond cell: techniques and applications. *Hyperfine Interactions*, **128**(1):307–321.

Boehler, R. & De Hantsetters, K. (2004). New anvil designs in diamond-cells. *High Pressure Research*, **24**(3):391–396.

Boehler, R., Nicol, M., Zha, C. S., & Johnson, M. L. (1986). Resistance heating of Fe and W in diamond-anvil cells. *Physica B+C*, **139**:916–918.

Bolfan-Casanova, N. (2005). Water in the Earth's mantle. *Mineralogical Magazine*, **69**(3):229–257.

Bolfan-Casanova, N., Keppler, H., & Rubie, D. C. (2000). Water partitioning between nominally anhydrous minerals in the MgO–SiO2–H2O system up to 24 GPa: implications for the distribution of water in the Earth's mantle. *Earth and Planetary Science Letters*, **182**(3-4):209–221.

Bolfan-Casanova, N., Mackwell, S., Keppler, H., McCammon, C., & Rubie, D. C. (2002). Pressure dependence of H solubility in magnesiowüstite up to 25 GPa: Implications for the storage of water in the Earth's lower mantle. *Geophysical Research Letters*, **29**(10):89–1.

Boyd, R. W. (1983). *Radiometry and the Detection of Optical Radiation*. John Wiley and Sons, New York. ISBN 978-0-471-86188-1.

Boyet, M. & Carlson, R. W. (2006). A new geochemical model for the Earth's mantle inferred from 146Sm–142Nd systematics. *Earth and Planetary Science Letters*, **250**(1-2):254–268.

Braithwaite, J. & Stixrude, L. (2019). Melting of $CaSiO_3$ perovskite at high pressure. *Geophysical Research Letters*, **46**(4):2037–2044.

Brandenburg, J. P., Hauri, E. H., van Keken, P. E., & Ballentine, C. J. (2008). A multiple-system study of the geochemical evolution of the mantle with force-balanced plates and thermochemical effects. *Earth and Planetary Science Letters*, **276**(1-2):1–13.

Brandenburg, J. P. & Van Keken, P. E. (2007). Deep storage of oceanic crust in a vigorously convecting mantle. *Journal of Geophysical Research: Solid Earth*, **112**(B6).

Bridgman, P. W. (1949). *The Physics of High Pressure*. G. Bell, London.

Bridgman, P. W. (1952). The Resistance of 72 Elements, Alloys and Compounds to 100,000 Kg/Cm^2. *Proceedings of the American Academy of Arts and Sciences*, **81**(4):165–251. doi:10.2307/20023677.

Briggs, R., Daisenberger, D., Lord, O., Salamat, A., Bailey, E., Walter, M., & McMillan, P. (2017). High-pressure melting behavior of tin up to 105 GPa. *Physical Review B*, **95**(5):054102.

Briggs, R., Gorman, M. G., Zhang, S., McGonegle, D., Coleman, A. L., Coppari, F., Morales-Silva, M. A., Smith, R. F., Wicks, J. K., Bolme, C. A., Gleason, A. E., Cunningham, E., Lee, H. J., Nagler, B., McMahon, M. I., Eggert, J. H., & Fratanduono, D. E. (2019). Coordination changes in liquid tin under shock compression determined using in situ femtosecond x-ray diffraction. *Applied Physics Letters*, **115**(26):264101.

Brodholt, J. P., Helffrich, G., & Trampert, J. (2007). Chemical versus thermal heterogeneity in the lower mantle: The most likely role of anelasticity. *Earth and Planetary Science Letters*, **262**(3-4):429–437.

Brown, J. M. & McQueen, R. G. (1986). Phase transitions, Grüneisen parameter, and elasticity for shocked iron between 77 GPa and 400 GPa. *Journal of Geophysical Research: Solid Earth*, **91**(B7):7485–7494.

Brown, P. J., Fox, A. G., Maslen, E. N., O'Keefe, M. A., & Willis, B. T. M. (2006). Intensity of diffracted intensities. *In:* Prince, E. (ed.), *International Tables for Crystallography Volume C: Mathematical, physical and chemical tables*, pp. 554–595. Springer, Dordrecht. doi:10.1107/97809553602060000600.

Brown, S. P., Thorne, M. S., Miyagi, L., & Rost, S. (2015). A compositional origin to ultralow-velocity zones. *Geophysical Research Letters*, **42**(4):1039–1045.

Buchen, J., Marquardt, H., Schulze, K., Speziale, S., Boffa Ballaran, T., Nishiyama, N., & Hanfland, M. (2018). Equation of state of polycrystalline stishovite across the tetragonal-orthorhombic phase transition. *Journal of Geophysical Research: Solid Earth*, **123**(9):7347–7360.

Buffett, B. A. (2000). Earth's core and the geodynamo. *Science*, **288**(5473):2007–2012.

Burkel, E. (2000). Phonon spectroscopy by inelastic x-ray scattering. *Reports on Progress in Physics*, **63**(2):171.

Bykov, M., Chariton, S., Fei, H., Fedotenko, T., Aprilis, G., Ponomareva, A. V., Tasnádi, F., Abrikosov, I. A., Merle, B., Feldner, P., Vogel, S., Schnick, W., Prakapenka, V. B., Greenberg, E., Hanfland, M., Pakhomova, A., Liermann, H.-P., Katsura, T., Dubrovinskaia, N., & Dubrovinsky, L. (2019). High-pressure synthesis of ultraincompressible hard rhenium nitride pernitride $Re_2(N_2)(N)_2$ stable at ambient conditions. *Nature Communications*, **10**(1):1–8.

Byrd, R. H., Lu, P., Nocedal, J., & Zhu, C. (1995). A limited memory algorithm for bound constrained optimization. *SIAM Journal on Scientific Computing*, **16**(5):1190–1208.

Campbell, A. J. (2008). Measurement of temperature distributions across laser heated samples by multispectral imaging radiometry. *Review of Scientific Instruments*, **79**(1):015108.

Campbell, A. J., Seagle, C. T., Heinz, D. L., Shen, G., & Prakapenka, V. B. (2007). Partial melting in the iron–sulfur system at high pressure: A synchrotron X-ray diffraction study. *Physics of the Earth and Planetary Interiors*, **162**(1-2):119–128.

Carpenter, M. A., Hemley, R. J., & Mao, H.-k. (2000). High-pressure elasticity of stishovite and the P42/mnm□ Pnnm phase transition. *Journal of Geophysical Research: Solid Earth*, **105**(B5):10807–10816.

Catalli, K., Shim, S.-H., Dera, P., Prakapenka, V. B., Zhao, J., Sturhahn, W., Chow, P., Xiao, Y., Cynn, H., & Evans, W. J. (2011). Effects of the Fe3+ spin transition on the properties of aluminous perovskite—New insights for lower-mantle seismic heterogeneities. *Earth and Planetary Science Letters*, **310**(3-4):293–302.

Cerantola, V., Bykova, E., Kupenko, I., Merlini, M., Ismailova, L., McCammon, C., Bykov, M., Chumakov, A. I., Petitgirard, S., Kantor, I., Svitlyk, V., Jacobs, J., Hanfland, M., Mezouar, M., Prescher, C., Rüffer, R., Prakapenka, V. B., & Dubrovinsky, L. (2017). Stability of iron-bearing carbonates in the deep Earth's interior. *Nature Communications*, **8**(1):1–9.

Chai, M. & Michael Brown, J. (1996). Effects of static non-hydrostatic stress on the R lines of ruby single crystals. *Geophysical Research Letters*, **23**(24):3539–3542.

Chakhmouradian, A. R. & Mitchell, R. H. (2000). Occurrence, alteration patterns and compositional variation of perovskite in kimberlites. *The Canadian Mineralogist*, **38**(4):975–994.

Chang, Y.-Y., Jacobsen, S. D., Lin, J.-F., Bina, C. R., Thomas, S.-M., Wu, J., Shen, G., Xiao, Y., Chow, P., Frost, D. J., McCammon, C. A., & Dera, P. (2013). Spin transition of Fe3+ in Al-bearing phase D: An alternative explanation for small-scale seismic scatterers in the mid-lower mantle. *Earth and Planetary Science Letters*, **382**:1–9.

Chen, B., Jackson, J. M., Sturhahn, W., Zhang, D., Zhao, J., Wicks, J. K., & Murphy, C. A. (2012). Spin crossover equation of state and sound velocities of (Mg0.65Fe0.35)O ferropericlase to 140 GPa. *Journal of Geophysical Research: Solid Earth*, **117**(B8).

Chen, J., Inoue, T., Weidner, D. J., Wu, Y., & Vaughan, M. T. (1998). Strength and water weakening of mantle minerals, olivine, wadsleyite and ringwoodite. *Geophysical Research Letters*, **25**(4):575–578.

Cheng, B., Lou, H., Sarkar, A., Zeng, Z., Zhang, F., Chen, X., Tan, L., Glazyrin, K., Yan, J., Wang, L., Djenadic, R., Hahn, H., & Zeng, Q. (2020). Lattice distortion and stability of $(Co_{0.2}Cu_{0.2}Mg_{0.2}Ni_{0.2}Zn_{0.2})O$ high-entropy oxide under high pressure. *Materials Today Advances*, **8**:100102.

Chervin, J. C., Canny, B., & Mancinelli, M. (2001). Ruby-spheres as pressure gauge for optically transparent high pressure cells. *International Journal of High Pressure Research*, **21**(6):305–314.

Chichkov, B. N., Momma, C., Nolte, S., Von Alvensleben, F., & Tünnermann, A. (1996). Femtosecond, picosecond and nanosecond laser ablation of solids. *Applied Physics A*, **63**(2):109–115.

Chijioke, A. D., Nellis, W. J., Soldatov, A., & Silvera, I. F. (2005). The ruby pressure standard to 150 GPa. *Journal of Applied Physics*, **98**(11):114905.

Chopelas, A. (1996). Thermal expansivity of lower mantle phases MgO and MgSiO3 perovskite at high pressure derived from vibrational spectroscopy. *Physics of the Earth and Planetary Interiors*, **98**(1-2):3–15.

Christensen, U. R. & Hofmann, A. W. (1994). Segregation of subducted oceanic crust in the convecting mantle. *Journal of Geophysical Research: Solid Earth*, **99**(B10):19867–19884.

Coltice, N. & Ricard, Y. (1999). Geochemical observations and one layer mantle convection. *Earth and Planetary Science Letters*, **174**(1-2):125–137.

Cook, R. F. & Michaels, C. A. (2017). coefficients for stress, temperature, and composition effects in fluorescence measurements of alumina. *Journal of Research of the National Institute of Standards and Technology*, **122**(43).

Cordier, P., Ungár, T., Zsoldos, L., & Tichy, G. (2004). Dislocation creep in MgSiO3 perovskite at conditions of the Earth's uppermost lower mantle. *Nature*, **428**(6985):837–840.

Corgne, A., Allan, N. L., & Wood, B. J. (2003). Atomistic simulations of trace element incorporation into the large site of MgSiO3 and CaSiO3 perovskites. *Physics of the Earth and Planetary Interiors*, **139**(1-2):113–127.

Corgne, A., Liebske, C., Wood, B. J., Rubie, D. C., & Frost, D. J. (2005). Silicate perovskite-melt partitioning of trace elements and geochemical signature of a deep perovskitic reservoir. *Geochimica et Cosmochimica Acta*, **69**(2):485–496.

Corgne, A. & Wood, B. J. (2002). CaSiO3 and CaTiO3 perovskite-melt partitioning of trace elements: Implications for gross mantle differentiation. *Geophysical Research Letters*, **29**(19):39–1.

Corgne, A. & Wood, B. J. (2005). Trace element partitioning and substitution mechanisms in calcium perovskites. *Contributions to Mineralogy and Petrology*, **149**(1):85–97.

Cottaar, S., Heister, T., Rose, I., & Unterborn, C. (2014). BurnMan: A lower mantle mineral physics toolkit. *Geochemistry, Geophysics, Geosystems*, **15**(4):1164–1179.

Cottaar, S. & Romanowicz, B. (2012). An unsually large ULVZ at the base of the mantle near Hawaii. *Earth and Planetary Science Letters*, **355**:213–222.

Creasy, N., Girard, J., Eckert Jr, J. O., & Lee, K. K. M. (2020a). The role of redox on bridgmanite crystal chemistry and calcium speciation in the lower mantle. *Journal of Geophysical Research: Solid Earth*, **125**(10):e2020JB020783.

Creasy, N., Long, M. D., & Ford, H. A. (2017). Deformation in the lowermost mantle beneath Australia from observations and models of seismic anisotropy. *Journal of Geophysical Research: Solid Earth*, **122**(7):5243–5267.

Creasy, N., Miyagi, L., & Long, M. D. (2020b). A library of elastic tensors for lowermost mantle seismic anisotropy studies and comparison with seismic observations. *Geochemistry, Geophysics, Geosystems*, **21**(4):e2019GC008883.

Criniti, G., Kurnosov, A., Boffa Ballaran, T., & Frost, D. J. (2021). Single-Crystal Elasticity of MgSiO3 Bridgmanite to Mid-Lower Mantle Pressure. *Journal of Geophysical Research: Solid Earth*, **126**(5):e2020JB020967.

Cristiglio, V., Cuello, G. J., Piarristeguy, A. A., & Pradel, A. (2009). The coordination number calculation from total structure factor measurements. *Journal of Non-crystalline Solids*, **355**(37-42):1811–1814.

Crowhurst, J. C., Brown, J. M., Goncharov, A. F., & Jacobsen, S. D. (2008). Elasticity of (Mg,Fe)O through the spin transition of iron in the lower mantle. *Science*, **319**(5862):451–453.

Dadashev, A., Pasternak, M. P., Rozenberg, G. K., & Taylor, R. D. (2001). Applications of perforated diamond anvils for very high-pressure research. *Review of Scientific Instruments*, **72**(6):2633–2637.

Dai, C., Hu, J., & Tan, H. (2009). Hugoniot temperatures and melting of tantalum under shock compression determined by optical pyrometry. *Journal of Applied Physics*, **106**(4):043519.

Dai, L., Kudo, Y., Hirose, K., Murakami, M., Asahara, Y., Ozawa, H., Ohishi, Y., & Hirao, N. (2013). Sound velocities of Na0.4Mg0.6Al1.6Si0.4O4 NAL and CF phases to 73 GPa determined by Brillouin scattering method. *Physics and Chemistry of Minerals*, **40**(3):195–201.

Dannberg, J., Myhill, R., Gassmöller, R., & Cottaar, S. (2021). The morphology, evolution and seismic visibility of partial melt at the core-mantle boundary: Implications for ULVZs. *Geophysical Journal International*, **227**(2):1028–1059.

Datchi, F. & Canny, B. (2004). Raman spectrum of cubic boron nitride at high pressure and temperature. *Physical Review B*, **69**(14):144106.

Datchi, F., LeToullec, R., & Loubeyre, P. (1997). Improved calibration of the SrB4O7:Sm2+ optical pressure gauge: advantages at very high pressures and high temperatures. *Journal of Applied Physics*, **81**(8):3333–3339.

Davies, D., Goes, S., & Sambridge, M. (2015). On the relationship between volcanic hotspot locations, the reconstructed eruption sites of large igneous provinces and deep mantle seismic structure. *Earth and Planetary Science Letters*, **411**:121–130.

Decremps, F., Antonangeli, D., Gauthier, M., Ayrinhac, S., Morand, M., Marchand, G. L., Bergame, F., & Philippe, J. (2014). Sound velocity of iron up to 152 GPa by picosecond acoustics in diamond anvil cell. *Geophysical Research Letters*, **41**(5):1459–1464.

Decremps, F., Belliard, L., Couzinet, B., Vincent, S., Munsch, P., Le Marchand, G., & Perrin, B. (2009). Liquid mercury sound velocity measurements under high pressure and high temperature by picosecond acoustics in a diamond anvils cell. *Review of Scientific Instruments*, **80**(7):073902.

Decremps, F., Gauthier, M., Ayrinhac, S., Bove, L., Belliard, L., Perrin, B., Morand, M., Le Marchand, G., Bergame, F., & Philippe, J. (2015). Picosecond acoustics method for measuring the thermodynamical properties of solids and liquids at high pressure and high temperature. *Ultrasonics*, **56**:129–140.

Demouchy, S. & Mackwell, S. (2006). Mechanisms of hydrogen incorporation and diffusion in iron-bearing olivine. *Physics and Chemistry of Minerals*, **33**(5):347–355.

Deng, J., Du, Z., Benedetti, L. R., & Lee, K. K. M. (2017). The influence of wavelength-dependent absorption and temperature gradients on temperature determination in laser-heated diamond-anvil cells. *Journal of Applied Physics*, **121**(2):025901.

Deschamps, F., Kaminski, E., & Tackley, P. J. (2011). A deep mantle origin for the primitive signature of ocean island basalt. *Nature Geoscience*, **4**(12):879–882.

Dewaele, A. (2019). Equations of state of simple solids (including Pb, NaCl and LiF) compressed in helium or neon in the Mbar range. *Minerals*, **9**(11):684.

Dewaele, A., Loubeyre, P., & Mezouar, M. (2004). Equations of state of six metals above 94 GPa. *Physical Review B*, **70**(9):094112.

Dewaele, A., Loubeyre, P., Occelli, F., Marie, O., & Mezouar, M. (2018). Toroidal diamond anvil cell for detailed measurements under extreme static pressures. *Nature Communications*, **9**(1):1–9.

Dewaele, A., Mezouar, M., Guignot, N., & Loubeyre, P. (2007). Melting of lead under high pressure studied using second-scale time-resolved x-ray diffraction. *Physical Review B*, **76**(14):144106.

Dewaele, A., Mezouar, M., Guignot, N., & Loubeyre, P. (2010). High melting points of tantalum in a laser-heated diamond anvil cell. *Physical Review Letters*, **104**(25):255701.

Dewaele, A., Stutzmann, V., Bouchet, J., Bottin, F., Occelli, F., & Mezouar, M. (2015). High pressure-temperature phase diagram and equation of state of titanium. *Physical Review B*, **91**(13):134108.

Dias, R. P. & Silvera, I. F. (2017). Observation of the Wigner-Huntington transition to metallic hydrogen. *Science*, **355**(6326):715–718.

Dickey, D. A. & Fuller, W. A. (1981). Likelihood ratio statistics for autoregressive time series with a unit root. *Econometrica: Journal of the Econometric Society*, **49**:1057–1072.

Dimitroulis, C., Raptis, T., & Raptis, V. (2015). POLYANA - A tool for the calculation of molecular radial distribution functions based on Molecular Dynamics trajectories. *Computer Physics Communications*, **197**:220–226.

Dobson, D. P., Lindsay-Scott, A., Hunt, S. A., Bailey, E., Wood, I. G., Brodholt, J. P., Vocadlo, L., & Wheeler, J. (2019). Anisotropic diffusion creep in postperovskite provides a new model for deformation at the core–mantle boundary. *Proceedings of the National Academy of Sciences*, **116**(52):26389–26393.

Dong, X., Oganov, A. R., Goncharov, A. F., Stavrou, E., Lobanov, S., Saleh, G., Qian, G.-R., Zhu, Q., Gatti, C., Deringer, V. L., Dronskowski, R., Zhou, X.-F., Prakapenka, V. B., Konôpková, Z., Popov, I. A., Boldyrev, A. I., & Wang, H.-T. (2017). A stable compound of helium and sodium at high pressure. *Nature Chemistry*, **9**(5):440–445.

Dorfman, S. M. (2016). Phase diagrams and thermodynamics of lower mantle materials. *In:* Terasaki, H. & Fischer, R. A. (eds.), *Deep Earth: Physics and Chemistry of the Lower Mantle and Core*, *American Geophysical Union (AGU) Geophysical Monograph Series*, vol. 217, chap. 19, pp. 241–252. John Wiley & Sons. ISBN 9781118992487. doi:10.1002/9781118992487.ch19.

Dorfman, S. M., Jiang, F., Mao, Z., Kubo, A., Meng, Y., Prakapenka, V. B., & Duffy, T. S. (2010). Phase transitions and equations of state of alkaline earth fluorides CaF_2, SrF_2, and BaF_2 to Mbar pressures. *Physical Review B*, **81**(17):174121.

Dorfman, S. M., Meng, Y., Prakapenka, V. B., & Duffy, T. S. (2013). Effects of Fe-enrichment on the equation of state and stability of (Mg,Fe)SiO3 perovskite. *Earth and Planetary Science Letters*, **361**:249–257.

Dorfman, S. M., Potapkin, V., Lv, M., Greenberg, E., Kupenko, I., Chumakov, A. I., Bi, W., Alp, E. E., Liu, J., Magrez, A., Dutton, S. E., Cava, R. J., McCammon, C. A., & Gillet, P. (2020). Effects of composition and pressure on electronic states of iron in bridgmanite. *American Mineralogist: Journal of Earth and Planetary Materials*, **105**(7):1030–1039.

Dorfman, S. M., Prakapenka, V. B., Meng, Y., & Duffy, T. S. (2012). Intercomparison of pressure standards (Au, Pt, Mo, MgO, NaCl and Ne) to 2.5 Mbar. *Journal of Geophysical Research: Solid Earth*, **117**(B8).

Dorogokupets, P. I. & Dewaele, A. (2007). Equations of state of MgO, Au, Pt, NaCl-B1, and NaCl-B2: Internally consistent high-temperature pressure scales. *High Pressure Research*, **27**(4):431–446.

Dorogokupets, P. I. & Oganov, A. (2003). Equations of state of Cu and Ag and revised ruby pressure scale. *Doklady Earth Sciences*, **391**:854–857.

Dorogokupets, P. I. & Oganov, A. R. (2006). Equations of state of Al, Au, Cu, Pt, Ta, and W and revised ruby pressure scale. *Doklady Earth Sciences*, **410**(7):1091.

Dorogokupets, P. I. & Oganov, A. R. (2007). Ruby, metals, and MgO as alternative pressure scales: A semiempirical description of shock-wave, ultrasonic, x-ray, and thermochemical data at high temperatures and pressures. *Physical Review B*, **75**(2):024115.

Doubrovine, P. V., Steinberger, B., & Torsvik, T. H. (2016). A failure to reject: Testing the correlation between large igneous provinces and deep mantle structures with EDF statistics. *Geochemistry, Geophysics, Geosystems*, **17**(3):1130–1163.

Drewitt, J. W., Hennet, L., Zeidler, A., Jahn, S., Salmon, P. S., Neuville, D. R., & Fischer, H. E. (2012). Structural transformations on vitrification in the fragile glass-forming system CaAl2O4. *Physical Review Letters*, **109**(23):235501.

Drewitt, J. W. E. (2021). Liquid structure under extreme conditions: High-pressure x-ray diffraction studies. *Journal of Physics: Condensed Matter*, **33**:503004.

Drewitt, J. W. E., Jahn, S., Sanloup, C., de Grouchy, C., Garbarino, G., & Hennet, L. (2015). Development of chemical and topological structure in aluminosilicate liquids and glasses at high pressure. *Journal of Physics: Condensed Matter*, **27**(10):105103.

Drewitt, J. W. E., Sanloup, C., Bytchkov, A., Brassamin, S., & Hennet, L. (2013). Structure of $(Fe_xCa_{1-x}O)_y(SiO_2)_{1-y}$ liquids and glasses from high-energy x-ray diffraction: Implications for the structure of natural basaltic magmas. *Physical Review B*, **87**:224201. doi:10.1103/PhysRevB.87.224201.

Drewitt, J. W. E., Turci, F., Heinen, B. J., Macleod, S. G., Qin, F., Kleppe, A. K., & Lord, O. T. (2020). Structural ordering in liquid gallium under extreme conditions. *Physical Review Letters*, **124**(14):145501.

Drewitt, J. W. E., Walter, M. J., Brodholt, J. P., Muir, J. M. R., & Lord, O. T. (2022). Hydrous silicate melts and the deep mantle H2O cycle. *Earth and Planetary Science Letters*, **581**:117408.

Drewitt, J. W. E., Walter, M. J., Zhang, H., McMahon, S. C., Edwards, D., Heinen, B. J., Lord, O. T., Anzellini, S., & Kleppe, A. K. (2019). The fate of carbonate in oceanic crust subducted into earth's lower mantle. *Earth and Planetary Science Letters*, **511**:213–222.

Du, Z., Amulele, G., Robin Benedetti, L., & Lee, K. K. M. (2013). Mapping temperatures and temperature gradients during flash heating in a diamond-anvil cell. *Review of Scientific Instruments*, **84**(7):075111.

Duan, Y., Sun, N., Wang, S., Li, X., Guo, X., Ni, H., Prakapenka, V. B., & Mao, Z. (2018). Phase stability and thermal equation of state of δ-AlOOH: Implication for water transportation to the Deep Lower Mantle. *Earth and Planetary Science Letters*, **494**:92–98.

Dubrovinskaia, N. & Dubrovinsky, L. (2003). Whole-cell heater for the diamond anvil cell. *Review of Scientific Instruments*, **74**(7):3433–3437.

Dubrovinskaia, N. & Dubrovinsky, L. (2005). Internal and external electrical heating in diamond anvil cells. *In: Advances in High-Pressure Technology for Geophysical Applications*, chap. 25, pp. 487–501. Elsevier.

Dubrovinskaia, N., Dubrovinsky, L., Caracas, R., & Hanfland, M. (2010). Diamond as a high pressure gauge up to 2.7 Mbar. *Applied Physics Letters*, **97**(25):251903.

Dubrovinsky, L., Annersten, H., Dubrovinskaia, N., Westman, F., Harryson, H., Fabrichnaya, O., & Carlson, S. (2001a). Chemical interaction of Fe and Al_2O_3 as a source of heterogeneity at the Earth's core–mantle boundary. *Nature*, **412**(6846):527–529.

Dubrovinsky, L., Dubrovinskaia, N., Narygina, O., Kantor, I., Kuznetzov, A., Prakapenka, V. B., Vitos, L., Johansson, B., Mikhaylushkin, A. S., Simak, S. I., & Abrikosov, I. A. (2007). Body-centered cubic iron-nickel alloy in Earth's core. *Science*, **316**(5833):1880–1883.

Dubrovinsky, L. S., Dubrovinskaia, N. A., Saxena, S. K., Tutti, F., Rekhi, S., Le Bihan, T., Shen, G., & Hu, J. (2001b). Pressure-induced transformations of cristobalite. *Chemical Physics Letters*, **333**(3-4):264–270.

Dziewonski, A. M. (1984). Mapping the lower mantle: determination of lateral heterogeneity in P velocity up to degree and order 6. *Journal of Geophysical Research: Solid Earth*, **89**(B7):5929–5952.

Dziewonski, A. M. & Anderson, D. L. (1981). Preliminary reference Earth model. *Physics of the Earth and Planetary Interiors*, **25**(4):297–356.

Eckersley, M. C., Gaskell, P. H., Barnes, A. C., & Chieux, P. (1988). Structural ordering in a calcium silicate glass. *Nature*, **335**(6190):525–527.

Edmund, E., Gauthier, M., Antonangeli, D., Ayrinhac, S., Boccato, S., Deletang, T., Morand, M., Garino, Y., Parisiades, P., & Decremps, F. (2020). Picosecond acoustics technique to measure the sound velocities of Fe-Si alloys and Si single-crystals at high pressure. *Minerals*, **10**(3):214.

Edwards, D. M. (2020). *Investigating the Deep Carbon Cycle through the Experimental Study of Simple Carbonate Systems*. Ph.D. thesis, University of Bristol.

Eggert, J. H., Goettel, K. A., & Silvera, I. F. (1989a). Ruby at high pressure. I. Optical line shifts to 156 GPa. *Physical Review B*, **40**(8):5724.

Eggert, J. H., Goettel, K. A., & Silvera, I. F. (1989b). Ruby at high pressure. II. Fluorescence lifetime of the R line to 130 GPa. *Physical Review B*, **40**(8):5733.

Eggert, J. H., Weck, G., Loubeyre, P., & Mezouar, M. (2002). Quantitative structure factor and density measurements of high-pressure fluids in diamond anvil cells by x-ray diffraction: Argon and water. *Physical Review B*, **65**(17):174105.

Eggleton, R. A., Boland, J. N., & Ringwood, A. E. (1978). High pressure synthesis of a new aluminium silicate: Al5Si5O17(OH). *Geochemical Journal*, **12**(3):191–194.

Eremets, M. (2003). Megabar high-pressure cells for Raman measurements. *Journal of Raman Spectroscopy*, **34**(7-8):515–518.

Errandonea, D. (2005). Improving the understanding of the melting behaviour of Mo, Ta, and W at extreme pressures. *Physica B: Condensed Matter*, **357**(3-4):356–364.

Errandonea, D. (2013). High-pressure melting curves of the transition metals Cu, Ni, Pd, and Pt. *Physical Review B*, **87**(5):054108.

Errandonea, D., Burakovsky, L., Preston, D. L., MacLeod, S. G., Santamaría-Perez, D., Chen, S., Cynn, H., Simak, S. I., McMahon, M. I., Proctor, J. E., & Mezouar, M. (2020). Experimental and theoretical confirmation of an orthorhombic phase transition in niobium at high pressure and temperature. *Communications Materials*, **1**(1):1–11.

Errandonea, D., MacLeod, S. G., Burakovsky, L., Santamaria-Perez, D., Proctor, J. E., Cynn, H., & Mezouar, M. (2019). Melting curve and phase diagram of vanadium under high-pressure and high-temperature conditions. *Physical Review B*, **100**(9):094111.

Errandonea, D., Schwager, B., Ditz, R., Gessmann, C., Boehler, R., & Ross, M. (2001). Systematics of transition-metal melting. *Physical Review B*, **63**(13):132104.

Faber, T. E. (1972). *An Introduction to the Theory of Liquid Metals*. Cambridge University Press, Cambridge. ISBN 978-0-521-15449-9.

Faber, T. E. & Ziman, J. M. (1965). A theory of the electrical properties of liquid metals: III. The resistivity of binary alloys. *Philosophical Magazine*, **11**(109):153–173.

Fan, D., Fu, S., Yang, J., Tkachev, S. N., Prakapenka, V. B., & Lin, J.-F. (2019). Elasticity of single-crystal periclase at high pressure and temperature: The effect of iron on the elasticity and seismic parameters of ferropericlase in the lower mantle. *American Mineralogist: Journal of Earth and Planetary Materials*, **104**(2):262–275.

Fedorov, F. I. (1968). *Theory of Elastic Waves in Crystals*. (Bradley, J. E. S., *tr.*). Springer, New York, USA. ISBN 978-4757-277-3.

Fedotenko, T., Dubrovinsky, L., Aprilis, G., Koemets, E., Snigirev, A., Snigireva, I., Barannikov, A., Ershov, P., Cova, F., Hanfland, M., & Dubrovinskaia, N. (2019). Laser heating setup for diamond anvil cells for in situ synchrotron and in house high and ultra-high pressure studies. *Review of Scientific Instruments*, **90**(10):104501.

Fei, Y., Li, J., Hirose, K., Minarik, W., Van Orman, J., Sanloup, C., van Westrenen, W., Komabayashi, T., & Funakoshi, K.-i. (2004). A critical evaluation of pressure scales at high

temperatures by in situ X-ray diffraction measurements. *Physics of the Earth and Planetary Interiors*, **143**:515–526.

Fei, Y., Ricolleau, A., Frank, M., Mibe, K., Shen, G., & Prakapenka, V. (2007). Toward an internally consistent pressure scale. *Proceedings of the National Academy of Sciences*, **104**(22):9182–9186.

Ferraro, J. R., Nakamoto, K., & Brown, C. W. (2003). *Introductory Raman Spectroscopy*. Academic Press, San Diego, 2nd edn. ISBN 978-0-12-254105-6.

Ferreira, A. M. G., Faccenda, M., Sturgeon, W., Chang, S.-J., & Schardong, L. (2019). Ubiquitous lower-mantle anisotropy beneath subduction zones. *Nature Geoscience*, **12**(4):301–306.

Finkelstein, G. J., Jackson, J. M., Said, A., Alatas, A., Leu, B. M., Sturhahn, W., & Toellner, T. S. (2018). Strongly anisotropic magnesiowüstite in Earth's lower mantle. *Journal of Geophysical Research: Solid Earth*, **123**(6):4740–4750.

Fiquet, G., Badro, J., Guyot, F., Bellin, C., Krisch, M., Antonangeli, D., Requardt, H., Mermet, A., Farber, D., Aracne-Ruddle, C., & Zhang, J. (2004). Application of inelastic X-ray scattering to the measurements of acoustic wave velocities in geophysical materials at very high pressure. *Physics of the Earth and Planetary Interiors*, **143**:5–18.

Fiquet, G., Dewaele, A., Andrault, D., Kunz, M., & Le Bihan, T. (2000). Thermoelastic properties and crystal structure of MgSiO3 perovskite at lower mantle pressure and temperature conditions. *Geophysical Research Letters*, **27**(1):21–24.

Fischer, R. A., Campbell, A. J., Chidester, B. A., Reaman, D. M., Thompson, E. C., Pigott, J. S., Prakapenka, V. B., & Smith, J. S. (2018). Equations of state and phase boundary for stishovite and CaCl2-type SiO2. *American Mineralogist: Journal of Earth and Planetary Materials*, **103**(5):792–802.

Fischer, R. A., Campbell, A. J., Reaman, D. M., Miller, N. A., Heinz, D. L., Dera, P., & Prakapenka, V. B. (2013). Phase relations in the Fe–FeSi system at high pressures and temperatures. *Earth and Planetary Science Letters*, **373**:54–64.

Forman, R. A., Piermarini, G. J., Barnett, J. D., & Block, S. (1972). Pressure measurement made by the utilization of ruby sharp-line luminescence. *Science*, **176**(4032):284–285.

French, S. & Romanowicz, B. A. (2014). Whole-mantle radially anisotropic shear velocity structure from spectral-element waveform tomography. *Geophysical Journal International*, **199**(3):1303–1327.

French, S. W. & Romanowicz, B. (2015). Broad plumes rooted at the base of the Earth's mantle beneath major hotspots. *Nature*, **525**(7567):95–99.

Frost, D. J., Liebske, C., Langenhorst, F., McCammon, C. A., Trønnes, R. G., & Rubie, D. C. (2004). Experimental evidence for the existence of iron-rich metal in the Earth's lower mantle. *Nature*, **428**(6981):409–412.

Fu, S., Yang, J., Karato, S.-i., Vasiliev, A., Presniakov, M. Y., Gavriliuk, A. G., Ivanova, A. G., Hauri, E. H., Okuchi, T., Purevjav, N., et al. (2019a). Water concentration in single-crystal (Al,Fe)-bearing Bridgmanite grown from the hydrous melt: Implications for dehydration melting at the topmost lower mantle. *Geophysical Research Letters*, **46**(17-18):10346–10357.

Fu, S., Yang, J., Tsujino, N., Okuchi, T., Purevjav, N., & Lin, J.-F. (2019b). Single-crystal elasticity of (Al, Fe)-bearing bridgmanite and seismic shear wave radial anisotropy at the topmost lower mantle. *Earth and Planetary Science Letters*, **518**:116–126.

Fu, S., Yang, J., Zhang, Y., Okuchi, T., McCammon, C., Kim, H.-I., Lee, S. K., & Lin, J.-F. (2018). Abnormal elasticity of Fe-bearing bridgmanite in the Earth's lower mantle. *Geophysical Research Letters*, **45**(10):4725–4732.

Fujino, K., Nishio-Hamane, D., Seto, Y., Sata, N., Nagai, T., Shinmei, T., Irifune, T., Ishii, H., Hiraoka, N., Cai, Y. Q., et al. (2012). Spin transition of ferric iron in Al-bearing Mg–perovskite up to 200 GPa and its implication for the lower mantle. *Earth and Planetary Science Letters*, **317**:407–412.

Fukao, Y. & Obayashi, M. (2013). Subducted slabs stagnant above, penetrating through, and trapped below the 660 km discontinuity. *Journal of Geophysical Research: Solid Earth*, **118**(11):5920–5938.

Fukui, H., Katsura, T., Kuribayashi, T., Matsuzaki, T., Yoneda, A., Ito, E., Kudoh, Y., Tsutsui, S., & Baron, A. Q. R. (2008). Precise determination of elastic constants by high-resolution inelastic X-ray scattering. *Journal of Synchrotron Radiation*, **15**(6):618–623.

Fukui, H., Sakai, T., Sakamaki, T., Kamada, S., Takahashi, S., Ohtani, E., & Baron, A. Q. R. (2013). A compact system for generating extreme pressures and temperatures: An application of laser-heated diamond anvil cell to inelastic X-ray scattering. *Review of Scientific Instruments*, **84**(11):113902.

Fukui, H., Yoneda, A., Nakatsuka, A., Tsujino, N., Kamada, S., Ohtani, E., Shatskiy, A., Hirao, N., Tsutsui, S., Uchiyama, H., et al. (2016). Effect of cation substitution on bridgmanite elasticity: A key to interpret seismic anomalies in the lower mantle. *Scientific Reports*, **6**(1):1–10.

Funamori, N., Yamamoto, S., Yagi, T., & Kikegawa, T. (2004). Exploratory studies of silicate melt structure at high pressures and temperatures by in situ X-ray diffraction. *Journal of Geophysical Research: Solid Earth*, **109**(B3).

Garnero, E. J. & McNamara, A. K. (2008). Structure and dynamics of Earth's lower mantle. *science*, **320**(5876):626–628.

Garnero, E. J., McNamara, A. K., & Shim, S.-H. (2016). Continent-sized anomalous zones with low seismic velocity at the base of Earth's mantle. *Nature Geoscience*, **9**(7):481–489.

Gaskell, P. H., Eckersley, M. C., Barnes, A. C., & Chieux, P. (1991). Medium-range order in the cation distribution of a calcium silicate glass. *Nature*, **350**(6320):675–677.

Gattass, R. R. & Mazur, E. (2008). Femtosecond laser micromachining in transparent materials. *Nature Photonics*, **2**(4):219–225.

Geballe, Z. M. & Jeanloz, R. (2012). Origin of temperature plateaus in laser-heated diamond anvil cell experiments. *Journal of Applied Physics*, **111**(12):123518.

Gillan, M. J., Alfe, D., Brodholt, J., Vočadlo, L., & Price, G. D. (2006). First-principles modelling of Earth and planetary materials at high pressures and temperatures. *Reports on Progress in Physics*, **69**(8):2365.

Giordano, D. & Dingwell, D. B. (2003). The kinetic fragility of natural silicate melts. *Journal of Physics: Condensed Matter*, **15**(11):S945.

Glazyrin, K., Ballaran, T. B., Frost, D., McCammon, C., Kantor, A., Merlini, M., Hanfland, M., & Dubrovinsky, L. (2014). Magnesium silicate perovskite and effect of iron oxidation state on its bulk sound velocity at the conditions of the lower mantle. *Earth and Planetary Science Letters*, **393**:182–186.

Gleason, A., Quiroga, C., Suzuki, A., Pentcheva, R., & Mao, W. (2013). Symmetrization driven spin transition in ε-FeOOH at high pressure. *Earth and Planetary Science Letters*, **379**:49–55.

Goncharov, A. F. (2012). Raman spectroscopy at high pressures. *International Journal of Spectroscopy*, **2012**.

Goncharov, A. F. & Crowhurst, J. C. (2005a). Pulsed laser Raman spectroscopy in the laser-heated diamond anvil cell. *Review of Scientific Instruments*, **76**(6):063905.

Goncharov, A. F. & Crowhurst, J. C. (2005b). Raman spectroscopy under extreme conditions. *Journal of Low Temperature Physics*, **139**(5):727–737.

Greaux, S., Gautron, L., Andrault, D., Bolfan-Casanova, N., Guignot, N., & Bouhifd, M. A. (2009). Experimental high pressure and high temperature study of the incorporation of uranium in Al-rich CaSiO3 perovskite. *Physics of the Earth and Planetary Interiors*, **174**(1-4):254–263.

Gréaux, S., Irifune, T., Higo, Y., Tange, Y., Arimoto, T., Liu, Z., & Yamada, A. (2019). Sound velocity of CaSiO3 perovskite suggests the presence of basaltic crust in the Earth's lower mantle. *Nature*, **565**(7738):218–221.

Gréaux, S., Kono, Y., Wang, Y., Yamada, A., Zhou, C., Jing, Z., Inoue, T., Higo, Y., Irifune, T., Sakamoto, N., & Yurimoto, H. (2016). Sound velocities of aluminum-bearing stishovite in the mantle transition zone. *Geophysical Research Letters*, **43**(9):4239–4246.

Griffiths, P. R. & De Haseth, J. A. (2007). *Fourier transform infrared spectrometry*, *Chemical Analysis: A Series of Monographs on Analytical Chemistry and Its Applications*, vol. 171. John Wiley & Sons, Hoboken, N.J. ISBN 9780471194040.

Grocholski, B., Shim, S.-H., & Prakapenka, V. B. (2013). Stability, metastability, and elastic properties of a dense silica polymorph, seifertite. *Journal of Geophysical Research: Solid Earth*, **118**(9):4745–4757.

Gu, T., Li, M., McCammon, C., & Lee, K. K. M. (2016). Redox-induced lower mantle density contrast and effect on mantle structure and primitive oxygen. *Nature Geoscience*, **9**(9):723–727.

Gubbins, D., Masters, G., & Nimmo, F. (2008). A thermochemical boundary layer at the base of Earth's outer core and independent estimate of core heat flux. *Geophysical Journal International*, **174**(3):1007–1018.

Guerain, M. (2020). A review on high pressure experiments for study of crystallographic behavior and polymorphism of pharmaceutical materials. *Journal of Pharmaceutical Sciences*, **109**(9).

Guignot, N. & Andrault, D. (2004). Equations of state of Na–K–Al host phases and implications for MORB density in the lower mantle. *Physics of the Earth and Planetary Interiors*, **143**:107–128.

Gupta, Y. M. & Shen, X. A. (1991). Potential use of the ruby R2 line shift for static high-pressure calibration. *Applied Physics Letters*, **58**(6):583–585.

Hall, S. A., Kendall, J.-M., & van der Baan, M. (2004). Some comments on the effects of lower-mantle anisotropy on SKS and SKKS phases. *Physics of the Earth and Planetary Interiors*, **146**(3-4):469–481.

Hanfland, M., Syassen, K., Fahy, S., Louie, S. G., & Cohen, M. L. (1985). Pressure dependence of the first-order Raman mode in diamond. *Physical Review B*, **31**(10):6896.

Hanfland, M., Syassen, K., Fahy, S., Louie, S. G., & Cohen, M. L. (1986). The first-order Raman mode of diamond under pressure. *Physica B+ C*, **139**:516–519.

Harris, C. R., Millman, K. J., van der Walt, S. J., Gommers, R., Virtanen, P., Cournapeau, D., Wieser, E., Taylor, J., Berg, S., Smith, N. J., Kern, R., Picus, M., Hoyer, S., van Kerkwijk, M. H., Brett, M., Haldane, A., del Río, J. F., Wiebe, M., Peterson, P., Gérard-Marchant, P., Sheppard, K., Reddy, T., Weckesser, W., Abbasi, H., Gohlke, C., & Oliphant, T. E. (2020). Array programming with NumPy. *Nature*, **585**(7825):357–362. doi: 10.1038/s41586-020-2649-2.

Heinen, B. J. (2017). *Hidden Reservoirs: Water Solubility in the CaTiO3–CaSiO3 System*. Master's thesis, School of Earth Sciences, University of Bristol.

Heinen, B. J., Drewitt, J. W. E., Walter, M. J., Clapham, C., Qin, F., Kleppe, A. K., & Lord, O. T. (2021). Internal resistive heating of non-metallic samples to 3000 K and >60 GPa in the diamond anvil cell. *Review of Scientific Instruments*, **92**(6):063904.

Heinz, D. L. & Jeanloz, R. (1987). Temperature Measurements in the Laser-Heated Diamond Cell. *In:* Manghnani, M. H. & Syono, Y. (eds.), *High-Pressure Research in Mineral Physics: A Volume in Honor of Syun-iti Akimoto*, *Geophysical Monograph Series*, vol. 39, pp. 113–127. American Geophysical Union, Washington, DC. ISBN 9781118664124. doi:10.1029/GM039p0113.

Helffrich, G. (2006). Heterogeneity in the mantle—Its creation, evolution and destruction. *Tectonophysics*, **416**(1-4):23–31.

Helffrich, G., Ballmer, M. D., & Hirose, K. (2018). Core-exsolved SiO2 dispersal in the Earth's mantle. *Journal of Geophysical Research: Solid Earth*, **123**(1):176–188.

Helffrich, G. R. & Wood, B. J. (2001). The Earth's mantle. *Nature*, **412**(6846):501–507.

Hemley, R. J. (2006). Erskine Williamson, extreme conditions, and the birth of mineral physics. *Physics Today*, **59**(4):50.

Hemley, R. J., Mao, H.-k., Shen, G., Badro, J., Gillet, P., Hanfland, M., & Häusermann, D. (1997). X-ray imaging of stress and strain of diamond, iron, and tungsten at megabar pressures. *Science*, **276**(5316):1242–1245.

Henry, L., Mezouar, M., Garbarino, G., Sifré, D., Weck, G., & Datchi, F. (2020). Liquid–liquid transition and critical point in sulfur. *Nature*, **684**:382–386.

Hernlund, J. W. & Houser, C. (2008). On the statistical distribution of seismic velocities in Earth's deep mantle. *Earth and Planetary Science Letters*, **265**(3-4):423–437.

Hernlund, J. W., Thomas, C., & Tackley, P. J. (2005). A doubling of the post-perovskite phase boundary and structure of the Earth's lowermost mantle. *Nature*, **434**(7035):882–886.

Herzberg, C., Condie, K., & Korenaga, J. (2010). Thermal history of the Earth and its petrological expression. *Earth and Planetary Science Letters*, **292**(1-2):79–88.

Hess, N. J. & Exarhos, G. J. (1989). Temperature and pressure dependence of laser induced fluorescence in Sm: YAG—A new pressure calibrant. *High Pressure Research*, **2**(1):57–64.

Hess, N. J. & Schiferl, D. (1992). Comparison of the pressure-induced frequency shift of Sm:YAG to the ruby and nitrogen vibron pressure scales from 6 to 820 K and 0 to 25 GPa and suggestions for use as a high-temperature pressure calibrant. *Journal of Applied Physics*, **71**(5):2082–2086.

Hill, R. (1963). Elastic properties of reinforced solids: some theoretical principles. *Journal of the Mechanics and Physics of Solids*, **11**(5):357–372.

Hirose, K., Sinmyo, R., & Hernlund, J. (2017). Perovskite in Earth's deep interior. *Science*, **358**(6364):734–738.

Hirose, K., Takafuji, N., Sata, N., & Ohishi, Y. (2005). Phase transition and density of subducted MORB crust in the lower mantle. *Earth and Planetary Science Letters*, **237**(1-2):239–251.

Hirschmann, M. M. (2006). Water, melting, and the deep Earth H2O cycle. *Annual Review of Earth and Planetary Sciences*, **34**:629–653.

Hofmeister, A. M. (1993). Interatomic potentials calculated from equations of state: Limitation of finite strain to moderate K'. *Geophysical Research Letters*, **20**(7):635–638.

Holland, T. J. B. & Powell, R. (2011). An improved and extended internally consistent thermodynamic dataset for phases of petrological interest, involving a new equation of state for solids. *Journal of Metamorphic Geology*, **29**(3):333–383.

Holzapfel, W. B. (1991). Equations of state for ideal and real solids under strong compression. *Europhysics Letters*, **16**(1):67.

Holzapfel, W. B. (2002). Equations of state for regular solids. *High Pressure Research*, **22**(1):209–216.

Holzapfel, W. B. (2003). Refinement of the ruby luminescence pressure scale. *Journal of Applied Physics*, **93**(3):1813–1818.

Hou, M., Liu, J., Zhang, Y., Du, X., Dong, H., Yan, L., Wang, J., Wang, L., & Chen, B. (2021). Melting of iron explored by electrical resistance jump up to 135 GPa. *Geophysical Research Letters*, **48**(20):e2021GL095739.

Hrubiak, R., Meng, Y., & Shen, G. (2017). Microstructures define melting of molybdenum at high pressures. *Nature Communications*, **8**(1):1–10.

Huang, Q., Yu, D., Xu, B., Hu, W., Ma, Y., Wang, Y., Zhao, Z., Wen, B., He, J., Liu, Z., & Tian, Y. (2014). Nanotwinned diamond with unprecedented hardness and stability. *Nature*, **510**(7504):250–253.

Huang, R., Boffa Ballaran, T., McCammon, C. A., Miyajima, N., & Frost, D. J. (2021). The Effect of Fe-Al Substitution on the Crystal Structure of MgSiO3 Bridgmanite. *Journal of Geophysical Research: Solid Earth*, **126**(9):e2021JB021936.

Huang, Y., He, Y., Sheng, H., Lu, X., Dong, H., Samanta, S., Dong, H., Li, X., Kim, D. Y., Mao, H.-k., Liu, Y., Li, H., Li, H., & Wang, L. (2019). Li-ion battery material under high pressure: Amorphization and enhanced conductivity of $Li_4Ti_5O_{12}$. *National Science Review*, **6**(2):239–246.

Huang, Y. K. & Chow, C. Y. (1974). The generalized compressibility equation of Tait for dense matter. *Journal of Physics D: Applied Physics*, **7**(15):2021.

Hubbell, J. H., Veigele, W. J., Briggs, E. A., Brown, R. T., Cromer, D. T., & Howerton, R. J. (1975). Atomic form factors, incoherent scattering functions, and photon scattering cross sections. *Journal of Physical and Chemical Reference Data*, **4**(3):471–538.

Hunt, S. A., Weidner, D. J., Li, L., Wang, L., Walte, N. P., Brodholt, J. P., & Dobson, D. P. (2009). Weakening of calcium iridate during its transformation from perovskite to post-perovskite. *Nature Geoscience*, **2**(11):794–797.

Idehara, K. (2011). Structural heterogeneity of an ultra-low-velocity zone beneath the Philippine Islands: Implications for core–mantle chemical interactions induced by massive partial melting at the bottom of the mantle. *Physics of the Earth and Planetary Interiors*, **184**(1-2):80–90.

Iitaka, T., Hirose, K., Kawamura, K., & Murakami, M. (2004). The elasticity of the MgSiO3 post-perovskite phase in the Earth's lowermost mantle. *Nature*, **430**(6998):442–445.

Imada, S., Hirose, K., Komabayashi, T., Suzuki, T., & Ohishi, Y. (2012). Compression of Na0.4Mg0.6Al1.6Si0.4O4 NAL and Ca-ferrite-type phases. *Physics and Chemistry of Minerals*, **39**(7):525–530.

Imada, S., Hirose, K., & Ohishi, Y. (2011). Stabilities of NAL and Ca-ferrite-type phases on the join NaAlSiO4-MgAl2O4 at high pressure. *Physics and Chemistry of Minerals*, **38**(7):557–560.

Immoor, J., Marquardt, H., Miyagi, L., Lin, F., Speziale, S., Merkel, S., Buchen, J., Kurnosov, A., & Liermann, H.-P. (2018). Evidence for {100}< 011> slip in ferropericlase in Earth's lower mantle from high-pressure/high-temperature experiments. *Earth and Planetary Science Letters*, **489**:251–257.

Immoor, J., Marquardt, H., Miyagi, L., Speziale, S., Merkel, S., Schwark, I., Ehnes, A., & Liermann, H.-P. (2020). An improved setup for radial diffraction experiments at high pressures and high temperatures in a resistive graphite-heated diamond anvil cell. *Review of Scientific Instruments*, **91**(4):045121.

Inoue, H., Suehiro, S., Ohta, K., Hirose, K., & Ohishi, Y. (2020). Resistivity saturation of hcp Fe-Si alloys in an internally heated diamond anvil cell: A key to assessing the Earth's core conductivity. *Earth and Planetary Science Letters*, **543**:116357.

Inoue, T., Ueda, T., Higo, Y., Yamada, A., Irifune, T., & Funakoshi, K.-i. (2006). High-pressure and high-temperature stability and equation of state of superhydrous phase B. *In:* Jacobsen, S. D. & Van Der Lee, S. (eds.), *Earth's Deep Water Cycle*, *Geophysical Monograph Series*, vol. 168, pp. 147–157. American Geophysical Union, Washington, DC. ISBN 9780875904337.

Irifune, T., Kurio, A., Sakamoto, S., Inoue, T., & Sumiya, H. (2003a). Correction: ultrahard polycrystalline diamond from graphite. *Nature*, **421**(6925):806–806.

Irifune, T., Kurio, A., Sakamoto, S., Inoue, T., & Sumiya, H. (2003b). Ultrahard polycrystalline diamond from graphite. *Nature*, **421**(6923):599–600.

Irifune, T., Shinmei, T., McCammon, C. A., Miyajima, N., Rubie, D. C., & Frost, D. J. (2010). Iron partitioning and density changes of pyrolite in Earth's lower mantle. *Science*, **327**(5962):193–195.

Ishii, T., Liu, Z., & Katsura, T. (2019). A breakthrough in pressure generation by a Kawai-type multi-anvil apparatus with tungsten carbide anvils. *Engineering*, **5**(3):434–440.

Ishimatsu, N., Matsumoto, K., Maruyama, H., Kawamura, N., Mizumaki, M., Sumiya, H., & Irifune, T. (2012). Glitch-free X-ray absorption spectrum under high pressure obtained using nano-polycrystalline diamond anvils. *Journal of Synchrotron Radiation*, **19**(5):768–772.

Ito, E. & Takahashi, E. (1989). Postspinel transformations in the system Mg2SiO4-Fe2SiO4 and some geophysical implications. *Journal of Geophysical Research: Solid Earth*, **94**(B8):10637–10646.

Jackson, I. & Rigden, S. M. (1996). Analysis of PVT data: constraints on the thermoelastic properties of high-pressure minerals. *Physics of the Earth and Planetary Interiors*, **96**(2-3):85–112.

Jackson, J. M., Sturhahn, W., Lerche, M., Zhao, J., Toellner, T. S., Alp, E. E., Sinogeikin, S. V., Bass, J. D., Murphy, C. A., & Wicks, J. K. (2013). Melting of compressed iron by monitoring atomic dynamics. *Earth and Planetary Science Letters*, **362**:143–150.

Jackson, J. M., Zhang, J., & Bass, J. D. (2004). Sound velocities and elasticity of aluminous MgSiO3 perovskite: implications for aluminum heterogeneity in Earth's lower mantle. *Geophysical Research Letters*, **31**(10).

Jackson, J. M., Zhang, J., Shu, J., Sinogeikin, S. V., & Bass, J. D. (2005). High-pressure sound velocities and elasticity of aluminous MgSiO3 perovskite to 45 GPa: Implications for lateral heterogeneity in Earth's lower mantle. *Geophysical Research Letters*, **32**(21).

Jackson, M. G. & Carlson, R. W. (2011). An ancient recipe for flood-basalt genesis. *Nature*, **476**(7360):316–319.

Jackson, M. G., Carlson, R. W., Kurz, M. D., Kempton, P. D., Francis, D., & Blusztajn, J. (2010). Evidence for the survival of the oldest terrestrial mantle reservoir. *Nature*, **466**(7308):853–856.

Jacobs, J. A. (1953). The Earth's inner core. *Nature*, **172**(4372):297–298.

Jacobsen, S. D., Reichmann, H. J., Kantor, A., & Spetzler, H. A. (2005). A gigahertz ultrasonic interferometer for the diamond anvil cell and high-pressure elasticity of some iron-oxide minerals. *In: Advances in High-Pressure Technology for Geophysical Applications*, chap. 2, pp. 25–48. Elsevier.

Jandeleit, J., Horn, A., Kreutz, E.-W., & Poprawe, R. (1997). Micromachining of metals and ceramics by nano- and picosecond laser radiation. *In:* Change, S.-C. & Pang, S. W. (eds.), *Micromachining and Microfabrication Process Technology III*, vol. 3223, pp. 34–42. International Society for Optics and Photonics, SPIE. doi:10.1117/12.284498.

Japel, S., Schwager, B., Boehler, R., & Ross, M. (2005). Melting of copper and nickel at high pressure: The role of d electrons. *Physical Review Letters*, **95**(16):167801.

Jayaraman, A. (1986). Ultrahigh pressures. *Review of Scientific Instruments*, **57**(6):1013–1031.

Jenei, Z., Cynn, H., Visbeck, K., & Evans, W. J. (2013). High-temperature experiments using a resistively heated high-pressure membrane diamond anvil cell. *Review of Scientific Instruments*, **84**(9):095114.

Jenei, Z., O'Bannon, E. F., Weir, S. T., Cynn, H., Lipp, M. J., & Evans, W. J. (2018). Single crystal toroidal diamond anvils for high pressure experiments beyond 5 megabar. *Nature Communications*, **9**(1):1–6.

Jenkins, J., Deuss, A., & Cottaar, S. (2017). Converted phases from sharp 1000 km depth mid-mantle heterogeneity beneath Western Europe. *Earth and Planetary Science Letters*, **459**:196–207.

Jenkins, J., Mousavi, S., Li, Z., & Cottaar, S. (2021). A high-resolution map of Hawaiian ULVZ morphology from ScS phases. *Earth and Planetary Science Letters*, **563**:116885.

Jing, Q., Wu, Q., Liu, L., Xu, J.-a., Bi, Y., Liu, Y., Chen, H., Liu, S., Zhang, Y., Xiong, L., Li, Y., & Liu, J. (2013). An experimental study on SrB4O7:Sm2+ as a pressure sensor. *Journal of Applied Physics*, **113**(2):023507.

Juhás, P., Davis, T., Farrow, C. L., & Billinge, S. J. (2013). PDFgetX3: a rapid and highly automatable program for processing powder diffraction data into total scattering pair distribution functions. *Journal of Applied Crystallography*, **46**(2):560–566.

Kamada, S., Fukui, H., Yoneda, A., Gomi, H., Maeda, F., Tsutsui, S., Uchiyama, H., Hirao, N., Ishikawa, D., & Baron, A. Q. R. (2019). Elastic constants of single-crystal Pt measured up to 20 GPa based on inelastic X-ray scattering: implication for the establishment of an equation of state. *Comptes Rendus Geoscience*, **351**(2-3):236–242.

Kaminsky, F. (2012). Mineralogy of the lower mantle: A review of 'super-deep'mineral inclusions in diamond. *Earth-Science Reviews*, **110**(1-4):127–147.

Kaneshima, S. & Helffrich, G. (2009). Lower mantle scattering profiles and fabric below Pacific subduction zones. *Earth and Planetary Science Letters*, **282**(1-4):234–239.

Kaneshima, S. & Helffrich, G. (2010). Small scale heterogeneity in the mid-lower mantle beneath the circum-Pacific area. *Physics of the Earth and Planetary Interiors*, **183**(1-2):91–103.

Kantor, A. P., Kantor, I. Y., Kurnosov, A. V., Kuznetsov, A. Y., Dubrovinskaia, N. A., Krisch, M., Bossak, A. A., Dmitriev, V. P., Urusov, V. S., & Dubrovinsky, L. S. (2007). Sound wave velocities of fcc Fe–Ni alloy at high pressure and temperature by mean of inelastic X-ray scattering. *Physics of the Earth and Planetary Interiors*, **164**(1-2):83–89.

Kantor, I., Prakapenka, V., Kantor, A., Dera, P., Kurnosov, A., Sinogeikin, S., Dubrovinskaia, N., & Dubrovinsky, L. (2012). BX90: A new diamond anvil cell design for X-ray diffraction and optical measurements. *Review of Scientific Instruments*, **83**(12):125102.

Kaplow, R., Strong, S. L., & Averbach, B. L. (1965). Radial density functions for liquid mercury and lead. *Physical Review*, **138**(5A):A1336.

Karandikar, A. & Boehler, R. (2016). Flash melting of tantalum in a diamond cell to 85 GPa. *Physical Review B*, **93**(5):054107.

Karato, S.-i. (1998). Seismic anisotropy in the deep mantle, boundary layers and the geometry of mantle convection. *In: Geodynamics of Lithosphere & Earth's Mantle*, pp. 565–587. Springer.

Karato, S.-i. & Karki, B. B. (2001). Origin of lateral variation of seismic wave velocities and density in the deep mantle. *Journal of Geophysical Research: Solid Earth*, **106**(B10):21771–21783.

Karki, B. B., Stixrude, L., & Crain, J. (1997). Ab initio elasticity of three high-pressure polymorphs of silica. *Geophysical Research Letters*, **24**(24):3269–3272.

Karki, B. B., Stixrude, L., & Wentzcovitch, R. M. (2001). High-pressure elastic properties of major materials of Earth's mantle from first principles. *Reviews of Geophysics*, **39**(4):507–534.

Katagiri, K., Ozaki, N., Ohmura, S., Albertazzi, B., Hironaka, Y., Inubushi, Y., Ishida, K., Koenig, M., Miyanishi, K., Nakamura, H., et al. (2021). Liquid Structure of Tantalum under Internal Negative Pressure. *Physical Review Letters*, **126**(17):175503.

Kautek, W. & Krüger, J. (1994). Femtosecond pulse laser ablation of metallic, semiconducting, ceramic, and biological materials. *In: Laser Materials Processing: Industrial and Microelectronics Applications*, vol. 2207, pp. 600–611. SPIE.

Kavner, A. & Nugent, C. (2008). Precise measurements of radial temperature gradients in the laser-heated diamond anvil cell. *Review of Scientific Instruments*, **79**(2):024902.

Kawai, K. & Tsuchiya, T. (2015). Small shear modulus of cubic CaSiO3 perovskite. *Geophysical Research Letters*, **42**(8):2718–2726.

Kawamoto, T., Matsukage, K. N., Nagai, T., Nishimura, K., Mataki, T., Ochiai, S., & Taniguchi, T. (2004). Raman spectroscopy of cubic boron nitride under high temperature and pressure conditions: A new optical pressure marker. *Review of Scientific Instruments*, **75**(7):2451–2454.

Keen, D. A. (2001). A comparison of various commonly used correlation functions for describing total scattering. *Journal of Applied Crystallography*, **34**(2):172–177.

Kendall, J.-M. & Silver, P. G. (1996). Constraints from seismic anisotropy on the nature of the lowermost mantle. *Nature*, **381**(6581):409–412.

Kendall, J. M. & Silver, P. G. (1998). Investigating causes of D" anisotropy. *In:* Gurnis, M., Wysession, M. E., Knittle, E., & Buffett, B. A. (eds.), *The Core-Mantle Boundary Region*, *Geodynamic Series*, vol. 28, pp. 97–118. Wiley Online Library.

Kenichi, T., Sahu, P. C., Yoshiyasu, K., & Yasuo, T. (2001). Versatile gas-loading system for diamond-anvil cells. *Review of Scientific Instruments*, **72**(10):3873–3876.

Kennett, B. L. N., Engdahl, E. R., & Buland, R. (1995). Constraints on seismic velocities in the Earth from traveltimes. *Geophysical Journal International*, **122**(1):108–124.

Kerley, G. I. (2003). Equations of state for titanium and Ti6A14V alloy. *Tech. Rep. SAND 2003-3785*, Sandia National Laboratories, Albuquerque, New Mexico 87185.

Khubbutdinov, R., Menushenkov, A. P., & Vartanyants, I. A. (2019). Coherence properties of the high-energy fourth-generation X-ray synchrotron sources. *Journal of Synchrotron Radiation*, **26**(6):1851–1862.

Kiarasi, S. & Secco, R. A. (2015). Pressure-induced electrical resistivity saturation of Fe17Si. *physica status solidi (b)*, **252**(9):2034–2042.

Kim, Y.-H., Yi, Y. S., Kim, H.-I., Chow, P., Xiao, Y., Shen, G., & Lee, S. K. (2019). Structural transitions in MgSiO3 glasses and melts at the core-mantle boundary observed via inelastic X-ray scattering. *Geophysical Research Letters*, **46**(23):13756–13764.

Kiseeva, E. S., Vasiukov, D. M., Wood, B. J., McCammon, C., Stachel, T., Bykov, M., Bykova, E., Chumakov, A., Cerantola, V., Harris, J. W., & Dubrovinsky, L. (2018). Oxidized iron in garnets from the mantle transition zone. *Nature Geoscience*, **11**(2):144–147.

Kitaigorodskiy, A. & Chomet, S. (1967). Elements of Order in Disorder. *In:* Chomet, S. (ed.), *Order and Disorder in the World of Atoms*, pp. 36–45. Springer, New York. doi:10.1007/978-1-4615-7559-7_3.

Klotz, S., Chervin, J. C., Munsch, P., & Le Marchand, G. (2009). Hydrostatic limits of 11 pressure transmitting media. *Journal of Physics D: Applied Physics*, **42**(7):075413.

Koelemeijer, P., Ritsema, J., Deuss, A., & Van Heijst, H.-J. (2016). SP12RTS: a degree-12 model of shear-and compressional-wave velocity for Earth's mantle. *Geophysical Journal International*, **204**(2):1024–1039.

Komabayashi, T., Fei, Y., Meng, Y., & Prakapenka, V. (2009). In-situ X-ray diffraction measurements of the γ-ε transition boundary of iron in an internally-heated diamond anvil cell. *Earth and Planetary Science Letters*, **282**(1-4):252–257.

Komabayashi, T., Hirose, K., Nagaya, Y., Sugimura, E., & Ohishi, Y. (2010). High-temperature compression of ferropericlase and the effect of temperature on iron spin transition. *Earth and Planetary Science Letters*, **297**(3-4):691–699.

Komabayashi, T. & Omori, S. (2006). Internally consistent thermodynamic data set for dense hydrous magnesium silicates up to 35 GPa, 1600 C: implications for water circulation in the Earth's deep mantle. *Physics of the Earth and Planetary Interiors*, **156**(1-2):89–107.

Komabayashi, T., Omori, S., & Maruyama, S. (2005). Experimental and theoretical study of stability of dense hydrous magnesium silicates in the deep upper mantle. *Physics of the Earth and Planetary Interiors*, **153**(4):191–209.

Kono, Y., Park, C., Kenney-Benson, C., Shen, G., & Wang, Y. (2014). Toward comprehensive studies of liquids at high pressures and high temperatures: Combined structure, elastic wave velocity, and viscosity measurements in the Paris–Edinburgh cell. *Physics of the Earth and Planetary Interiors*, **228**:269–280.

Kono, Y., Shibazaki, Y., Kenney-Benson, C., Wang, Y., & Shen, G. (2018). Pressure-induced structural change in MgSiO3 glass at pressures near the Earth's core–mantle boundary. *Proceedings of the National Academy of Sciences*, **115**(8):1742–1747.

Kono, Y., Shu, Y., Kenney-Benson, C., Wang, Y., & Shen, G. (2020). Structural evolution of SiO2 glass with Si coordination number greater than 6. *Physical Review Letters*, **125**(20):205701.

Kovács, I., Green, D. H., Rosenthal, A., Hermann, J., O'neill, H. S. C., Hibberson, W. O., & Udvardi, B. (2012). An experimental study of water in nominally anhydrous minerals in the upper mantle near the water-saturated solidus. *Journal of Petrology*, **53**(10):2067–2093.

Kovács, I., O'Neill, H. S. C., Hermann, J., & Hauri, E. H. (2010). Site-specific infrared OH absorption coefficients for water substitution into olivine. *American Mineralogist*, **95**(2-3):292–299.

Kraft, D. (1988). A software package for sequential quadratic programming. *Tech. Rep. DFVLR-FB 88-28*, Deutsche Forschungs- und Versuchsanstalt für Luft- und Raumfahrt (DFVLR) - Institut für Dynamik der Flugsysteme, Köln, Germany.

Krishnan, R. S. (1945). Raman spectrum of diamond. *Nature*, **155**(3928):171–171.

Krogh-Moe, J. (1956). A method for converting experimental X-ray intensities to an absolute scale. *Acta Crystallographica*, **9**(11):951–953.

Kubo, A., Suzuki, T., & Akaogi, M. (1997). High pressure phase equilibria in the system $CaTiO_3$-$CaSiO_3$: Stability of perovskite solid solutions. *Physics and Chemistry of Minerals*, **24**(7):488–494.

Kudo, Y., Hirose, K., Murakami, M., Asahara, Y., Ozawa, H., Ohishi, Y., & Hirao, N. (2012). Sound velocity measurements of CaSiO3 perovskite to 133 GPa and implications for lowermost mantle seismic anomalies. *Earth and Planetary Science Letters*, **349**:1–7.

Kunc, K., Loa, I., & Syassen, K. (2003). Equation of state and phonon frequency calculations of diamond at high pressures. *Physical Review B*, **68**(9):094107.

Kunc, K., Loa, I., & Syassen, K. (2004). Diamond under pressure: Ab-initio calculations of the equation of state and optical phonon frequency revisited. *High Pressure Research*, **24**(1):101–110.

Kunimoto, T., Irifune, T., Tange, Y., & Wada, K. (2016). Pressure generation to 50 GPa in Kawai-type multianvil apparatus using newly developed tungsten carbide anvils. *High Pressure Research*, **36**(2):97–104.

Kupenko, I., Dubrovinsky, L., Dubrovinskaia, N., McCammon, C., Glazyrin, K., Bykova, E., Ballaran, T. B., Sinmyo, R., Chumakov, A. I., Potapkin, V., Kantor, A., Rüffer, R., Hanfland, M., Chrichton, W., & Merlini, M. (2012). Portable double-sided laser-heating system for Mössbauer spectroscopy and X-ray diffraction experiments at synchrotron facilities with diamond anvil cells. *Review of Scientific Instruments*, **83**(12):124501.

Kupenko, I., McCammon, C., Sinmyo, R., Cerantola, V., Potapkin, V., Chumakov, A., Kantor, A., Rüffer, R., & Dubrovinsky, L. (2015). Oxidation state of the lower mantle: In situ observations of the iron electronic configuration in bridgmanite at extreme conditions. *Earth and Planetary Science Letters*, **423**:78–86.

Kuribayashi, T., Sano-Furukawa, A., & Nagase, T. (2014). Observation of pressure-induced phase transition of δ-AlOOH by using single-crystal synchrotron X-ray diffraction method. *Physics and Chemistry of Minerals*, **41**(4):303–312.

Kurnosov, A., Kantor, I., Boffa-Ballaran, T., Lindhardt, S., Dubrovinsky, L., Kuznetsov, A., & Zehnder, B. H. (2008). A novel gas-loading system for mechanically closing of various types of diamond anvil cells. *Review of Scientific Instruments*, **79**(4):045110.

Kurnosov, A., Marquardt, H., Dubrovinsky, L., & Potapkin, V. (2019). A waveguide-based flexible CO_2-laser heating system for diamond-anvil cell applications. *Comptes Rendus Geoscience*, **351**(2-3):280–285.

Kurnosov, A., Marquardt, H., Frost, D. J., Ballaran, T. B., & Ziberna, L. (2017). Evidence for a Fe3+-rich pyrolitic lower mantle from (Al,Fe)-bearing bridgmanite elasticity data. *Nature*, **543**(7646):543–546.

Kurnosov, A., Marquardt, H., Frost, D. J., Ballaran, T. B., & Ziberna, L. (2018). Kurnosov et al. reply. *Nature*, **564**(7736):E27–E31.

Labrosse, S., Hernlund, J. W., & Coltice, N. (2007). A crystallizing dense magma ocean at the base of the Earth's mantle. *Nature*, **450**(7171):866–869.

Lacam, A. & Chateau, C. (1989). High-pressure measurements at moderate temperatures in a diamond anvil cell with a new optical sensor: SrB4O7:Sm2+. *Journal of Applied Physics*, **66**(1):366–372.

Lakshtanov, D. L., Sinogeikin, S. V., Litasov, K. D., Prakapenka, V. B., Hellwig, H., Wang, J., Sanches-Valle, C., Perrillat, J.-P., Chen, B., Somayazulu, M., et al. (2007). The post-stishovite phase transition in hydrous alumina-bearing SiO2 in the lower mantle of the earth. *Proceedings of the National Academy of Sciences*, **104**(34):13588–13590.

Lan, M. T., Duong, T. T., Huy, N. V., & Van Hong, N. (2017a). Network structure of SiO2 and MgSiO3 in amorphous and liquid States. *Materials Research Express*, **4**(3):035202.

Lan, M. T., Duong, T. T., Iitaka, T., & Van Hong, N. (2017b). Computer simulation of CaSiO3 glass under compression: Correlation between Si–Si pair radial distribution function and intermediate range order structure. *Materials Research Express*, **4**(6):065201.

Lanczos, C. (1966). *Discourse on Fourier Series*. Oliver & Boyd, Edinbugh.

Laniel, D., Winkler, B., Fedotenko, T., Pakhomova, A., Chariton, S., Milman, V., Prakapenka, V., Dubrovinsky, L., & Dubrovinskaia, N. (2020). High-pressure polymeric nitrogen allotrope with the black phosphorus structure. *Physical Review Letters*, **124**(21):216001.

Lau, H. C. P. & Faul, U. H. (2019). Anelasticity from seismic to tidal timescales: Theory and observations. *Earth and Planetary Science Letters*, **508**:18–29.

Lazor, P., Shen, G., & Saxena, S. K. (1993). Laser-heated diamond anvil cell experiments at high pressure: Melting curve of nickel up to 700 kbar. *Physics and Chemistry of Minerals*, **20**(2):86–90.

Le Bail, A. (2005). Whole powder pattern decomposition methods and applications: A retrospection. *Powder Diffraction*, **20**(4):316–326.

Le Bail, A., Duroy, H., & Fourquet, J. L. (1988). Ab-initio structure determination of LiSbWO6 by X-ray powder diffraction. *Materials Research Bulletin*, **23**(3):447–452.

Le Roux, S. & Petkov, V. (2010). ISAACS–interactive structure analysis of amorphous and crystalline systems. *Journal of Applied Crystallography*, **43**(1):181–185.

Lee, S. K., Lin, J.-F., Cai, Y. Q., Hiraoka, N., Eng, P. J., Okuchi, T., Mao, H.-k., Meng, Y., Hu, M. Y., Chow, P., et al. (2008). X-ray Raman scattering study of MgSiO3 glass at high pressure: Implication for triclustered MgSiO3 melt in Earth's mantle. *Proceedings of the National Academy of Sciences*, **105**(23):7925–7929.

Lei, L., Yan, B., & Ji-An, X. (2013). Ruby fluorescence pressure scale: Revisited. *Chinese Physics B*, **22**(5):056201.

Letoullec, R., Pinceaux, J. P., & Loubeyre, P. (1988). The membrane diamond anvil cell: a new device for generating continuous pressure and temperature variations. *International Journal of High Pressure Research*, **1**(1):77–90.

Li, B., Ding, Y., Kim, D. Y., Ahuja, R., Zou, G., & Mao, H.-K. (2011). Rhodium dihydride (RhH_2) with high volumetric hydrogen density. *Proceedings of the National Academy of Sciences*, **108**(46):18618–18621.

Li, B., Ji, C., Yang, W., Wang, J., Yang, K., Xu, R., Liu, W., Cai, Z., Chen, J., & Mao, H.-k. (2018). Diamond anvil cell behavior up to 4 Mbar. *Proceedings of the National Academy of Sciences*, **115**(8):1713–1717.

Li, B., Kung, J., Uchida, T., & Wang, Y. (2005). Pressure calibration to 20 GPa by simultaneous use of ultrasonic and X-ray techniques. *Journal of Applied Physics*, **98**(1):013521.

Li, C., van der Hilst, R. D., Engdahl, E. R., & Burdick, S. (2008). A new global model for P wave speed variations in Earth's mantle. *Geochemistry, Geophysics, Geosystems*, **9**(5).

Li, L., Weidner, D. J., Brodholt, J., Alfe, D., Price, G. D., Caracas, R., & Wentzcovitch, R. (2006). Elasticity of CaSiO3 perovskite at high pressure and high temperature. *Physics of the Earth and Planetary Interiors*, **155**(3-4):249–259.

Li, X., Liu, Y., Wang, R., Yoshino, T., Xu, J., Zhang, D., Grützner, T., Zhang, J., & Wu, X. (2021). Thermal equation of state of F-bearing superhydrous phase B (Mg10Si3O14(OH,F)4): Implications for the transportation of fluorine and water into the lower mantle. *Physics of the Earth and Planetary Interiors*, **323**:106824.

Li, X., Mao, Z., Sun, N., Liao, Y., Zhai, S., Wang, Y., Ni, H., Wang, J., Tkachev, S. N., & Lin, J.-F. (2016). Elasticity of single-crystal superhydrous phase B at simultaneous high pressure-temperature conditions. *Geophysical Research Letters*, **43**(16):8458–8465.

Li, Z. & Scheraga, H. A. (1987). Monte Carlo-minimization approach to the multiple-minima problem in protein folding. *Proceedings of the National Academy of Sciences*, **84**(19):6611–6615.

Libowitzky, E. & Rossman, G. R. (1997). An IR absorption calibration for water in minerals. *American Mineralogist*, **82**(11-12):1111–1115.

Liebermann, R. C. (2011). Multi-anvil, high pressure apparatus: a half-century of development and progress. *High Pressure Research*, **31**(4):493–532.

Lin, J.-F., Fei, Y., Sturhahn, W., Zhao, J., Mao, H.-k., & Hemley, R. J. (2004a). Magnetic transition and sound velocities of Fe3S at high pressure: implications for Earth and planetary cores. *Earth and Planetary Science Letters*, **226**(1-2):33–40.

Lin, J.-F., Jacobsen, S. D., Sturhahn, W., Jackson, J. M., Zhao, J., & Yoo, C.-S. (2006). Sound velocities of ferropericlase in the Earth's lower mantle. *Geophysical Research Letters*, **33**(22).

Lin, J.-F., Mao, Z., Yang, J., & Fu, S. (2018). Elasticity of lower-mantle bridgmanite. *Nature*, **564**(7736):E18–E26.

Lin, J.-F., Santoro, M., Struzhkin, V. V., Mao, H.-k., & Hemley, R. J. (2004b). In situ high pressure-temperature Raman spectroscopy technique with laser-heated diamond anvil cells. *Review of Scientific Instruments*, **75**(10):3302–3306.

Lin, J.-F., Shu, J., Mao, H.-k., Hemley, R. J., & Shen, G. (2003). Amorphous boron gasket in diamond anvil cell research. *Review of Scientific Instruments*, **74**(11):4732–4736.

Lin, J.-F., Speziale, S., Mao, Z., & Marquardt, H. (2013). Effects of the electronic spin transitions of iron in lower mantle minerals: Implications for deep mantle geophysics and geochemistry. *Reviews of Geophysics*, **51**(2):244–275.

Lister, J. R. & Buffett, B. A. (1995). The strength and efficiency of thermal and compositional convection in the geodynamo. *Physics of the Earth and Planetary Interiors*, **91**(1-3):17–30.

Litasov, K. D., Dorogokupets, P. I., Ohtani, E., Fei, Y., Shatskiy, A., Sharygin, I. S., Gavryushkin, P. N., Rashchenko, S. V., Seryotkin, Y. V., Higo, Y., Funakoshi, K., Chanyshev, A. D., & Lobanov, S. S. (2013). Thermal equation of state and thermodynamic properties of molybdenum at high pressures. *Journal of Applied Physics*, **113**(9):093507.

Litasov, K. D., Ohtani, E., Ghosh, S., Nishihara, Y., Suzuki, A., & Funakoshi, K. (2007). Thermal equation of state of superhydrous phase B to 27 GPa and 1373 K. *Physics of the Earth and Planetary Interiors*, **164**(3-4):142–160.

Liu, C., Gao, H., Hermann, A., Wang, Y., Miao, M., Pickard, C. J., Needs, R. J., Wang, H.-T., Xing, D., & Sun, J. (2020). Plastic and superionic helium ammonia compounds under high pressure and high temperature. *Physical Review X*, **10**(2):021007.

Liu, J., Li, J., Hrubiak, R., & Smith, J. S. (2016). Origins of ultralow velocity zones through slab-derived metallic melt. *Proceedings of the National Academy of Sciences*, **113**(20):5547–5551.

Liu, J. & Vohra, Y. K. (1993). Pressure dependence of the fluorescence spectra of the Sm: doped YAG to 73 GPa. *Solid State Communications*, **88**(6):417–419.

Liu, L.-G. & Bassett, W. A. (1975). The melting of iron up to 200 kbar. *Journal of Geophysical Research*, **80**(26):3777–3782.

Liu, L.-g., Okamoto, K., Yang, Y.-j., Chen, C.-c., & Lin, C.-C. (2004). Elasticity of single-crystal phase D (a dense hydrous magnesium silicate) by Brillouin spectroscopy. *Solid State Communications*, **132**(8):517–520.

Liu, S., Tang, Q., Wu, B., Zhang, F., Liu, J., Fan, C., & Lei, L. (2021a). Raman scattering from highly-stressed anvil diamond. *Chinese Physics B*, **30**(1):016301.

Liu, Z., Ballaran, T. B., Huang, R., Frost, D. J., & Katsura, T. (2019). Strong correlation of oxygen vacancies in bridgmanite with Mg/Si ratio. *Earth and Planetary Science Letters*, **523**:115697.

Liu, Z., Fei, H., Chen, L., McCammon, C., Wang, L., Liu, R., Wang, F., Liu, B., & Katsura, T. (2021b). Bridgmanite is nearly dry at the top of the lower mantle. *Earth and Planetary Science Letters*, **570**:117088.

Lobanov, S. S. & Speziale, S. (2019). Radiometric temperature measurements in nongray ferropericlase with pressure-spin-and temperature-dependent optical properties. *Journal of Geophysical Research: Solid Earth*, **124**(12):12825–12836.

Lobanov, S. S., Speziale, S., & Brune, S. (2021a). Modelling Mie scattering in pyrolite in the laser-heated diamond anvil cell: Implications for the core-mantle boundary temperature determination. *Physics of the Earth and Planetary Interiors*, **318**:106773.

Lobanov, S. S., Speziale, S., Lin, J.-F., Schifferle, L., & Schreiber, A. (2021b). Radiometric temperature determination in nongray bridgmanite: applications to melting curve and post-perovskite transition boundary in the lower mantle. *Journal of Geophysical Research: Solid Earth*, **126**(5):e2021JB021723.

Long, D. A. (1977). *Raman Spectroscopy*. McGraw-Hill, New York. ISBN 9780070386754.

Lorch, E. (1969). Neutron diffraction by germania, silica and radiation-damaged silica glasses. *Journal of Physics C: Solid State Physics*, **2**(2):229–237.

Lord, O. T., Walter, M. J., Dasgupta, R., Walker, D., & Clark, S. M. (2009). Melting in the Fe–C system to 70 GPa. *Earth and Planetary Science Letters*, **284**(1-2):157–167.

Lord, O. T., Walter, M. J., Dobson, D., Armstrong, L., Clark, S., & Kleppe, A. (2010). The FeSi phase diagram to 150 GPa. *Journal of Geophysical Research: Solid Earth*, **115**(B6).

Lord, O. T. & Wang, W. (2018). MIRRORS: A MATLAB® GUI for temperature measurement by multispectral imaging radiometry. *Review of Scientific Instruments*, **89**(10):104903.

Lord, O. T., Wann, E. T. H., Hunt, S. A., Walker, A. M., Santangeli, J., Walter, M. J., Dobson, D. P., Wood, I. G., Vočadlo, L., Morard, G., & Mezouar, M. (2014a). The NiSi melting curve to 70 GPa. *Physics of the Earth and Planetary Interiors*, **233**:13–23.

Lord, O. T., Wood, I. G., Dobson, D. P., Vočadlo, L., Wang, W., Thomson, A. R., Wann, E. T., Morard, G., Mezouar, M., & Walter, M. J. (2014b). The melting curve of Ni to 1 Mbar. *Earth and Planetary Science Letters*, **408**:226–236.

Loubeyre, P., Occelli, F., & Dumas, P. (2020). Synchrotron infrared spectroscopic evidence of the probable transition to metal hydrogen. *Nature*, **577**(7792):631–635.

Louvel, M., Drewitt, J. W. E., Ross, A., Thwaites, R., Heinen, B. J., Keeble, D. S., Beavers, C. M., Walter, M. J., & Anzellini, S. (2020). The HXD95: a modified Bassett-type hydrothermal diamond-anvil cell for in situ XRD experiments up to 5 GPa and 1300 K. *Journal of Synchrotron Radiation*, **27**(2).

Lundin, S., Catalli, K., Santillan, J., Shim, S.-H., Prakapenka, V., Kunz, M., & Meng, Y. (2008). Effect of Fe on the equation of state of mantle silicate perovskite over 1 Mbar. *Physics of the Earth and Planetary Interiors*, **168**(1-2):97–102.

MacKinnon, J. G. (2010). Critical values for Cointegration Tests. *Working Paper 1227*, Economics Department, Queen's University. URL `http://qed.econ.queensu.ca/working_papers/papers/qed_wp_1227.pdf`.

Maglić, K. D. & Pavičić, D. Z. (2001). Thermal and electrical properties of titanium between 300 and 1900 K. *International Journal of Thermophysics*, **22**(6):1833–1841.

Manghnani, M. H., Ming, L. C., & Jamieson, J. C. (1980). Prospects of using synchrotron radiation facilities with diamond-anvil cells: High-pressure research applications in geophysics. *Nuclear Instruments and Methods*, **177**(1):219–226.

Mao, H., Bell, P., Shaner, J. t., & Steinberg, D. (1978). Specific volume measurements of Cu, Mo, Pd, and Ag and calibration of the ruby R 1 fluorescence pressure gauge from 0.06 to 1 Mbar. *Journal of Applied Physics*, **49**(6):3276–3283.

Mao, H. K., Bell, P. M., Dunn, K. J., Chrenko, R. M., & DeVries, R. C. (1979). Absolute pressure measurements and analysis of diamonds subjected to maximum static pressures of 1.3–1.7 Mbar. *Review of Scientific Instruments*, **50**(8):1002–1009.

Mao, H. K., Chen, L., Hemley, R., Jephcoat, A., Wu, Y., & Bassett, W. (1989). Stability and equation of state of CaSiO3-perovskite to 134 GPa. *Journal of Geophysical Research: Solid Earth*, **94**(B12):17889–17894.

Mao, H.-k. & Hemley, R. J. (1994). Ultrahigh-pressure transitions in solid hydrogen. *Reviews of Modern Physics*, **66**(2):671.

Mao, H. K., Hemley, R. J., Wu, Y., Jephcoat, A. P., Finger, L. W., Zha, C. S., & Bassett, W. A. (1988). High-pressure phase diagram and equation of state of solid helium from single-crystal X-ray diffraction to 23.3 GPa. *Physical Review Letters*, **60**(25):2649.

Mao, H. K., Xu, J.-A., & Bell, P. M. (1986). Calibration of the ruby pressure gauge to 800 kbar under quasi-hydrostatic conditions. *Journal of Geophysical Research: Solid Earth*, **91**(B5):4673–4676.

Mao, Z., Lin, J.-F., Jacobsen, S. D., Duffy, T. S., Chang, Y.-Y., Smyth, J. R., Frost, D. J., Hauri, E. H., & Prakapenka, V. B. (2012). Sound velocities of hydrous ringwoodite to 16 GPa and 673 K. *Earth and Planetary Science Letters*, **331**:112–119.

Mao, Z., Lin, J.-F., Liu, J., & Prakapenka, V. B. (2011). Thermal equation of state of lower-mantle ferropericlase across the spin crossover. *Geophysical Research Letters*, **38**(23).

Mao, Z., Lin, J.-F., Yang, J., Inoue, T., & Prakapenka, V. B. (2015). Effects of the Fe3+ spin transition on the equation of state of bridgmanite. *Geophysical Research Letters*, **42**(11):4335–4342.

Mao, Z., Wang, F., Lin, J.-F., Fu, S., Yang, J., Wu, X., Okuchi, T., Tomioka, N., Prakapenka, V. B., Xiao, Y., et al. (2017). Equation of state and hyperfine parameters of high-spin bridgmanite in the Earth's lower mantle by synchrotron X-ray diffraction and Mössbauer spectroscopy. *American Mineralogist*, **102**(2):357–368.

Marquardt, H., Buchen, J., Mendez, A., Kurnosov, A., Wendt, M., Rothkirch, A., Pennicard, D., & Liermann, H.-P. (2018). Elastic softening of (Mg0.8Fe0.2)O ferropericlase across the iron spin crossover measured at seismic frequencies. *Geophysical Research Letters*, **45**(14):6862–6868.

Marquardt, H., Gleason, A., Marquardt, K., Speziale, S., Miyagi, L., Neusser, G., Wenk, H.-R., & Jeanloz, R. (2011). Elastic properties of MgO nanocrystals and grain boundaries at high pressures by Brillouin scattering. *Physical Review B*, **84**(6):064131.

Marquardt, H. & Miyagi, L. (2015). Slab stagnation in the shallow lower mantle linked to an increase in mantle viscosity. *Nature Geoscience*, **8**(4):311–314.

Marquardt, H., Speziale, S., Reichmann, H. J., Frost, D. J., & Schilling, F. R. (2009a). Single-crystal elasticity of (Mg0.9Fe0.1)O to 81 GPa. *Earth and Planetary Science Letters*, **287**(3-4):345–352.

Marquardt, H., Speziale, S., Reichmann, H. J., Frost, D. J., Schilling, F. R., & Garnero, E. J. (2009b). Elastic shear anisotropy of ferropericlase in Earth's lower mantle. *Science*, **324**(5924):224–226.

Marquardt, H. & Thomson, A. R. (2020). Experimental elasticity of Earth's deep mantle. *Nature Reviews Earth & Environment*, **1**(9):455–469.

Mashino, I., Murakami, M., Miyajima, N., & Petitgirard, S. (2020). Experimental evidence for silica-enriched Earth's lower mantle with ferrous iron dominant bridgmanite. *Proceedings of the National Academy of Sciences*, **117**(45):27899–27905.

Matas, J. & Bukowinski, M. S. T. (2007). On the anelastic contribution to the temperature dependence of lower mantle seismic velocities. *Earth and Planetary Science Letters*, **259**(1-2):51–65.

McBride, E. E., White, T. G., Descamps, A., Fletcher, L. B., Appel, K., Condamine, F. P., Curry, C. B., Dallari, F., Funk, S., Galtier, E., Gauthier, M., Goede, S., Kim, J. B., Lee, H. J., Ofori-Okai, B. K., Oliver, M., Rigby, A., Schoenwaelder, C., Sun, P., Tschentscher, T., Witte, B. B. L., Zastrau, U., Gregori, G., Nagler, B., Hastings, J., Glenzer, S. H., & Monaco, G. (2018). Setup for meV-resolution inelastic X-ray scattering measurements and X-ray diffraction at the Matter in Extreme Conditions endstation at the Linac Coherent Light Source. *Review of Scientific Instruments*, **89**(10):10F104.

McCammon, C. (2021). Mössbauer Spectroscopy with High Spatial Resolution: Spotlight on Geoscience. *In:* Yoshida, Y. & Langouche, G. (eds.), *Modern Mössbauer Spectroscopy*, *Topics in Applied Physics*, vol. 137, pp. 221–266. Springer, Singapore.

McCammon, C., Caracas, R., Glazyrin, K., Potapkin, V., Kantor, A., Sinmyo, R., Prescher, C., Kupenko, I., Chumakov, A., & Dubrovinsky, L. (2016). Sound velocities of bridgmanite from density of states determined by nuclear inelastic scattering and first-principles calculations. *Progress in Earth and Planetary Science*, **3**(1):1–10.

McCammon, C., Glazyrin, K., Kantor, A., Kantor, I., Kupenko, I., Narygina, O., Potapkin, V., Prescher, C., Sinmyo, R., Chumakov, A., Rüffer, R., Sergueev, I., Smirnov, G., & Dubrovinsky, L. (2013). Iron spin state in silicate perovskite at conditions of the Earth's deep interior. *High Pressure Research*, **33**(3):663–672.

McCammon, C., Hutchison, M., & Harris, J. (1997). Ferric iron content of mineral inclusions in diamonds from Sao Luiz: A view into the lower mantle. *Science*, **278**(5337):434–436.

McCammon, C., Kantor, I., Narygina, O., Rouquette, J., Ponkratz, U., Sergueev, I., Mezouar, M., Prakapenka, V., & Dubrovinsky, L. (2008). Stable intermediate-spin ferrous iron in lower-mantle perovskite. *Nature Geoscience*, **1**(10):684–687.

McCarthy, C. & Takei, Y. (2011). Anelasticity and viscosity of partially molten rock analogue: Toward seismic detection of small quantities of melt. *Geophysical Research Letters*, **38**(18).

McCluney, W. R. (2014). *Introduction to Radiometry and Photometry*. Artech House, Norwood, MA, USA, 2nd edn. ISBN 978-1-60807-833-2.

McDonough, W. F. & Rudnick, R. L. (1998). Mineralogy and Composition of the Upper Mantle. *In:* Hemley, R. J. (ed.), *Ultrahigh Pressure Mineralogy: Physics and Chemistry of the Earth's Deep Interior*, *Reviews in Mineralogy*, vol. 37, chap. 4. De Gruyter. doi:10.1515/9781501509179-006.

McNamara, A. K. (2019). A review of large low shear velocity provinces and ultra low velocity zones. *Tectonophysics*, **760**:199–220.

McNamara, A. K., Garnero, E. J., & Rost, S. (2010). Tracking deep mantle reservoirs with ultra-low velocity zones. *Earth and Planetary Science Letters*, **299**(1-2):1–9.

McNamara, A. K., van Keken, P. E., & Karato, S.-I. (2003). Development of finite strain in the convecting lower mantle and its implications for seismic anisotropy. *Journal of Geophysical Research: Solid Earth*, **108**(B5).

McQueen, R. G., Marsh, S. P., Taylor, J. W., Fritz, J. N., & Carter, W. J. (1970). The Equation of State of Solids from Shock Wave Studies. *In:* Kinslow, R. (ed.), *High-Velocity Impact Phenomena*, chap. 7, pp. 293–417. Academic Press. ISBN 978-0-12-408950-1.

Mead, R. N. & Mountjoy, G. (2006). A molecular dynamics study of the atomic structure of (CaO)x(SiO2)1-x Glasses. *The Journal of Physical Chemistry B*, **110**(29):14273–14278.

Meade, C., Hemley, R. J., & Mao, H. K. (1992). High-pressure X-ray diffraction of SiO2 glass. *Physical Review Letters*, **69**(9):1387.

Mégnin, C. & Romanowicz, B. (2000). The three-dimensional shear velocity structure of the mantle from the inversion of body, surface and higher-mode waveforms. *Geophysical Journal International*, **143**(3):709–728.

Mei, S. & Kohlstedt, D. (2000). Influence of water on plastic deformation of olivine aggregates: 1. Diffusion creep regime. *Journal of Geophysical Research: Solid Earth*, **105**(B9):21457–21469.

Méndez, A. S. J., Marquardt, H., Husband, R. J., Schwark, I., Mainberger, J., Glazyrin, K., Kurnosov, A., Otzen, C., Satta, N., Bednarcik, J., & Liermann, H.-P. (2020). A resistively-heated dynamic diamond anvil cell (RHdDAC) for fast compression X-ray diffraction experiments at high temperatures. *Review of Scientific Instruments*, **91**(7):073906.

Menéndez-Proupin, E. & Singh, A. K. (2007). Ab initio calculations of elastic properties of compressed Pt. *Physical Review B*, **76**(5):054117.

Meng, Y., Weidner, D. J., & Fei, Y. (1993). Deviatoric stress in a quasi-hydrostatic diamond anvil cell: Effect on the volume-based pressure calibration. *Geophysical Research Letters*, **20**(12):1147–1150.

Merkel, S. & Yagi, T. (2005). X-ray transparent gasket for diamond anvil cell high pressure experiments. *Review of Scientific Instruments*, **76**(4):046109.

Michaud-Agrawal, N., Denning, E. J., Woolf, T. B., & Beckstein, O. (2011). MDAnalysis: a toolkit for the analysis of molecular dynamics simulations. *Journal of Computational Chemistry*, **32**(10):2319–2327.

Millot, M., Hamel, S., Rygg, J. R., Celliers, P. M., Collins, G. W., Coppari, F., Fratanduono, D. E., Jeanloz, R., Swift, D. C., & Eggert, J. H. (2018). Experimental evidence for superionic water ice using shock compression. *Nature Physics*, **14**(3):297–302.

Ming, L.-c. & Bassett, W. A. (1974). Laser heating in the diamond anvil press up to 2000 C sustained and 3000 C pulsed at pressures up to 260 kilobars. *Review of Scientific Instruments*, **45**(9):1115–1118.

Miyagi, L., Kanitpanyacharoen, W., Kaercher, P., Lee, K. K., & Wenk, H.-R. (2010). Slip systems in MgSiO3 post-perovskite: implications for D" anisotropy. *Science*, **329**(5999):1639–1641.

Mookherjee, M. (2011). Mid-mantle anisotropy: Elasticity of aluminous phases in subducted MORB. *Geophysical Research Letters*, **38**(14).

Mookherjee, M., Karki, B. B., Stixrude, L., & Lithgow-Bertelloni, C. (2012). Energetics, equation of state, and elasticity of NAL phase: Potential host for alkali and aluminum in the lower mantle. *Geophysical Research Letters*, **39**(19).

Morard, G., Andrault, D., Guignot, N., Siebert, J., Garbarino, G., & Antonangeli, D. (2011). Melting of Fe–Ni–Si and Fe–Ni–S alloys at megabar pressures: implications for the core–mantle boundary temperature. *Physics and Chemistry of Minerals*, **38**(10):767–776.

Morris, C. E. (1991). Shock-wave equation-of-state studies at Los Alamos. *Shock Waves*, **1**(3):213–222.

Mosca, I., Cobden, L., Deuss, A., Ritsema, J., & Trampert, J. (2012). Seismic and mineralogical structures of the lower mantle from probabilistic tomography. *Journal of Geophysical Research: Solid Earth*, **117**(B6).

Mössbauer, R. L. (1958). Kernresonanzfluoreszenz von gammastrahlung in Ir^{191} [Nuclear resonance fluorescence from gamma radiation in Ir^{191}]. *Zeitschrift für Physik*, **151**(2):124–143. (In German).

Moulik, P. & Ekström, G. (2016). The relationships between large-scale variations in shear velocity, density, and compressional velocity in the Earth's mantle. *Journal of Geophysical Research: Solid Earth*, **121**(4):2737–2771.

Muir, J. M. R., Thomson, A. R., & Zhang, F. (2021). The miscibility of calcium silicate perovskite and bridgmanite: A single perovskite solid solution in hot, iron-rich regions. *Earth and Planetary Science Letters*, **566**:116973.

Mulyukova, E., Steinberger, B., Dabrowski, M., & Sobolev, S. V. (2015). Survival of LLSVPs for billions of years in a vigorously convecting mantle: Replenishment and destruction of chemical anomaly. *Journal of Geophysical Research: Solid Earth*, **120**(5):3824–3847.

Murakami, M., Asahara, Y., Ohishi, Y., Hirao, N., & Hirose, K. (2009). Development of in situ Brillouin spectroscopy at high pressure and high temperature with synchrotron radiation and infrared laser heating system: Application to the Earth's deep interior. *Physics of the Earth and Planetary Interiors*, **174**(1-4):282–291.

Murakami, M., Hirose, K., Kawamura, K., Sata, N., & Ohishi, Y. (2004). Post-perovskite phase transition in MgSiO3. *Science*, **304**(5672):855–858.

Murakami, M., Hirose, K., Ono, S., & Ohishi, Y. (2003). Stability of CaCl2-type and α-PbO2-type SiO2 at high pressure and temperature determined by in-situ X-ray measurements. *Geophysical Research Letters*, **30**(5).

Murakami, M., Ohishi, Y., Hirao, N., & Hirose, K. (2012). A perovskitic lower mantle inferred from high-pressure, high-temperature sound velocity data. *Nature*, **485**(7396):90–94.

Murakami, M., Sinogeikin, S. V., Bass, J. D., Sata, N., Ohishi, Y., & Hirose, K. (2007a). Sound velocity of MgSiO3 post-perovskite phase: A constraint on the D ″discontinuity. *Earth and Planetary Science Letters*, **259**(1-2):18–23.

Murakami, M., Sinogeikin, S. V., Hellwig, H., Bass, J. D., & Li, J. (2007b). Sound velocity of MgSiO3 perovskite to Mbar pressure. *Earth and Planetary Science Letters*, **256**(1-2):47–54.

Murakami, M. & Takata, N. (2019). Absolute primary pressure scale to 120 GPa: Toward a pressure benchmark for Earth's lower mantle. *Journal of Geophysical Research: Solid Earth*, **124**(7):6581–6588.

Murphy, C. A., Jackson, J. M., Sturhahn, W., & Chen, B. (2011). Melting and thermal pressure of hcp-Fe from the phonon density of states. *Physics of the Earth and Planetary Interiors*, **188**(1-2):114–120.

Nakagawa, T. & Tackley, P. J. (2014). Influence of combined primordial layering and recycled MORB on the coupled thermal evolution of Earth's mantle and core. *Geochemistry, Geophysics, Geosystems*, **15**(3):619–633.

Nakao, H., Einaga, M., Sakata, M., Kitagaki, M., Shimizu, K., Kawaguchi, S., Hirao, N., & Ohishi, Y. (2019). Superconductivity of pure H_3S synthesized from elemental sulfur and hydrogen. *Journal of the Physical Society of Japan*, **88**(12):123701.

Nakatsuka, A., Fukui, H., Kamada, S., Hirao, N., Ohkawa, M., Sugiyama, K., & Yoshino, T. (2021). Incorporation mechanism of Fe and Al into bridgmanite in a subducting mid-ocean ridge basalt and its crystal chemistry. *Scientific Reports*, **11**(1):1–15.

Nasu, S. (2013). General Introduction to Mössbauer Spectroscopy. *In:* Yoshida, Y. & G, L. (eds.), *Mössbauer Spectroscopy: Tutorial Book*, pp. 1–22. Springer, Berlin.

Neuville, D. R., De Ligny, D., & Henderson, G. S. (2014). Advances in Raman spectroscopy applied to earth and material sciences. *Reviews in Mineralogy and Geochemistry*, **78**(1):509–541.

Newville, M., Stensitzki, T., Allen, D. B., & Ingargiola, A. (2014). LMFIT: Non-Linear Least-Square Minimization and Curve-Fitting for Python. doi:10.5281/zenodo.11813.

Nishi, M., Irifune, T., Tsuchiya, J., Tange, Y., Nishihara, Y., Fujino, K., & Higo, Y. (2014). Stability of hydrous silicate at high pressures and water transport to the deep lower mantle. *Nature Geoscience*, **7**(3):224–227.

Nishi, M., Kuwayama, Y., Tsuchiya, J., & Tsuchiya, T. (2017). The pyrite-type high-pressure form of FeOOH. *Nature*, **547**(7662):205–208.

Nishi, M., Tsuchiya, J., Arimoto, T., Kakizawa, S., Kunimoto, T., Tange, Y., Higo, Y., & Irifune, T. (2018). Thermal equation of state of MgSiO4H2 phase H determined by in situ X-ray diffraction and a multianvil apparatus. *Physics and Chemistry of Minerals*, **45**(10):995–1001.

Noguchi, M., Komabayashi, T., Hirose, K., & Ohishi, Y. (2013). High-temperature compression experiments of CaSiO3 perovskite to lowermost mantle conditions and its thermal equation of state. *Physics and Chemistry of Minerals*, **40**(1):81–91.

Nomura, R., Hirose, K., Sata, N., & Ohishi, Y. (2010). Precise determination of post-stishovite phase transition boundary and implications for seismic heterogeneities in the mid-lower mantle. *Physics of the Earth and Planetary Interiors*, **183**(1-2):104–109.

Nomura, R., Zhou, Y., & Irifune, T. (2017). Melting phase relations in the MgSiO3–CaSiO3 system at 24 GPa. *Progress in Earth and Planetary Science*, **4**(1):1–11.

Norman, N. (1957). The Fourier transform method for normalizing intensities. *Acta Crystallographica*, **10**(5):370–373.

O'Bannon III, E. F., Jenei, Z., Cynn, H., Lipp, M. J., & Jeffries, J. R. (2018). Contributed Review: Culet diameter and the achievable pressure of a diamond anvil cell: Implications for the upper pressure limit of a diamond anvil cell. *Review of Scientific Instruments*, **89**(11):111501.

Obayashi, M., Yoshimitsu, J., Nolet, G., Fukao, Y., Shiobara, H., Sugioka, H., Miyamachi, H., & Gao, Y. (2013). Finite frequency whole mantle P wave tomography: Improvement of subducted slab images. *Geophysical Research Letters*, **40**(21):5652–5657.

Occelli, F., Loubeyre, P., & LeToullec, R. (2003). Properties of diamond under hydrostatic pressures up to 140 GPa. *Nature Materials*, **2**(3):151–154.

Oganov, A. R. & Ono, S. (2004). Theoretical and experimental evidence for a post-perovskite phase of MgSiO3 in Earth's D″ layer. *Nature*, **430**(6998):445–448.

Ohfuji, H., Okada, T., Yagi, T., Sumiya, H., & Irifune, T. (2010). Laser heating in nano-polycrystalline diamond anvil cell. *Journal of Physics: Conference Series*, **215**(1):012192.

Ohira, I., Murakami, M., Kohara, S., Ohara, K., & Ohtani, E. (2016). Ultrahigh-pressure acoustic wave velocities of SiO_2-Al_2O_3 glasses up to 200 GPa. *Progress in Earth and Planetary Science*, **3**(1):18.

Ohira, I., Ohtani, E., Sakai, T., Miyahara, M., Hirao, N., Ohishi, Y., & Nishijima, M. (2014). Stability of a hydrous δ-phase, AlOOH–MgSiO2(OH)2, and a mechanism for water transport into the base of lower mantle. *Earth and Planetary Science Letters*, **401**:12–17.

Ohta, K., Kuwayama, Y., Hirose, K., Shimizu, K., & Ohishi, Y. (2016). Experimental determination of the electrical resistivity of iron at Earth's core conditions. *Nature*, **534**(7605):95–98.

Ohtani, E. (2015). Hydrous minerals and the storage of water in the deep mantle. *Chemical Geology*, **418**:6–15.

Ohtani, E. (2020). The role of water in Earth's mantle. *National Science Review*, **7**(1):224–232.

Ohtani, E. (2021). Hydration and Dehydration in Earth's Interior. *Annual Review of Earth and Planetary Sciences*, **49**.

Ohtani, E., Amaike, Y., Kamada, S., Sakamaki, T., & Hirao, N. (2014). Stability of hydrous phase H MgSiO4H2 under lower mantle conditions. *Geophysical Research Letters*, **41**(23):8283–8287.

Ohtani, E., Litasov, K., Hosoya, T., Kubo, T., & Kondo, T. (2004). Water transport into the deep mantle and formation of a hydrous transition zone. *Physics of the Earth and Planetary Interiors*, **143**:255–269.

Ohtani, E., Litasov, K., Suzuki, A., & Kondo, T. (2001a). Stability field of new hydrous phase, δ-AlOOH, with implications for water transport into the deep mantle. *Geophysical Research Letters*, **28**(20):3991–3993.

Ohtani, E., Mibe, K., Sakamaki, T., Kamada, S., Takahashi, S., Fukui, H., Tsutsui, S., & Baron, A. Q. R. (2015). Sound velocity measurement by inelastic X-ray scattering at high pressure and temperature by resistive heating diamond anvil cell. *Russian Geology and Geophysics*, **56**(1-2):190–195.

Ohtani, E., Shibazaki, Y., Sakai, T., Mibe, K., Fukui, H., Kamada, S., Sakamaki, T., Seto, Y., Tsutsui, S., & Baron, A. Q. R. (2013). Sound velocity of hexagonal close-packed iron up to core pressures. *Geophysical Research Letters*, **40**(19):5089–5094.

Ohtani, E., Toma, M., Kubo, T., Kondo, T., & Kikegawa, T. (2003). In situ X-ray observation of decomposition of superhydrous phase B at high pressure and temperature. *Geophysical Research Letters*, **30**(2).

Ohtani, E., Toma, M., Litasov, K., Kubo, T., & Suzuki, A. (2001b). Stability of dense hydrous magnesium silicate phases and water storage capacity in the transition zone and lower mantle. *Physics of the Earth and Planetary Interiors*, **124**(1-2):105–117.

Okamoto, H. (2010). *Desk Handbook: Phase Diagrams for Binary Alloys*. ASM International, Materials Park, Ohio, 2nd edn. ISBN 978-1-61503-046-0.

Ono, S., Hirose, K., Kikegawa, T., & Saito, Y. (2002). The compressibility of a natural composition calcium ferrite-type aluminous phase to 70 GPa. *Physics of the Earth and Planetary Interiors*, **131**(3-4):311–318.

Ono, S., Mibe, K., Hirao, N., & Ohishi, Y. (2015). In situ Raman spectroscopy of cubic boron nitride to 90 GPa and 800 K. *Journal of Physics and Chemistry of Solids*, **76**:120–124.

Ono, S., Mibe, K., & Ohishi, Y. (2014). Raman spectra of culet face of diamond anvils and application as optical pressure sensor to high temperatures. *Journal of Applied Physics*, **116**(5):053517.

Osipov, A. A. (2019). High-temperature Raman spectroscopy. *Pure and Applied Chemistry*, **91**(11):1749–1756.

Otsuka, K. & Karato, S.-i. (2012). Deep penetration of molten iron into the mantle caused by a morphological instability. *Nature*, **492**(7428):243–246.

Ozawa, H., Tateno, S., Xie, L., Nakajima, Y., Sakamoto, N., Kawaguchi, S. I., Yoneda, A., & Hirao, N. (2018). Boron-doped diamond as a new heating element for internal-resistive heated diamond-anvil cell. *High Pressure Research*, **38**(2):120–135.

Pacchioni, G. (2019). An upgrade to a bright future. *Nature Reviews Physics*, **1**(2):100–101.

Pachhai, S., Li, M., Thorne, M. S., Dettmer, J., & Tkalčić, H. (2022). Internal structure of ultralow-velocity zones consistent with origin from a basal magma ocean. *Nature Geoscience*, **15**(1):79–84.

Palmer, A., Silevitch, D., Feng, Y., Wang, Y., Jaramillo, R., Banerjee, A., Ren, Y., & Rosenbaum, T. F. (2015). Sub-Kelvin magnetic and electrical measurements in a diamond anvil cell with in situ tunability. *Review of Scientific Instruments*, **86**(9):093901.

Pamato, M. G., Kurnosov, A., Ballaran, T. B., Frost, D. J., Ziberna, L., Giannini, M., Speziale, S., Tkachev, S. N., Zhuravlev, K. K., & Prakapenka, V. B. (2016). Single crystal elasticity of majoritic garnets: Stagnant slabs and thermal anomalies at the base of the transition zone. *Earth and Planetary Science Letters*, **451**:114–124.

Panero, W. R., Pigott, J. S., Reaman, D. M., Kabbes, J. E., & Liu, Z. (2015). Dry (Mg,Fe)SiO3 perovskite in the Earth's lower mantle. *Journal of Geophysical Research: Solid Earth*, **120**(2):894–908.

Parai, R. & Mukhopadhyay, S. (2012). How large is the subducted water flux? New constraints on mantle regassing rates. *Earth and Planetary Science Letters*, **317**:396–406.

Parisiades, P. (2021). A Review of the Melting Curves of Transition Metals at High Pressures Using Static Compression Techniques. *Crystals*, **11**(4):416.

Parisiades, P., Cova, F., & Garbarino, G. (2019). Melting curve of elemental zirconium. *Physical Review B*, **100**(5):054102.

Parsons, C. A. (1907). Some notes on carbon at high temperatures and pressures. *Proceedings of the Royal Society of London. Series A, Containing Papers of a Mathematical and Physical Character*, **79**(533):532–535.

Parsons, C. A. (1920). Bakerian Lecture, 1918.—Experiments on the artificial production of diamond. *Philosophical Transactions of the Royal Society of London. Series A, Containing Papers of a Mathematical or Physical Character*, **220**(571-581):67–107.

Paterson, M. (1982). The determination of hydroxyl by infrared absorption in quartz, silicate glasses and similar materials. *Bulletin de Minéralogie*, **105**(1):20–29.

Patterson, A. L. (1939). The Scherrer formula for X-ray particle size determination. *Physical Review*, **56**(10):978.

Pearson, D. G., Brenker, F. E., Nestola, F., McNeill, J., Nasdala, L., Hutchison, M. T., Matveev, S., Mather, K., Silversmit, G., Schmitz, S., Vekemans, B., & Vincze, L. (2014). Hydrous mantle transition zone indicated by ringwoodite included within diamond. *Nature*, **507**(7491):221–224.

Petitgirard, S., Malfait, W. J., Sinmyo, R., Kupenko, I., Hennet, L., Harries, D., Dane, T., Burghammer, M., & Rubie, D. C. (2015). Fate of MgSiO3 melts at core–mantle boundary conditions. *Proceedings of the National Academy of Sciences*, **112**(46):14186–14190.

Petkov, P. V., Dimov, S. S., Minev, R. M., & Pham, D. T. (2008). Laser milling: pulse duration effects on surface integrity. *Proceedings of the Institution of Mechanical Engineers, Part B: Journal of Engineering Manufacture*, **222**(1):35–45.

Petkov, V. (1989). RAD, a program for analysis of X-ray diffraction data from amorphous materials for personal computers. *Journal of Applied Crystallography*, **22**(4):387–389.

Petkov, V. (2012). Pair Distribution Functions Analysis. *In: Characterization of Materials*, pp. 1361–1372. Wiley. ISBN 9780471266969. doi:doi.org/10.1002/0471266965.com159.

Pfeifenberger, M. J., Mangang, M., Wurster, S., Reiser, J., Hohenwarter, A., Pfleging, W., Kiener, D., & Pippan, R. (2017). The use of femtosecond laser ablation as a novel tool for rapid micro-mechanical sample preparation. *Materials & Design*, **121**:109–118.

Piermarini, G. J., Block, S., Barnett, J., & Forman, R. (1975). Calibration of the pressure dependence of the R1 ruby fluorescence line to 195 kbar. *Journal of Applied Physics*, **46**(6):2774–2780.

Piermarini, G. J., Block, S., & Barnett, J. D. (1973). Hydrostatic limits in liquids and solids to 100 kbar. *Journal of Applied Physics*, **44**(12):5377–5382.

Pings, C. J. & Waser, J. (1968). Analysis of scattering data for mixtures of amorphous solids or liquids. *The Journal of Chemical Physics*, **48**(7):3016–3018.

Pistorius, C. W. F. T. (1965). Melting curves of the potassium halides at high pressures. *Journal of Physics and Chemistry of Solids*, **26**(9):1543–1548.

Planck, M. (1914). *The Theory of Heat Radiation*. (Masius, M., *tr.*). P. Blakiston's Son & Co., Philadelphia, USA.

Polian, A. (2003). Brillouin scattering at high pressure: an overview. *Journal of Raman Spectroscopy*, **34**(7-8):633–637.

Popov, M. (2004). Pressure measurements from Raman spectra of stressed diamond anvils. *Journal of Applied Physics*, **95**(10):5509–5514.

Portner, D. E., Rodríguez, E. E., Beck, S., Zandt, G., Scire, A., Rocha, M. P., Bianchi, M. B., Ruiz, M., França, G. S., Condori, C., & Alvarado, P. (2020). Detailed structure of

the subducted Nazca slab into the lower mantle derived from continent-scale teleseismic P wave tomography. *Journal of Geophysical Research: Solid Earth*, **125**(5):e2019JB017884.

Potapkin, V., Chumakov, A. I., Smirnov, G. V., Celse, J.-P., Rüffer, R., McCammon, C., & Dubrovinsky, L. (2012). The 57Fe synchrotron Mössbauer source at the ESRF. *Journal of Synchrotron Radiation*, **19**(4):559–569.

Powell, M. J. (1998). Direct search algorithms for optimization calculations. *Acta Numerica*, **7**:287–336.

Powell, M. J. D. (1994). A direct search optimization method that models the objective and constraint functions by linear interpolation. *In:* Gomez, S. & Hennar, J. P. (eds.), *Advances in Optimization and Numerical Analysis*, pp. 51–67. Springer, Netherlands. doi:http://dx.doi.org/10.1007/978-94-015-8330-5_4.

Powell, M. J. D. (2007). A view of algorithms for optimization without derivatives. *Mathematics Today - Bulletin of the Institute of Mathematics and its Applications*, **43**(5):170–174.

Powell, R. C. (1966). *The Interaction of Chromium Ions in Ruby Crystals*. Ph.D. thesis, Air Force Cambridge Research Laboratories, Hanscom Air Force Base, MA, USA. An optional note.

Pozzo, M. & Alfè, D. (2016). Saturation of electrical resistivity of solid iron at Earth's core conditions. *SpringerPlus*, **5**(1):1–6.

Pradhan, G. K., Fiquet, G., Siebert, J., Auzende, A.-L., Morard, G., Antonangeli, D., & Garbarino, G. (2015). Melting of MORB at core–mantle boundary. *Earth and Planetary Science Letters*, **431**:247–255.

Prakapenka, V. B., Kubo, A., Kuznetsov, A., Laskin, A., Shkurikhin, O., Dera, P., Rivers, M. L., & Sutton, S. R. (2008). Advanced flat top laser heating system for high pressure research at GSECARS: Application to the melting behavior of germanium. *High Pressure Research*, **28**(3):225–235.

Prakapenka, V. P., Shen, G., Dubrovinsky, L. S., Rivers, M. L., & Sutton, S. R. (2004). High pressure induced phase transformation of SiO2 and GeO2: difference and similarity. *Journal of Physics and Chemistry of Solids*, **65**(8-9):1537–1545.

Prescher, C. (2017). Glassure: An API and GUI program for analyzing angular dispersive total X-ray diffraction data. Version 1.0.0. doi:10.5281/zenodo.880836.

Prescher, C., Prakapenka, V. B., Stefanski, J., Jahn, S., Skinner, L. B., & Wang, Y. (2017). Beyond sixfold coordinated Si in SiO2 glass at ultrahigh pressures. *Proceedings of the National Academy of Sciences*, **114**(38):10041–10046.

Pugh, E. (2016). Note: Moissanite backing plates for use in diamond anvil high pressure cells. *Review of Scientific Instruments*, **87**(3):036102.

Rainey, E. & Kavner, A. (2014). Peak scaling method to measure temperatures in the laser-heated diamond anvil cell and application to the thermal conductivity of MgO. *Journal of Geophysical Research: Solid Earth*, **119**(11):8154–8170.

Rapp, R. P., Irifune, T., Shimizu, N., Nishiyama, N., Norman, M. D., & Inoue, T. (2008). Subduction recycling of continental sediments and the origin of geochemically enriched reservoirs in the deep mantle. *Earth and Planetary Science Letters*, **271**(1-4):14–23.

Regenauer-Lieb, K., Yuen, D. A., & Branlund, J. (2001). The initiation of subduction: criticality by addition of water? *Science*, **294**(5542):578–580.

Reichlin, R. L. (1983). Measuring the electrical resistance of metals to 40 GPa in the diamond-anvil cell. *Review of Scientific Instruments*, **54**(12):1674–1677.

Ricolleau, A., Fei, Y., Cottrell, E., Watson, H., Deng, L., Zhang, L., Fiquet, G., Auzende, A.-L., Roskosz, M., Morard, G., & Prakapenka, V. (2009). Density profile of pyrolite under the lower mantle conditions. *Geophysical Research Letters*, **36**(6).

Ricolleau, A., Perrillat, J.-p., Fiquet, G., Daniel, I., Matas, J., Addad, A., Menguy, N., Cardon, H., Mezouar, M., & Guignot, N. (2010). Phase relations and equation of state of a natural MORB: Implications for the density profile of subducted oceanic crust in the Earth's lower mantle. *Journal of Geophysical Research: Solid Earth*, **115**(B8).

Rietveld, H. M. (1969). A profile refinement method for nuclear and magnetic structures. *Journal of Applied Crystallography*, **2**(2):65–71.

Ringwood, A. E. (1975). *Composition and Petrology of the Earth's Mantle*. McGraw-Hill, New York. ISBN 0070529329.

Ritsema, J., Deuss, A., Van Heijst, H. J., & Woodhouse, J. H. (2011). S40RTS: a degree-40 shear-velocity model for the mantle from new Rayleigh wave dispersion, teleseismic traveltime and normal-mode splitting function measurements. *Geophysical Journal International*, **184**(3):1223–1236.

Ritsema, J. & Lekić, V. (2020). Heterogeneity of seismic wave velocity in Earth's mantle. *Annual Review of Earth and Planetary Sciences*, **48**:377–401.

Rivers, M., Prakapenka, V. B., Kubo, A., Pullins, C., Holl, C. M., & Jacobsen, S. D. (2008). The COMPRES/GSECARS gas-loading system for diamond anvil cells at the Advanced Photon Source. *High Pressure Research*, **28**(3):273–292.

Robinson, V. N. & Hermann, A. (2020). Plastic and superionic phases in ammonia–water mixtures at high pressures and temperatures. *Journal of Physics: Condensed Matter*, **32**(18):184004.

Rodríguez, E. E., Portner, D. E., Beck, S. L., Rocha, M. P., Bianchi, M. B., Assumpção, M., Ruiz, M., Alvarado, P., Condori, C., & Lynner, C. (2021). Mantle dynamics of the Andean Subduction Zone from continent-scale teleseismic S-wave tomography. *Geophysical Journal International*, **224**(3):1553–1571.

Rodríguez, I., Valladares, R. M., Valladares, A., Hinojosa-Romero, D., Santiago, U., & Valladares, A. A. (2021). Correlation: An Analysis Tool for Liquids and for Amorphous Solids. *Journal of Open Source Software*, **6**(65):2976. doi:10.21105/joss.02976.

Romanenko, A. V., Rashchenko, S. V., Kurnosov, A., Dubrovinsky, L., Goryainov, S. V., Likhacheva, A. Y., & Litasov, K. D. (2018). Single-standard method for simultaneous pressure and temperature estimation using Sm2+:SrB4O7 fluorescence. *Journal of Applied Physics*, **124**(16):165902.

Rosa, A., Mathon, O., Torchio, R., Jacobs, J., Pasternak, S., Irifune, T., & Pascarelli, S. (2020). Nano-polycrystalline diamond anvils: Key devices for XAS at extreme conditions: their use, scientific impact, present status and future needs. *High Pressure Research*, **40**(1):65–81.

Rosa, A. D., Sanchez-Valle, C., & Ghosh, S. (2012). Elasticity of phase D and implication for the degree of hydration of deep subducted slabs. *Geophysical Research Letters*, **39**(6).

Rossman, G. R. (1988). Vibrational spectroscopy of hydrous components. *In:* Hawthorne, F. C. (ed.), *Spectroscopic Method in Mineralogy and Geology*, *Reviews in Mineralogy & Geochemistry*, vol. 18, chap. 6, pp. 193–206. de Gruyter.

Rost, S., Garnero, E. J., Williams, Q., & Manga, M. (2005). Seismological constraints on a possible plume root at the core–mantle boundary. *Nature*, **435**(7042):666–669.

Rumble, J. R. (ed.) (2021). *CRC Handbook of Chemistry and Physics*. CRC Press/Taylor & Francis, Boca Raton, FL, 102nd edn. Internet Version (2021).

Sagatova, D. N., Shatskiy, A. F., Sagatov, N. E., & Litasov, K. D. (2021). Phase relations in CaSiO3 system up to 100 GPa and 2500 K. *Geochemistry International*, **59**(8):791–800.

Sakai, T., Dekura, H., & Hirao, N. (2016). Experimental and theoretical thermal equations of state of MgSiO3 post-perovskite at multi-megabar pressures. *Scientific Reports*, **6**(1):1–8.

Sakairi, T., Sakamaki, T., Ohtani, E., Fukui, H., Kamada, S., Tsutsui, S., Uchiyama, H., & Baron, A. Q. R. (2018). Sound velocity measurements of hcp Fe-Si alloy at high pressure and high temperature by inelastic X-ray scattering. *American Mineralogist: Journal of Earth and Planetary Materials*, **103**(1):85–90.

Salmon, P. S., Moody, G. S., Ishii, Y., Pizzey, K. J., Polidori, A., Salanne, M., Zeidler, A., Buscemi, M., Fischer, H. E., Bull, C. L., Klotz, S., Weber, R., Benmore, C. J., & MacLeod, S. G. (2019). Pressure induced structural transformations in amorphous MgSiO3 and CaSiO3. *Journal of Non-Crystalline Solids: X*, **3**:100024.

Sambridge, M., Gerald, J. F., Kovács, I., O'Neill, H. S. C., & Hermann, J. (2008). Quantitative absorbance spectroscopy with unpolarized light: Part I. Physical and mathematical development. *American Mineralogist*, **93**(5-6):751–764.

Sanchez-Valle, C. & Bass, J. D. (2010). Elasticity and pressure-induced structural changes in vitreous MgSiO3-enstatite to lower mantle pressures. *Earth and Planetary Science Letters*, **295**(3-4):523–530.

Sanloup, C., Drewitt, J. W. E., Crépisson, C., Kono, Y., Park, C., McCammon, C., Hennet, L., Brassamin, S., & Bytchkov, A. (2013a). Structure and density of molten fayalite at high pressure. *Geochimica et Cosmochimica Acta*, **118**:118–128.

Sanloup, C., Drewitt, J. W. E., Konôpková, Z., Dalladay-Simpson, P., Morton, D. M., Rai, N., van Westrenen, W., & Morgenroth, W. (2013b). Structural change in molten basalt at deep mantle conditions. *Nature*, **503**(7474):104–107.

Sano, A., Ohtani, E., Kondo, T., Hirao, N., Sakai, T., Sata, N., Ohishi, Y., & Kikegawa, T. (2008). Aluminous hydrous mineral δ-AlOOH as a carrier of hydrogen into the core-mantle boundary. *Geophysical Research Letters*, **35**(3).

Sano, A., Ohtani, E., Kubo, T., & Funakoshi, K.-i. (2004). In situ X-ray observation of decomposition of hydrous aluminum silicate AlSiO3OH and aluminum oxide hydroxide d-AlOOH at high pressure and temperature. *Journal of Physics and Chemistry of Solids*, **65**(8-9):1547–1554.

Sano-Furukawa, A., Komatsu, K., Vanpeteghem, C. B., & Ohtani, E. (2008). Neutron diffraction study of δ-AlOOD at high pressure and its implication for symmetrization of the hydrogen bond. *American Mineralogist*, **93**(10):1558–1567.

Santamaría-Pérez, D., Ross, M., Errandonea, D., Mukherjee, G. D., Mezouar, M., & Boehler, R. (2009). X-ray diffraction measurements of Mo melting to 119 GPa and the high pressure phase diagram. *The Journal of Chemical Physics*, **130**(12):124509.

Sato, T. & Funamori, N. (2008). Sixfold-coordinated amorphous polymorph of SiO 2 under high pressure. *Physical Review Letters*, **101**(25):255502.

Satta, N., Criniti, G., Kurnosov, A., Boffa Ballaran, T., Ishii, T., & Marquardt, H. (2021). High-Pressure Elasticity of δ-(Al, Fe) OOH Single Crystals and Seismic Detectability of Hydrous MORB in the Shallow Lower Mantle. *Geophysical Research Letters*, **48**(23):e2021GL094185.

Schaeffer, A. M. J., Talmadge, W. B., Temple, S. R., & Deemyad, S. (2012). High pressure melting of lithium. *Physical Review Letters*, **109**(18):185702.

Schmandt, B. & Lin, F.-C. (2014). P and S wave tomography of the mantle beneath the United States. *Geophysical Research Letters*, **41**(18):6342–6349.

Schmidt, M. W. (1995). Lawsonite: upper pressure stability and formation of higher density hydrous phases. *American Mineralogist*, **80**(11-12):1286–1292.

Schuberth, B. S. A. & Bigalke, T. (2021). From Mantle Convection to Seismic Observations: Quantifying the Uncertainties Related to Anelasticity. *In:* Marquardt, H., Ballmer, M., Cottaar, S., & Konter, J. (eds.), *Mantle Convection and Surface Expressions*, *American Geophysical*

Union (AGU) Geophysical Monograph Series, vol. 263, chap. 4, pp. 97–119. John Wiley & Sons, Hoboken, NJ. ISBN 9781119528609. doi:10.1002/9781119528609.ch4.

Schulze, K., Marquardt, H., Kawazoe, T., Ballaran, T. B., McCammon, C., Koch-Müller, M., Kurnosov, A., & Marquardt, K. (2018). Seismically invisible water in Earth's transition zone? *Earth and Planetary Science Letters*, **498**:9–16.

Shapiro, S. S. & Wilk, M. B. (1965). An analysis of variance test for normality (complete samples). *Biometrika*, **52**(3/4):591–611.

Shearer, P. M. (2009). *Introduction to Seismology*. Cambridge University Press, Cambridge, 2nd edn. ISBN 978-0-521-70842-5.

Shen, G. & Lazor, P. (1995). Measurement of melting temperatures of some minerals under lower mantle pressures. *Journal of Geophysical Research: Solid Earth*, **100**(B9):17699–17713.

Shen, G. & Mao, H. K. (2016). High-pressure studies with x-rays using diamond anvil cells. *Reports on Progress in Physics*, **80**(1):016101.

Shen, G., Prakapenka, V. B., Rivers, M. L., & Sutton, S. R. (2003). Structural investigation of amorphous materials at high pressures using the diamond anvil cell. *Review of Scientific Instruments*, **74**(6):3021–3026.

Shen, G., Rivers, M. L., Sutton, S. R., Sata, N., Prakapenka, V. B., Oxley, J., & Suslick, K. S. (2004). The structure of amorphous iron at high pressures to 67 GPa measured in a diamond anvil cell. *Physics of the Earth and Planetary Interiors*, **143**:481–495.

Shen, G., Rivers, M. L., Wang, Y., & Sutton, S. R. (2001). Laser heated diamond cell system at the Advanced Photon Source for in situ X-ray measurements at high pressure and temperature. *Review of Scientific Instruments*, **72**(2):1273–1282.

Shen, G., Wang, L., Ferry, R., Mao, H.-k., & Hemley, R. J. (2010). A portable laser heating microscope for high pressure research. *In: Journal of Physics: Conference Series*, vol. 215, p. 012191. IOP Publishing.

Shen, G., Wang, Y., Dewaele, A., Wu, C., Fratanduono, D. E., Eggert, J., Klotz, S., Dziubek, K. F., Loubeyre, P., Fat'yanov, O. V., Asimov, P. D., Mashimo, T., Wentzcovitch, R. M. M., & other members of the IPPS task group (2020). Toward an international practical pressure scale: A proposal for an IPPS ruby gauge (IPPS-Ruby2020). *High Pressure Research*, **40**(3):299–314.

Shephard, G. E., Houser, C., Hernlund, J. W., Valencia-Cardona, J. J., Trønnes, R. G., & Wentzcovitch, R. M. (2021). Seismological expression of the iron spin crossover in ferropericlase in the Earth's lower mantle. *Nature Communications*, **12**(1):1–11.

Shieh, S. R., Duffy, T. S., & Shen, G. (2005). X-ray diffraction study of phase stability in SiO2 at deep mantle conditions. *Earth and Planetary Science Letters*, **235**(1-2):273–282.

Shim, S.-H., Duffy, T. S., & Shen, G. (2000). The stability and P–V–T equation of state of CaSiO3 perovskite in the Earth's lower mantle. *Journal of Geophysical Research: Solid Earth*, **105**(B11):25955–25968.

Shim, S.-H., Grocholski, B., Ye, Y., Alp, E. E., Xu, S., Morgan, D., Meng, Y., & Prakapenka, V. B. (2017). Stability of ferrous-iron-rich bridgmanite under reducing midmantle conditions. *Proceedings of the National Academy of Sciences*, **114**(25):6468–6473.

Shim, S.-H., Kubo, A., & Duffy, T. S. (2007). Raman spectroscopy of perovskite and post-perovskite phases of MgGeO3 to 123 GPa. *Earth and Planetary Science Letters*, **260**(1-2):166–178.

Shinmei, T., Sanehira, T., Yamazaki, D., Inoue, T., Irifune, T., Funakoshi, K.-ì., & Nozawa, A. (2005). High-temperature and high-pressure equation of state for the hexagonal phase in the system NaAlSiO4–MgAl2O4. *Physics and Chemistry of Minerals*, **32**(8):594–602.

Silvera, I. F., Chijioke, A. D., Nellis, W. J., Soldatov, A., & Tempere, J. (2007). Calibration of the ruby pressure scale to 150 GPa. *physica status solidi (b)*, **244**(1):460–467.

Simmons, N. A., Forte, A. M., & Grand, S. P. (2009). Joint seismic, geodynamic and mineral physical constraints on three-dimensional mantle heterogeneity: Implications for the relative importance of thermal versus compositional heterogeneity. *Geophysical Journal International*, **177**(3):1284–1304.

Simonova, D., Bykova, E., Bykov, M., Kawazoe, T., Simonov, A., Dubrovinskaia, N., & Dubrovinsky, L. (2020). Structural Study of δ-AlOOH Up to 29 GPa. *Minerals*, **10**(12):1055.

Sinelnikov, Y. D., Chen, G., & Liebermann, R. C. (1998). Elasticity of CaTiO3–CaSiO3 perovskites. *Physics and Chemistry of Minerals*, **25**(7):515–521.

Singh, A. K., Andrault, D., & Bouvier, P. (2012). X-ray diffraction from stishovite under non-hydrostatic compression to 70 GPa: Strength and elasticity across the tetragonal orthorhombic transition. *Physics of the Earth and Planetary Interiors*, **208**:1–10.

Singh, A. K. & Kenichi, T. (2001). Measurement and analysis of nonhydrostatic lattice strain component in niobium to 145 GPa under various fluid pressure-transmitting media. *Journal of Applied Physics*, **90**(7):3269–3275.

Sinmyo, R. & Hirose, K. (2010). The Soret diffusion in laser-heated diamond-anvil cell. *Physics of the Earth and Planetary Interiors*, **180**(3-4):172–178.

Sinmyo, R. & Hirose, K. (2013). Iron partitioning in pyrolitic lower mantle. *Physics and Chemistry of Minerals*, **40**(2):107–113.

Sinmyo, R., Hirose, K., & Ohishi, Y. (2019). Melting curve of iron to 290 GPa determined in a resistance-heated diamond-anvil cell. *Earth and Planetary Science Letters*, **510**:45–52.

Sinogeikin, S. V., Bass, J. D., & Katsura, T. (2001). Single-crystal elasticity of γ-(Mg0. 91Fe0. 09 (2SiO4 to high pressures and to high temperatures. *Geophysical Research Letters*, **28**(22):4335–4338.

Sinogeikin, S. V., Lakshtanov, D. L., Nicholas, J. D., & Bass, J. D. (2004). Sound velocity measurements on laser-heated MgO and Al2O3. *Physics of the Earth and Planetary Interiors*, **143**:575–586.

Skinner, L. B., Benmore, C. J., Weber, J. K. R., Tumber, S., Lazareva, L., Neuefeind, J., Santodonato, L., Du, J., & Parise, J. B. (2012). Structure of molten CaSiO3: neutron diffraction isotope substitution with aerodynamic levitation and molecular dynamics study. *The Journal of Physical Chemistry B*, **116**(45):13439–13447.

Smirnov, G. V., Van Bürck, U., Chumakov, A. I., Baron, A. Q. R., & Rüffer, R. (1997). Synchrotron Mössbauer source. *Physical Review B*, **55**(9):5811.

Smith, A. D., Donoghue, J., Garner, A., Winiarski, B., Bousser, E., Carr, J., Behnsen, J., Burnett, T. L., Wheeler, R., Wilford, K., Withers, P. J., & Preuss, M. (2019). On the application of Xe+ plasma FIB for micro-fabrication of small-scale tensile specimens. *Experimental Mechanics*, **59**(8):1113–1125.

Smith, E. & Dent, G. (2019). *Modern Raman Spectroscopy: A Practical Approach*. John Wiley & Sons, 2nd edn. ISBN 9781119440550. doi:10.1002/9781119440598.

Snider, E., Dasenbrock-Gammon, N., McBride, R., Debessai, M., Vindana, H., Vencatasamy, K., Lawler, K. V., Salamat, A., & Dias, R. P. (2020). Room-temperature superconductivity in a carbonaceous sulfur hydride. *Nature*, **586**(7829):373–377.

Soignard, E., Benmore, C. J., & Yarger, J. L. (2010). A perforated diamond anvil cell for high-energy X-ray diffraction of liquids and amorphous solids at high pressure. *Review of Scientific Instruments*, **81**(3):035110.

Solozhenko, V. L., Bushlya, V., & Zhou, J. (2019). Mechanical properties of ultra-hard nanocrystalline cubic boron nitride. *Journal of Applied Physics*, **126**(7):075107.

Soper, A. (2017). Gudrun — Routines for Reducing Total Scattering Data. url: https://www.isis.stfc.ac.uk/Pages/Gudrun.aspx [accessed March 2022].

Speziale, S., Marquardt, H., & Duffy, T. S. (2014). Brillouin scattering and its application in geosciences. *Reviews in Mineralogy and Geochemistry*, **78**(1):543–603.

Stachel, T., Aulbach, S., Brey, G. P., Harris, J. W., Leost, I., Tappert, R., & Viljoen, K. S. F. (2004). The trace element composition of silicate inclusions in diamonds: a review. *Lithos*, **77**(1-4):1–19.

Stewart, S. M. & Johnson, R. B. (2016). *Blackbody Radiation: A History of Thermal Radiation Computational Aids and Numerical Methods*. CRC Press, Boca Raton, Florida, USA.

Stishov, S. M. & Belov, N. V. (1962). Crystal structure of the new dense modification of silica. *Doklady Akademii Nauk SSSR*, **143**:951–964.

Stixrude, L. & Lithgow-Bertelloni, C. (2011). Thermodynamics of mantle minerals II: Phase equilibria. *Geophysical Journal International*, **184**(3):1180–1213.

Stixrude, L., Lithgow-Bertelloni, C., Kiefer, B., & Fumagalli, P. (2007). Phase stability and shear softening in CaSiO3 perovskite at high pressure. *Physical Review B*, **75**(2):024108.

Stokes, A. R. & Wilson, A. J. C. (1942). A method of calculating the integral breadths of Debye-Scherrer lines. *Mathematical Proceedings of the Cambridge Philosophical Society*, **38**(3):313–322.

Stutzmann, V., Dewaele, A., Bouchet, J., Bottin, F., & Mezouar, M. (2015). High-pressure melting curve of titanium. *Physical Review B*, **92**(22):224110.

Su, W.-j. & Dziewonski, A. M. (1997). Simultaneous inversion for 3-D variations in shear and bulk velocity in the mantle. *Physics of the Earth and Planetary Interiors*, **100**(1-4):135–156.

Suehiro, S., Wakamatsu, T., Ohta, K., Hirose, K., & Ohishi, Y. (2019). High-temperature electrical resistivity measurements of hcp iron to Mbar pressure in an internally resistive heated diamond anvil cell. *High Pressure Research*, **39**(4):579–587.

Sugano, S. & Tanabe, Y. (1958). Absorption spectra of Cr3+ in Al2O3. Part A: Theoretical studies of the absorption bands and lines. *Journal of the Physical Society of Japan*, **13**(8):880–899.

Sugimura, E., Komabayashi, T., Ohta, K., Hirose, K., Ohishi, Y., & Dubrovinsky, L. S. (2012). Experimental evidence of superionic conduction in H_2O ice. *The Journal of Chemical Physics*, **137**(19):194505.

Sukhomlinov, S. V. & Müser, M. H. (2017). Determination of accurate, mean bond lengths from radial distribution functions. *The Journal of Chemical Physics*, **146**(2):024506.

Sukhomlinov, S. V. & Müser, M. H. (2020). Erratum. *The Journal of Chemical Physics*, **152**(4):049902.

Sun, L., Ruoff, A. L., & Stupian, G. (2005). Convenient optical pressure gauge for multimegabar pressures calibrated to 300 GPa. *Applied Physics Letters*, **86**(1):014103.

Sun, N., Mao, Z., Yan, S., Wu, X., Prakapenka, V. B., & Lin, J.-F. (2016). Confirming a pyrolitic lower mantle using self-consistent pressure scales and new constraints on CaSiO3 perovskite. *Journal of Geophysical Research: Solid Earth*, **121**(7):4876–4894.

Sun, N., Shi, W., Mao, Z., Zhou, C., & Prakapenka, V. B. (2019). High Pressure-Temperature Study on the Thermal Equations of State of Seifertite andCaCl2-Type SiO2. *Journal of Geophysical Research: Solid Earth*, **124**(12):12620–12630.

Sun, N., Wei, W., Han, S., Song, J., Li, X., Duan, Y., Prakapenka, V. B., & Mao, Z. (2018). Phase transition and thermal equations of state of (Fe,Al)-bridgmanite and post-perovskite: implication for the chemical heterogeneity at the lowermost mantle. *Earth and Planetary Science Letters*, **490**:161–169.

Sundqvist, B. & Tolpygo, V. K. (2018). Saturation and pressure effects on the resistivity of titanium and two Ti-Al alloys. *Journal of Physics and Chemistry of Solids*, **122**:41–50.

Suzuki, A., Ohtani, E., & Kamada, T. (2000). A new hydrous phase δ-AlOOH synthesized at 21 GPa and 1000 C. *Physics and Chemistry of Minerals*, **27**(10):689–693.

Syassen, K. (2008). Ruby under pressure. *High Pressure Research*, **28**(2):75–126.

Takahashi, S., Ohtani, E., Sakamaki, T., Kamada, S., Fukui, H., Tsutsui, S., Uchiyama, H., Ishikawa, D., Hirao, N., Ohishi, Y., & Baron, A. Q. R. (2019). Sound velocity of Fe3C at high pressure and high temperature determined by inelastic X-ray scattering. *Comptes Rendus Geoscience*, **351**(2-3):190–196.

Takemura, K. (2001). Evaluation of the hydrostaticity of a helium-pressure medium with powder X-ray diffraction techniques. *Journal of Applied Physics*, **89**(1):662–668.

Takemura, K. (2021). Hydrostaticity in high pressure experiments: some general observations and guidelines for high pressure experimenters. *High Pressure Research*, pp. 1–20.

Takemura, K. & Dewaele, A. (2008). Isothermal equation of state for gold with a He-pressure medium. *Physical Review B*, **78**(10):104119.

Takeuchi, H. & Kanamori, H. (1966). Equations of state of matter from shock wave experiments. *journal of Geophysical Research*, **71**(16):3985–3994.

Tanaka, H. (2020). Liquid–liquid transition and polyamorphism. *The Journal of Chemical Physics*, **153**(13):130901.

Tange, Y., Irifune, T., & Funakoshi, K.-I. (2008). Pressure generation to 80 GPa using multi-anvil apparatus with sintered diamond anvils. *High Pressure Research*, **28**(3):245–254.

Tange, Y., Kuwayama, Y., Irifune, T., Funakoshi, K.-i., & Ohishi, Y. (2012). P-V-T equation of state of MgSiO3 perovskite based on the MgO pressure scale: A comprehensive reference for mineralogy of the lower mantle. *Journal of Geophysical Research: Solid Earth*, **117**(B6).

Tange, Y., Nishihara, Y., & Tsuchiya, T. (2009). Unified analyses for P-V-T equation of state of MgO: A solution for pressure-scale problems in high P-T experiments. *Journal of Geophysical Research: Solid Earth*, **114**(B3).

Taniguchi, T., Okuno, M., & Matsumoto, T. (1997). X-ray diffraction and EXAFS studies of silicate glasses containing Mg, Ca and Ba atoms. *Journal of Non-crystalline Solids*, **211**(1-2):56–63.

Tański, M. & Mizeraczyk, J. (2016). Parametric studies on the nanosecond laser micromachining of the materials. *In: Laser Technology 2016: Progress and Applications of Lasers*, vol. 10159, p. 101590Q. International Society for Optics and Photonics.

Tateno, S., Hirose, K., Sata, N., & Ohishi, Y. (2009). Determination of post-perovskite phase transition boundary up to 4400 K and implications for thermal structure in D″ layer. *Earth and Planetary Science Letters*, **277**(1-2):130–136.

Tateno, S., Komabayashi, T., Hirose, K., Hirao, N., & Ohishi, Y. (2019). Static compression of B2 KCl to 230 GPa and its PVT equation of state. *American Mineralogist: Journal of Earth and Planetary Materials*, **104**(5):718–723.

Tatsumi, Y. (2005). The subduction factory: How it operates in the evolving Earth. *GSA Today*, **15**(7):4.

Terasaki, H. & Fischer, R. A. (eds.) (2016). *Deep Earth: Physics and Chemistry of the Lower Mantle and Core*, *American Geophysical Union (AGU) Geophysical Monograph Series*, vol. 217. John Wiley & Sons, Hoboken, NJ. ISBN 978-1-118-99250-0.

Thompson, E. C., Davis, A. H., Brauser, N. M., Liu, Z., Prakapenka, V. B., & Campbell, A. J. (2020). Phase transitions in ε-FeOOH at high pressure and ambient temperature. *American Mineralogist: Journal of Earth and Planetary Materials*, **105**(12):1769–1777.

Thomson, A., Kohn, S., Bulanova, G., Smith, C., Araujo, D., & Walter, M. (2016a). Trace element composition of silicate inclusions in sub-lithospheric diamonds from the Juina-5 kimberlite: Evidence for diamond growth from slab melts. *Lithos*, **265**:108–124.

Thomson, A. R., Crichton, W. A., Brodholt, J. P., Wood, I. G., Siersch, N. C., Muir, J. M. R., Dobson, D. P., & Hunt, S. A. (2019). Seismic velocities of $CaSiO_3$ perovskite can explain LLSVPs in Earth's lower mantle. *Nature*, **572**(7771):643–647.

Thomson, A. R., Walter, M. J., Kohn, S. C., & Brooker, R. A. (2016b). Slab melting as a barrier to deep carbon subduction. *Nature*, **529**(7584):76–79.

Thomson, A. R., Walter, M. J., Lord, O. T., & Kohn, S. C. (2014). Experimental determination of melting in the systems enstatite-magnesite and magnesite-calcite from 15 to 80 GPa. *American Mineralogist*, **99**(8-9):1544–1554.

Tkalčić, H., Young, M., Muir, J. B., Davies, D. R., & Mattesini, M. (2015). Strong, multi-scale heterogeneity in Earth's lowermost mantle. *Scientific Reports*, **5**:18416.

Toby, B. H. & Von Dreele, R. B. (2013). GSAS-II: The genesis of a modern open-source all purpose crystallography software package. *Journal of Applied Crystallography*, **46**(2):544–549.

Tomasino, D., Kim, M., Smith, J., & Yoo, C.-S. (2014). Pressure-induced symmetry-lowering transition in dense nitrogen to layered polymeric nitrogen (LP-N) with colossal Raman intensity. *Physical Review Letters*, **113**(20):205502.

Torsvik, T. H., Smethurst, M. A., Burke, K., & Steinberger, B. (2006). Large igneous provinces generated from the margins of the large low-velocity provinces in the deep mantle. *Geophysical Journal International*, **167**(3):1447–1460.

Torsvik, T. H., Steinberger, B., Cocks, L. R. M., & Burke, K. (2008). Longitude: linking Earth's ancient surface to its deep interior. *Earth and Planetary Science Letters*, **276**(3-4):273–282.

Trampert, J., Deschamps, F., Resovsky, J., & Yuen, D. (2004). Probabilistic tomography maps chemical heterogeneities throughout the lower mantle. *Science*, **306**(5697):853–856.

Trieloff, M., Kunz, J., Clague, D. A., Harrison, D., & Allègre, C. J. (2000). The nature of pristine noble gases in mantle plumes. *Science*, **288**(5468):1036–1038.

Trots, D. M., Kurnosov, A., Ballaran, T. B., Tkachev, S., Zhuravlev, K., Prakapenka, V., Berkowski, M., & Frost, D. J. (2013). The Sm:YAG primary fluorescence pressure scale. *Journal of Geophysical Research: Solid Earth*, **118**(11):5805–5813.

Tschauner, O., Huang, S., Yang, S., Humayun, M., Liu, W., Gilbert Corder, S. N., Bechtel, H. A., Tischler, J., & Rossman, G. R. (2021). Discovery of davemaoite, CaSiO3-perovskite, as a mineral from the lower mantle. *Science*, **374**(6569):891–894.

Tschauner, O., Kiefer, B., Liu, H., Sinogeikin, S., Somayazulu, M., & Luo, S.-N. (2008). Possible structural polymorphism in Al-bearing magnesiumsilicate post-perovskite. *American Mineralogist*, **93**(4):533–539.

Tse, J. S. (2019). First-Principles Methods in the Investigation of the Chemical and Transport Properties of Materials under Extreme Conditions. *Engineering*, **5**(3):421–433.

Tsuchiya, T. (2011). Elasticity of subducted basaltic crust at the lower mantle pressures: Insights on the nature of deep mantle heterogeneity. *Physics of the Earth and Planetary Interiors*, **188**(3-4):142–149.

Tsuchiya, T., Tsuchiya, J., Dekura, H., & Ritterbex, S. (2020). Ab initio study on the lower mantle minerals. *Annual Review of Earth and Planetary Sciences*, **48**:99–119.

Turri, G., Webster, S., Chen, Y., Wickham, B., Bennett, A., & Bass, M. (2017). Index of refraction from the near-ultraviolet to the near-infrared from a single crystal microwave-assisted CVD diamond. *Optical Materials Express*, **7**(3):855–859.

Umemoto, K., Kawamura, K., Hirose, K., & Wentzcovitch, R. M. (2016). Post-stishovite transition in hydrous aluminous SiO2. *Physics of the Earth and Planetary Interiors*, **255**:18–26.

Van Der Spoel, D., Lindahl, E., Hess, B., Groenhof, G., Mark, A. E., & Berendsen, H. J. C. (2005). GROMACS: fast, flexible, and free. *Journal of Computational Chemistry*, **26**(16):1701–1718.

van Keken, P. E., Hacker, B. R., Syracuse, E. M., & Abers, G. A. (2011). Subduction factory: 4. Depth-dependent flux of H2O from subducting slabs worldwide. *Journal of Geophysical Research: Solid Earth*, **116**(B1).

Vanacore, E. & Niu, F. (2011). Characterization of the D" beneath the Galapagos Islands using SKKS and SKS waveforms. *Earthquake Science*, **24**(1):87–99.

Vanpeteghem, C. B., Ohtani, E., Kondo, T., Takemura, K., & Kikegawa, T. (2003a). Compressibility of phase Egg AlSiO3OH: Equation of state and role of water at high pressure. *American Mineralogist*, **88**(10):1408–1411.

Vanpeteghem, C. B., Ohtani, E., Litasov, K., Kondo, T., Watanuki, T., Isshiki, M., & Takemura, K. (2003b). The compressibility of hexagonal Al-rich NAL phase: similarities and differences with calcium ferrite-type (CF) phase with implications for the lower mantle. *Physics of the Earth and Planetary Interiors*, **138**(3-4):223–230.

Velisavljevic, N., MacLeod, S., & Cynn, H. (2012). Titanium Alloys at Extreme Pressure Conditions. *In:* Amin, A. K. M. N. (ed.), *Titanium Alloys*, chap. 4. IntechOpen, Rijeka. doi: 10.5772/36038.

Vinet, P., Ferrante, J., Rose, J. H., & Smith, J. R. (1987). Compressibility of solids. *Journal of Geophysical Research: Solid Earth*, **92**(B9):9319–9325.

Vinnik, L., Oreshin, S., Speziale, S., & Weber, M. (2010). Mid-mantle layering from SKS receiver functions. *Geophysical Research Letters*, **37**(24).

Virtanen, P., Gommers, R., Oliphant, T. E., Haberland, M., Reddy, T., Cournapeau, D., Burovski, E., Peterson, P., Weckesser, W., Bright, J., van der Walt, S. J., Brett, M., Wilson, J., Millman, K. J., Mayorov, N., Nelson, A. R. J., Jones, E., Kern, R., Larson, E., Carey, C. J., Polat, I., Feng, Y., Moore, E. W., VanderPlas, J., Laxalde, D., Perktold, J., Cimrman, R., Henriksen, I., Quintero, E. A., Harris, C. R., Archibald, A. M., Ribeiro, A. H., Pedregosa, F., van Mulbregt, P., & SciPy 1.0 Contributors (2020). SciPy 1.0: Fundamental Algorithms for Scientific Computing in Python. *Nature Methods*, **17**:261–272. doi: 10.1038/s41592-019-0686-2.

Von der Linde, D. & Sokolowski-Tinten, K. (2000). The physical mechanisms of short-pulse laser ablation. *Applied Surface Science*, **154**:1–10.

Wakamatsu, T., Ohta, K., Yagi, T., Hirose, K., & Ohishi, Y. (2018). Measurements of sound velocity in iron–nickel alloys by femtosecond laser pulses in a diamond anvil cell. *Physics and Chemistry of Minerals*, **45**(6):589–595.

Wales, D. J. & Doye, J. P. K. (1997). Global optimization by basin-hopping and the lowest energy structures of Lennard-Jones clusters containing up to 110 atoms. *The Journal of Physical Chemistry A*, **101**(28):5111–5116.

Walter, M. J. & Koga, K. T. (2004). The effects of chromatic dispersion on temperature measurement in the laser-heated diamond anvil cell. *Physics of the Earth and Planetary Interiors*, **143**:541–558.

Walter, M. J., Kohn, S. C., Araujo, D., Bulanova, G. P., Smith, C. B., Gaillou, E., Wang, J., Steele, A., & Shirey, S. B. (2011). Deep mantle cycling of oceanic crust: evidence from diamonds and their mineral inclusions. *Science*, **334**(6052):54–57.

Walter, M. J., Thomson, A. R., Wang, W., Lord, O. T., Ross, J., McMahon, S. C., Baron, M. A., Melekhova, E., Kleppe, A. K., & Kohn, S. C. (2015). The stability of hydrous silicates in Earth's lower mantle: Experimental constraints from the systems $MgO–SiO_2–H_2O$ and $MgO–Al_2O_3–SiO_2–H_2O$. *Chemical Geology*, **418**:16–29.

Walton, F., Bolling, J., Farrell, A., MacEwen, J., Syme, C. D., Jiménez, M. G., Senn, H. M., Wilson, C., Cinque, G., & Wynne, K. (2020). Polyamorphism mirrors polymorphism in the liquid–liquid transition of a molecular liquid. *Journal of the American Chemical Society*, **142**(16):7591–7597.

Wang, B., Zhang, Y., Fu, S., Yan, W., Takahashi, E., Li, L., Lin, J.-F., & Song, M. (2022). Single-crystal elasticity of phase Egg AlSiO3OH and δ-AlOOH by Brillouin spectroscopy. *American Mineralogist: Journal of Earth and Planetary Materials*, **107**(1):147–152.

Wang, H., Eremets, M. I., Troyan, I., Liu, H., Ma, Y., & Vereecken, L. (2015a). Nitrogen backbone oligomers. *Scientific Reports*, **5**:13239.

Wang, H., Yu, M., Wang, Y., Feng, Z., Wang, Y., Lü, X., Zhu, J., Ren, Y., & Liang, C. (2018). In-situ investigation of pressure effect on structural evolution and conductivity of Na_3SbS_4 superionic conductor. *Journal of Power Sources*, **401**:111–116.

Wang, X., Tsuchiya, T., & Hase, A. (2015b). Computational support for a pyrolitic lower mantle containing ferric iron. *Nature Geoscience*, **8**(7):556–559.

Wang, Z., Mao, H., & Saxena, S. (2000). The melting of corundum (Al2O3) under high pressure conditions. *Journal of Alloys and Compounds*, **299**(1-2):287–291.

Warren, B. E. (1969). *X-Ray Diffraction*. Addison Wesley, Reading, Massachusetts.

Warren, B. E., Krutter, H., & Morningstar, O. (1936). Fourier analysis of X-ray patterns of vitreous SiO2 and B2O2. *Journal of the American Ceramic Society*, **19**(1-12):202–206.

Waseda, Y. (1980). *The Structure of Non Crystalline Materials: Liquids and Amorphous Solids*. McGraw-Hill, New York. ISBN 0-07-068426-X.

Waseda, Y. & Suzuki, K. (1972). Structure factor and atomic distribution in liquid metals by X-ray diffraction. *physica status solidi (b)*, **49**(1):339–347.

Waseda, Y. & Toguri, J. (1977). The structure of molten binary silicate systems CaO-SiO2 and MgO-SiO2. *Metallurgical Transactions B*, **8**(4):563–568.

Watt, J. P., Davies, G. F., & O'Connell, R. J. (1976). The elastic properties of composite materials. *Reviews of Geophysics*, **14**(4):541–563.

Weck, G., Recoules, V., Queyroux, J.-A., Datchi, F., Bouchet, J., Ninet, S., Garbarino, G., Mezouar, M., & Loubeyre, P. (2020). Determination of the melting curve of gold up to 110 GPa. *Physical Review B*, **101**(1):014106.

Weir, S. T., Lipp, M. J., Falabella, S., Samudrala, G., & Vohra, Y. K. (2012). High pressure melting curve of tin measured using an internal resistive heating technique to 45 GPa. *Journal of Applied Physics*, **111**(12):123529.

Weir, S. T., Mitchell, A. C., & Nellis, W. J. (1996). Metallization of fluid molecular hydrogen at 140 GPa (1.4 Mbar). *Physical Review Letters*, **76**(11):1860.

Wenk, H.-R., Speziale, S., McNamara, A., & Garnero, E. (2006). Modeling lower mantle anisotropy development in a subducting slab. *Earth and Planetary Science Letters*, **245**(1-2):302–314.

White, W. M. (2010). Oceanic island basalts and mantle plumes: The geochemical perspective. *Annual Review of Earth and Planetary Sciences*, **38**:133–160.

Wicks, J. K. & Duffy, T. S. (2016). Crystal structures of minerals in the lower mantle. *In:* Terasaki, H. & Fischer, R. A. (eds.), *Deep Earth: Physics and Chemistry of the Lower Mantle and*

Core, *American Geophysical Union (AGU) Geophysical Monograph Series*, vol. 217, chap. 6, pp. 69–87. John Wiley & Sons. ISBN 9781118992487. doi:10.1002/9781118992487.ch6.

Wicks, J. K., Jackson, J. M., & Sturhahn, W. (2010). Very low sound velocities in iron-rich (Mg,Fe)O: Implications for the core-mantle boundary region. *Geophysical Research Letters*, **37**(15).

Wicks, J. K., Jackson, J. M., Sturhahn, W., & Zhang, D. (2017). Sound velocity and density of magnesiowüstites: Implications for ultralow-velocity zone topography. *Geophysical Research Letters*, **44**(5):2148–2158.

Wilding, M. C., Benmore, C. J., & Weber, J. K. R. (2010). Changes in the local environment surrounding magnesium ions in fragile MgO-SiO2 liquids. *Europhysics Letters*, **89**(2):26005.

Wilding, M. C., Benmore, C. J., & Weber, J. R. (2008). In situ diffraction studies of magnesium silicate liquids. *Journal of Materials Science*, **43**(14):4707–4713.

Williams, E., Brousseau, E. B., & Rees, A. (2014). Nanosecond Yb fibre laser milling of aluminium: effect of process parameters on the achievable surface finish and machining efficiency. *The International Journal of Advanced Manufacturing Technology*, **74**(5):769–780.

Williams, Q. (1995). Infrared, Raman and Optical Spectroscopy of Earth Materials. *In:* Ahrens, T. J. (ed.), *Mineral Physics & Crystallography: A Handbook of Physical Constants*, *AGU Reference Shelf*, vol. 2, pp. 291–302. American Geophysical Union, Washington, DC. ISBN 9781118668191.

Williams, Q. & Garnero, E. J. (1996). Seismic evidence for partial melt at the base of Earth's mantle. *Science*, **273**(5281):1528–1530.

Williamson, G. K. & Hall, W. H. (1953). X-ray line broadening from filed aluminium and wolfram. *Acta Metallurgica*, **1**(1):22–31.

Willmott, P. (2019). *An Introduction to Synchrotron Radiation: Techniques and Applications*. John Wiley & Sons, 2nd edn. ISBN 9781119280453.

Wojdyr, M. (2010). Fityk: A general-purpose peak fitting program. *Journal of Applied Crystallography*, **43**(5-1):1126–1128.

Wolf, A. S., Jackson, J. M., Dera, P., & Prakapenka, V. B. (2015). The thermal equation of state of (Mg,Fe)SiO3 bridgmanite (perovskite) and implications for lower mantle structures. *Journal of Geophysical Research: Solid Earth*, **120**(11):7460–7489.

Wood, B. J. & Corgne, A. (2015). Mineralogy of the Earth: Trace Elements and Hydrogen in the Earth's Transition Zone and Lower Mantle. *In:* Schubert, G. (ed.), *Treatise on Geophysics*, vol. 2, chap. 4, pp. 61–84. Elsevier, Oxford, second edition edn. ISBN 978-0-444-53803-1. doi:10.1016/B978-0-444-53802-4.00031-2.

Wookey, J. & Kendall, J.-M. (2007). Seismic anisotropy of post-perovskite and the lowermost mantle. *In:* Hirose, K., Brodholt, J., Lay, T., & Yuen, D. (eds.), *Post-Perovskite: The Last Mantle Phase Transition*, *American Geophysical Union (AGU) Geophysical Monograph Series*, vol. 174,

pp. 171–189. American Geophysical Union, Washington, DC. ISBN 9781118666401. doi:10.1029/174GM13.

Wookey, J., Stackhouse, S., Kendall, J.-M., Brodholt, J., & Price, G. D. (2005). Efficacy of the post-perovskite phase as an explanation for lowermost-mantle seismic properties. *Nature*, **438**(7070):1004–1007.

Wu, Y., Wu, X., Lin, J.-F., McCammon, C. A., Xiao, Y., Chow, P., Prakapenka, V. B., Yoshino, T., Zhai, S., & Qin, S. (2016a). Spin transition of ferric iron in the NAL phase: Implications for the seismic heterogeneities of subducted slabs in the lower mantle. *Earth and Planetary Science Letters*, **434**:91–100.

Wu, Y., Yang, J., Wu, X., Song, M., Yoshino, T., Zhai, S., Qin, S., Huang, H., & Lin, J.-F. (2016b). Elasticity of single-crystal NAL phase at high pressure: A potential source of the seismic anisotropy in the lower mantle. *Journal of Geophysical Research: Solid Earth*, **121**(8):5696–5707.

Xu, C. & Inoue, T. (2019). Phase relations in MAFSH system up to 21 GPa: Implications for water cycles in Martian interior. *Minerals*, **9**(9):559.

Xu, C., Nishi, M., & Inoue, T. (2019). Solubility behavior of δ-AlOOH and ε-FeOOH at high pressures. *American Mineralogist: Journal of Earth and Planetary Materials*, **104**(10):1416–1420.

Xu, F., Yamazaki, D., Sakamoto, N., Sun, W., Fei, H., & Yurimoto, H. (2017). Silicon and oxygen self-diffusion in stishovite: Implications for stability of SiO2-rich seismic reflectors in the mid-mantle. *Earth and Planetary Science Letters*, **459**:332–339.

Xu, J. A., Mao, H. K., & Bell, P. M. (1986). High-pressure ruby and diamond fluorescence: observations at 0.21 to 0.55 terapascal. *Science*, **232**(4756):1404–1406.

Xue, X., Kanzaki, M., Trønnes, R. G., & Stebbins, J. F. (1989). Silicon coordination and speciation changes in a silicate liquid at high pressures. *Science*, **245**(4921):962–964.

Yagafarov, O. F., Katayama, Y., Brazhkin, V. V., Lyapin, A. G., & Saitoh, H. (2012). Energy dispersive x-ray diffraction and reverse Monte Carlo structural study of liquid gallium under pressure. *Physical Review B*, **86**(17):174103.

Yamada, A., Inoue, T., Urakawa, S., Funakoshi, K.-i., Funamori, N., Kikegawa, T., Ohfuji, H., & Irifune, T. (2007). In situ X-ray experiment on the structure of hydrous Mg-silicate melt under high pressure and high temperature. *Geophysical Research Letters*, **34**(10).

Yamada, A., Wang, Y., Inoue, T., Yang, W., Park, C., Yu, T., & Shen, G. (2011). High-pressure x-ray diffraction studies on the structure of liquid silicate using a Paris–Edinburgh type large volume press. *Review of Scientific Instruments*, **82**(1):015103.

Yamazaki, D., Ito, E., Yoshino, T., Tsujino, N., Yoneda, A., Gomi, H., Vazhakuttiyakam, J., Sakurai, M., Zhang, Y., Higo, Y., & Tange, Y. (2019). High-pressure generation in the Kawai-type multianvil apparatus equipped with tungsten-carbide anvils and sintered-diamond anvils,

and X-ray observation on $CaSnO_3$ and (Mg,Fe)SiO_3. *Comptes Rendus Geoscience*, **351**(2-3):253–259.

Yamazaki, D., Ito, E., Yoshino, T., Tsujino, N., Yoneda, A., Guo, X., Xu, F., Higo, Y., & Funakoshi, K. (2014). Over 1 Mbar generation in the Kawai-type multianvil apparatus and its application to compression of $(Mg_{0.92}Fe_{0.08})SiO_3$ perovskite and stishovite. *Physics of the Earth and Planetary Interiors*, **228**:262–267.

Yamazaki, D. & Karato, S.-i. (2001). Some mineral physics constraints on the rheology and geothermal structure of Earth's lower mantle. *American Mineralogist*, **86**(4):385–391.

Yang, J., Lin, J.-F., Jacobsen, S. D., Seymour, N. M., Tkachev, S. N., & Prakapenka, V. B. (2016). Elasticity of ferropericlase and seismic heterogeneity in the Earth's lower mantle. *Journal of Geophysical Research: Solid Earth*, **121**(12):8488–8500.

Yang, J., Tong, X., Lin, J.-F., Okuchi, T., & Tomioka, N. (2015). Elasticity of ferropericlase across the spin crossover in the Earth's lower mantle. *Scientific Reports*, **5**(1):1–9.

Yang, L., Karandikar, A., & Boehler, R. (2012). Flash heating in the diamond cell: Melting curve of rhenium. *Review of Scientific Instruments*, **83**(6):063905.

Yang, R. & Wu, Z. (2014). Elastic properties of stishovite and the CaCl2-type silica at the mantle temperature and pressure: An ab initio investigation. *Earth and Planetary Science Letters*, **404**:14–21.

Yasa, E. & Kruth, J.-P. (2010). Investigation of laser and process parameters for Selective Laser Erosion. *Precision Engineering*, **34**(1):101–112.

Yen, C. E., Williams, Q., & Kunz, M. (2020). Thermal pressure in the laser-heated diamond anvil cell: A quantitative study and implications for the density versus mineralogy correlation of the mantle. *Journal of Geophysical Research: Solid Earth*, **125**(10).

Yin, C. D., Okuno, M., Morikawa, H., Marumo, F., & Yamanaka, T. (1986). Structural analysis of CaSiO3 glass by X-ray diffraction and Raman spectroscopy. *Journal of Non-crystalline Solids*, **80**(1-3):167–174.

Yu, T., Prescher, C., Ryu, Y. J., Shi, F., Greenberg, E., Prakapenka, V., Eng, P., Stubbs, J., Kono, Y., Shen, G., Watson, H., Rivers, M. L., Sutton, S. R., & Wang, Y. (2019). A Paris-Edinburgh Cell for High-Pressure and High-Temperature Structure Studies on Silicate Liquids Using Monochromatic Synchrotron Radiation. *Minerals*, **9**(11):715.

Yuan, H., Zhang, L., Ohtani, E., Meng, Y., Greenberg, E., & Prakapenka, V. B. (2019). Stability of Fe-bearing hydrous phases and element partitioning in the system MgO–Al2O3–Fe2O3–SiO2–H2O in Earth's lowermost mantle. *Earth and Planetary Science Letters*, **524**:115714.

Yuan, K. & Romanowicz, B. (2017). Seismic evidence for partial melting at the root of major hot spot plumes. *Science*, **357**(6349):393–397.

Yuan, L., Ohtani, E., Ikuta, D., Kamada, S., Tsuchiya, J., Naohisa, H., Ohishi, Y., & Suzuki, A. (2018). Chemical reactions between Fe and H2O up to megabar pressures and implications for water storage in the Earth's mantle and core. *Geophysical Research Letters*, **45**(3):1330–1338.

Zaghoo, M. & Silvera, I. F. (2017). Conductivity and dissociation in liquid metallic hydrogen and implications for planetary interiors. *Proceedings of the National Academy of Sciences*, **114**(45):11873–11877.

Zeidler, A., Wezka, K., Rowlands, R. F., Whittaker, D. A. J., Salmon, P. S., Polidori, A., Drewitt, J. W. E., Klotz, S., Fischer, H. E., Wilding, M. C., Bull, C. L., Tucker, M. G., & Wilson, M. (2014). High-pressure transformation of SiO2 glass from a tetrahedral to an octahedral network: A joint approach using neutron diffraction and molecular dynamics. *Physical Review Letters*, **113**(13):135501.

Zeng, Z.-Y., Hu, C.-E., Cai, L.-C., Chen, X.-R., & Jing, F.-Q. (2010). Lattice dynamics and thermodynamics of molybdenum from first-principles calculations. *The Journal of Physical Chemistry B*, **114**(1):298–310.

Zeng, Z.-Y., Hu, C.-E., Cai, L.-C., Chen, X.-R., & Jing, F.-Q. (2011). Molecular dynamics study of the melting curve of NiTi alloy under pressure. *Journal of Applied Physics*, **109**(4):043503–043503.

Zha, C.-S. & Bassett, W. A. (2003). Internal resistive heating in diamond anvil cell for in situ X-ray diffraction and Raman scattering. *Review of Scientific Instruments*, **74**(3):1255–1262.

Zha, C.-s., Duffy, T. S., Downs, R. T., Mao, H.-k., & Hemley, R. J. (1998). Brillouin scattering and X-ray diffraction of San Carlos olivine: direct pressure determination to 32 GPa. *Earth and Planetary Science Letters*, **159**(1-2):25–33.

Zha, C.-S., Mao, H.-k., & Hemley, R. J. (2000). Elasticity of MgO and a primary pressure scale to 55 GPa. *Proceedings of the National Academy of Sciences*, **97**(25):13494–13499.

Zha, C.-S., Mibe, K., Bassett, W. A., Tschauner, O., Mao, H.-K., & Hemley, R. J. (2008). P-V-T equation of state of platinum to 80 GPa and 1900 K from internal resistive heating/X-ray diffraction measurements. *Journal of Applied Physics*, **103**(5):054908.

Zhang, D., Jackson, J. M., Zhao, J., Sturhahn, W., Alp, E. E., Hu, M. Y., Toellner, T. S., Murphy, C. A., & Prakapenka, V. B. (2016). Temperature of Earth's core constrained from melting of Fe and Fe0.9Ni0.1 at high pressures. *Earth and Planetary Science Letters*, **447**:72–83.

Zhang, J. S. & Bass, J. D. (2016). Sound velocities of olivine at high pressures and temperatures and the composition of Earth's upper mantle. *Geophysical Research Letters*, **43**(18):9611–9618.

Zhang, J. S., Bass, J. D., & Zhu, G. (2015). Single-crystal Brillouin spectroscopy with CO2 laser heating and variable q. *Review of Scientific Instruments*, **86**(6):063905.

Zhang, Y., Fu, S., Wang, B., & Lin, J.-F. (2021). Elasticity of a Pseudoproper Ferroelastic Transition from Stishovite to Post-Stishovite at High Pressure. *Physical Review Letters*, **126**(2):025701.

Zhu, C., Byrd, R. H., Lu, P., & Nocedal, J. (1997). Algorithm 778: L-BFGS-B: Fortran subroutines for large-scale bound-constrained optimization. *ACM Transactions on Mathematical Software (TOMS)*, **23**(4):550–560.

Zindler, A. & Hart, S. (1986). Chemical Geodynamics. *Annual Review of Earth and Planetary Sciences*, **14**(1):493–571.

Appendices

Appendix A

Supplementary Information for Chapter 2

A.1 Supplementary Figures for Chapter 2

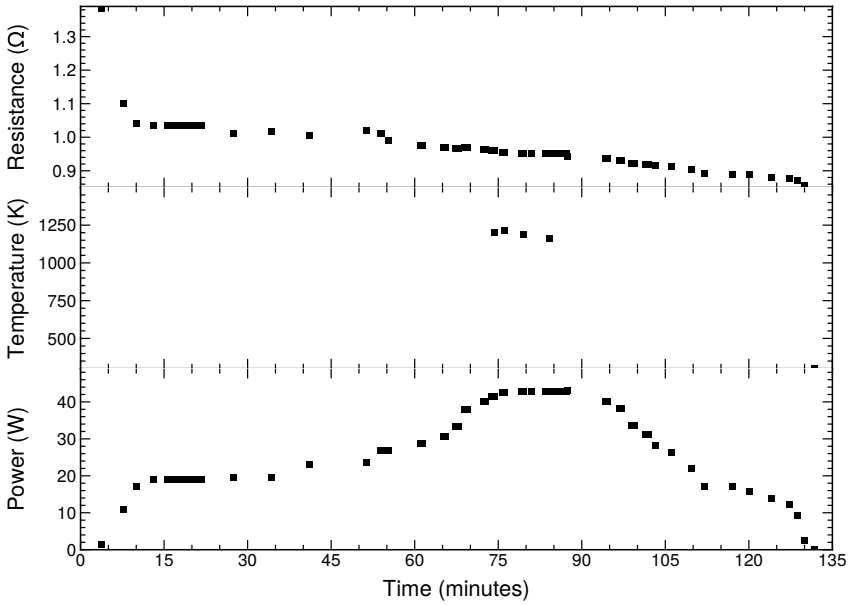

Figure A.1: *Plot of electrical power, measured sample temperature, and circuit resistance over the duration of experiment #3a.*

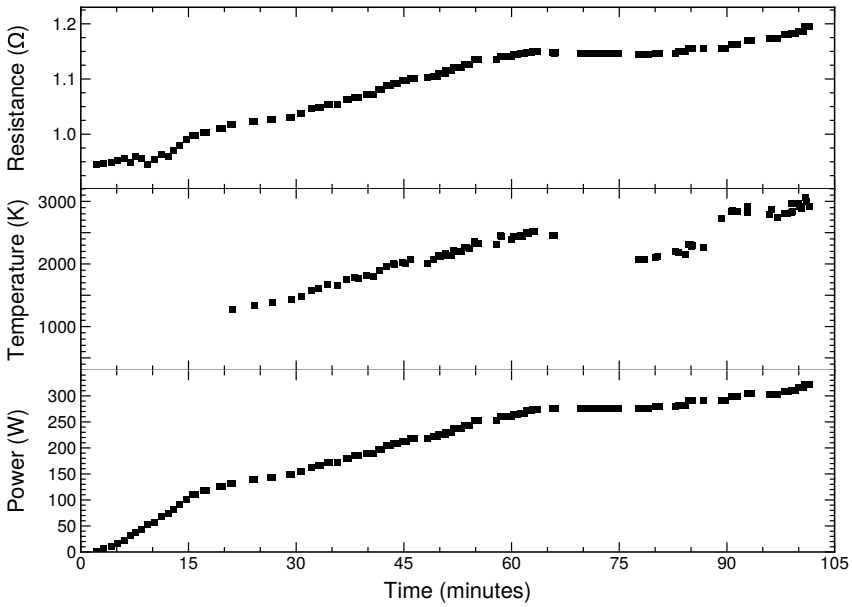

Figure A.2: *Plot of electrical power, measured sample temperature, and circuit resistance over the duration of experiment #5c.*

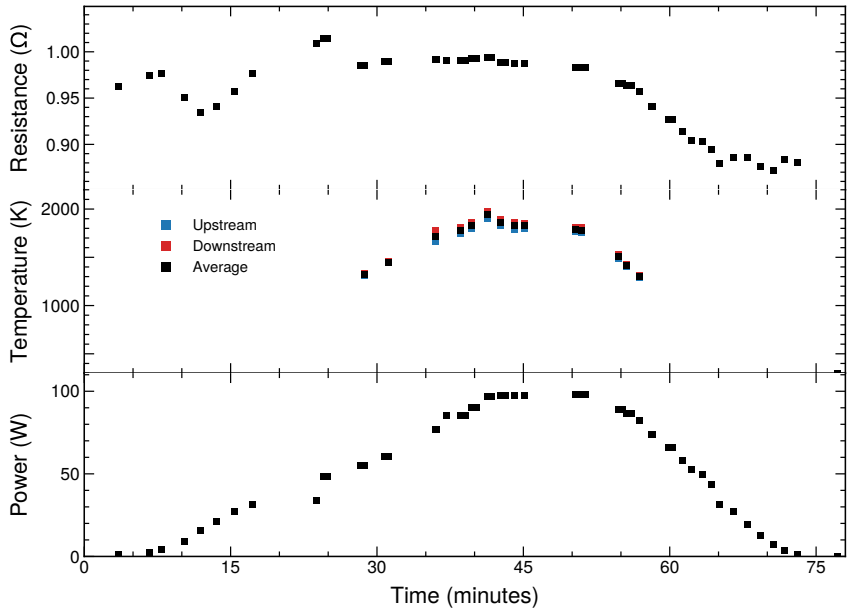

Figure A.3: *Plot of electrical power, measured sample temperature, and circuit resistance over the duration of experiment #6a.*

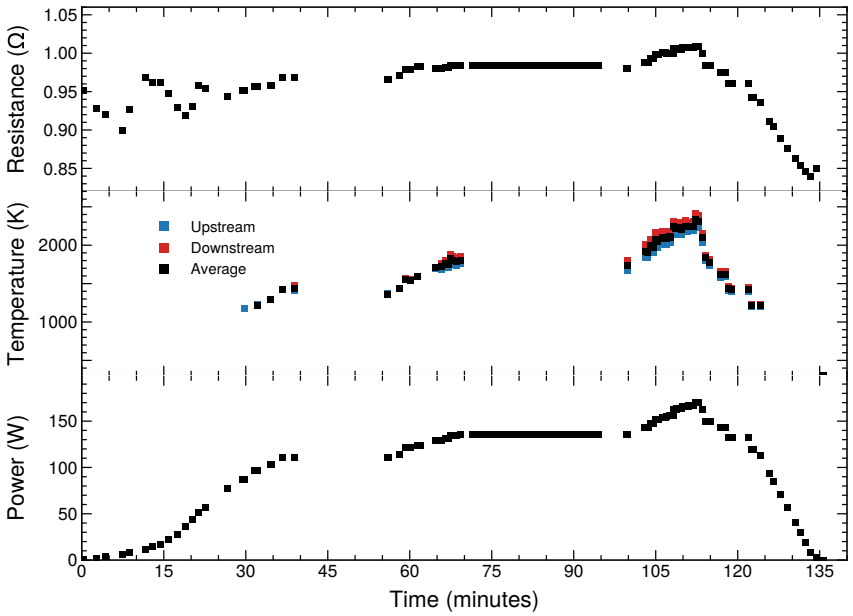

Figure A.4: *Plot of electrical power, measured sample temperature, and circuit resistance over the duration of experiment #6b.*

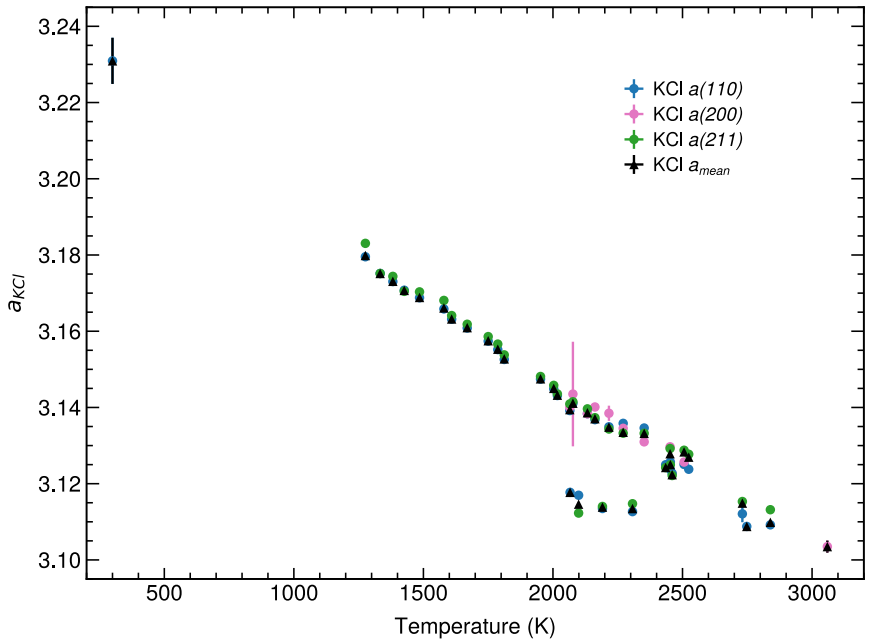

Figure A.5: *Plot of temperature vs KCl unit cell parameter, a_{KCl}, in experiment #5c. There is a linear reduction in cell volume with temperature due to the heating geometry in IRH experiments (which is essentially opposite to a laser-heating experiment). Heat is generated around the sample (instead of from within) in the filament, which thermally expands, compressing the sample further.*

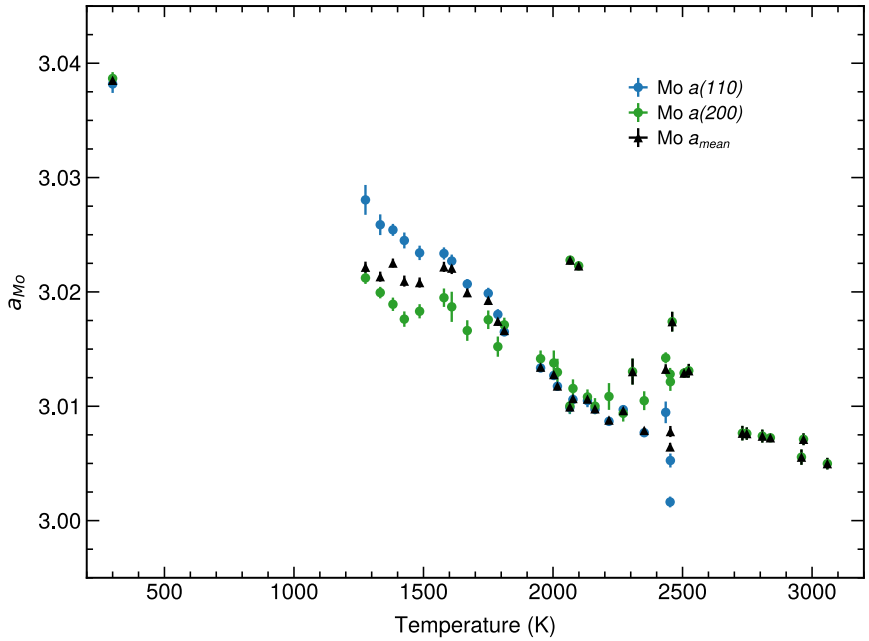

Figure A.6: *Plot of temperature vs Mo unit cell parameter, a_{Mo}, in experiment #5c. There is a linear reduction in cell volume with temperature due to the heating geometry in IRH experiments (which is essentially opposite to a laser-heating experiment). Heat is generated around the sample (instead of from within) in the filament, which thermally expands, compressing the sample further.*

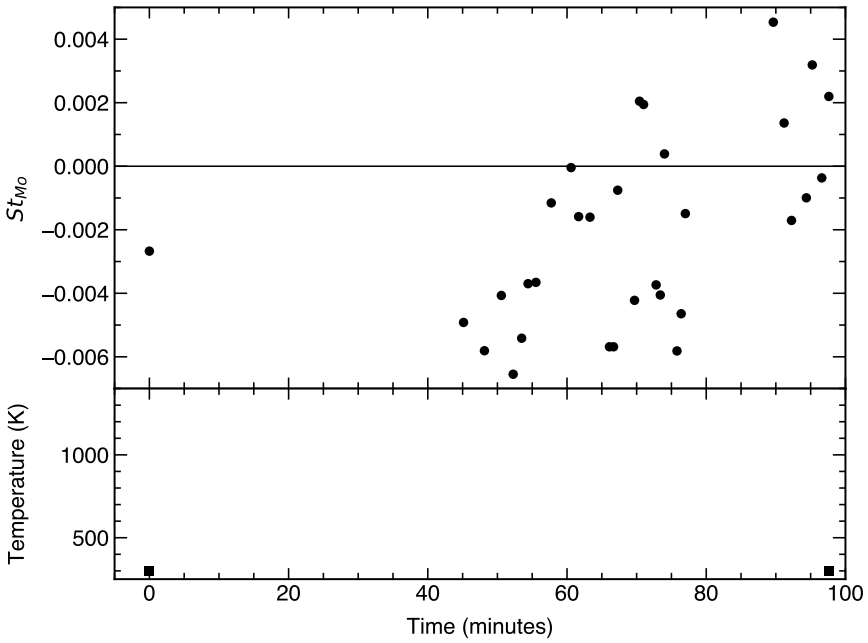

Figure A.7: *Stress indicator values, St, of Mo derived from gamma plots for experiment #5a along with measured temperature plotted as a function of experiment duration*

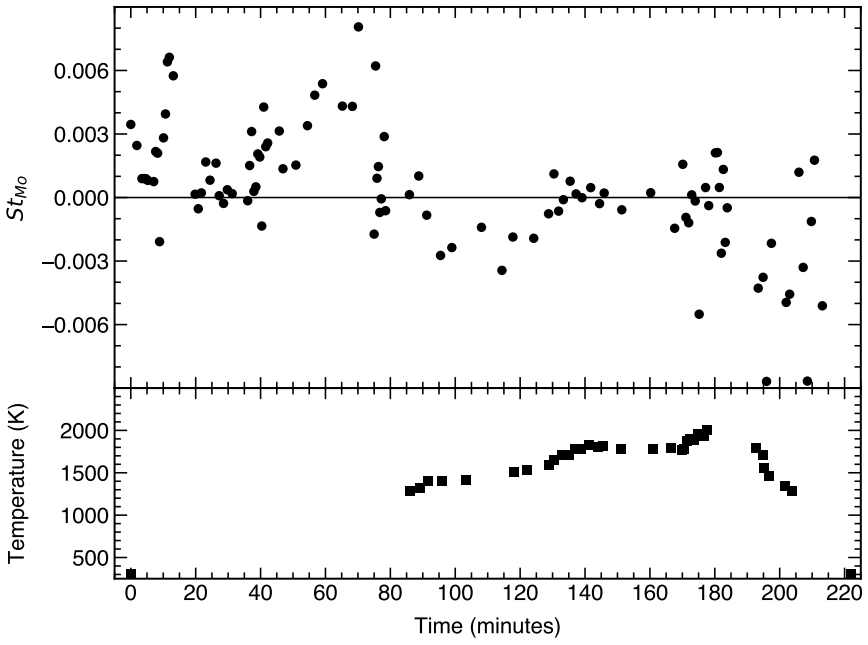

Figure A.8: *Stress indicator values, St, of Mo derived from gamma plots for experiment #5b along with measured temperature plotted as a function of experiment duration*

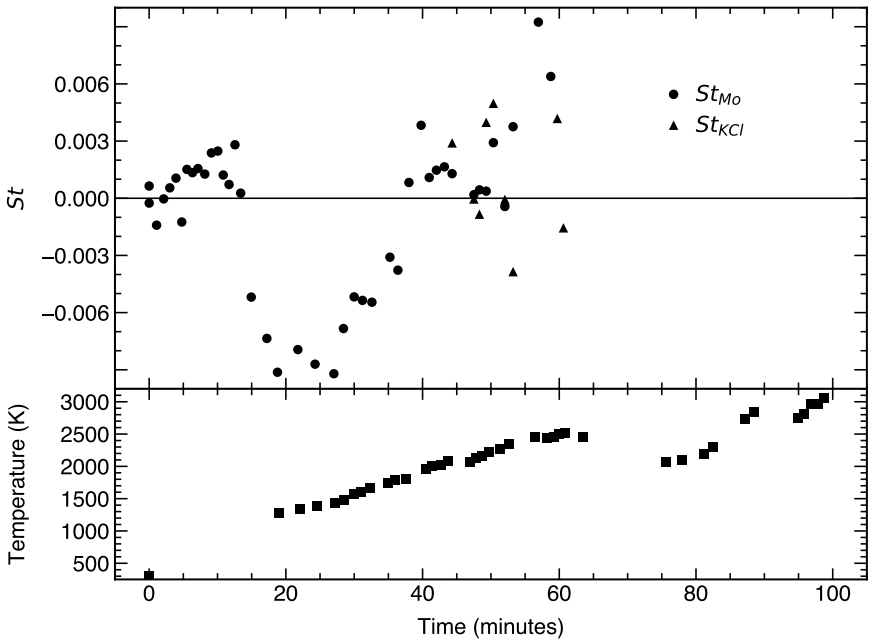

Figure A.9: *Stress indicator values, St, of Mo and KCl derived from gamma plots for experiment #5c along with measured temperature plotted as a function of experiment duration*

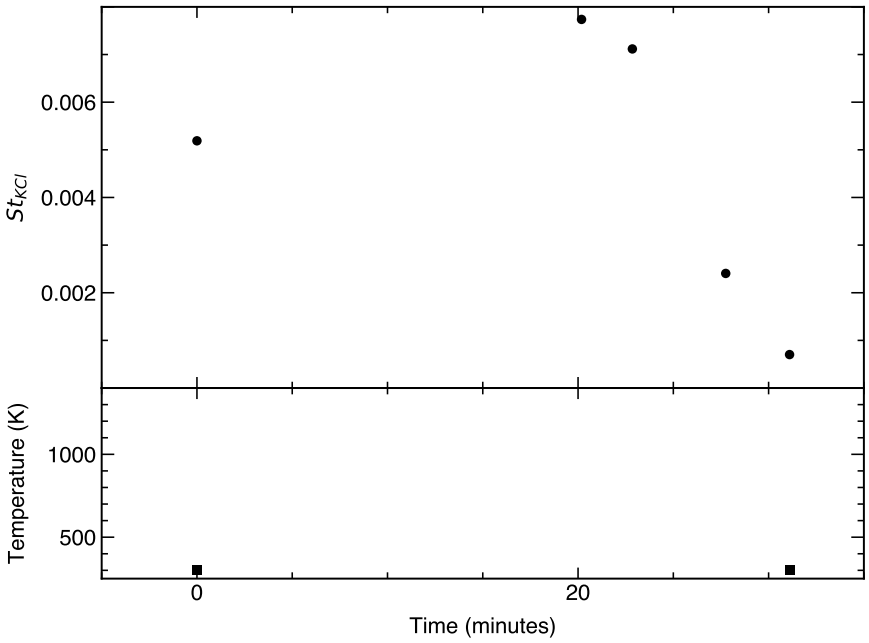

Figure A.10: *Stress indicator values, St, of KCl derived from gamma plots for experiment #4a along with measured temperature (although temperature in this experiment was too low to measure with spectroradiometry) plotted as a function of experiment duration*

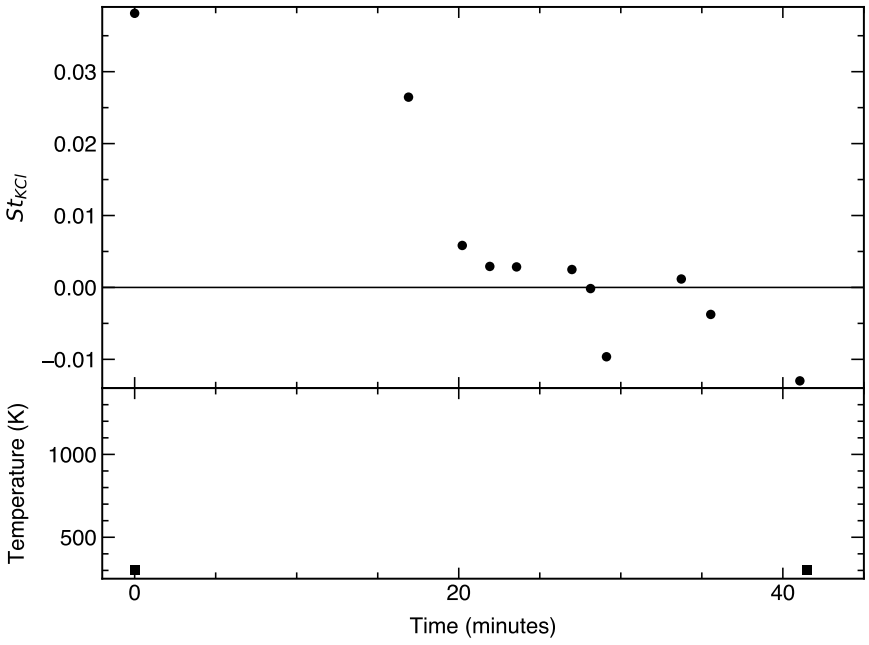

Figure A.11: *Stress indicator values, St, of KCl derived from gamma plots for experiment #4b along with measured temperature (although temperature in this experiment was too low to measure with spectroradiometry) plotted as a function of experiment duration*

A.2 Supplementary Data for Chapter 2

The electrical data, measured temperatures, and refined unit cell volumes for the experiments performed at Diamond Light Source described in chapter 2 are archived online in the supplementary materials of Heinen et al. (2021). These are directly available at: `https://aip.scitation.org/doi/suppl/10.1063/5.0038917`

Appendix B

Laser Micro-Machining Process Parameters

B.1 IRH Filaments

B.1.1 Titanium IRH Filaments

Ti Filament

Operation	Cut
Shape	Custom (G-code)
PRF	3 kHz
Power	1.5 %
Cut speed	0.03 mm/sec
Passes	11

B.1.2 Rhenium IRH Filaments

Sample chamber

Operation	Drill
PRF	0.2 kHz
Power	60 %
Drill time	0.08 sec

Re Filament

Operation	Cut
Shape	Custom (G-code)
PRF	5 kHz
Power	2.5 %
Cut speed	0.1 mm/sec
Passes	42

B.2 IRH Gaskets

B.2.1 Stainless Steel (0.25 mm thick) IRH Gaskets

M1 Holes

Operation	Cut
Shape	1 mm dia. circle
PRF	3 kHz
Power	57 %
Cut speed	4 mm/sec
Passes	625

Stainless Steel Gasket

Operation	Cut
Shape	Custom (G-code)
PRF	3 kHz
Power	57 %
Cut speed	4 mm/sec
Passes	680

B.2.2 Slots in IRH Gaskets

The slots splitting the stainless steel IRH gaskets in half are cut after the gasket is indented. The slots are milled and are 100 µm wide. As the indentation results in variable thickness of the gasket the slots are milled in three stages: 1) A thinned region from the culet edge to ∼0.05 to 0.06 mm from the culet edge, 2) A thickened region from the thin region to the indentation edge (generally ∼0.15 mm from the culet edge), 3) The main region through the 0.25 mm thick gasket unaffected by the indentation.

Main slots

Operation	Mill
Shape	0.1 mm wide
PRF	3 kHz
Power	50 %
Cut speed	4 mm/sec
(Double) Passes	53
Hatch pitch	0.005 mm
Z step	0.005 mm

Thick region

Operation	Mill
Shape	0.1 mm wide
PRF	5 kHz
Power	10 %
Cut speed	4 mm/sec
(Double) Passes	125
Hatch pitch	0.005 mm
Z step	0.003 mm

Thin region

Operation	Mill
Shape	0.1 mm wide
PRF	5 kHz
Power	4 %
Cut speed	4 mm/sec
(Double) Passes	105
Hatch pitch	0.005 mm
Z step	0.003 mm

B.2.3 IRH Pressure Chamber and Culet Slots

The culet geometry of IRH experiments is cut at low power to prevent thermal distortion of the stainless steel. To cut through at lower power the cuts are also performed in a sequence with progressively lower power. The central pressure chamber is also cut using a polishing method, where a slightly smaller diameter hole is first cut at a higher power, and then the final diameter at a lower power. This helps cut away the heat affected zone. The slots are cut to slightly overlap the epoxy filled slots in the gasket to ensure no material (and circuit) exists at the culet edges.

1: Pressure chamber

Operation	Cut
Shape	0.147 mm dia. circle
PRF	3 kHz
Power	4 %
Cut speed	0.17 mm/sec
Passes	24

2: 2 × slots

Operation	Cut
Shape	0.08 × 0.18 mm (500 µm culet) or 0.08 × 0.13 mm (400 µm culet)
PRF	3 kHz
Power	4 %
Cut speed	0.17 mm/sec
Passes	24

3: 2 × slots

Operation	Cut
Shape	0.08 × 0.18 mm (500 µm culet) or 0.08 × 0.13 mm (400 µm culet)
PRF	3 kHz
Power	3 %
Cut speed	0.17 mm/sec
Passes	20

4: Pressure chamber

Operation	Cut
Shape	0.149 mm dia. circle
PRF	3 kHz
Power	3 %
Cut speed	0.17 mm/sec
Passes	20

5: 2 × slots

Operation	Cut
Shape	0.08 × 0.18 mm (500 µm culet) or 0.08 × 0.13 mm (400 µm culet)
PRF	3 kHz
Power	2 %
Cut speed	0.17 mm/sec
Passes	15

6: Pressure chamber

Operation	Cut
Shape	0.149 mm dia. circle
PRF	3 kHz
Power	2 %
Cut speed	0.17 mm/sec
Passes	17

B.2.4 Etching Stainless Steel Gaskets

Etching (stainless)

Operation	Cut
Shape	Custom (mm scale)
PRF	100 kHz
Power	4 %
Cut speed	5 mm/sec
Passes	100

B.3 Polycrystalline Alumina Insulation

B.3.1 Insulation for Ti Ribbon Filaments

Depression for Ti filament in ∼50 µm alumina

Operation	Mill
Shape	0.03 mm wide
PRF	0.2 kHz
Power	25 %
Cut speed	0.09 mm/sec
(Double) Passes	2
Hatch pitch	0.005 mm
Z step	0 mm

50 µm thick alumina insulation 'pills'

Operation	Cut
Shape	0.147 mm dia. circle
PRF	0.2 kHz
Power	50 %
Cut speed	0.1 mm/sec
Passes	30

B.3.2 Insulation 'blocks' for Culet Slots

∼75 µm thick alumina insulation 'blocks'

Operation	Cut
Shape	0.065 × 0.12 mm (400 µm culet) or 0.065 × 0.17 mm (500 µm culet)
PRF	0.2 kHz
Power	45 %
Cut speed	0.1 mm/sec
Passes	11

B.3.3 Insulation 'doughnuts'* for Sample Isolation

~25 µm thick alumina insulation 'doughnuts': Milling from 50 µm thickness

Operation	Mill
Shape	1.1 × 1.1 mm
PRF	0.2 kHz
Power	16 %
Cut speed	0.1 mm/sec
(Double) Passes	17
Hatch pitch	0.003 mm
Z step	0 mm

~25 µm thick alumina insulation 'doughnuts': External diameter

Operation	Cut
Shape	0.135–0.145 mm dia. circle
PRF	0.2 kHz
Power	25 %
Cut speed	0.1 mm/sec
Passes	8

~25 µm thick alumina insulation 'doughnuts': Internal diameter

Operation	Cut
Shape	0.03 mm dia. circle
PRF	0.2 kHz
Power	25 %
Cut speed	0.06 mm/sec
Passes	5

*It has been pointed out that they look a little bit more like Cheerios